Molecular Magnetism:

The Design, Synthesis, and Characterization of New Building Blocks for Molecule-based Magnetic Materials

by

Nicholas J. Hurley

A thesis submitted to the Department of Chemistry
in partial fulfillment of the requirements for the degree of
Master of Science

Supervised by
Professor M. Pilkington
Brock University
St. Catharines, Ontario, Canada
July 2012

I dedicate this thesis to my grandparents:

Joan Hurley

&

Alexander J. Hurley

Mary Timbrell (June 28th, 1926 - January 12th, 2000)

&

Dennis Timbrell (April 10th, 1926 - January 17th, 2011)

Abstract

Two classes of building blocks have been prepared and characterized and their coordination chemistry explored working towards the preparation of new molecule-based magnetic materials. In the first project, the amine functionality of 3,3'-diamino-2,2'-bipyridine was exploited for the preparation of a new family of ligands **(H_2L^1)-(H_2L^4)**. The molecular structures of three ligands have been fully characterized by X-ray crystallography.

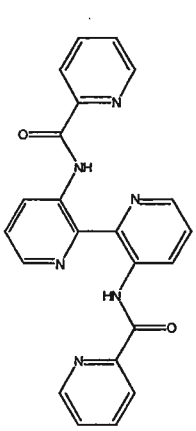

(H_2L^1)

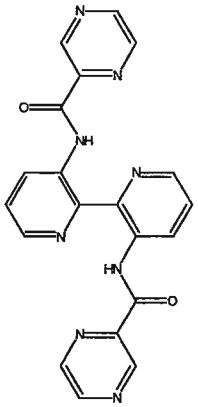

(H_2L^2)

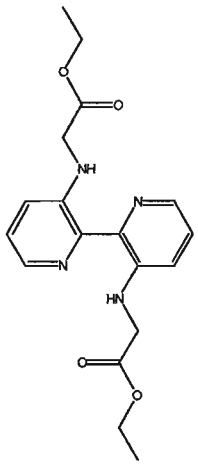

(H_2L^3)

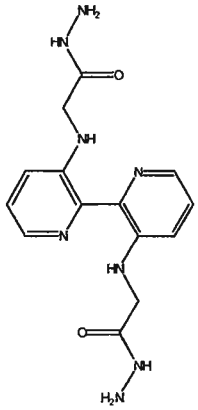

(H_2L^4)

The coordination chemistry of these ligands with divalent first row transition metal ions was investigated. For ligand **(H_2L^1)**, the molecular structures of four coordination complexes with stoichiometries $[Zn_2(L^1)(OAc)(MeO)]_2$ **(I)**, $[Cu_2(L^1)(OAc)_2]$ **(II)**, $[Ni(L^1)]_3$ **(III)**, and $[Ni(L^1)]_3$ **(IV)** were determined by X-ray crystallography. For ligand **(H_2L^2)**, a Cu(II) complex of stoichiometry $[Cu_3(L^2)(OAc)_3MeO]$ **(V)** was determined by X-ray crystallography. The magnetic properties of complexes **(II)**, **(III)**, and **(V)** have been fully elucidated.

In project two, synthetic strategies for the preparation of porphyrin molecules bearing triol substituents is presented. Following this approach, three new porphyrin derivatives have been prepared and characterized [Zn(HPTPP-$CH_2C(CH_2OH)_3$)] **(VI)**, $[P(TPP)(OCH_2C(CH_2OH)_3)_2]^+Cl^-$ **(VII)**, and $[P(OEP)(C_6H_5)(OCH_2C(CH_2OH)_3)]^+Cl^-$ **(VIII)**. Attempts to exchange the labile methoxide bridges of a tetrairon^{III} single molecule magnet of stoichiometry $[Fe_4(OMe)_6(dpm)_6]$ (Hdpm = dipivaloylmethane) with the triol appended porphyrins will be discussed.

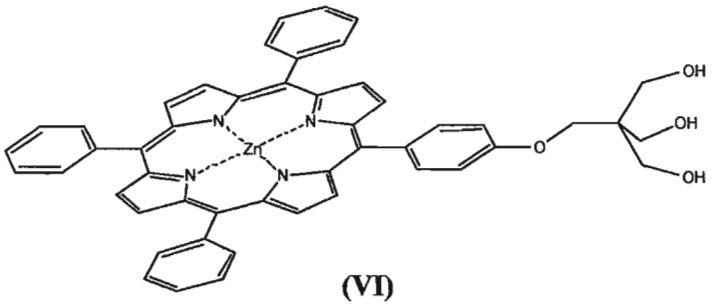

(VI)

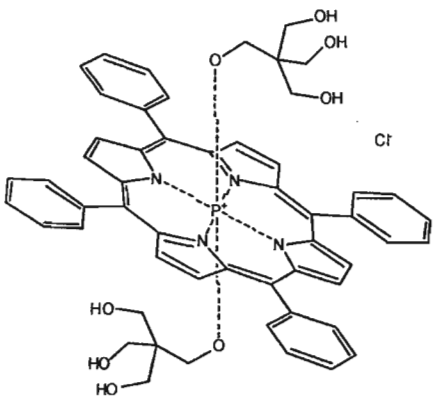

(VII)

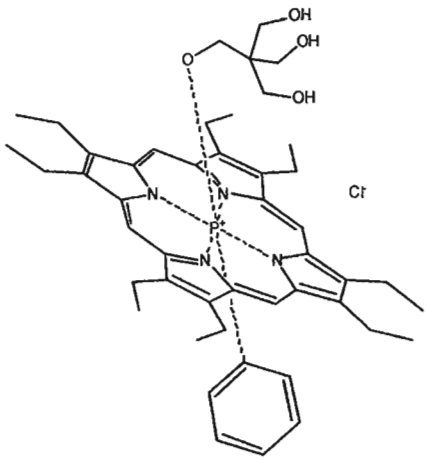

(VIII)

Acknowledgements

First and foremost, I would like to thank Professor M. Pilkington for giving me the opportunity to continue my graduate studies at Brock University. Without her meaningful guidance this thesis project would not have been possible. Her continued support and encouragement shall not be forgotten.

I would also like to thank Professor J. Atkinson and Professor G. Nikonov for their roles as members of my supervisory committee. Many thanks are in order to Roger Gumbau-Brisa, Roland Acha, and Dr. Prashanth Poddutoori for their insight into many important aspects of my projects. Thanks to past and present members of the Pilkington research group: Shari Venneri, Peter Fenlon, Emma Gavey, Niloofar Zarrabi, Justin Wilson and Leila Munro.

Thanks to Professor M. Lemaire and Dr. M. Murrie (University of Glasgow) for their help with magnetic susceptibility measurements. Thanks to Sam Mula for his help with EPR measurements. Thanks also to Tim Jones and Razvan Simionescu for the countless mass spectrometry and nuclear magnetic resonance experiments.

I also wish to thank Dr. J. M. Rawson (University of Windsor) for his help with magnetic modelling.

Finally, I wish to thank my family for their moral support and encouragement throughout my years at Brock University.

Table of Contents

List of Tables

List of Figures

List of Schemes

List of Compounds

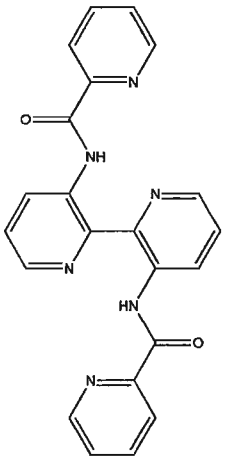

(H_2L^1) (2.1)

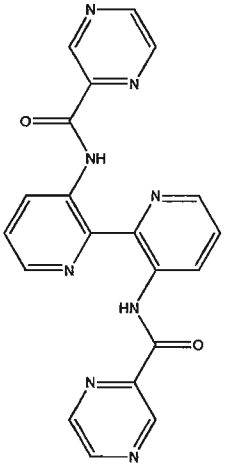

(H_2L^2) (2.2)

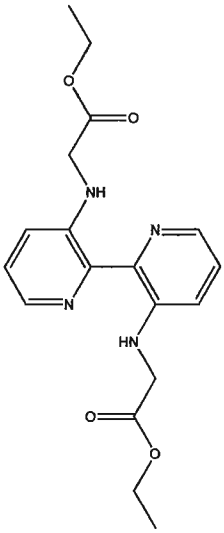

(H_2L^3) (2.3)

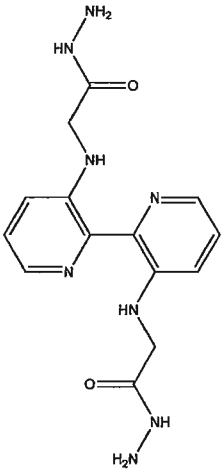

(H_2L^4) (2.4)

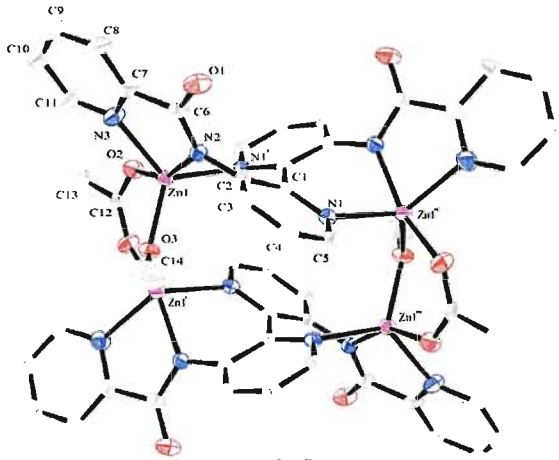

(2.6)

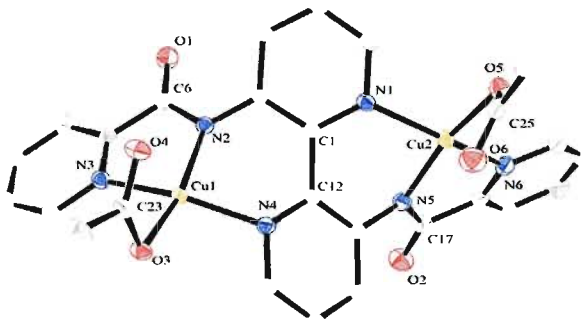

(2.7)

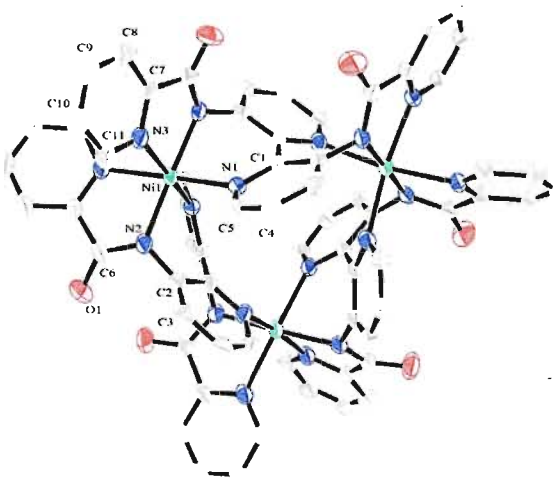

(2.8)

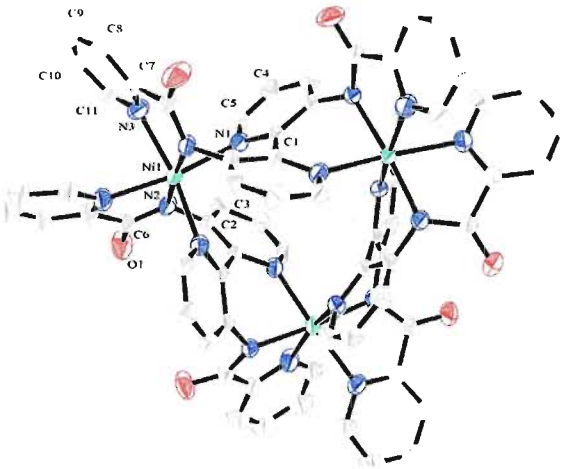

(2.9)

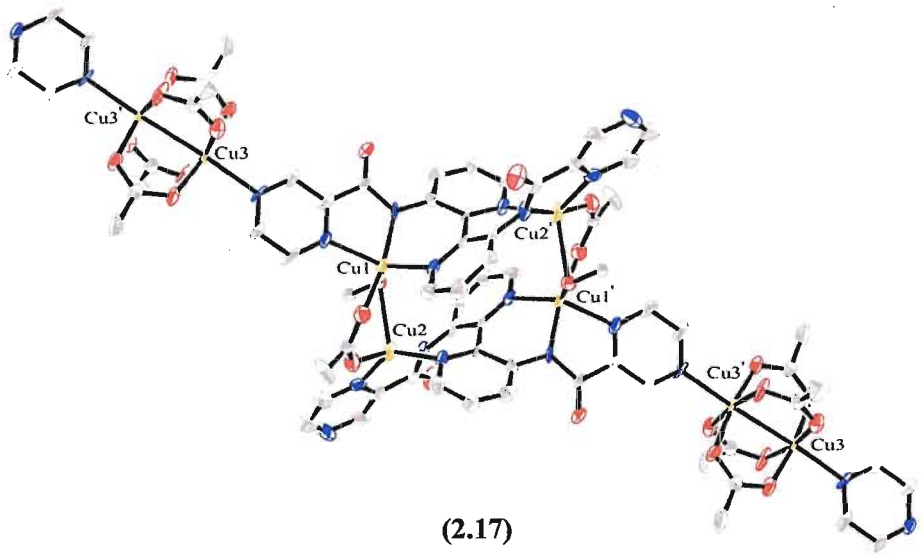
Cu3'
Cu3
Cu2'
Cu1
Cu1'
Cu2
Cu3'
Cu3

(2.17)

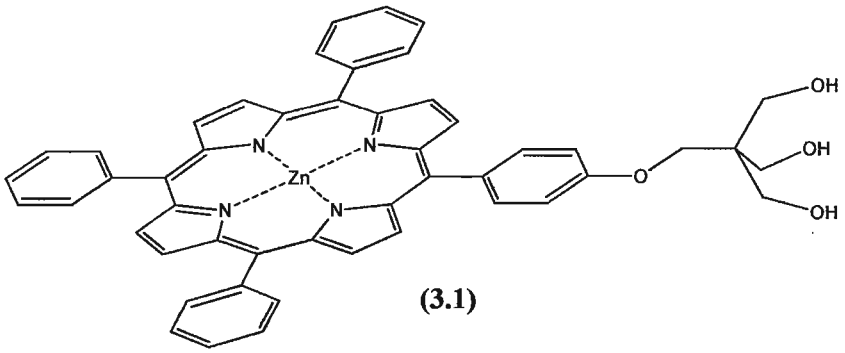
N
N
Zn
N
N
O
OH
OH
OH

(3.1)

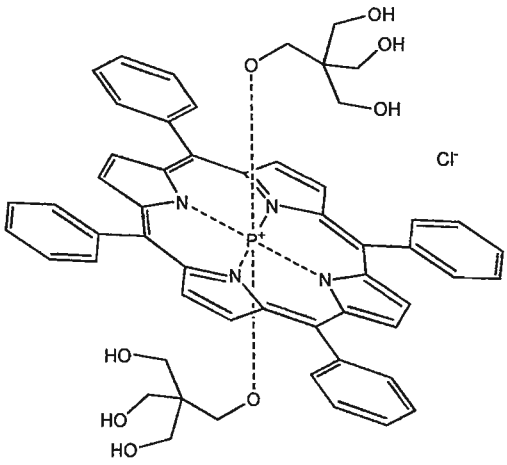
OH
OH
OH
O
Cl⁻
N
N
P⁺
N
N
HO
HO
HO
O

(3.2)

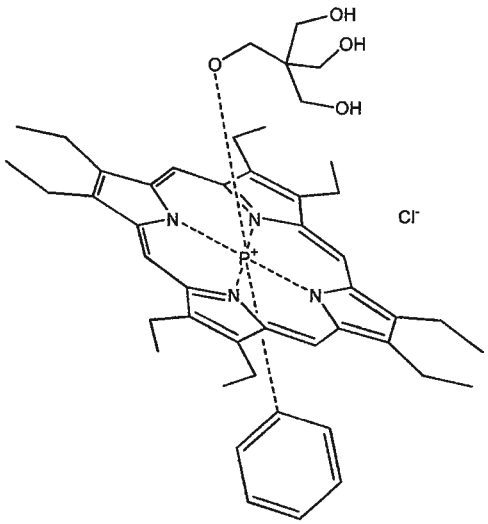
OH
OH
OH
O
Cl⁻
N
N
P⁺
N
N

(3.3)

List of Abbreviations

0-D	zero-dimensional
1-D	one-dimensional
2-D	two-dimensional
3-D	three-dimensional
Å	angstrom
AC	alternating current
amu	atomic mass unit
bipy	2,2'-bipyridine
br	broad (IR and NMR descriptor)
°C	degree Celsius
calcd	calculated
$CDCl_3$	deuterated chloroform
CH_3CN	acetonitrile
CN	cyanide
d	doublet (NMR)
DC	direct current
DCM	dichloromethane
dd	doublet of doublets (NMR)
DIEA	*N,N*-diisopropylethylamine
DMF	*N,N*-dimethylformamide
DMSO	dimethylsulfoxide
e	electron charge
EI	electron impact (MS)
emu	electromagnetic units
EPR	electron paramagnetic resonance
Et_3N	triethylamine
Et_2O	diethyl ether
EtOAc	ethyl acetate
EtOH	ethanol
FAB	fast atom bombardment (MS)

H	external magnetic field, spin Hamiltonian
H_c	coercive field
hfac	1,1,1,5,5,5-hexafluoroacetylacetonate
hr/hrs	hour/hours
IR	Infrared spectroscopy
J	coupling constant (NMR), magnetic exchange parameter
K	Kelvin
KBr	potassium bromide
m	multiplet (NMR)
MeO	methoxide
MeOD	deuterated methanol
MeOH	methanol
min/mins	minute/minutes
MLCT	metal to ligand charge transfer
mmol	millimole
mol	mole
m.p.	melting point
M_r	remnant magnetization
m_s	electron spin state
M_s	magnetic saturation
MS	mass spectrometry
m/z	mass/charge ratio (MS)
nm	nanometer
NMR	nuclear magnetic resonance
OAc	acetate
ORTEP	oak ridge thermal ellipsoid plot[153]
$PhPCl_2$	*P,P*-dichlorophenylphosphine
ppm	parts per million
py	pyridine
pz	pyrazine
R	agreement factor

RT	room temperature
s	singlet (NMR)
S	spin multiplicity
SCM	single chain magnet
sh	sharp (IR descriptor)
SMM	single molecule magnet
SQUID	superconducting quantum interference device
S_T	total spin state
str	stretch (IR)
t	triplet (NMR)
T	temperature
T_B	blocking temperature
T_c	critical temperature
THF	tetrahydrofuran
TLC	thin layer chromatography
UV-Vis	ultraviolet-visible light spectroscopy
δ	chemical shift
θ	Weiss constant
λ	wavelength
μ_B	Bohr magneton
χ	magnetic susceptibility
χ_M	molar magnetic susceptibility

Chapter 1 – Introduction

1.1 – Magnetism

From ancient times to the modern day and age, the discovery and subsequent utilization of magnetic materials has significantly impacted technological advancements, affecting mankind to some degree.[1,2] Discovered by the Chinese approximately one thousand years ago, the first device of such importance was the 'south-pointing' compass which exploited the properties of magnetite (a mixed-valence composite of iron oxide).[3] Magnetic devices have continued to impact the technological world ranging from acoustic devices, telecommunications, and electrical motors, to storage devices.[1,3,4] These modern-day magnetic materials are comprised mainly of magnetic alloys and oxides of metals (e.g. AlNiCo, SmCo, Fe_3O_4), and are commonly referred to as traditional magnets.

Many important mathematical expressions and theories were established by Dirac, Maxwell, Poisson, Weiss and Faraday in order to understand magnetism.[4] In 1873 Maxwell formulated a mathematical expression for the *flux density* of magnetic induction, B:

$$B = H + 4\pi M \tag{1}$$

where H is the *external magnetic field* and M is the *magnetization*. Magnetization is the magnetic moment per unit volume.[5] In many materials M is proportional to H:

$$M = \chi H \tag{2}$$

where χ is referred to as *magnetic susceptibility*, which is the ease of alignment of spins within a sample that is placed into an external magnetic field. Magnetic susceptibility is thus *magnetization vs. field.*

$$\chi = \mu_0 \frac{M}{B} = \frac{M}{H} \tag{3}$$

where μ_0 is the *permeability* of the sample. The material is classified as 'paramagnetic' if $\chi > 0$ and 'diamagnetic' if $\chi < 0$.[5]

Magnetic susceptibility measurements can also be carried out at varying temperatures and applied magnetic fields. Magnetic interactions are typically characterized by their responses to these variations.[4]

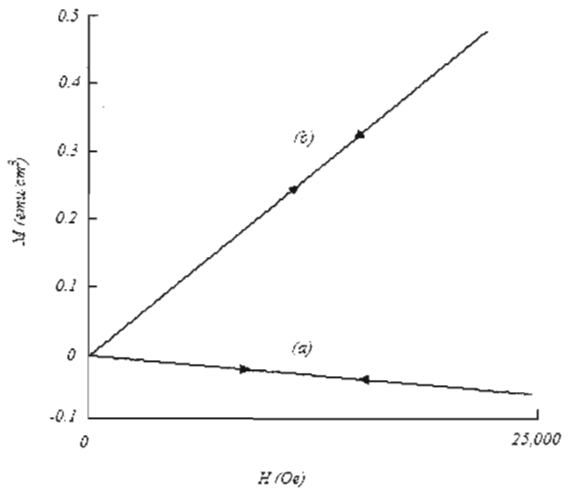

Figure 1.1: Magnetization *vs.* field plot for a) a diamagnetic material, and b) a paramagnetic material. Adapted from reference 5.

The elementary particles (proton, neutron, and electron) possess intrinsic angular momentum. Magnetism is intimately connected with this. The magnetic moment arising from nuclear motion is much less than that arising from the electron and in practice is often disregarded.[4] The electron is therefore the main source of magnetic moments in solids. It has two distinct sources of angular momentum, *orbital* and *spin*, Figure 1.2.

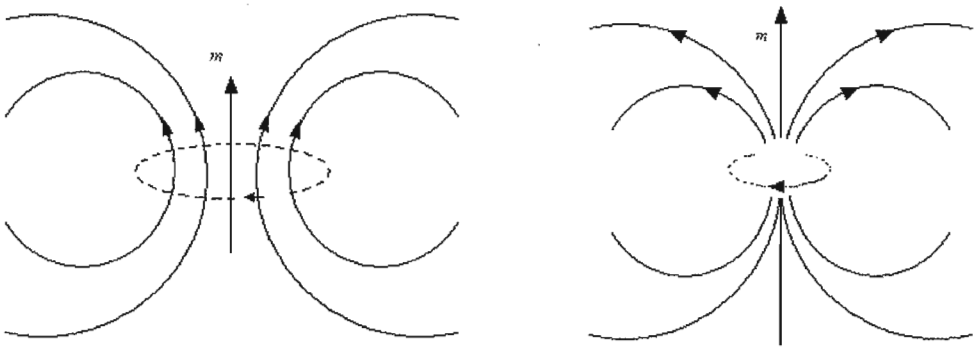

Figure 1.2: Magnetic moments associated with the angular momenta of an electron. (a) *orbital* and (b) *spin*. Adapted from reference 4, Figure 3.1.

All matter is comprised of atoms which contain at least one electron, however, only a handful of these materials are magnetic. Within a material, electrical charges in motion, specifically the aforementioned *spin* and *orbital* angular momenta of electrons, lead to its associated magnetic field.[3] Each of these motions has a magnetic moment which is a vector quantity, parallel to the axis of spin (for *spin*) and normal to the plane of the orbit (for *orbital*).[3] If all electrons in a given compound are paired (closed-shell) the compound lacks a magnetic moment and is referred to as diamagnetic. On the other hand, if there are unpaired electrons (open-shell) the material will exhibit a magnetic moment and is referred to as paramagnetic. Therefore, the critical factor that distinguishes a

diamagnet from a paramagnet is the existence of a magnetic moment resulting from at least one unpaired electron.[1] Magnets are materials in which these spins are ordered. How these spins interact with each other determines the magnetic behaviour of all magnets.

As previously mentioned, the electron intrinsically spins about its own axis and orbits around the nucleus. The moment arising from the former is known as the spin-only magnetic moment, μ_s. An initial approximation for the magnetic moment of any substance can be calculated using the spin-only formula, equation (4), which ignores the *orbital* angular momentum.[6] This method can predict the magnetic moment, μ, of a substance based on the number of unpaired electrons, n.[6] Each electron has a spin quantum number of S = ½.

$$\mu = 2\sqrt{S(S+1)} \tag{4}$$

1.2 – Magnetic Measurements

The bulk magnetic properties of any substance can be measured and used to classify it as diamagnetic or paramagnetic (this latter category can be further subdivided based on spin-spin interactions). The typical measurements are susceptibility, χ, and magnetic saturation, M_S.[4] These measurements are structure-insensitive.

Susceptibility, χ, is a measure of the magnetic response when a material is placed into an external magnetic field and is typically measured over a wide temperature range (300 - 5 K).[5,7] This is converted to molar susceptibility, χ_M, which can be defined as a measure of the degree to which a mole of a substance interacts with an applied magnetic field.[6] Diamagnets, when placed into an external magnetic field, display a slight

repulsive interaction. This is attributed to the paired electrons repelling the external field and is a universal property of all materials. Paramagnets exhibit attractive forces (to varying degrees) resulting in positive measurements. This occurs because the unpaired electrons are attracted to the external field and align themselves. All paramagnetic materials have a diamagnetic component which decreases the observed susceptibility, χ_{obs}. The diamagnetism in the sample is accounted for by using a diamagnetic susceptibility correction where:

$$\chi_{obs} = \chi_{para} + \chi_{dia} \tag{5}$$

The correction is estimated using a set of empirical values known as Pascal's constants.[8]

The degree to which a paramagnet is attracted to an external magnetic field is governed by both the number of unpaired electrons and their interactions with each other.[3,5,7,9,10] The absolute magnitude and temperature dependence of paramagnets distinguishes the types of interactions apart.[9] There exists simple paramagnetism, where in the absence of an applied external magnetic field the magnetic moments (spins) are randomly oriented. Placing a simple paramagnetic material into an external magnetic field results in alignment of the magnetic moments, producing a weak interaction (although this interaction is two orders of magnitude stronger than diamagnetism). When the material is removed from the field thermal motion is sufficient to randomly disorient the spins and magnetization is lost. These simple paramagnetic materials abide by the Curie law (6), which states that the susceptibility is inversely proportional to temperature:

$$\chi = \frac{C}{T} \tag{6}$$

where C is the Currie constant.[3]

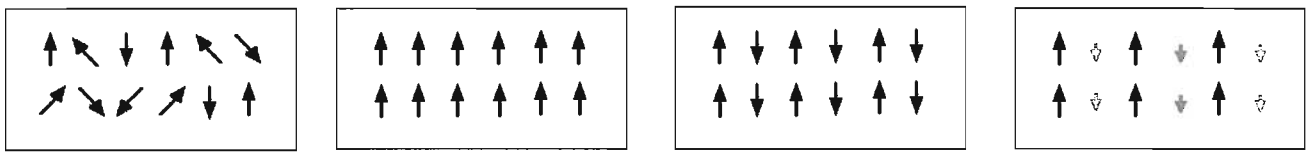

(a) (b) (c) (d)

Figure 1.3: Representations of a) simple paramagnetic disorder, b) ferromagnetic order, c) antiferromagnetic order, and d) ferrimagnetic order. Adapted from reference 4, Figures 6.19 and 6.21.

The magnetic moments of the unpaired spins of simple paramagnetic materials do not interact (couple); however, there are other paramagnetic materials that have interactions, Figure 1.3. These materials display temperature dependence and the magnetic moments from each of the unpaired electrons interact. The magnetic susceptibility can vary over a temperature range and is related to the number of unpaired electrons in the molecule via equation (7):

$$\chi_M T = \frac{N_A g^2 \beta^2}{3k_B}[S(S+1)] \tag{7}$$

where T is the absolute temperature, N_A is Avogadro's constant, g is the Landé factor or electronic magnetogyric constant, β is the Bohr magneton, k_B is the Boltzmann constant, and S is the overall spin state of the molecular substance.[8]

Ordering of the spins (magnetic moments) results in three common classes: (i) ferromagnetism, the parallel alignment of the magnetic moments; (ii) antiferromagnetism, the alignment of two equivalently but oppositely oriented magnetic moments; and (iii) ferrimagnetism, the alignment of two non-equivalent oppositely oriented magnetic moments. Ferromagnetism, which results in a parallel interaction of the magnetic moments of the spins, results in a positive deviation from the Curie law.[9] Above a critical temperature, referred to as the Curie point, this ordering breaks down and simple paramagnetism is observed.[7,9,10] Antiferromagnetism, which is the anti-parallel alignment of spins, results in a negative deviation from the Curie law.[9] The critical temperature at which this occurs is referred to as the Néel point.[3] Ferrimagnetism is the anti-parallel alignment of non-equivalent spins resulting in an overall non-zero net magnetic moment. Since these magnetic interactions are temperature dependent various graphs can be plotted which present information about the type of magnetic interaction exhibited. In this regard, a plot of $\chi_M T$ *vs.* T is extremely useful, Figure 1.4. A ferromagnetic response results in an upward curvature; an antiferromagnetic response results in a downward curve; and a ferrimagnetic response is at first a downward curvature followed by an upward curvature. A simple paramagnetic material, since it is temperature independent, has a linear response.

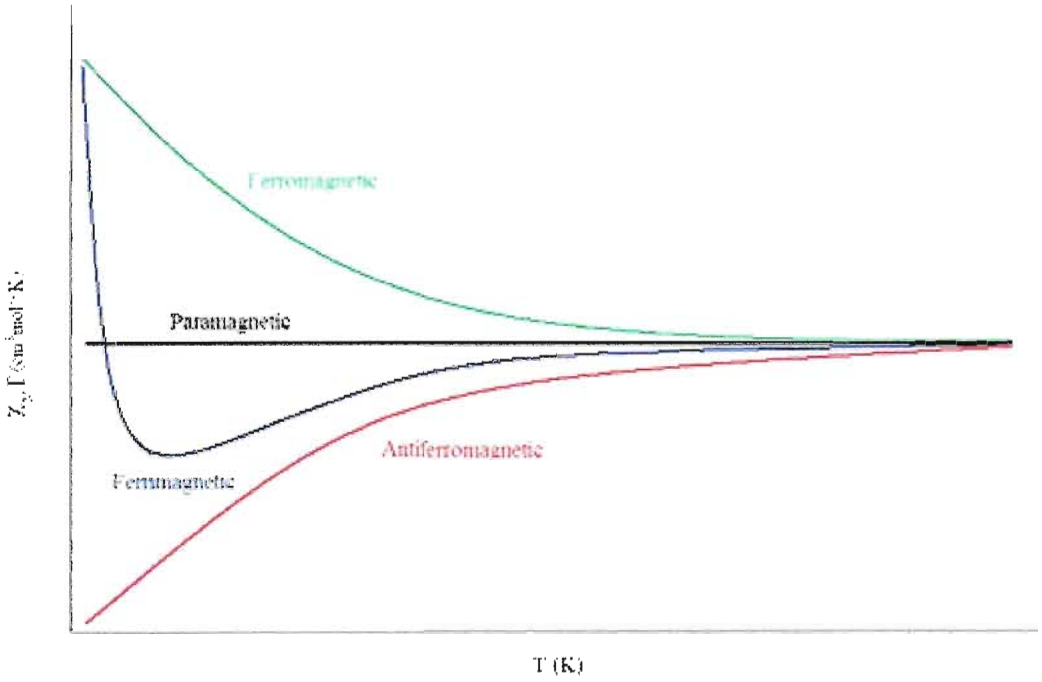

Figure 1.4: A plot of $\chi_M T$ *vs.* T displaying responses from the four most common types of magnetic materials. This type of plot is extremely useful in determining the type of interaction. Adapted from reference 2, Figure 2.

Since ideal Curie behaviour is seldom observed, the Curie-Weiss law (8), where θ is the Weiss constant, is used to indicate the coupling of spins.

$$\chi = \frac{C}{(T-\theta)} \tag{8}$$

The sign and magnitude of θ is proportional to the type and strength of coupling. Ferromagnetism results in $\theta > 0$, while antiferromagnetism results in $\theta < 0$. Since these magnetic interactions are temperature dependent, a graph of $1/\chi_M$ *vs.* T can be used to extrapolate the Weiss constant from the $\chi^{-1} = 0$ intercept, Figure 1.5. A simple paramagnetic material has a $\chi^{-1} = 0$ intercept at zero.

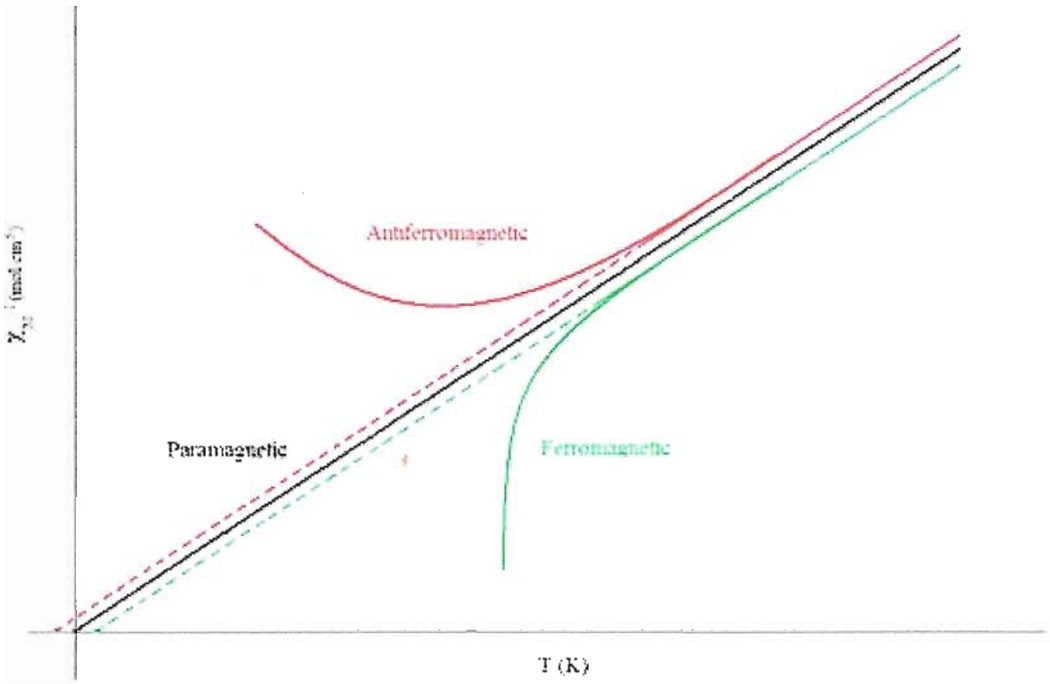

Figure 1.5: A plot of $1/\chi_M$ *vs.* *T* displaying ferromagnetic and antiferromagnetic responses. Adapted from reference 2, Figure 2.

It is extremely important to emphasize that magnetic ordering is *not* a property of an individual molecule, rather it is a cooperative solid-state (bulk) materials property.[1,2] It is also worth mentioning that above the critical temperatures (ordering temperatures) of ferromagnetic, antiferromagnetic, and ferrimagnetic materials the spins randomly orient because thermal motion overcomes all ordering behaviour.

At high field or low temperature the molar magnetization approaches a constant value, $N_A g \mu_B S$, which depends only upon the value of *S*. This is called magnetic saturation and occurs when the external field has aligned all of the spins and thermal energy cannot misalign them. The magnetization is typically converted to reduced magnetization ($M/N_A\mu_B$) because:

$$M/(N_A\mu_B) = gS = (2)(n/2) = n \tag{9}$$

where n is the number of unpaired electrons in the ground state of the system. Therefore, a plot of $M/N_A\mu_B$ *vs.* H is used to determine the number of unpaired electrons in a system, Figure 1.6. Normally this can be derived from the $\chi_M T$ *vs.* T at high temperatures for the value of $\chi_M T$ is proportional to the number of unpaired electrons.

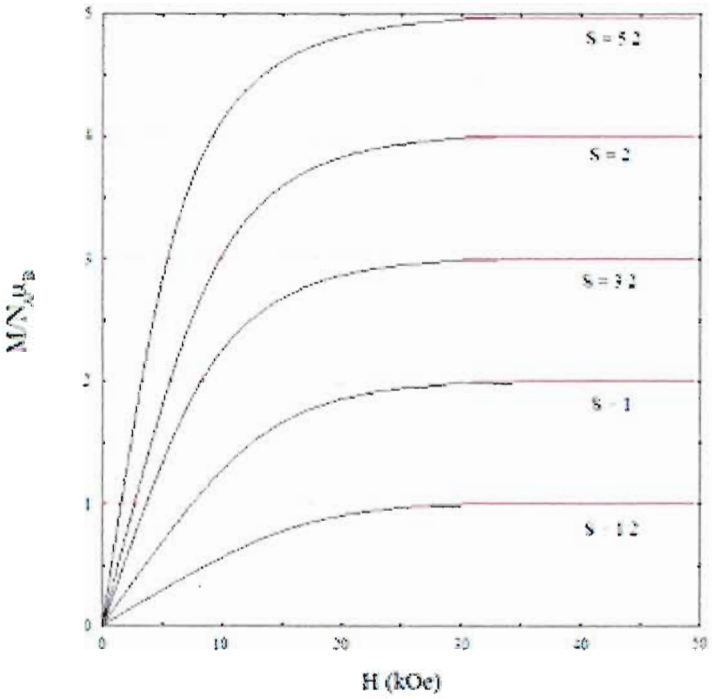

Figure 1.6: A plot of $M/N_A\mu_B$ *vs.* H. Adapted from reference 2, Figure 2.

In 1881 James Ewing studied the spontaneous magnetization of ferromagnetic materials and their associated hysteresis loops, Figure 1.7. This loop is the irreversible nonlinear response of magnetization, M, to an applied external magnetic field, H.[4] In 1907, Weiss continued these studies and was the first to hypothesize domains in ferromagnetic materials that were spontaneously magnetized even in the absence of an

external magnetic field. He deduced that a ferromagnet is just a paramagnet with a large internal molecular field. A ferromagnet in the demagnetized state has an overall magnetization of zero. This is because the domains, although ordered within, are randomly oriented throughout the sample.[4] When an external field is applied to a sample the domains all orient their spins in the same direction resulting in an overall magnetic moment. If the sample is below its critical temperature the removal of the external field results in a remnant magnetization (M_r), i.e. the sample retains its magnetic alignment. Applying a demagnetizing field (opposite direction of magnetization) results in a coercive field (H_c) which eventually reduces magnetization back to zero. This is the origin of hysteresis. These 'tiny magnetic domains' were later established by Lev Landau and Evgenii Lifschitz in 1935 and gave rise to the modern domain theory.[4]

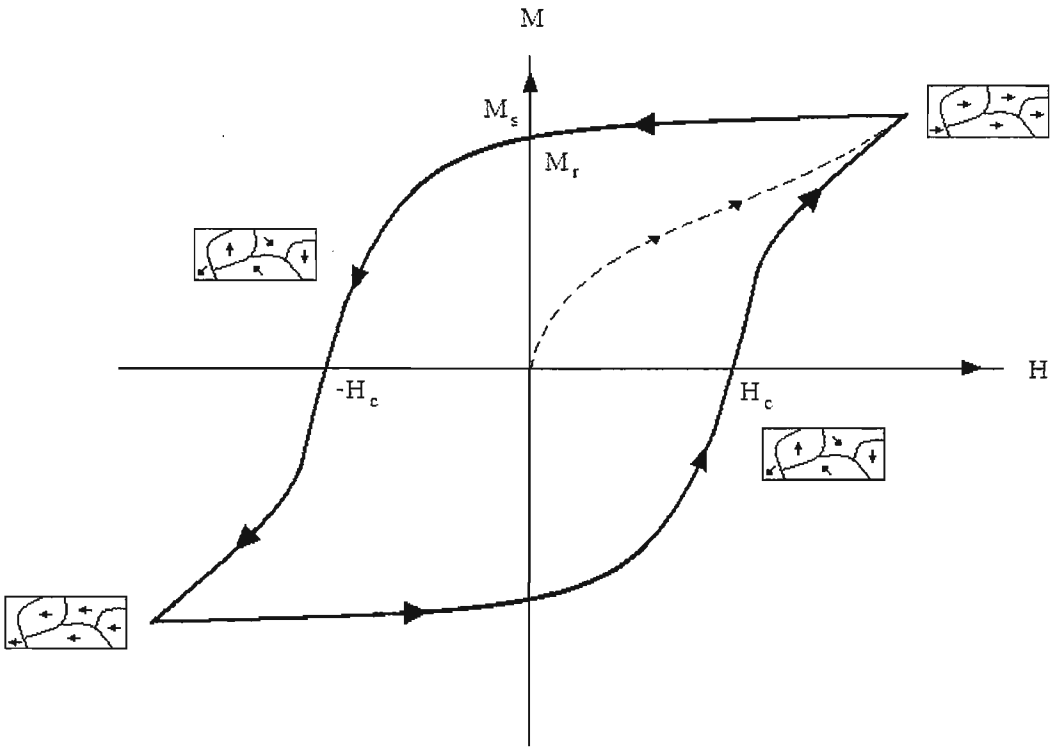

Figure 1.7: A hysteresis loop, named after James Ewing. From the Greek 'to lag behind'. Adapted from reference 4, Figure 1.3.

Hard magnetic materials have a broad hysteresis loop, Figure 1.8. They are suitable as permanent magnets since if they are placed into an external field which is sufficient to saturate the magnetization (M_s) they remain magnetized once the field is removed.[4] Examples of hard magnetic materials include the traditional magnets: magnetite, Alnico, and samarium-cobalt magnets. Soft magnetic materials have a more narrow hysteresis loop and are readily magnetized and demagnetized.[4]

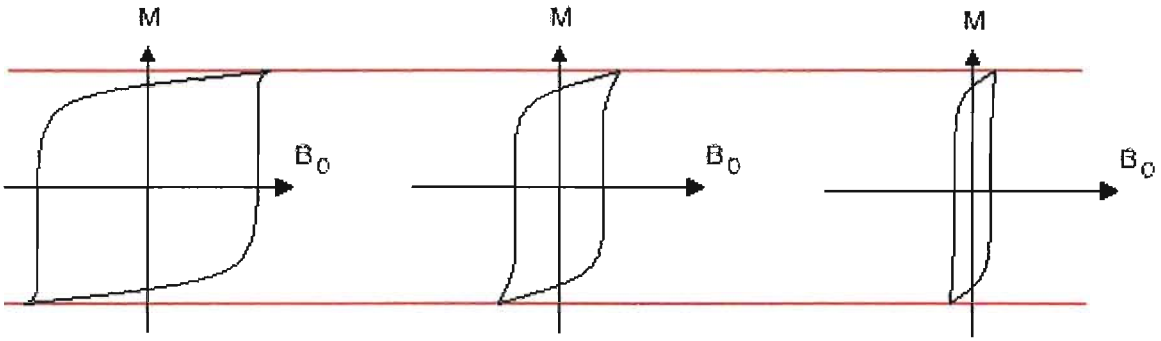

Figure 1.8: Hysteresis loops for hard magnetic materials, intermediate, and soft magnetic materials. Adapted from reference 5.

It is the existence of the hysteresis loop that confers a type of memory effect on a magnetic material. For information storage the two magnetic saturation orientations of the spins are used to represent zero and one in the binary code. One necessary requirement is that the system exhibits hysteresis but also has a critical temperature that is easily reached (to remove remnant magnetization).

With this information in mind it is now necessary to compare traditional magnetic materials and molecule-based magnetic materials.

1.3 – Traditional Magnets versus Molecule-based Magnets

Molecule-based materials are compounds built from discrete molecules, often referred to as building blocks.[11] Molecule-based magnets are comprised of organic or organic/inorganic hybrid materials consisting of organic radicals or paramagnetic metal ions.[12] They can be purely organic in nature, consist of coordination compounds or contain a combination of both. The macroscopic properties of these materials are determined by the collective interactions of these molecules in the crystalline structure.[1] These are based on the molecular rather than the metallic or ionic lattices of the traditional magnets.[13] Traditional magnets rely solely on the alignment of metal or metal oxide *d*- or *f*-orbital based spin sites orientated in three-dimensional networks.[12] This 3-D bonding leads to their insolubility and their preparation requires energy-intensive metallurgical methods.[12] On the other hand, molecule-based magnetic materials can be prepared through mild organic syntheses and coordination chemistry methodologies.[1,2] This allows for the chemical tailoring of molecular building blocks to fine tune the magnetic interactions within a sample. The active spin sites in molecule-based magnetic materials can not only be situated in the *d*- or *f-orbitals* of isolated metal ions but can reside in *s* or *p* atomic orbitals of purely organic species.[1] Moreover, molecule-based magnets can display various dimensionalities. They can form zero-dimensional single finite units known as single molecule magnets, SMMs, or form one-dimensional structures known as single chain magnets, SCMs. There are also examples of 2- and 3-D materials whose self-assembly is controlled by hydrogen bonding interactions or the bridging of discrete molecular structures. A 3-D organization is particularly favourable for long range spin-spin interactions within a sample. Since magnetism is a co-operative

effect, the optimization of the spin-spin interactions is important and ideally should extend in all three dimensions, either through bonds or through space. Molecule-based magnetic materials also display characteristics that are not available from the metal and metal-oxide traditional magnets. Such properties include high magnetic susceptibility, high remnant magnetizations, high solubility (conventional solvents), compatibility with polymers, and biocompatibility.[13]

The magnetic moments of traditional magnets are coupled in such a way that the individual moments respond all together to an external stimulus.[13] These materials consist of the aforementioned magnetic domains. At this level the materials contain at least billions of individual spins.[13] The need for storage of greater quantities of information on smaller surfaces is the driving force behind the development of magnetic particles of nanoscale dimensions. To this end there are two approaches: 'top-down' and 'bottom-up'.

The 'top-down' approach seeks to miniaturize traditional magnets in order to prepare smaller and smaller magnets. This is achieved by the fragmentation of ferromagnetic or ferrimagnetic materials, such as magnetite. On reducing the size of the magnetic particle eventually the formation of domains is energetically unfavourable and the particle forms one single domain.[13] This results in a change of the magnetic properties. Short range order results in a remnant magnetization when an external field is applied and then removed. Moreover, the magnetic anisotropy is dependent on the size of the particle. This leads to a phenomenon known as *superparamagnetism*, where the relaxation of magnetization is dependent on the crystal shape.[13] This can drastically affect the hysteresis associated with the sample and these materials can be used a storage

devices. Unfortunately, the fragmentation process yields particles of varying size and the separation is extremely difficult. Figure 1.9 outlines the number of spins and magnetic hysteresis loops for various groups of magnetic materials. The far left represents the traditional magnets where the hysteresis loop is indicative of a multidomain material. The far right is based on the individual spins of molecule-based magnetic materials.

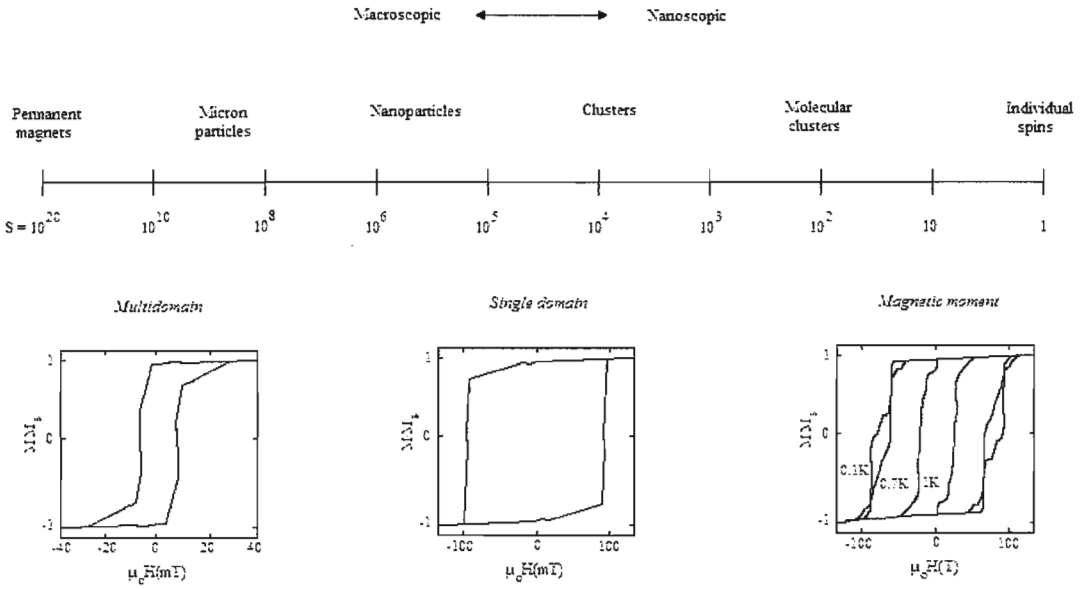

Figure 1.9: Transition from macroscopic to nanoscopic (microscopic) magnets. *S* is the total number of spins within the sample. Adapted from reference 13, Figure 1.3.

The alternate to the 'top-down' approach is the 'bottom-up' approach, also referred to as the molecular approach.[13,14] The bottom-up approach is essentially synonymous with molecule-based magnetic materials, where the synthesis is centered around assembling molecules with increasing numbers of paramagnetic centres (spins) capable of magnetic interactions. Initially, the preparation of three dimensional structures assembled from paramagnetic metal ions and organic ligands was targeted; however, it was soon realized that molecules naturally favoured the formation of low-dimensional

magnetic structures.[15] The presence of organic ligands often lead to isolated oligomers, wheel-shaped structures and molecular clusters.[15] Nevertheless, molecule-based magnetic materials of all dimensions have been prepared from the 'bottom-up' approach.

The idea of adding magnetic centres one at a time to prepare molecules of increasing nuclearity is certainly appealing, but the chemistry is not that simple. Nevertheless, Christou and co-workers have displayed a rather remarkable assembly of manganese clusters which increase in size, Figure 1.10.[14] The largest cluster prepared, which consists of 84 manganese metal ions, is approaching the limitation of the 'top-down' approach. This is where the two worlds (quantum and classical) have intersected.

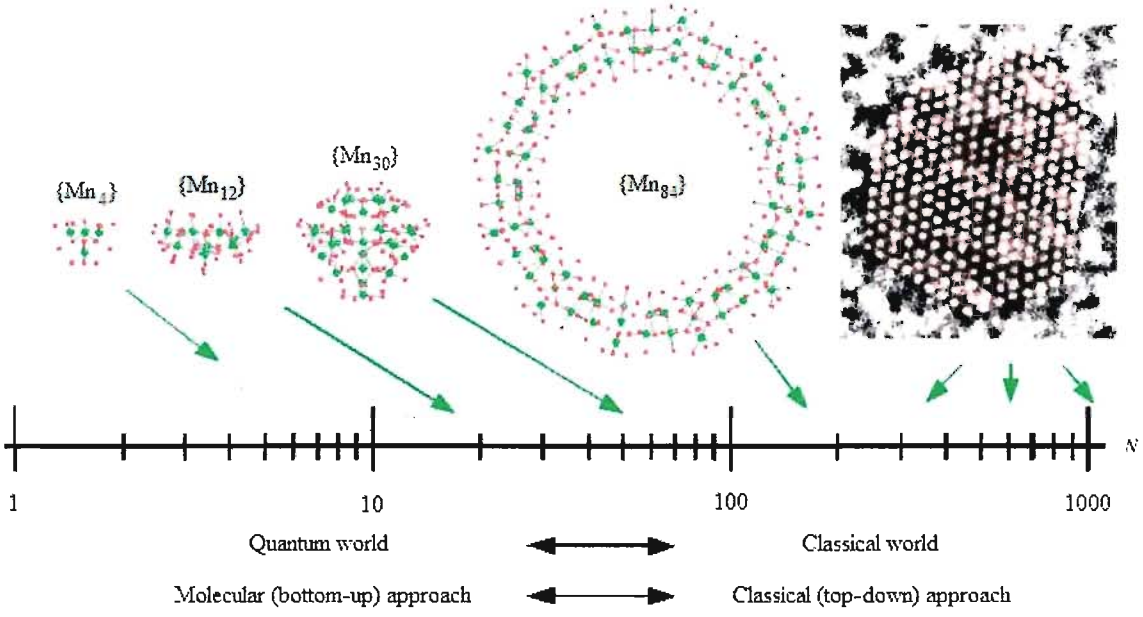

Figure 1.10: Increasing size and nuclearity of manganese molecular clusters. A nanoparticle prepared from the top-down approach is displayed on the right hand side of the page. Reprinted with permission from reference 14.

1.4 – Molecular Magnetism

The design, synthesis, and investigation of the magnetic properties of molecule-based materials is a research area collectively known as *molecular magnetism*.[16] Any

magnetic material that can be synthesized using the 'bottom-up' approach falls into this area of research. Molecular magnetic materials have only been added to the library of magnetism at the end of the twentieth century through the concerted action of chemists and physicists.[16] The history of molecular magnetism is certainly recent, with the metal ion/organic ligand complexes (coordination complexes) starting in the 1950s.[17] At this time the exchange mechanisms of small clusters was the driving force. One of the very first molecule-based magnets ever reported was an iron(III) dithiocarbamate chloride complex **(1.1)**, Figure 1.11.[18] The iron(III) has $S = 3/2$ and displayed ferromagnetic ordering at 2.96 K. Following this, Gregson, Martin, and Mitra observed long range ferromagnetic order in *d*-block phthalocyanine complexes.[19] Other contributors to this field included Day,[20] Carlin,[21] de Longh,[22] and Miedema[23]. Pei *et al.* also reported spontaneous magnetization in a bimetallic system consisting of Mn(II) and Cu(II) centres separated by oxamato-type ligands.[24]

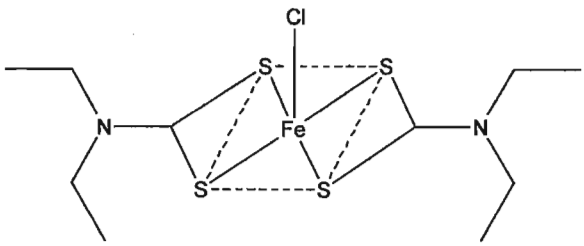

(1.1)

Figure 1.11: Structure of the iron(III) dithiocarbamate chloride prepared by Wickman *et al.* in 1967. Adapted from reference 18.

After these initial discoveries, the field of molecular magnetism grew exponentially soon requiring a classification system of compounds.

1.5 – Classifications of Molecule-based Magnetic Materials

1.5.1 Organic Radicals

Attempts to synthesize a purely organic ferromagnet began in the 1970s; it had been shown earlier that conductors and superconductors of purely organic nature could be obtained which could have technological applications.[25] The task of synthesizing a purely organic ferromagnet had proven very difficult; however, Itoh was able to show that strong ferromagnetic coupling could be induced between organic building blocks consisting of carbene centres separated by benzene rings.[25] Kinoshita reported the first genuine example of a purely organic ferromagnet in 1991.[26] This organic ferromagnet was the *p*-nitrophenyl nitronyl nitroxide radical.

The combination of paramagnetic metals with organic radicals was employed to introduce additional spin density and in doing so increase the potential magnetic properties. Examples which coupled a *p*-nitrophenyl nitronyl nitroxide radical with manganese, copper, and nickel were reported by Gatteschi *et al.* in 1989 and later followed up by Echegoyen *et al.* in 1999.[27,28] J. S. Miller and co-workers in 1985 prepared a ferromagnetic salt of decamethylferrocenium tetracyanoethylenide $[Fe(C_5Me_5)_2]^{+}$ $[TCNE]^{-}$ that displayed long range ferromagnetic order.[29]

1.5.2 Polycyanometalates

Cyanide linkers are exceptionally good at bridging metal centres because of their ambidentate nature and strong back-bonding ability.[30] In recent years, the coordination chemistry of cyanometallate precursors has been widely exploited in the field of

molecular magnetism affording high spin clusters as well as 3-D networks that include the Prussian Blue family of room temperature molecule-based magnets.[31]

The structure of Prussian Blue ($Fe^{III}_4[Fe^{II}(CN)_6]_3$) was elucidated by powder diffraction techniques in 1973.[31] It is a disordered cubic cell. The preparation of Prussian Blue analogues has remained at the forefront of scientific interest.[31] These compounds are prepared by the exchange of various paramagnetic metal centres for the iron centres (Fe(III) and Fe(II)) in Prussian Blue and has yielded compounds that display ferromagnetic order around room temperature, which is a great realization in this field. In this respect, a $V[Cr(CN)_6]\cdot 2.8H_2O$ compound has a T_C of 317 K.[31] Furthermore, a Co-Fe Prussian Blue analogue also displayed a reversible photoinduced magnetization effect upon irradiation with red light switching it from a paramagnetic to ferrimagnetic state.[32] Advances in this class of molecule-based magnetic materials are focused on this photomagnetic switching ability.

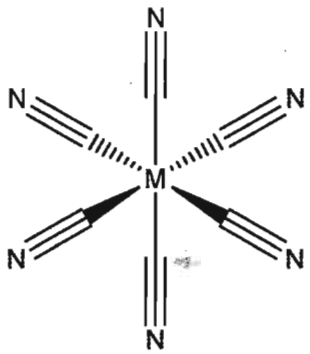

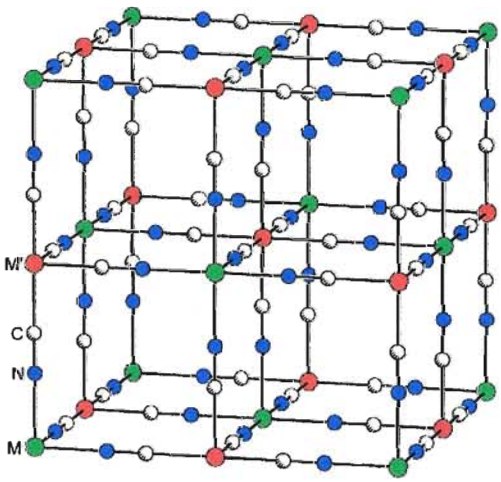

Figure 1.12: Structural representation of octahedral cyanometallic group in Prussian Blue. Reprinted with permission from reference 38. Copyright {2005} American Chemical Society.

1.5.3 Spin Crossover Compounds

Spin crossover compounds are materials that differ only in their spin values.[16] The first example of SCO behaviour was observed by Cambi in the 1930s.[33] Octahedral coordination complexes of first row transition metals having d^4-d^7 electronic configurations have received considerable investigation. The *d*-orbitals are split into the doubly degenerate e_g and triply degenerate t_{2g} levels. Depending on the strength of the ligand field, the spin state may be low (LS) or high (HS). Low-spin state is favoured when the ligand field is strong and high-spin state is favoured when the field is weak.[16,34] An intermediate ligand field results in comparative energies for both states and the material may be in equilibrium. A slight perturbation may result in the population of either the HS or LS state. Such perturbations include heat, light, or pressure. Iron(II) and iron(III) complexes have by far received the most scientific interest in regards to SCO behaviour.[34] Figure 1.13 displays the transition from LS → HS for an octahedral iron(II) and iron(III) complex. There is still a considerable amount of research being carried out on SCO compounds and their potential applications are diverse.[34]

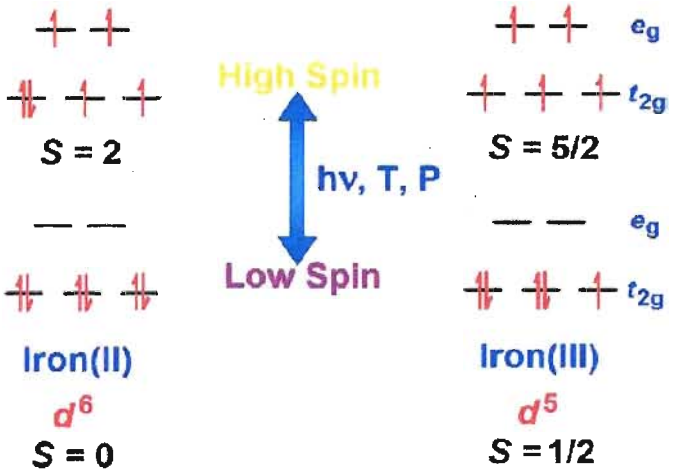

Figure 1.13: Diagram showing the spin states (HS and LS) of Fe(II) and Fe(III) in the octahedral environment. Transitions can occur via light (hν), temperature (T), or pressure (P). Reprinted with permission from reference 34. Copyright {2009} Royal Society of Chemistry.

1.5.4 Single Molecule Magnets (SMMs)

One class of molecule-based magnets that will be more thoroughly reviewed since they are specific to this research are single molecule magnets. Single molecule magnets are molecular clusters, comprised of paramagnetic metal ions. These compounds have gained considerable interest since it was discovered that they can exhibit magnetic bistability and posses a slow magnetic relaxation at cryogenic temperatures.[35] In order to be thorough it is necessary to clarify from the beginning that the term 'single molecule magnet', although evocative, is not completely correct. The divergence of the spin correlation length defines a magnet, but this cannot occur in finite systems such as the zero-dimensional single molecule magnets.[36] Nevertheless, the term single molecule magnet is in mainstream use and commonly refers to a molecule that functions as a nanoscale, single-domain magnetic particle that exhibits magnetic hysteresis of purely molecular origin below a specific temperature known as the blocking temperature.[37] Therefore, the magnetic properties arise from individual molecules and are not a cooperative effect. A single molecule magnet displays a large energy barrier to relaxation of its magnetization attributed to a combination of a large ground state spin (S_T) value and a large easy-axis type of uniaxial magnetoanisotropy (negative value for axial zero-field splitting parameter, D), Figure 1.14. The ground spin state is split in zero field by the magnetic anisotropy with the m $\pm$ S states lying lowest.[37] The upper limit magnetization barrier is defined as $S_T^2|D|$ or $(S_T^2\text{-}1/4)|D|$ for integer and non-integer spins, respectively.[38] This results in the slow relaxation of magnetization of the SMM below its blocking temperature, since the thermal energy is insufficient to overcome the barrier, and the spin is trapped in one of two configurations, Figure 1.14.[38]

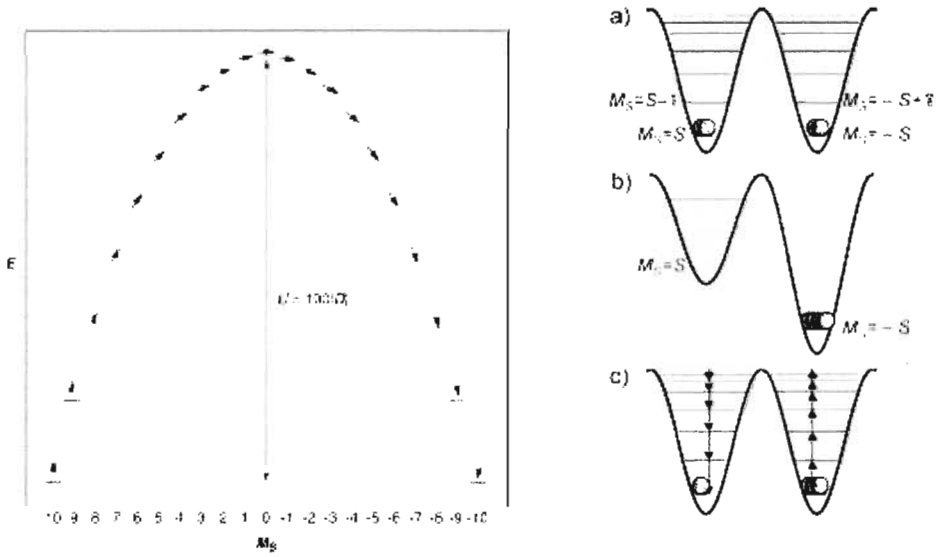

Figure 1.14: Energy level diagram for an $S = 10$ ground state with an axial zero-field splitting of $D < 0$. The spin reversal barrier is thus $U = S_T^2|D| = 100|D|$. The diagram on the right represents the relaxation of the magnetization. Reprinted with permission from references 38 and 39. Copyright {2005} American Chemical Society.

Single molecule magnets also display a very unusual property referred to as quantum tunneling.[39] This phenomenon is related to the fact that a quantum object has a wave nature. This property dictates that if a spin is trapped in one of the energy wells it can transfer to the other well without climbing the energy barrier. It does so by tunneling, Figure 1.15. This is one of the most typical manifestations of quantum mechanics.[40]

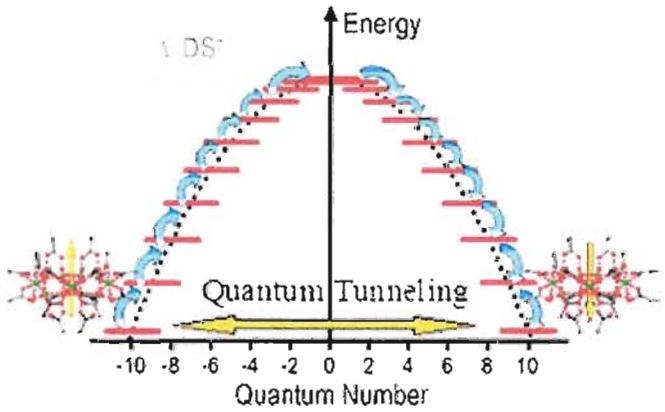

Figure 1.15: Energy level diagram displaying the slow relaxation of the magnetization in SMMs, highlighting the quantum tunneling of spins. The $Mn_{12}OAc$ cluster is used as an illustration. Reprinted with permission from reference 15. Copyright {2008} Royal Society of Chemistry.

Single molecule magnet behaviour is confirmed by the use of AC susceptibility measurements. If out-of-phase AC magnetic susceptibility signals are observed, this indicates SMM behaviour.[13] These measurements indicate a slow magnetic relaxation and the susceptibility is strongly dependent on the applied frequency which indicates that bulk magnetic order cannot occur.[13] In other words, the magnetic anisotropy and the large spin value induce a sort of internal field that makes the fast spin-spin relaxation inefficient. Thus, $\chi'' \neq 0$ is observed in zero static field, and its presence is considered to be a fingerprint for SMM behaviour.

In order for single molecule magnetic behaviour to be observed in a compound a few criteria have to be met. The compound must contain: (i) a high-spin ground state, (ii) a high zero-field splitting, and (iii) have negligible interactions between molecules (isolated units). Chemists strive to reach full control over the outcome of any synthetic procedure they carry out. The synthesis of single-molecule magnets is no exception. This achievement can occur through a long and not always straightforward process of rationalization of the factors that determine the resulting molecular structure.[13] This has certainly been achieved in some rare, fortunate cases. A well-known example is the polycyanometalate $Cr(CN)_6^{-3}$, which can bind six additional metal ions forming a cluster which has the shape of an octahedron with the chromium metal ion in the centre.[41] This rational design of SMMs is not necessarily the best strategy.[42] Luck or serendipity has also played a crucial role in the preparation of various SMMs. The ingenuity of chemists has also played a major role in this serendipitous approach, forcing nature to go towards unprecedented structures.[13,42]

In order to prepare molecular clusters that have large ground spin states (S) which can potentially display single molecule magnet behaviour, high-spin first row transition metals have been used.[35] The first of such molecular clusters to display single molecule magnet characteristics was the infamous $Mn_{12}OAc$ ($[Mn_{12}O_{12}(CH_3COO)_{16}]$) **(1.2)**, Figure 1.17. $Mn_{12}OAc$ was obtained as the unexpected byproduct of the reaction of Mn^{2+} and MnO_4^- in the presence of acetic acid.[43] This cluster was shown to have magnetic relaxation as slow as 2 months at low temperature (approx. 2 K) and has a magnetic hysteresis cycle below 4 K, which is similar to that observed for bulk magnets, Figure 1.16. The $Mn_{12}OAc$ cluster has a ground spin state of $S = 10$. The large ground state spin arises from ferrimagnetic interactions between the $S = 3/2$ spins of Mn(IV) and the $S = 2$ spins of Mn(III) ions, which do not cancel each other out. The zero-field splitting results in 21 M_s levels, Figure 1.14. Therefore, at the blocking temperature the spins are trapped in one of the energy wells. The reversal of magnetization is hindered by the energy barrier and the $Mn_{12}OAc$ cluster displays a magnetic hysteresis when a demagnetizing field is applied, Figure 1.16.

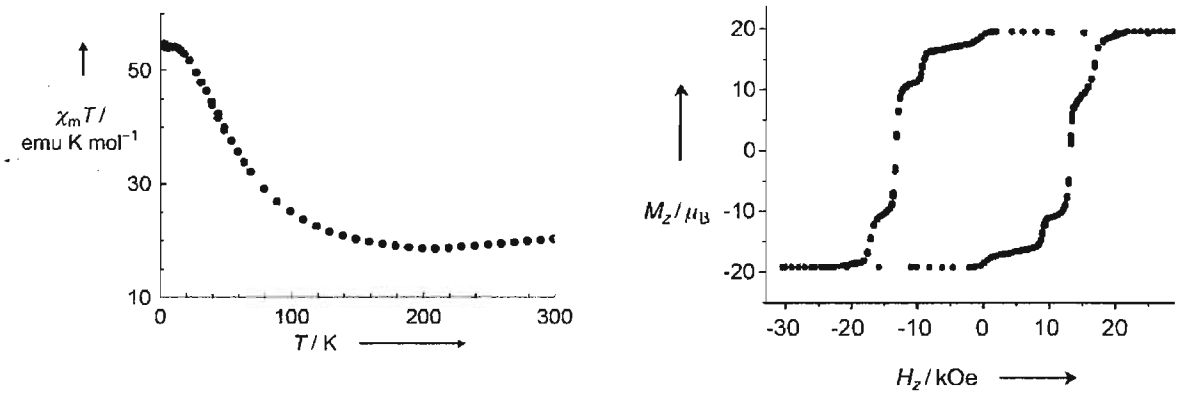

Figure 1.16: $\chi_M T$ *vs.* T plot of the $Mn_{12}OAc$ displaying the ferromagnetic interaction. Hysteresis loop of $Mn_{12}OAc$ at 2.1 K. Reprinted with permission from reference 39.

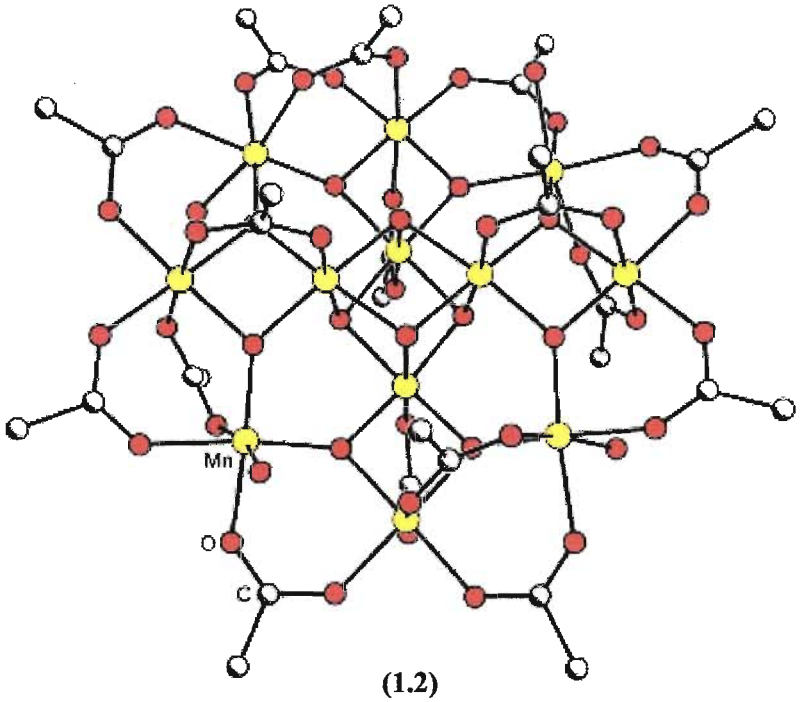

(1.2)

Figure 1.17: Structure of a single molecule magnet containing twelve manganese metal ions **(1.2)**. The inner four manganese ions are in the +3 oxidation state, while the outer eight manganese ions are in the +4 oxidation state. Reprinted with permission from reference 38. Copyright {2005} American Chemical Society.

Other single-molecule magnets that have been reported in the literature include V_4,[44] Ni_{12},[45] and Mn_{10} clusters.[39,46] In recent years it has become apparent that for SMM behaviour it is not necessarily the size of the cluster that dictates the magnetic properties but rather the value of *S* in the ground state and the anisotropy associated with the metal ions.[39] In this regard, iron(III) has been used to synthesize molecular clusters. In principle iron(III) would not give rise to large anisotropies, however, a study indicated that the zero-field splitting of a pseudo-octahedral complex coordinated to oxygen could be as high as 0.3 cm^{-1}.[35] One of the first iron(III) based SMMs prepared and investigated was an Fe_8 complex of stoichiometry $[Fe_8O_2(OH)_{12}(tacn)_6]Br_8(H_2O)_9$ **(1.3)**, Figure 1.18.

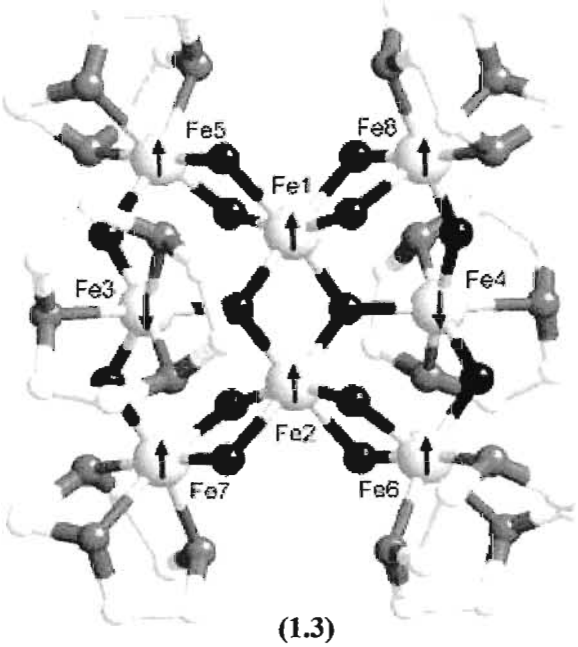

(1.3)

Figure 1.18: Molecular structure of the Fe_8 single molecule magnet. $[Fe_8O_2(OH)_{12}(tacn)_6]Br_8(H_2O)_9$, tacn = (1,4,7-triazcyclononane) **(1.3)**. Reprinted with permission from reference 47.

The Fe_8 SMM **(1.3)** was not very stable, however, another iron(III) SMM of stoichiometry $[Fe_4(OMe)_6(dpm)_6]$ (**(1.4)**, Hdpm = dipivaloylmethane) was reported in 1999, Figure 1.19.[35] It crystallized as an Fe_4 ferric star and was stable in solution. This tetrairon^{III} single molecule magnet was first reported as a one-pot synthesis using iron(III) chloride, sodium methoxide and dipivaloylmethane (Hdpm) resulting in a yield of 20-45%.[35] A new synthetic methodology was developed utilizing a dimeric intermediate $[Fe_2(OMe)_2(dpm)_4]$, which was isolated and reacted to form the tetrairon^{III} cluster in better yields (65%).[48] This cluster has been the subject of intensive research over the past decade. With a high-spin state of S = 5/2 for each iron(III) ion, the cluster has an overall ground state of S = 5 (three spins up, one spin down). Polycrystalline powder HF-EPR spectra gave a D = -0.20 cm^{-1} indicating a barrier to reorientation of magnetization of about 7 K with slow relaxation of magnetization occurring below 30 K.

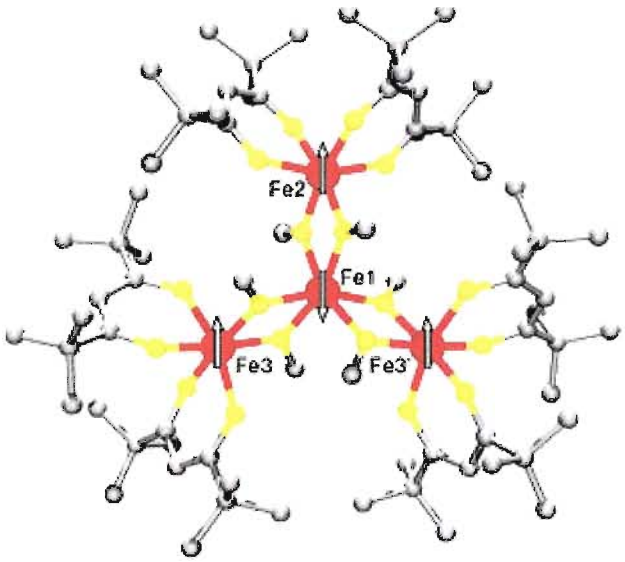

(1.4)

Figure 1.19: Structure of a single molecule magnet containing four iron(III) metal ions bridged by methoxide ligands and surrounded by Hdpm ligands **(1.4)**. The iron(III) centres are in a distorted octahedral environment. Reprinted with permission from reference 35. Copyright {1999} American Chemical Society.

One of the major drawbacks associated with single molecule magnets is that the magnetic properties are only observed at liquid helium temperatures. For potential applications in information storage a long relaxation of magnetization is required at or around room temperature. Since SMMs are essentially synthetically designed nanomagnets, they can be tailored via the systematic changes made to their structures. One synthetic design strategy was to exchange the acetate bridging ligands within the $Mn_{12}OAc$ cluster **(1.2)** and record any variations in the magnetic properties. One example exchanged the acetate bridges for *tert*-butoxide ligands **(1.5)**, Figure 1.20.[49] Other ligand exchange reactions included: $[Mn_{12}O_{12}(RCOO)_{16}]$, R = CH_2CH_3, C_6H_5, C_6H_4-*p*-CH_3.[50]

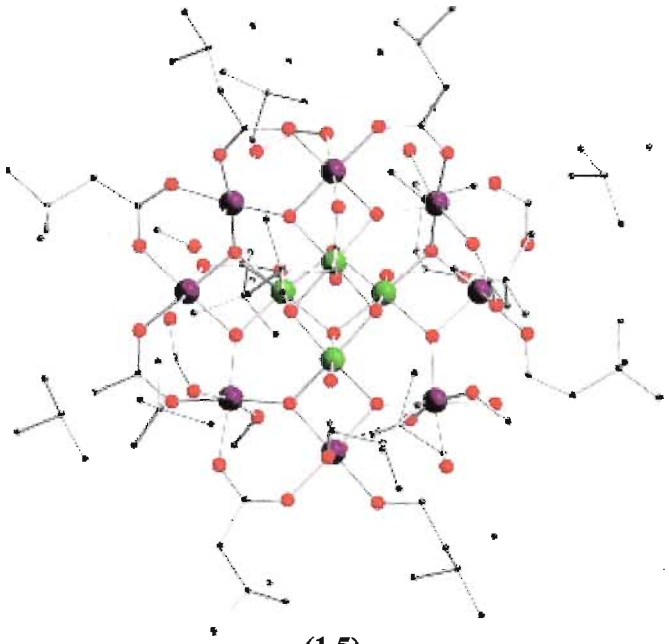

(1.5)

Figure 1.20: Structure of a single molecule magnet of $[Mn_{12}O_{12}(RCOO)_{16}]$, R = $CH_2C(CH_3)_3$. Reprinted with permission from reference 49.

The magnetic properties of the $Mn_{12}OAc$ cluster were strongly affected by these ligand exchange reactions.[49,50] The variations were attributed to the elongation of one of the axes of the manganese ions. This Jahn-Teller isomerisation was believed to be the source of the magnetic variations, affecting the symmetry of the molecule, the anisotropy, and the spin state energy distribution.[51] The easy substitution of the acetate groups in $Mn_{12}OAc$ was eventually exploited to introduce additional functional groups. Sulphur-based groups were exchanged to allow for interactions of the $Mn_{12}OAc$ SMM with a gold surface.[52] This preceded a step further with the organization of $Mn_{12}OAc$ where this SMM has been appended to gold, appended to silica, organized into polymeric films and separated within polymeric matrixes, Figure 1.21.[16] A major drawback to this organization is that the hysteresis may be reduced or sometimes lost.

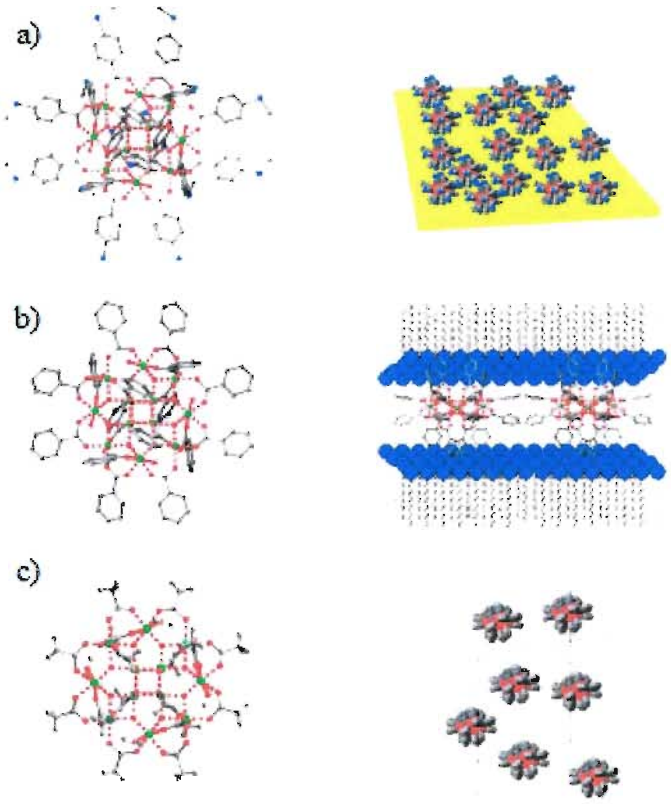

Figure 1.21: Different possible organizations of appropriately functionalized $Mn_{12}OAc$ derivatives (a) deposited on a gold surface; (b) in Langmuir-Blodgett films; and (c) dispersed in a polymeric matrix. Reprinted with permission from reference 16.

The $[Fe_4(OMe)_6(dpm)_6]$ **(1.4)** single molecule magnet was also investigated with regards to ligand exchange reactions. The $Mn_{12}OAc$ SMM **(1.2)** allowed for carboxylate ligand exchange whereas the tetrairon^{III} cluster was particular towards ligand exchange with derivatives of 2-(hydroxymethyl)propane-1,3-diol, $RC(CH_2OH)_3$. These triol compounds are widely used as versatile ligands in transition-metal chemistry because they can adopt a large variety of binding modes. In this case they can exchange with the methoxide bridges within the $[Fe_4(\mathbf{OMe})_6(dpm)_6]$ cluster, resulting in derivatives of stoichiometry $[Fe_4(\mathbf{RC(CH_2O)_3})_2(dpm)_6]$ (R = CH_3, Ph, CH_2Br), Figure 1.22.[48] Upon ligand replacement, the magnetic properties were in general enhanced and the anisotropy

barrier was larger than that in the parent compound **(1.4)**, reaching up to 17 K.[48]

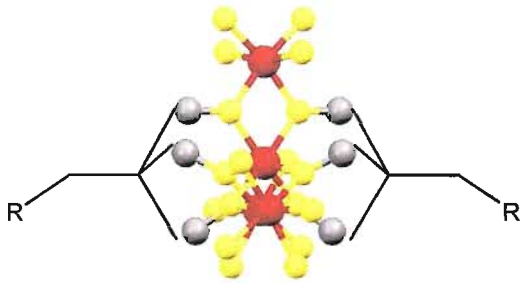

Figure 1.22: Representation of the exchanged tetrairon^{III} cluster. R = H, Ph, or Br. Adapted from reference 48. Copyright {2006} American Chemical Society.

The tetrairon^{III} single molecule magnet has only recently been appended to a gold surface via the exchange of the methoxide bridges for a sulphur-containing triol ligand, Figure 1.23.[53]

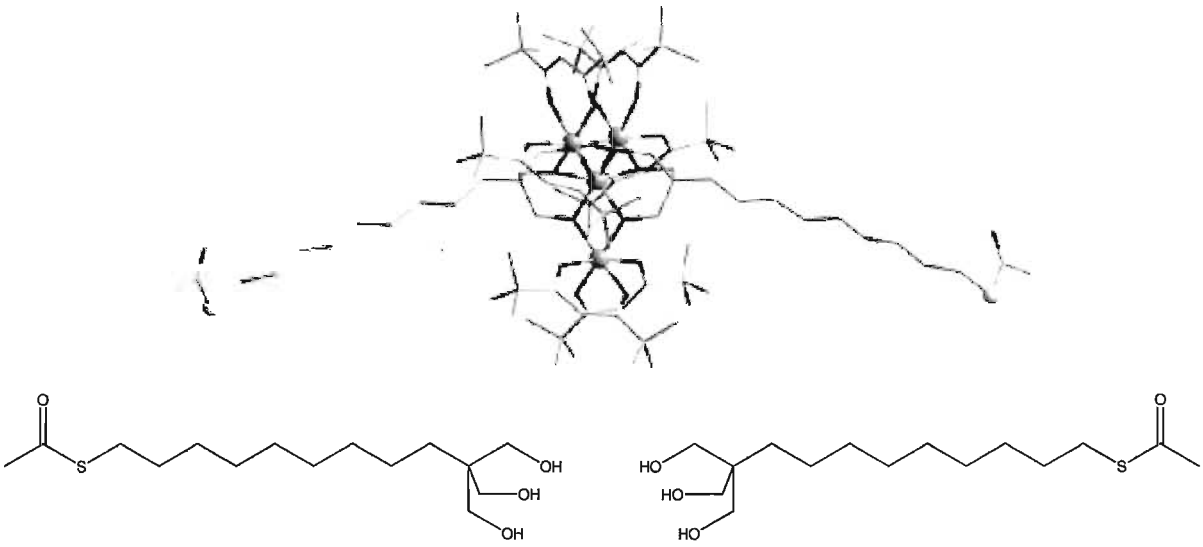

Figure 1.23: Representation of the tetrairon^{III} cluster exchanged with a thioester group. Adapted with permission from reference 53. Copyright {2010} Royal Society of Chemistry.

Clearly lanthanide-based polynuclear systems are an important avenue to explore in the pursuit of SMMs with higher anisotropic barriers, because of the strong spin-orbit

coupling commonly observed in 4*f* systems.[54] However, lanthanide only SMMs are rare in the chemical literature.[54] The problem arises from the fact that it is difficult to promote magnetic interactions among the lanthanide metal ions. Nevertheless, to-date the SMM with the largest anisotropic barrier has been reported to be a dysprosium based cluster.[54] Examples of mixed lanthanide and transition metal complexes have also been reported in the literature, for example the $\{Cu_3Dy_3\}_2$ SMM.[55] However, much scientific interest has continued to focus on complexes prepared from the early transition metal ions. The $Mn_{12}OAc$ family of SMMs has been studied the most compared to other systems. This family of SMMs continues to be the one with the highest blocking temperatures and has continued to receive great scientific interest from chemists and physicists alike.[53] The Fe_4 family of SMMs has also received a considerable amount of scientific interest. There are various literature reports outlining the success and challenges of this field.[56]

The field continues to progress towards the realization of SMM behaviour at or around room temperature. Currently, the addressability of single molecule magnets has been targeted with the overall goal of trying to perturb or control their magnetic properties.

1.5.5 Single Chain Magnets (SCMs)

Single chain magnets arose from the idea that the introduction of another degree of order, from zero-dimension to one-dimension, would allow for a higher blocking temperature of magnetization, increasing the relaxation time.[16] Statistical physics dictates that a 1-D chain cannot display long range order at finite temperature, however,

at low temperatures longer and longer segments of the chain would have their spins ordered and as such the relaxation time would increase.[16] An Ising-type magnetic anisotropy, which dictates that the spins must preferentially order in one direction, is required. Gatteschi *et al.* synthesized the first chain structure that displayed this phenomenon.[57]

1.6 – Design and Synthetic Strategies for Molecule-based Magnets

Molecule-based magnets can be classified into two main categories. One category is composed of purely organic building blocks where the spin component is satisfied by radicals. The other category involves organic ligands coordinated to paramagnetic metal ions. The latter category is centered on coordination chemistry which was mapped out by Alfred Werner 150 years ago.[6] In this thesis project, the design strategy involving organic ligands and paramagnetic metal ions has been used to try and prepare various molecule-based magnetic materials, Figure 1.24. In this regard, considering which particular ligands (oxamato, oxalate, carboxylate, etc.) and which paramagnetic metal ions should be used is not always straightforward. The factors affecting the structure and packing of molecules in the solid-state are very complex and still not completely understood.[58] Various structures can result from changing any one of a number of factors that include; the metal ion, the counter ions, pH and solvent. In this regard, a metal salt provides the specific coordinating metal ion (example, Cu^{II} from $CuCl_2$) as well as the counter ions. The resulting coordination complexes give rise to unique properties associated with the chemical reactivity and electronic, magnetic and/or optical properties of the metal ions together with the nature of the organic ligands and their interactions.[58]

First row transition metal ions have predictable magnetic moments and have the ability to adopt various stereochemical geometries.[6] Certain anionic ligands serve not only to balance the overall charge of the complex but can also allow bridging of neighbouring metal centres affording a wealth of solid state structures with interesting physical properties. Such anions include chloride, acetate, and perchlorate.

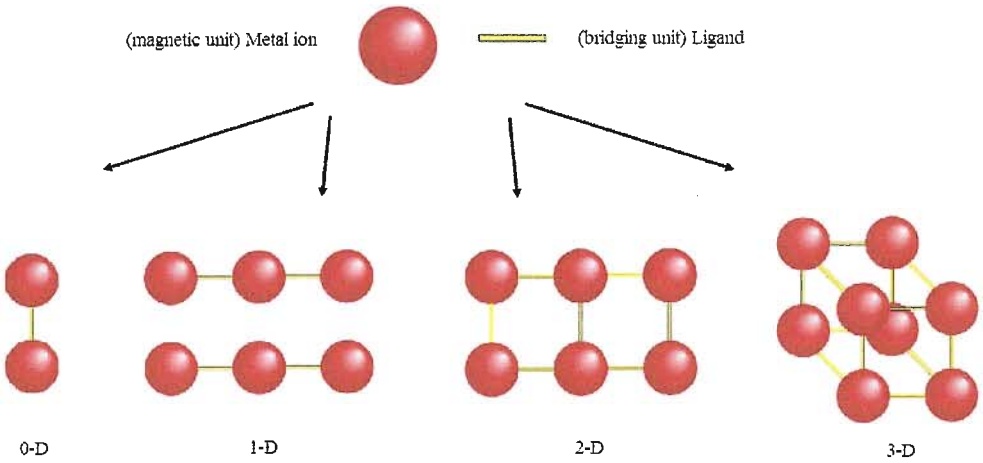

Figure 1.24: Cartoon representations of : 0-D, representative of single molecule magnets; 1-D, representing single chain magnets; 2-D and 3-D, normally representative of traditional magnets with a few molecular exceptions (such as Prussian Blue compounds).

The design and synthesis of polydentate ligands and their assembly into coordination complexes with paramagnetic metal ions with predictable magnetic properties has interested inorganic chemists in the field of magnetochemistry.[60] The controlled assembly of coordination complexes which will yield a ferromagnetic interaction has been at the core of these studies. Two theoretical strategies are used by synthetic chemists to predict and to achieve ferromagnetic spin alignment. These strategies are based on orbital symmetry or spin polarization effects. For orbital symmetry considerations, if the metal *d*-orbitals are close enough in proximity to overlap then the sign of the magnetic interaction is dictated by their relative symmetry.[61-63] The

electronic wave functions on neighbouring atoms can result in an exchange overlap integral, which is a very important parameter for determining the overall magnetic structure of a particular compound. This exchange parameter is represented by *J*. The sign and magnitude of *J* predicts the type of magnetic behaviour as well as the strength of the interaction. The atomic distances of neighbouring atoms, which are subject to crystal lattice parameters and size effects, dictates the overlap. If the atoms are close enough the potential to produce long range order may be present. For a bimetallic system, Isotropic superexchange interaction is expressed by the spin Hamiltonian, $H = -2J_{ij}S_i \cdot S_j$, in which *J* is the exchange coupling constant.[64] A positive *J* value means the occurrence of ferromagnetic interactions, whereas a negative value indicates antiferromagnetic interactions. Non-orthogonal, spatially overlapping orbitals give rise to antiferromagnetic exchange. Orthogonal, non-spatially overlapping orbitals give rise to ferromagnetic exchange. A great example that displays this orbital symmetry is depicted by the work reported by Olivier Kahn.[65] In this work, one compound [CuVO] **(1.6)** displayed a ferromagnetic interaction between the metal centres. This is because the orbitals are orthogonal and therefore couple ferromagnetically. The second compound [CuCu] **(1.7)** displays an antiferromagnetic coupling for the orbitals are non-orthogonal. Antiferromagnetic contributions generally take precedence over ferromagnetic couplings.[65]

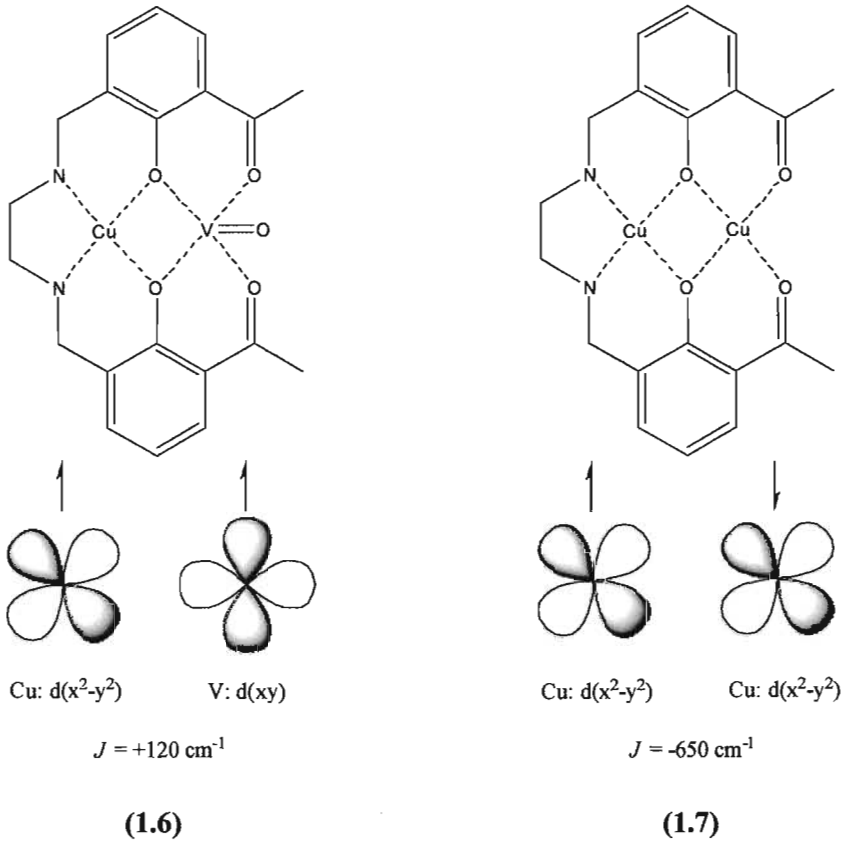

Figure 1.25: Cartoon representation of orthogonal and non-orthogonal orbitals, resulting in ferromagnetic and antiferromagnetic coupling, respectively. Adapted from reference 64.

Metal *d*-orbitals that are spatially distant cannot directly overlap. However, bridging ligand orbitals can play a crucial role in mediating such interactions. This process is known as superexchange.[64] The ligand properties, as well as the metal properties, are taken into account.[64,65] When two homometal ions are bridged by an anion with a bridging angle of 180°, for example, strong antiferromagnetic interactions occur through ligand-to-metal (LM) CT interactions and a low-spin ground state is stabilized, Figure 1.26 **(a)**. Typically, antiferromagnetic interactions are observed for bridged metal ions; however, ferromagnetic interactions can occur for hetero- and homometal systems, Figure 1.26 **(b) (c)**. These ferromagnetic exchanges can occur

through a strictly orthogonal pathway or can occur as the result of an accidental orthogonality.[64]

To further study the magnetic interactions between paramagnetic metal centres, inorganic chemists utilize families of bridging ligands and examine the magnetic interactions in the resulting coordination complexes. In this regard, the effects of ligand size, conformation, coordination, and topology can be studied in detail.

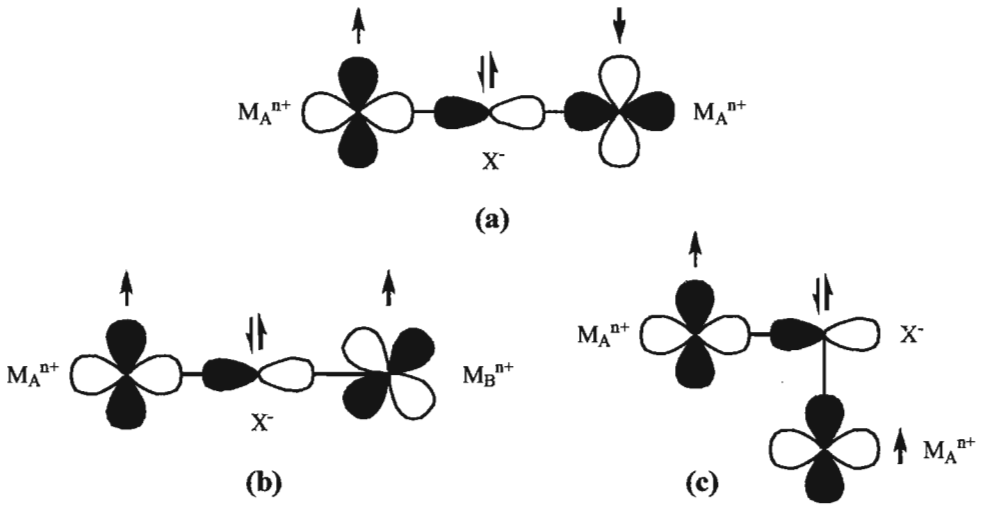

Figure 1.26: Cartoon representation of a) antiferromagnetic exchange, b) strict orthogonal exchange, and c) accidental orthogonal exchange. Adapted from reference 64.

A second mechanism, which takes into account spin-polarization, was developed by McCleverty and Ward.[66] It is based on the topology of the bridging ligand that connects two paramagnetic fragments. The connecting pathway through the ligand involves the alteration of induced spins.[66] This induced 'spin-polarization' occurs by the metal ion polarizing the electron cloud of the adjacent atom which in turn polarizes the next atom and so on, Figure 1.27.

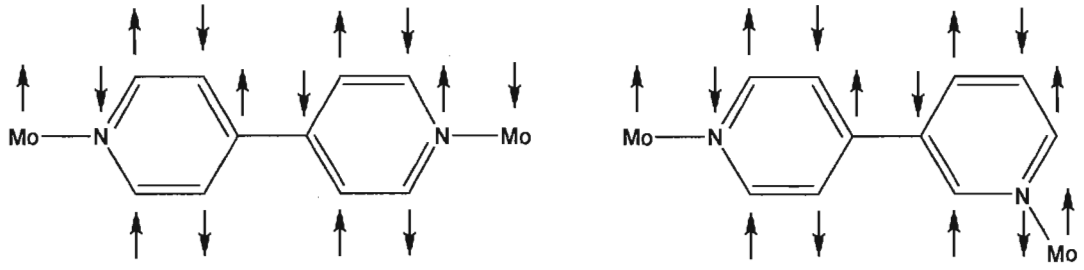

Figure 1.27: Cartoon representation of 'spin-polarization' process in Mo bipyridine structure. The large arrows indicate the induced spins through the bridging ligand. Adapted with permission from reference 66. Copyright {1998} American Chemical Society.

These processes seek to understand the complicated interactions associated with magnetism in molecule-based magnetic materials.

1.7 – Ligand Design for Molecule-based Magnets

For the preparation of molecule-based magnetic materials, paramagnetic metal centres must be separated by specific lengths in order to convey appropriate magnitudes of spin-spin interactions.[64] Particular classes of organic ligands may potentially fulfill this spacing requirement or allow for superexchange. Moreover, nitrogen-heterocyclic ligands have displayed considerable versatility in building extended networks with different coordination modes which can mediate significant magnetic interactions between paramagnetic metal centres.[58] One class of organic ligands that has received considerable attention is the bipyridine family.

1.8 – Bipyridine Chemistry

This family of molecules consists of a heteroaromatic analogue of biphenyl containing nitrogen. Bipyridine ligands chelate transition metal ions through the lone

pairs on their nitrogen atoms. They also accept electron density from transition metal *d*-orbitals and are therefore classified as both σ-donors and π-acceptors.[67] The six isomers of the bipyridine family of ligands: 2,2' **(1.8)**, 2,3' **(1.9)**, 2,4' **(1.10)**, 3,3' **(1.11)**, 3,4' **(1.12)**, and 4,4' **(1.13)**, are represented below in Figure 1.28.

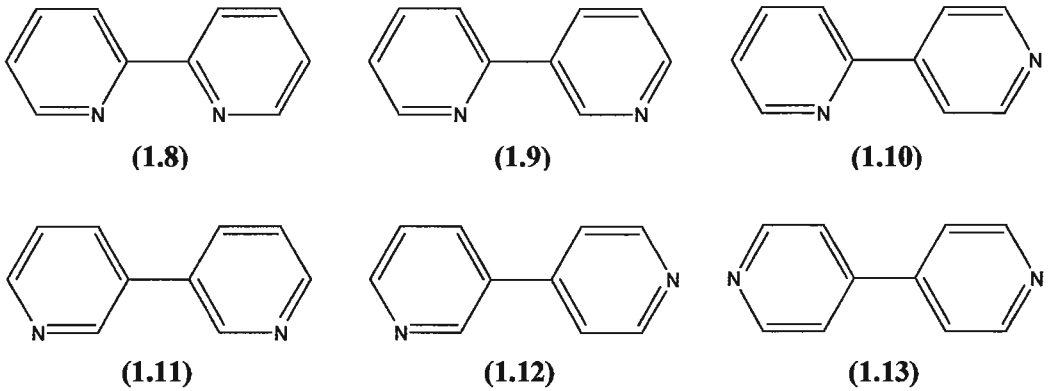

Figure 1.28: Regioisomers of bipyridine.

Of the above structures, the 2,2'-isomer **(1.8)**, commonly referred to as bipy, is one of the most exploited ligands in the fields of supramolecular and coordination chemistry. This is mainly because of its proven tendency to form well characterized coordination systems with various transition metal ions. The first synthesis of 2,2'-bipyridine was carried out more than 110 years ago by Fritz Blau, who dry-distilled the copper salt of picolinic acid.[68] Currently, there are a number of alternative synthetic methodologies for the preparation of 2,2'-bipyridines that include Ullmann, Stille, Suzuki, and Negishi-type reactions which couple pyridine and pyridine derivatives together.[69] One example is the reported Ullmann coupling of 2-bromo-3-methylpyridine affording 3,3'-dimethyl-2,2'-bipyridine.[69] These reactions offer a straightforward approach to the desired 2,2'-bipyridine or substituted derivatives in relatively high yields (50-80%). A

comprehensive review evaluating the various synthetic approaches for the preparation of 2,2'-bipyridines was published by Newkome *et al.* in 2004.[69]

1.9 – Disubstituted-2,2'-Bipyridines

As previously stated, 2,2'-bipyridine has a proven tendency to chelate transition metal ions in various oxidation states.[69] Furthermore, 2,2'-bipyridine can be synthetically modified to afford new ligands with different chelating modes. This modification is normally done symmetrically on the 3,3', 4,4', 5,5', or the 6,6'-positions. There are also reports of combinations of synthetically modified positions; a 4,4',6,6'-tetrasubstituted-2,2'-bipyridine by Rasmussen and co-workers[70] and a 4,4',5,5',6,6'-hexasubstituted-2,2'-bipyridine by Perumal and co-workers.[71] There are also asymmetrical systems reported in the literature.[72]

A comprehensive review of the chemical literature reveals that the disubstituted-2,2'-bipyridines have been exploited as ligands yielding various coordination complexes with interesting physical properties (including magnetism).[73,74,75] The use of 3,3'-disubstituted-2,2'-bipyridines has recently received a great deal of attention with regards to the preparation of coordination complexes. There have been studies carried out on 3,3'-disubstituted-2,2'-bipyridines when the 3,3' positions contain small functional groups such as methyl **(1.14)**, hydroxyl **(1.15)**, carboxyl **(1.16)**, or amino **(1.17)**, Figure 1.29.

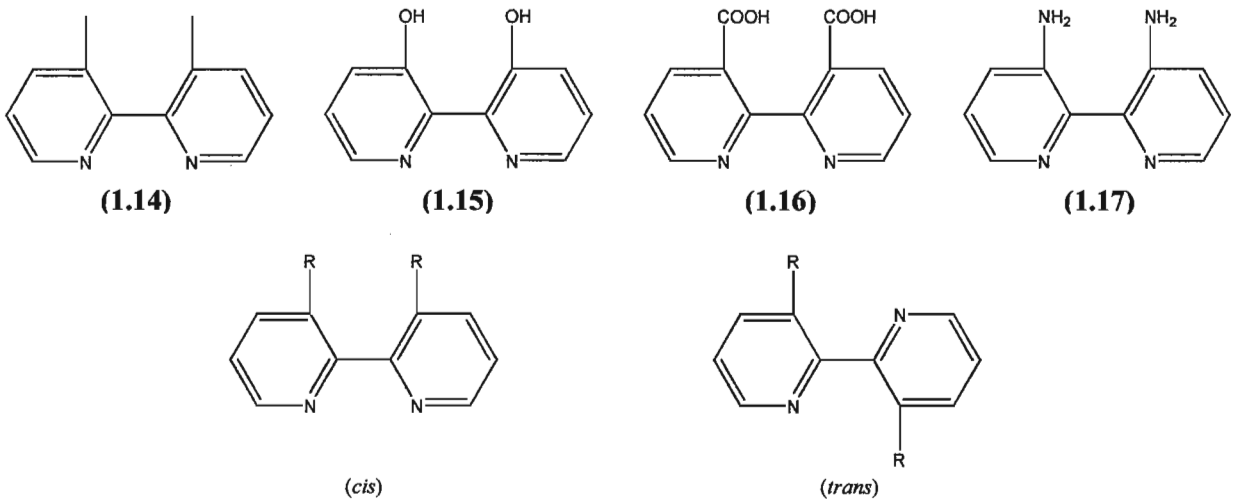

Figure 1.29: Examples of 3,3'-disubstituted-2,2'-bipyridines. The *cis* configuration is predominant when the substituents are small, normally causing the bipyridine rings to twist by a torsion angle of 30-35°. Large substituents dictate the *trans* configuration of bipyridine which is seen in the familiar 180° form.

Starova, Denisova, and Dem'yanchuk reported a coordination complex of 3,3'-dicarbometoxy-2,2'-bipyridine with Cu(II) **(1.18)**, Figure 1.30.[76] The authors report the uncoordinated ligand as having a torsion angle between the best planes of the bipyridine rings of 123.4°, but when coordinated with Cu(II) the angle changed to 34.0°.

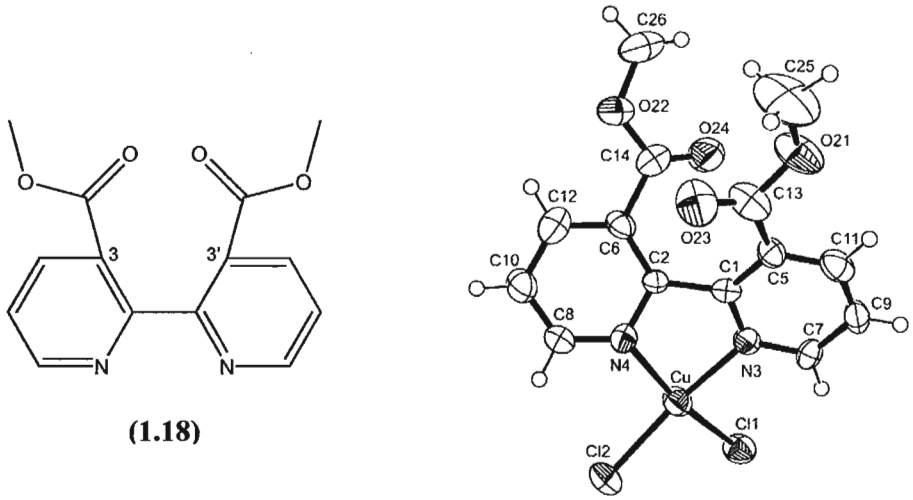

Figure 1.30: 3,3'-Dicarbometoxy-2,2'-bipyridine coordinated with Cu(II). Reprinted with permission from reference 76.

The coordination complex **(1.18)** displays that the nitrogen atoms of the bipyridine moiety coordinate to the copper(II) metal centre approximating a *cis*-coordination mode. Various reports throughout the literature also display this coordination mode for bipyridine-based ligands with first row transition metal ions.[73,75] To study this further, Pilkington *et al.* prepared 3,3'-diamino-2,2'-bipyridine **(1.17)** and studied its coordination chemistry with various transition metal ions.[67]

1.10 – 3,3'-Diamino-2,2'-Bipyridine

The work done by Pilkington *et al.* revealed that 3,3'-diamino-2,2'-bipyridine **(1.17)** could coordinate a range of divalent transition metal ions preferentially through the lone pairs of electrons on the pyridyl nitrogen atoms.[67] The molecular structure of a copper(II) dichloride complex **(1.19)** of this ligand is shown in Figure 1.31.

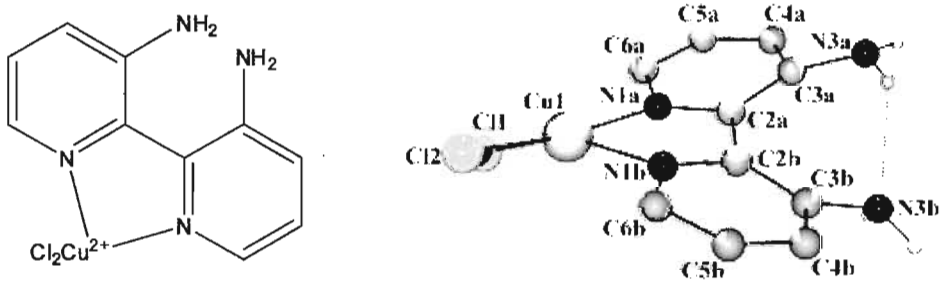

(1.19)

Figure 1.31: Coordination of Cu(II) chloride to 3,3'-diamino-2,2'-bipyridine. The molecular structure of the complex was elucidated by X-ray crystallography and reveals that the pyridine rings are twisted by an angle of 24.4° with respect to their best planes. Reprinted with permission from reference 67.

Exploiting this coordination chemistry, Pilkington *et al.* have also reported a *tris*-(3,3'-diamino-2,2'-bipyridine) zinc(II) complex **(1.20)** where the pyridyl nitrogen atoms are coordinated to the metal centre, Figure 1.32.[67] Shi *et al.*[77] and Min *et al.*[78] obtained

the same coordination geometry with cadmium **(1.21)** and nickel **(1.22)**, respectively, Figure 1.32.

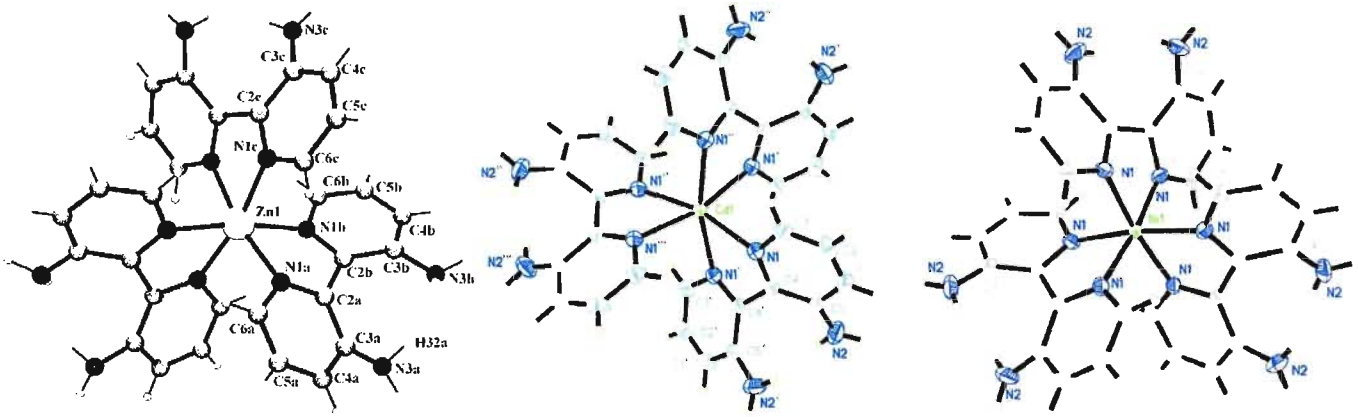

(1.20) **(1.21)** **(1.22)**

Figure 1.32: *Tris*-(3,3'-diamino-2,2'-bipyridine) coordinated with zinc(II)[67], cadmium(II)[77], and nickel(II)[78]. Counter ions are omitted for clarity. Bipyridine distortion angles of best planes are 31.3°, 36.4°, and 32.4°, respectively. Reprinted with permission from reference 67, 77, and 78.

These studies indicated that 3,3'-diamino-2,2'-bipyridine **(1.17)** preferentially coordinated through the nitrogen atoms of the bipyridine unit. The synthetic modification of 3,3'-diamino-2,2'-bipyridine was carried out in order to investigate other coordination modes that could be adopted by the ligand derivatives. As such, the synthetic modification of the amine functionality of 3,3'-diamino-2,2'-bipyridine was targeted. One such modification resulted in the Schiff-base *bis*-imine ligand **(1.23)** which was prepared via the condensation reaction between 3,3'-diamino-2,2'-bipyridine and two equivalents of pyridine-2-carbaldehyde, Figure 1.33.[79] Schiff-base ligands are known for their various coordination modes and capability of forming multi-metallic complexes.[80] The coordination of this ligand **(1.23)** to a transition metal ion was expected to occur through the bipyridine, pyridine, and imine nitrogens, affording two available *tri*-dentate binding sites for the metal ions. However, an unexpected complex was isolated after reacting this

ligand with cobalt(II) perchlorate, Figure 1.34. This was attributed to the reactivity of the imine which participated in a rearrangement process to afford the quaterpyridine type coordination complex **(1.24)**.

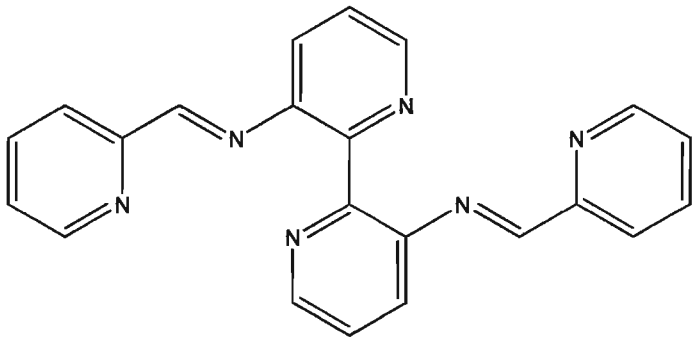

(1.23)

Figure 1.33: Structure of the *bis*-imine ligand **(1.23)**.

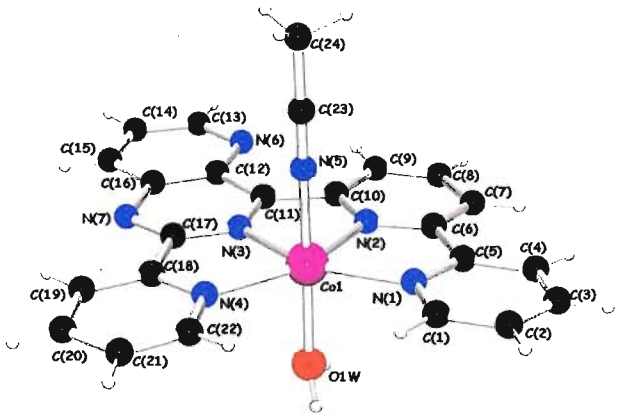

(1.24)

Figure 1.34: Molecular structure of $[Co(L)(OH_2)CH_3CN]\cdot 2ClO_4$ **(1.24)**. (L) = Rearranged Schiff-base *bis*-imine ligand **(1.23)**. Counter ions are omitted for clarity. Reprinted with permission from reference 79. Copyright {2007} Royal Society of Chemistry.

This result was the first reported example of a one pot synthesis of a quaterpyridine type coordination complex. The investigation of this ligand was continued by the Pilkington group. However, given the reactivity of the *bis*-imine series of ligands

the objectives of this project were to prepare and investigate the coordination chemistry of a more stable family of carboxamide ligands.[81]

1.11 – Carboxamide Ligands

Nature is quite conservative when it comes to the primary protein structure which always contains the carboxamide (peptide) bond as the linkage between amino acid residues.[82] This peptide bond is essential for the coordination of metal ions to various enzymes and macromolecular complexes, as outlined by Ross and Burrows.[83] Therefore, drawing from nature, the carboxamide moiety is extremely important for coordination chemists for ligand construction. Many studies have been carried out on the carboxamide moiety, ultimately leading to the preparation of pyridine carboxamides. They are a class of multidentate ligands which are synthesized via the condensation of pyridyl-bearing amines with carboxylic acid precursors.[81] Deprotonation of the carboxamide nitrogen yields an anion which chelates to metal ions via this unit and the pyridyl ring(s) on the rest of the molecule.[82,84] Pyridine carboxamide ligands have found applications in asymmetric catalysis, as molecular receptors, in dendrimer synthesis, as well as for the preparation of platinum(II) complexes with anti-tumour properties.[82] The ambidentate nature of the amide bond has been the subject of research over the past six decades, notably as a basic model to understand the biological interactions of complex metal-peptide systems and enzymes.[84] Biological investigation of the behaviour of pyridine carboxamides with *d*-block metals, specifically towards copper, has yielded fruitful results.[81,82] Cu(I) and Cu(II) are in fact an integral requirement for various enzymes (such as copper/zinc superoxide dismutase). In this regard, it is present in the active sites

of electron transfer proteins as well as oxygenase metalloproteins.[83] Subsequently, pyridine carboxamides support a range of coordination numbers and geometries for the copper(II) metal ion.[81,85] The coordination of these complexes is dictated by the necessity to avoid the formation of four member chelate rings, easily averted by the flexibility of the pyridine carboxamide functional groups.[82] Recent years have afforded a wealth of information about the ligation of pyridine carboxamide nitrogens which have been found to stabilize metals in higher oxidation states.[86] Belda and Moberg have indicated that coordination via the oxygen atom of a carboxamide ligand occurs when it is neutral; however, upon deprotonation the coordination occurs through the nitrogen atom.[87] A complex **(1.25)** reported in the literature displays a coordination mode of a biphenyl pyridine carboxamide ligand, Figure 1.35.[88]

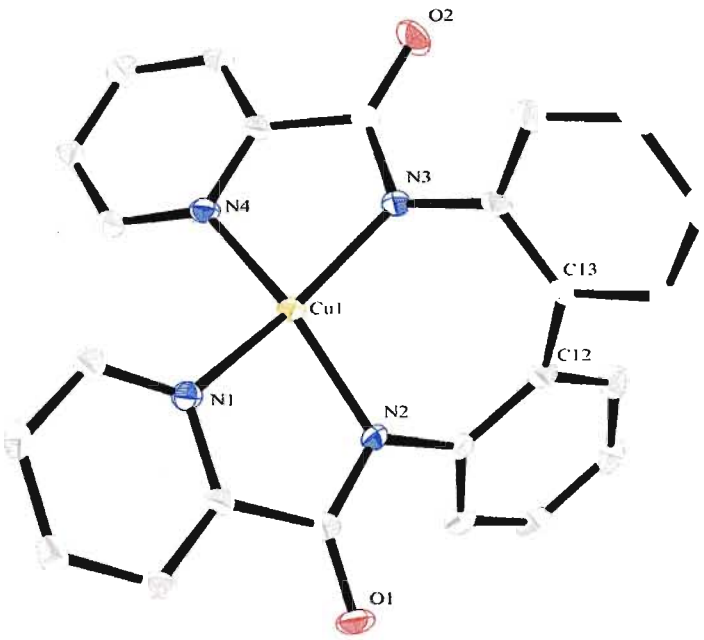

(1.25)

Figure 1.35: ORTEP[153] representation of the molecular structure of a Cu(II) complex **(1.25)**. Adapted from reference 88.

The coordination of the ligand to the copper centre in complex **(1.25)** occurs through the deprotonated amide nitrogen atom. The carbonyl oxygen atom is not involved in coordination. The authors indicated that no base was added to the reaction mixture, therefore, the copper(II) metal ion was able to deprotonate the amide which allowed for coordination via the nitrogen atom. First row transition metal ions are Lewis acidic and are capable of facilitating the deprotonation of amides.[87]

Although pyridine carboxamide ligands have already been studied for possible medical,[89] catalytic,[90] and receptor-binding applications,[91] these ligands have only recently been investigated with regards to their suitability as molecular building blocks for the preparation of molecule-based magnetic materials. As such, work in the Pilkington Group has focused on carboxamide ligands, the first ligand prepared and studied was 2,2'-bipyridine-3,3'-(2-pyridinecarboxamide) **(H_2L^1) (2.1)**, Figure 1.36. This ligand essentially combines 3,3'-diamino-2,2'-bipyridine **(1.17)** with a pyridine carboxamide moiety.

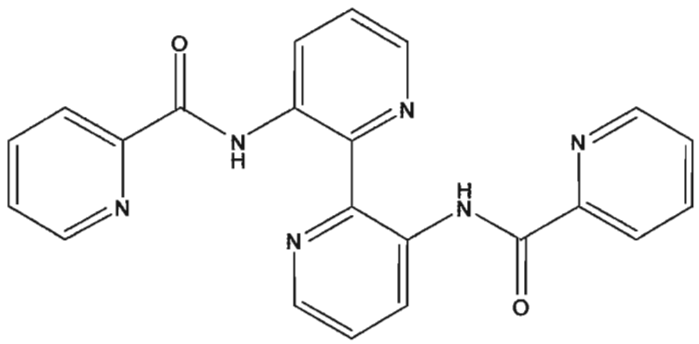

(2.1)

Figure 1.36: Structure of the *bis*-carboxamide ligand, 2,2'-bipyridine-3,3'-(2-pyridinecarboxamide) **(H_2L^1) (2.1)**.

Two dinuclear Cu(II) coordination complexes containing this *bis*-tridentate deprotonated ligand **(L^1) (2.1)** were prepared.[81] Methanolic solutions of the ligand

together with two equivalents of $Cu(hfac)_2$ or $CuCl_2$ produced green microcrystalline materials of $[Cu_2(\mathbf{L^1})(hfac)_2]$ **(1.26)** and $[Cu_2(\mathbf{L^1})Cl_2]$ **(1.27)**. The molecular structure of each of the Cu(II) complexes is shown in Figure 1.37 and 1.38, respectively.

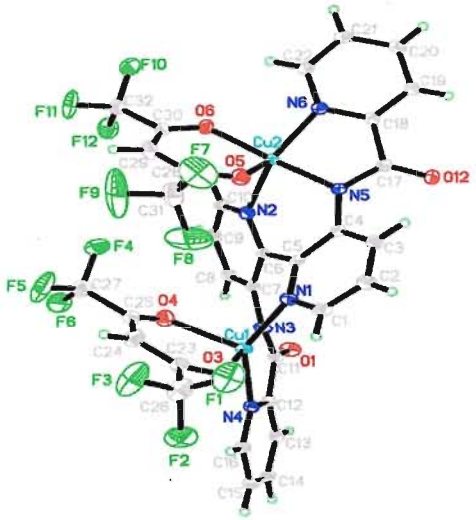

$L^1 =$

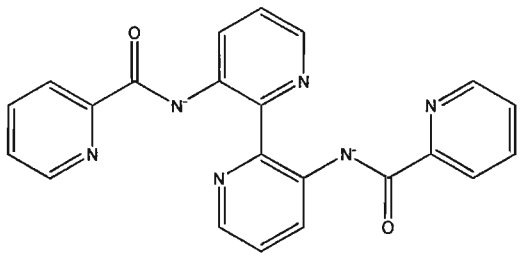

(1.26)

Figure 1.37: An ORTEP[153] representation of one independent molecule of the $[Cu_2(\mathbf{L^1})(hfac)_2]\cdot 3CH_3CN\cdot H_2O$ complex **(1.26)** showing the labelling scheme (thermal ellipsoids are plotted at 50% probability). Solvent molecules are omitted for clarity. Reprinted with permission from reference 81. Copyright {2007} American Chemical Society.

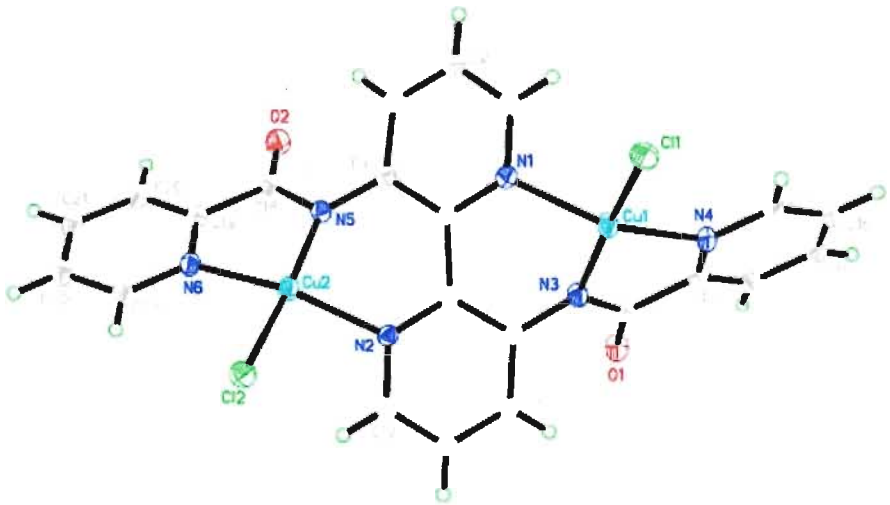

(1.27)

Figure 1.38: ORTEP[153] representation of the molecular structure of the $[Cu_2(\mathbf{L^1})Cl_2]\cdot CH_3CN$ complex **(1.27)** showing the labelling scheme (thermal ellipsoids are plotted at 50% probability). Solvent molecules are omitted for clarity. Reprinted with permission from reference 81. Copyright {2007} American Chemical Society.

The coordination compound **(1.27)** forms a chloride bridge with a neighbouring dimer, Figure 1.39. The ligand is in the dianionic form and coordinates to the divalent Cu^{II} ions via one amido and two pyridine nitrogen donor atoms. The dimeric structures form tetramers (Figure 1.39) where the Cu(2) ion adopts a (4+1) distorted square pyramidal geometry. The Cu(1) ion forms a longer apical bond to an adjacent carbonyl oxygen atom, whereas the Cu(2) ion is chelated to a neighbouring Cu-Cl and chloride ion to afford the chloride bridged linear $[Cu_2(\mathbf{L}^1)Cl_2]_2$ tetramers. A distance of 5.84 Å separates the Cu(1) and Cu(2) centres resulting in weak antiferromagnetic coupling (J = -10.1 K), while the two chloride bridged copper ions are separated by a distance of 3.64 Å and are more strongly ferromagnetically coupled (J = 32.9 K). The four copper centres lie in the same plane and are therefore considered pseudo-linear.

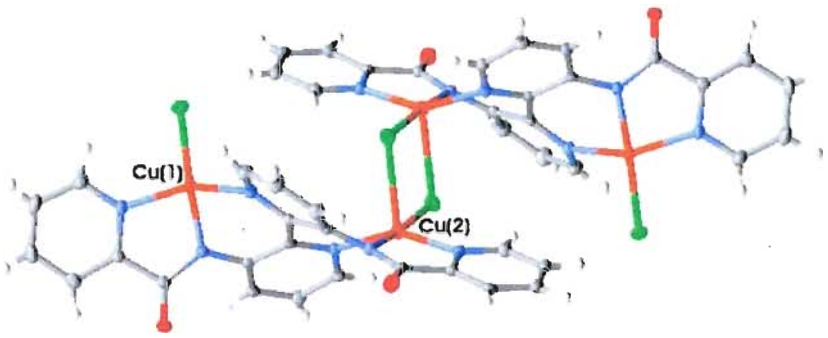

Figure 1.39: A Mercury[152] representation of the dinuclear copper dichloride bridged complex. Reprinted with permission from reference 81. Copyright {2007} American Chemical Society.

For complex **(1.26)**, the presence of two Cu(II) ions per molecule was confirmed by a Curie constant of 0.75 cm^3 K mol^{-1} (expected 0.76 for two S = 1/2 and g = 2.10) and a value for the Weiss constant of θ = -6.29 K. A fit of the experimental data gave g = 2.10, J = -4.93 K. Thus the overall magnetic interaction was antiferromagnetic.

These initial results sparked the further interest in this ligand and are the foundation for this study. In this respect, the goal of my project was to investigate the coordination chemistry of this ligand further with divalent first row transition metal ions that include Cu, Ni, Mn, Co, and Zn.

1.12 – Photo-induced Perturbation of Molecule-based Magnetic Materials

Just like the properties associated with spin-crossover materials other types of molecule-based magnetic materials can be affected by external stimuli. To this end, photo-induced magnetization or the perturbation of magnetization of molecule-based magnetic materials has received increased scientific interest.[92] In particular, the photo-control of magnetic properties may have potential applications in magneto-optical devices.[92] The suppression or enhancement of magnetic instability by light is the fundamental objective of magneto-optical control. Since light cannot couple directly with spin states an effective mechanism that combines both electronic induced photo irradiation and magnetic instability is needed.[92] One classic example of this switching ability is seen in the family of spin-Peierls (SP) systems. These systems operate via the switching of a monomeric paramagnetic state to a dimeric diamagnetic state via light irradiation at low temperatures. There are also Prussian Blue systems that switch from paramagnetic to ferrimagnetic upon irradiation with light.[94] Other examples include cyanometalate-based compounds, organic radicals, and valence tautomerism in Co(II)/(III) complexes.[93,95]

In order to use light as an effective external stimulus to affect the magnetic properties of molecule-based magnetic materials, light harvesting components have been

appended to various compounds. Typical light harvesting materials include anthracene, pyrene, and porphyrin as well as phthalocyanine type materials. The porphyrin and phthalocyanine classes of these materials exhibit fluorescence which is long-lived and can potentially be used as molecular markers.[96]

1.13 – Photo-induced Magnetic Perturbation of Single Molecule Magnets

Of all the molecule-based magnetic materials available for study, single molecule magnets have received a great deal of attention.[13,97] The study of quantum tunneling effects is not the only area of study that has interested various scientific groups.[98] The design of SMMs whose magnetic properties can be reversibly switched by applying external stimuli is important and would bring about new applications for SMMs.[99] The use of light to change or induce magnetic interactions of SMMs has recently been targeted. This focuses on the addressability of the SMMs and forms the basis of the second project of this thesis.

In this regard, a Mn_4 SMM which was linked via a photochromic ligand resulting in a 1-D chain-like structure has been reported in the literature, Figure 1.40.[99] The 1-D chain comprises alternating SMMs and photochromic molecules, essentially yielding a single chain magnet. The photochromic diarylethene ligand undergoes isomerisation between open and closed ring isomers when irradiated with UV and visible light.[99] This structural change affected the magnetism of the single-molecule magnets linked in the structure. After irradiation the magnetization was decreased as evident by the $\chi_M T$ *vs.* T susceptibility plots of the two isomeric compounds, Figure 1.41.

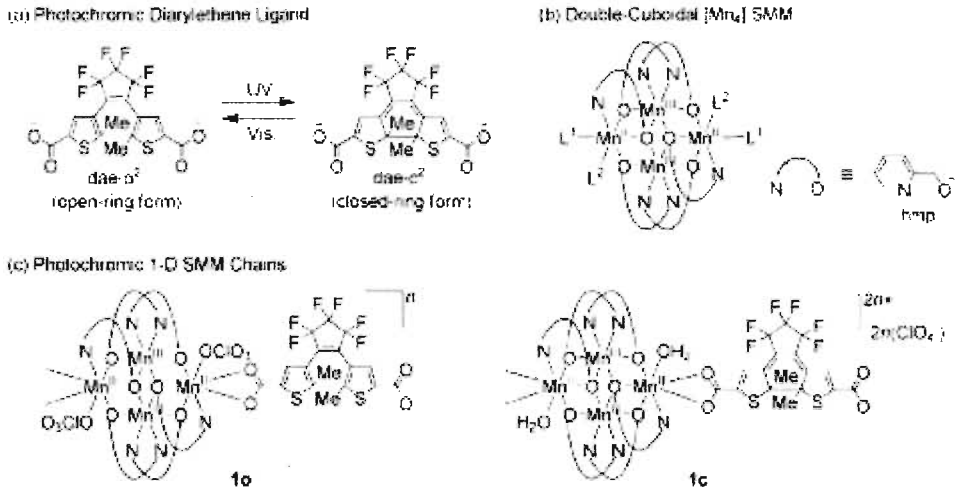

Figure 1.40: Use of a photochromic compound linked to a Mn_4 SMM. Upon irradiation the magnetic properties are affected. Reprinted with permission from reference 99. Copyright {2009} American Chemical Society.

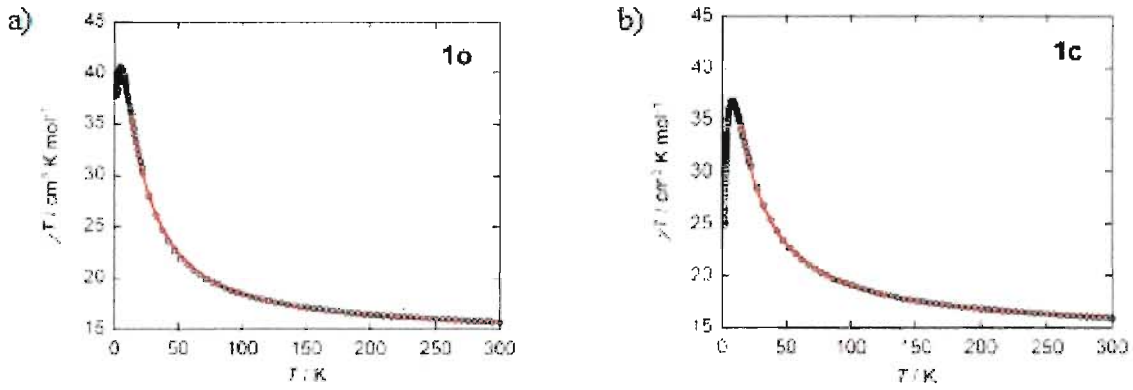

Figure 1.41: Resulting $\chi_M T$ *vs.* T susceptibility plots for the Mn_4 SMM. 1o refers to the open ring structure whereas, 1c refers to the closed structure. Reprinted with permission from reference 99. Copyright {2009} American Chemical Society.

Very recently in 2010 a $Mn_{12}OAc$ cluster was also investigated for its magnetic perturbation via light irradiation.[100] A derivative of stoichiometry $[Mn_{12}O_{12}(L_{3,4,5\text{-}H6F6})_{16}(H_2O)_4]$ where $L_{3,4,5\text{-}H6F6}$ = a gallate derivative, was prepared.[100] This compound displayed a rather remarkable switching ability of its magnetization. This process was attributed to the so called avalanche of magnetization where the flipping of a single

molecule initiated a 'thermal runaway'.[100] The report highlights that a short pulse of light in the visible region can trigger an increase/decrease of the magnetization, or even demagnetize the sample. The authors indicate that in the present state of their research, the impact of the light pulse triggers a chain reaction mediated by the coherent emission of phonons and/or photons, i.e. phonon or photon super-radiance.[100]

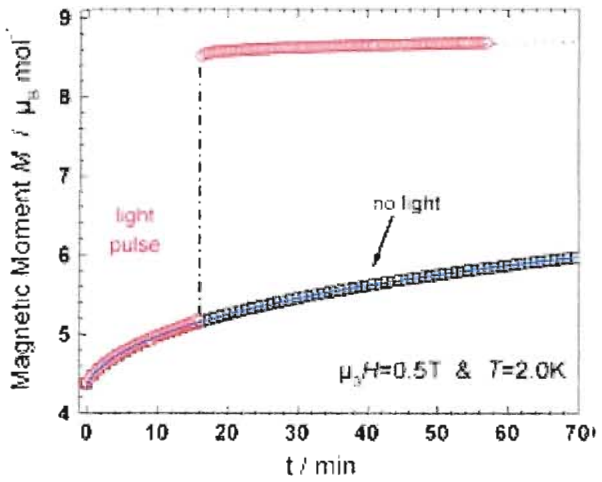

Figure 1.42: Plot of magnetic moment *vs.* time for the complex prepared by Gallani *et al.*. Reprinted with permission from reference 100. Copyright {2010} Royal Society of Chemistry.

Not only can light harvesting ligands be used to affect the magnetization of single molecule magnets but they may also be utilized in the detection of single molecules which is of vital importance in the field of molecular electronics.[96] Furthermore, the photoluminescent properties of these ligands may be used to determine the exact concentration of SMMs on surfaces as well as provide a new tool for the study of fundamental quantum behaviour of SMMs below their blocking temperatures. A photoluminescent ligand appended to a Mn_4 SMM **(1.28)** has been reported in the literature.[96] The compound has stoichiometry $[Mn_4(anca)_4(Hmdea)_2(mdea)_2]\cdot 2CHCl_3$ (Figure 1.43), where $anca^-$ is the anion of 9-anthracenecarboxylic acid and $Hmdea^-$ and

$mdea^{2-}$ are the monoanion and dianion of *N*-methyldiethanolamine, respectively. The authors measured the room temperature UV-Vis spectra as outlined in Figure 1.43. The authors speculate that subtle changes in the luminescent lifetimes and steric considerations of appended photoluminescent ligands may have dramatic effects on the magnetic properties of SMMs.[96]

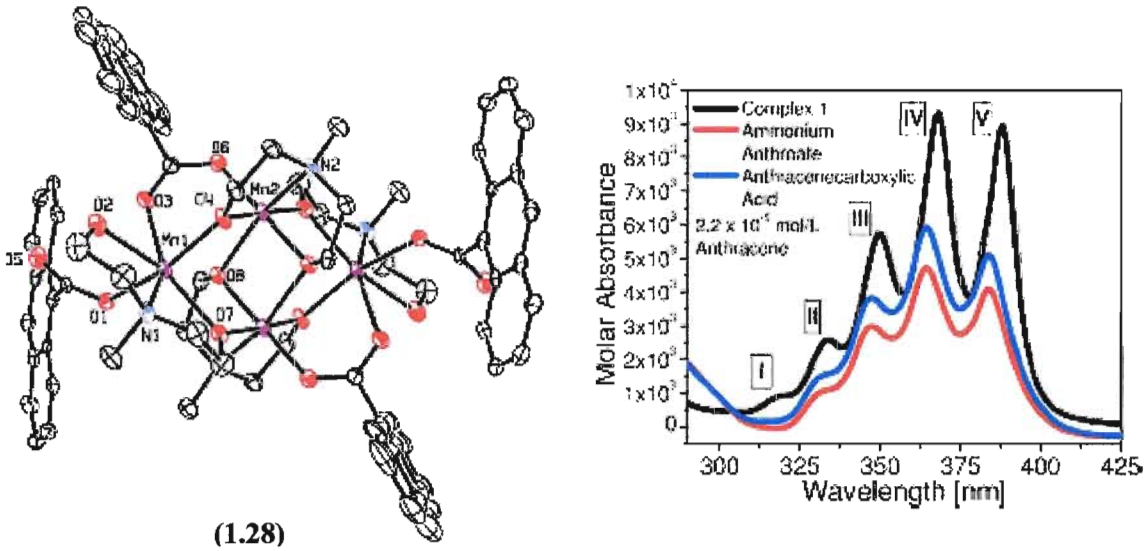

(1.28)

Figure 1.43: ORTEP[153] drawing of the $[Mn_4(anca)_4(Hmdea)_2(mdea)_2]$ **(1.28)** single molecule magnet. Thermal ellipsoids are plotted at 30% probability. Hydrogen atoms have been omitted for clarity. Reprinted with permission from reference 96. Copyright {2008} American Chemical Society.

There are reports in the chemical literature in which porphyrins are used to perturb the electronic properties of fullerene based compounds.[101] There have also been reports on porphyrins appended to polyoxometalate single molecule magnets. These authors were interested in the photoelectrochemistry of the system towards the preparation of catalytic compounds, and the magnetic properties were not measured.[102] Nevertheless, these reports indicate that the electronic properties of single molecule magnets can be affected by light irradiation. Examples of porphyrins appended to SMMs remain scarce in the chemical literature. Therefore, the second project of the thesis seeks

to determine if a single molecule magnet can be affected by external stimuli; specifically the photoinduced magnetic perturbation arising from the excitation of porphyrinic type molecules. The tetrairon[III] single molecule magnet **(1.4)** was selected since it can be synthesized easily and it has been demonstrated that six of its methoxide bridging ligands are labile and can be exchange for triol ligands in a controlled reproducible manner.[81] In this respect, the objectives of the second project were to devise a synthetic strategy for the preparation of porphyrin molecules bearing triol substituents and investigate whether or not these triol groups could exchange for the labile methoxide bridging ligands of the original Fe_4 single molecule magnet **(1.4)**, Figure 1.44. In order to realize these objectives a fundamental knowledge of porphyrin chemistry is required.

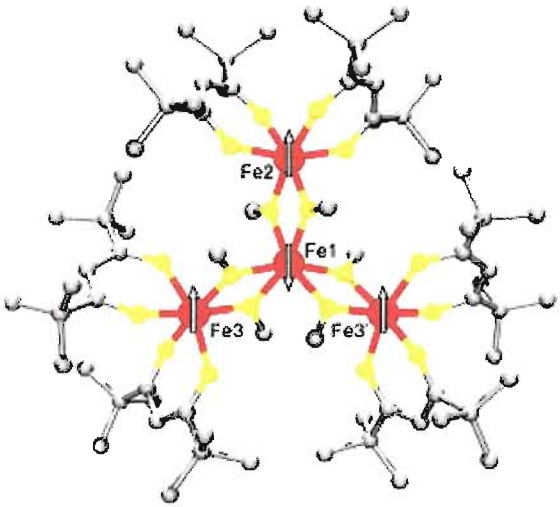

(1.4)

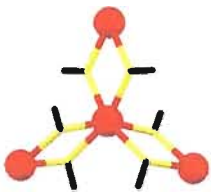

(a)

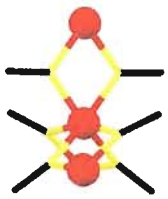

(b)

Figure 1.44: Structure of the Fe_4 single molecule magnet **(1.4)**. Reprinted with permission from reference 35. Copyright {1999} American Chemical Society. (a) view of the Fe_4 single molecule magnet highlighting the bridging methoxide ligands in black. (b) side view of the Fe_4 single molecule magnet highlighting the two available triol exchange sites of the methoxide bridges.

1.14 – Porphyrin Chemistry

The word *porphyrin* has its origins from ancient Greece. In those days the word *porphura* was used to describe the colour purple.[103] This colour arises from the conjugated structure of the porphine moiety, the simplest of all porphyrins, Figure 1.45.

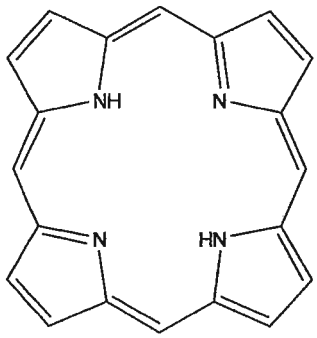

Figure 1.45: Structural representation of the porphine moiety, the simplest of all porphyrins.

Originally this macrocyclic structure was proposed by Küster in 1912 which, ironically, was refuted by Hans Fischer (the father of modern porphyrin chemistry) because it was thought such a large ring was intrinsically unstable.[103] It was not until 1929 when Fischer and his students synthesized heme, the iron porphyrin in hemoproteins, that this macrocyclic structure was accepted by the scientific community.[103]

Before Hans Fischer's nomenclature of porphyrins in 1934, the names of porphyrins were given solely by trivial terms. Following this, Fischer established a semi-trivial naming system which was later replaced by the IUPAC (International Union of Pure and Applied Chemistry) nomenclature in 1979. The IUPAC system numbered all of the atoms (including nitrogen) starting at 1 at a designated α-carbon, Figure 1.46.

Although the IUPAC naming is the most efficient of all naming systems the trivial and semi-trivial systems are still used. This thesis shall use the IUPAC system.

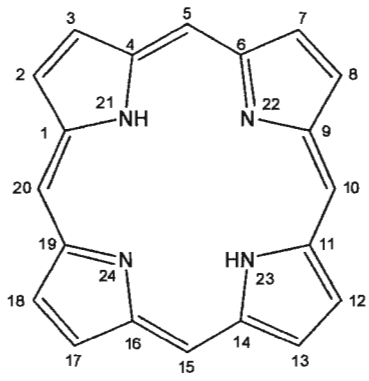

Figure 1.46: IUPAC porphyrin nomenclature system. All atoms are given a number.

Porphyrins are the most common naturally occurring tetrapyrrole macrocyclic ligands and have received great scientific investigation and review.[104] Various metalloporphyrins have physiological properties, such as oxygen transport and involvement in photosynthesis. Furthermore, porphyrins have been studied for their catalytic, non-linear optical, and phototherapeutic properties.[104]

The overall structure of a free base porphyrin is essentially planar.[105] The term 'free base' refers to a porphyrin unit that contains two hydrogen atoms in the central cavity. Various metal and non-metal ions have been complexed into the central cavity of countless porphyrin molecules. The list includes: vanadium, manganese, cobalt, copper, zinc, antimony, and phosphorus. The incorporation of an atom into the central cavity can result in significant distortion of the porphyrin structure. For example 2,3,7,8,12,13,17,18-octaethylporphyrin (OEP), has a planar central cavity in its free base form, but the addition of the small divalent nickel ion results in twisting of the OEP macrocycle to accommodate the metal and maximize binding, Figure 1.47.[106] The most

commonly used porphyrins are tetraphenylporphyrin (TPP) and 2,3,7,8,12,13,17,18-octaethylporphyrin (OEP).[105]

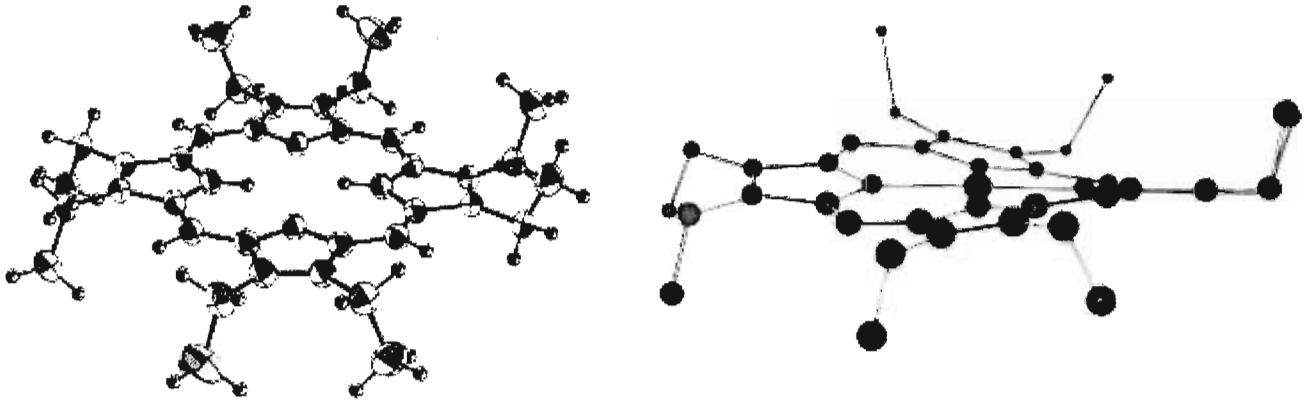

(OEP) **([Ni(OEP)])**

Figure 1.47: Free base OEP and [Ni(OEP)] outlining the twisting capabilities of porphyrin units for complexation. Reprinted with permission from reference 106. Copyright {2002} American Chemical Society.

The incorporation of an atom into the central cavity not only changes the structure of the porphyrin macrocycle it also changes its chemical and physical properties. The most commonly used metal for insertion is zinc and the most commonly used non-metal is phosphorus (particularly hyper valent P^V).[105] The zinc metalloporphyrins tend to transfer electrons (act as donors) while phosphorus porphyrins tend to remove electrons (act as acceptors).[105]

The insertion of an atom into the central cavity also changes the electronic spectra of the porphyrins as evident by UV-Vis measurements. The absorption spectra of porphyrins consist of two distinct regions. One occurs in the near-ultraviolent while the other occurs in the visible region of the electromagnetic spectrum. There is an intense band between 390 - 425 nm ($\log \varepsilon = \sim 5.40$) referred to as the B band or more commonly as the Soret band. In the visible region there are two to four weaker bands ($\log \varepsilon = \sim 4.48$

- 3.69) referred to as the Q-bands. The intensity and number of these Q-bands can give powerful clues as to the overall structure of the porphyrin and whether it is free-base or metallated. Free-base porphyrins consist of four Q-bands referred to as IV, III, II, and I which are labelled according to their relative wavelength. Figure 1.48 displays the spectrum for tetraphenylporphyrin (TPP).

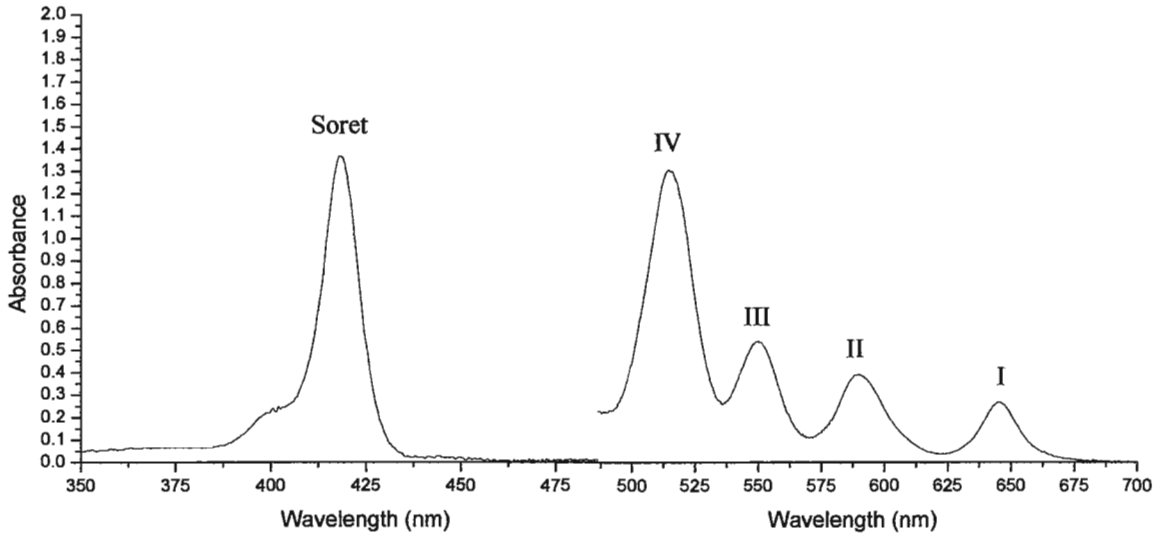

Figure 1.48: UV-Vis spectrum of free-base TTP.

Metalloporphyrins have higher symmetry than the free-base porphyrins and generally consist of two Q-bands referred to as α- and β-bands. The relative intensities of these two bands dictate the relative stability of the compound. When $\alpha > \beta$ the complex is quite stable. However, if $\beta > \alpha$ the resulting metalloporphyrin is easily demetallated by protons. The UV-Vis spectrum of ZnTPP indicates a $\beta > \alpha$ which means that this metalloporphyrin is easily demetallated by the addition of dilute acid, Figure 1.49.

A model prepared by Gouterman explains the spectral differences observed between free-base and metalloporphyrins.[107] Essentially, the differences are attributed to the symmetry of the porphyrins. Free-base porphyrins belong to the D_{2h} point group

whereas metalloporphyrins belong to the D_{4h} point group. This results in 4 Q-bands for free-base porphyrins (D_{2h}) and 2 Q-bands for metalloporphyrins (D_{4h}). Q-bands are forbidden transitions and simply shouldn't exist, however, molecular vibrations in the porphyrin structure marginally lifts the degeneracy allowing these transitions to occur.[103,107]

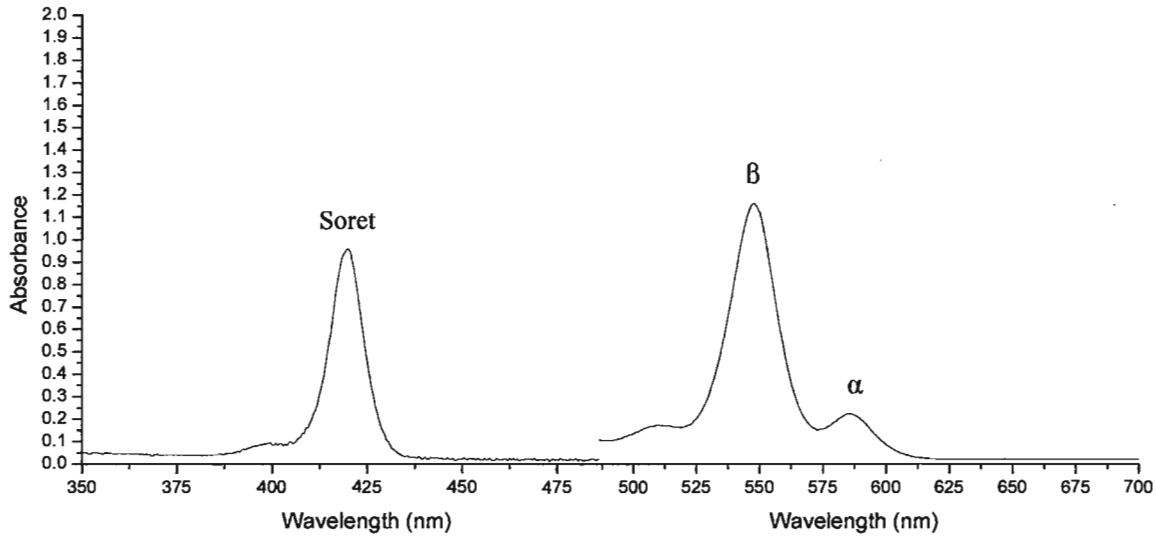

Figure 1.49: UV-Vis spectrum of ZnTTP. Since β > α this metalloporphyrin is susceptible to demetallation via the addition of dilute acid.

Porphyrin excitation occurs via irradiation of the complex with light. Porphyrin excitation energy transfer occurs through two main processes: Photoinduced Electron Transfer (PET) and Excitation Energy Transfer (EET).[108] An outline of both of the processes is depicted in Figure 1.50. After excitation PET or EET can occur depending on the nature of the porphyrinic unit and the quencher. Porphyrins have long lived excited states and as such there is a competition between the normal relaxation processes and energy transfer to an adjacent compound.

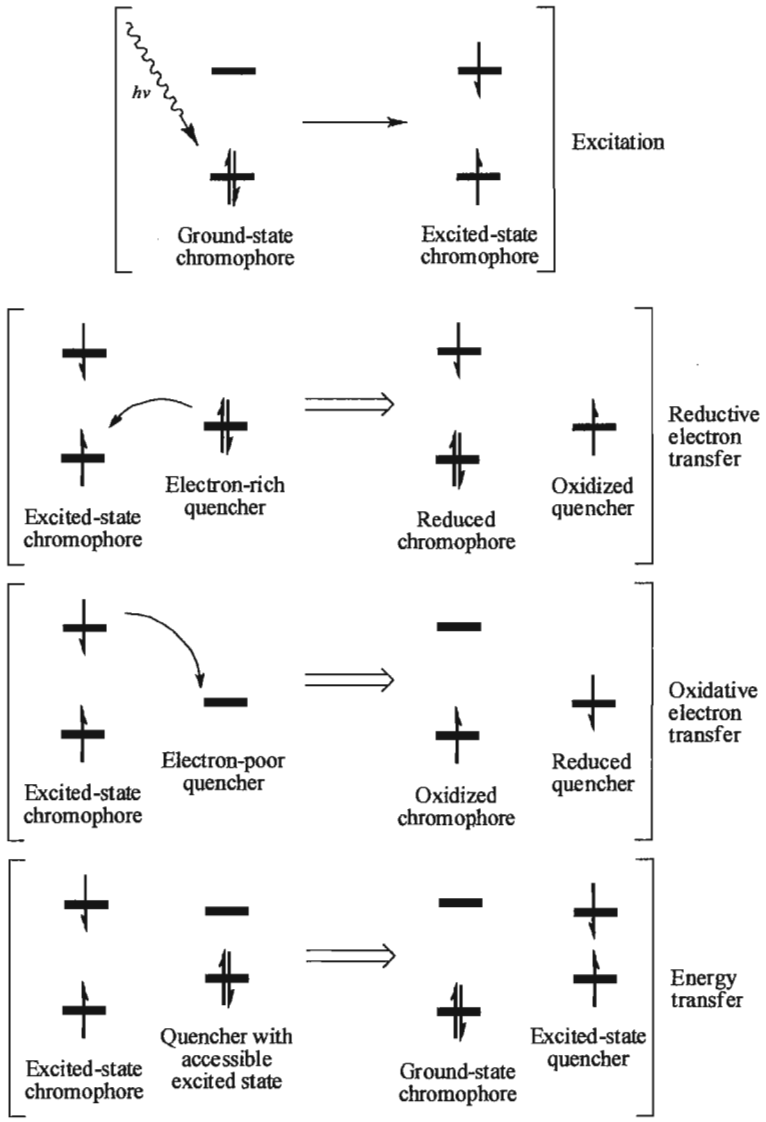

Figure 1.50: Outline of the processes for energy transfer from an excited state porphyrin to a quencher. Adapted from reference 108. Copyright {1997} Royal Society of Chemistry.

Porphyrins have also been used in the preparation of molecule-based magnetic materials, such as the 1-D chain-like structure reported by Miller *et al,* Figure 1.51.[109] This compound displayed an overall ferrimagnetic ordering at 16 K. Furthermore, this structure displayed a photomagnetic perturbation when irradiated with light at low temperature resulting in an increase of its magnetic susceptibility.[109] There has also been

a report of a complex synthesized from porphyrinic type molecules and lanthanide metal ions that displayed single molecule magnet behaviour.[110]

Thus, the overall goal of the second project of this thesis is to synthesize and characterize appropriate porphyrin ligand derivatives and append these materials onto the tetrairon^{III} single molecule magnet. Once again, this particular single molecule magnet was chosen because of its reported ease of synthesis and synthetic modification via ligand exchange.

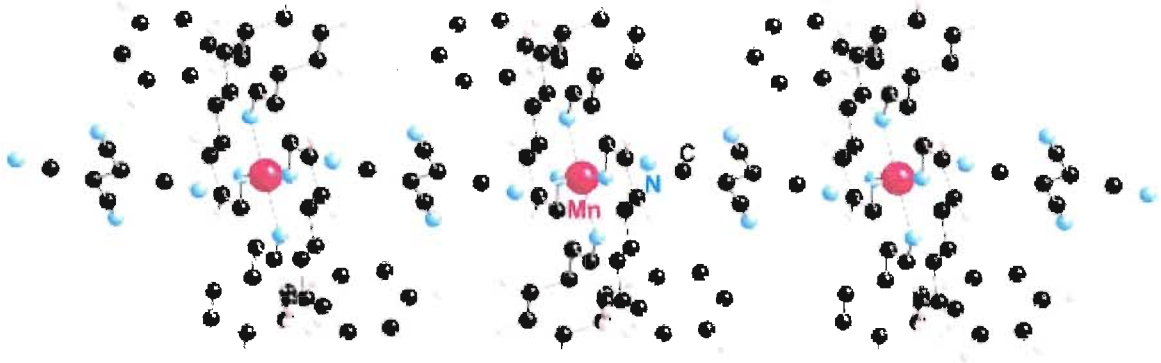

Figure 1.51: Structural representation of the 1-D chain like structure prepared by Miller *et al.*. The compound is ferrimagnetic below 16 K. Reprinted with permission from reference 109. Copyright {2011} Royal Society of Chemistry.

Chapter 2 – Results and Discussion – Project 1

Synthesis and Study of 3,3'-Disubstituted-2,2'-Bipyridine-based Ligands

2.1 – Introduction

The objective of the first project was to functionalize 3,3'-diamino-2,2'-bipyrdine **(1.17)** by adopting a ligand design strategy which would introduce substituents onto the amine moiety, Figure 2.1. The overall goal was to investigate the coordination chemistry of these ligands with various divalent first row transition metal ions (Cu, Ni, Mn, Co, and Zn). The use of multitopic ligands with two or more discrete metal binding sites which allows separation of the metal sites are key building blocks in synthetic chemistry and materials science. In principle the carbon-carbon bond in the bipyridine rings can rotate and as such the ligands have the capability of adopting multiple orientations.

Much like the coordination chemistry of pyridine carboxamide based ligands glycine-based ligands have also been shown to coordinate with various transition metal ions.[111] Glycine derivatives normally coordinate through the nitrogen atoms even if they are not deprotonated.[112] Glycine derivatives have also been investigated towards the preparation of model systems to understand complex metalloprotein structures.[113] The synthesis of $\mathbf{H_2L^3}$ **(2.3)** was targeted to test the coordination ability of a glycine-based bipyridine ligand. Furthermore, this ligand can be further synthetically modified to yield various derivatives such as the $\mathbf{H_2L^4}$ **(2.4)** ligand.

These ligands and their coordination compounds were evaluated with respect to their usefulness as buildings blocks for the preparation of molecule-based magnetic materials. For those coordination complexes whose molecular structures could be

determined by X-ray crystallography, their magnetic properties were then measured and modelled.

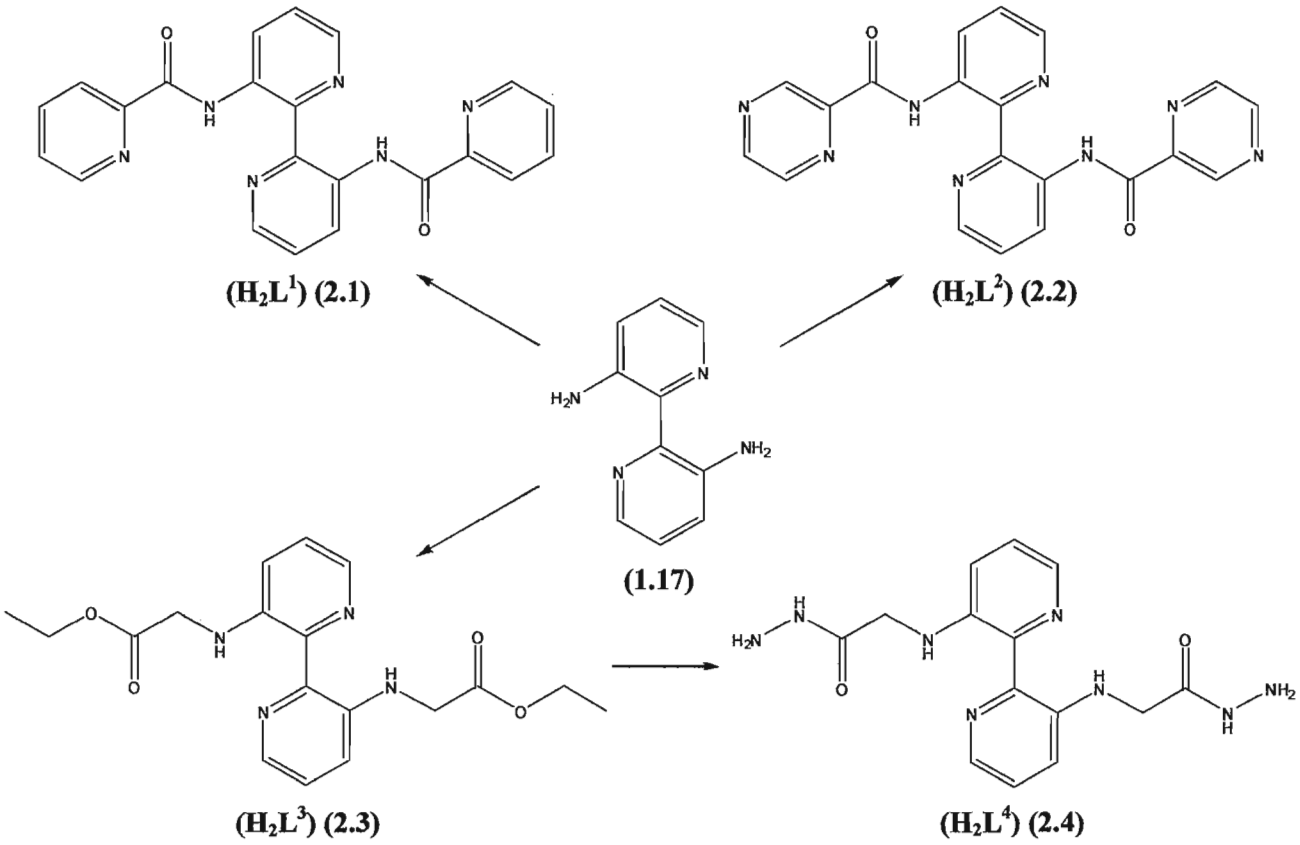

Figure 2.1: The four new ligands prepared in project 1, **(2.1) - (2.4)**, starting from 3,3'-diamino-2,2'-bipyridine **(1.17)**.

The investigation started with the preparation of the first ligand, 2,2'-bipyridine-3,3'-(2-pyridinecarboxamide) **(H_2L^1) (2.1)**.

2.2 – 2,2'-Bipyridine-3,3'-(2-Pyridinecarboxamide) (H_2L^1) (2.1) [81]

The synthetic route for the preparation of 3,3'-diamino-2,2'-bipyrdine **(1.17)** together with an overview of its coordination chemistry was reported in 2002.[67] As reviewed in the *Introduction* section to this thesis, exploitation of the amine functionality of 3,3'-diamino-2,2'-bipyridine **(1.17)** by the Pilkington group afforded a multidentate bipyridine dicarboxamide ligand **(H_2L^1) (2.1)**. This ligand was prepared by reaction of 3,3'-diamino-2,2'-bipyridine **(1.17)** together with 2-pyridine carbonyl chloride **(2.5)**.[81] An overview of the synthetic pathway is presented in Scheme 2.1. An excess of dry triethylamine was added to deprotonate the hydrogen chloride salt of 2-pyridine carbonyl chloride affording the triethylamine hydrogen chloride salt, which was removed by washing the ligand with water during work up.[81] This procedure was followed in order to synthesize the ligand to investigate further its solid-state structure and its coordination chemistry towards first row divalent transition metal ions.

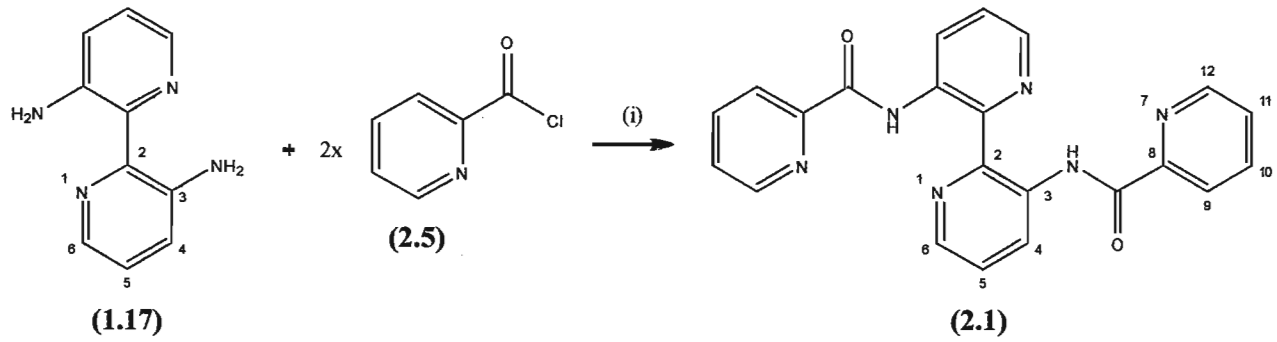

Scheme 2.1: Synthetic route for the preparation of 2,2'-bipyridine-3,3'-(2-pyridinecarboxamide) **(2.1)**. Reagent and conditions: (i) Et_3N / DCM, 0 °C, 2 hrs, 50 °C, 3 hrs.

Ligand **(2.1)** was obtained in 52% yield and its molecular structure was confirmed by ^{1}H-NMR, ^{13}C-NMR, mass spectrometry (EI), UV-Vis and IR spectroscopy. All data for this ligand matched that reported in the chemical literature.[81] Elemental analysis data was within the acceptable limit of ± 0.4% for $C_{22}H_{16}N_6O_2$.

During the course of these studies, single crystals of the ligand were grown via slow evaporation of a saturated dichloromethane solution at room temperature.

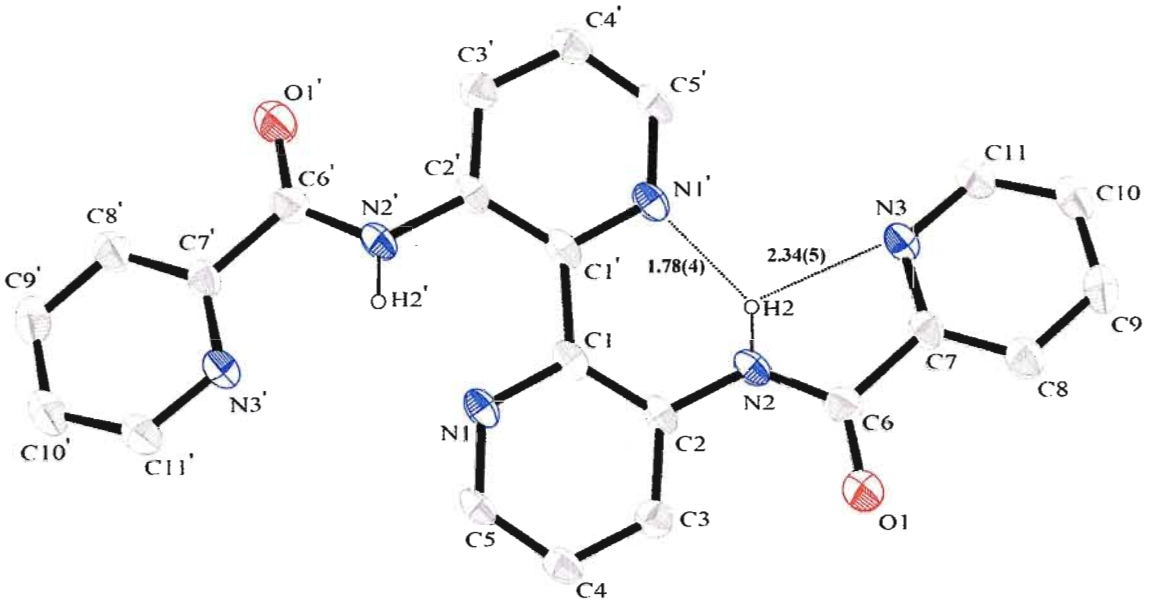

(2.1)

Figure 2.2: ORTEP[153] representation of the molecular structure of **(2.1)** showing the labelling scheme. Thermal ellipsoids are plotted at 50% probability. Hydrogen atoms have been omitted, except for CONH, for clarity. Intramolecular H-bonds are shown as dashed lines and distances are reported in Å.

The ligand crystallizes in the monoclinic space group $P2_1/c$ with one independent molecule per unit cell. An ORTEP[153] view of the molecular structure of one complete ligand molecule along with the atom-numbering scheme is shown in Figure 2.2. The ligand crystallizes in the *trans* configuration with respect to its bipyridine rings. The amide hydrogen atom is bifurcated forming intramolecular H-bonds with the bipyridine (N-H2···N1 = 1.78 Å) and the terminal pyridine (N-H2···N3 = 2.34 Å) nitrogen atoms, Figure 2.2. This bonding stabilizes the *trans* configuration of the ligand. The terminal pyridyl rings are twisted by an angle of 21.3° with respect to the best plane of the bipyridine rings. The packing arrangement of the molecules in the crystal lattice is shown

in Figure 2.3. A view down the *a*-axis of the unit cell reveals that the molecules are π-π stacked in a zigzag arrangement. The separation of 3.47 Å between molecules is ideal for offset π-π interactions as determined by Hunter and Sanders.[114]

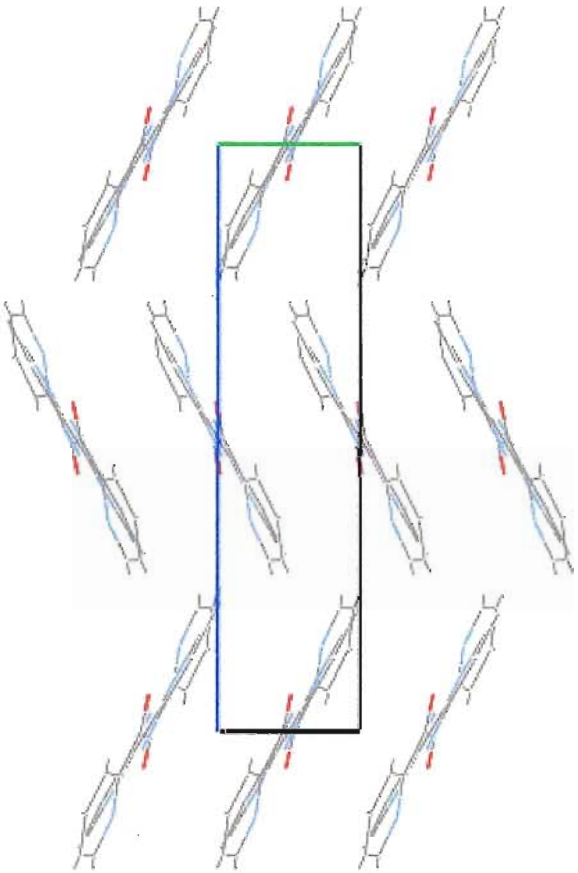

Figure 2.3: Packing diagram of 2,2'-bipyridine-3,3'-(2-pyridinecarboxamide) **(2.1)**. View down the *a*-axis.

Tables 2.1 and 2.2 summarize the bond lengths and bond angles for **(2.1)**.

Table 2.1: Selected bond lengths [Å] for ligand **(2.1)**.

Atoms	Bond [Å]	Atoms	Bond [Å]
O(1) - C(6)	1.226(3)	C(1) - C(1')	1.496(3)
N(1) - C(1)	1.345(3)	C(2) - C(3)	1.403(3)
N(1) - C(5)	1.332(3)	C(3) - C(4)	1.386(3)
N(2) - C(2)	1.395(3)	C(4) - C(5)	1.378(3)
N(2) - C(6)	1.356(3)	C(6) - C(7)	1.513(3)
N(3) - C(7)	1.334(3)	C(7) - C(8)	1.390(3)
N(3) - C(11)	1.341(3)	C(8) - C(9)	1.398(4)
C(1) - C(2)	1.424(3)	C(9) - C(10)	1.374(4)
N(2) - H(2)	0.95(4)	C(10) - C(11)	1.383(4)

Table 2.2: Selected bond angles [°] for ligand **(2.1)**.

Atoms	Angle [°]	Atoms	Angle [°]
C(1) - N(1) - C(5)	120.93(19)	N(1) - C(5) - C(4)	122.6(2)
C(2) - N(2) - C(6)	127.76(19)	O(1) - C(6) - N(2)	126.0(2)
C(7) - N(3) - C(11)	116.9(2)	O(1) - C(6) - C(7)	120.8(2)
N(1) - C(1) - C(2)	120.24(17)	N(2) - C(6) - C(7)	113.25(19)
N(1) - C(1) - C(1')	115.16(17)	N(3) - C(7) - C(6)	118.39(19)
C(2) - C(1) - C(1')	124.61(17)	N(3) - C(7) - C(8)	123.5(2)
N(2) - C(2) - C(1)	121.44(17)	C(6) - C(7) - C(8)	118.1(2)
N(2) - C(2) - C(3)	120.97(19)	C(7) - C(8) - C(9)	118.5(2)
C(1) - C(2) - C(3)	117.59(18)	C(8) - C(9) - C(10)	118.2(2)
C(2) - C(3) - C(4)	120.4(2)	C(9) - C(10) - C(11)	119.2(2)
C(3) - C(4) - C(5)	118.2(2)	N(3) - C(11) - C(10)	123.6(2)

Once ligand **(2.1)** had been prepared and fully characterized, the next objective was to investigate its coordination chemistry with the aforementioned divalent transition metal ions.

2.3 – Coordination Chemistry of Ligand (H_2L^1) (2.1)

As presented in the *Introduction* chapter of the thesis the coordination chemistry of ligand **(2.1)** was previously investigated with two Cu(II) salts ($CuCl_2$ and $Cu(hfac)_2$). In the case of $CuCl_2$ a tetrameric complex, $[Cu_2(\mathbf{L^1})Cl_2]$ **(1.27)**, was assembled which had interesting magnetic properties.[81] Moving forward with this research, the objective of my project was to further investigate the coordination chemistry of this ligand with other metal salts. As mentioned, the investigation focused on divalent first row transition metals: Cu, Ni, Mn, Co, and Zn. The counter ions used were chloride and acetate. Chloride offers the possibility of exchange reactions or bridging while acetate ions offer the possibility of multiple modes of bridging interactions. Thus the metal salts used were: $CuCl_2$, $Cu(OAc)_2$, $NiCl_2$, $Ni(OAc)_2$, $MnCl_2$, $Mn(OAc)_2$, $CoCl_2$, $Co(OAc)_2$, and $Zn(OAc)_2$.

In a typical experiment, 2.1 equivalents of the metal salt were reacted together with one equivalent of ligand **(2.1)**. Although Lewis acidic transition metals can facilitate the deprotonation of amides, two equivalents of triethylamine were added to greater facilitate the deprotonation of the ligand. Triethylamine is a strong base ($pK_b = 2.99$) and is non-nucleophilic, making it suitable for these reactions. All reactions were carried out at room temperature in a 3:1 mixture of DCM:MeOH. The ligand was soluble in DCM, whereas the salts were soluble in MeOH.

The ligand can potentially coordinate transition metal ions via two N_3 tridentate binding pockets. Following this procedure a series of coordination complexes have been prepared and characterized.

In the field of molecule-based magnetic materials it is of vital importance to obtain the molecular structures of compounds in the solid state by X-ray diffraction. This is because magnetic modeling requires the exact positions of paramagnetic metal centres in order to produce an accurate model. We then turned our attention to the growth of suitable single crystals of the complexes in order to elucidate their molecular structures in the solid state via X-ray diffraction. Those compounds that did not yield suitable single crystals for X-ray diffraction were compared via UV-Vis, IR, MS, and CHN to those that did crystallize.

2.3.1 – Zinc Acetate Complex (2.6)

The reaction of zinc acetate with the ligand **(2.1)** yielded a yellow crystalline powder in 60% yield. Initially the preparation of the zinc complex was carried out in order to investigate if coordination of the ligand had occurred via ^{1}H- and ^{13}C-NMR experiments. However, suitable single crystals for X-ray diffraction were obtained via the slow evaporation of a 1:1 DCM:MeOH solution of the previously isolated yellow powder. The molecular structure of the zinc complex **(2.6)** along with the atom-numbering scheme is shown in Figure 2.4. The complex crystallizes as a tetramer.

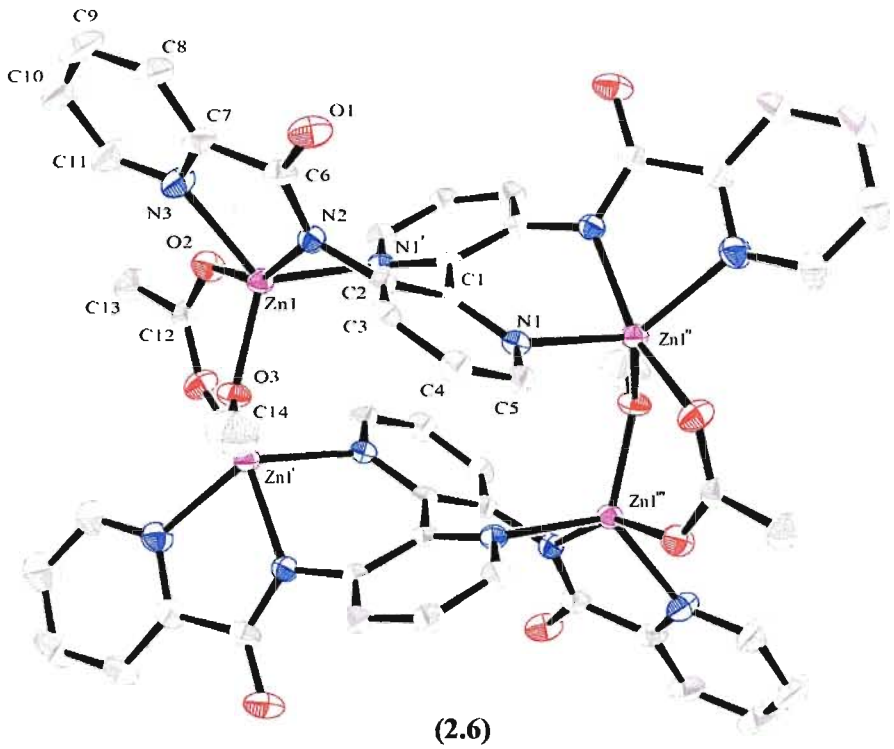

(2.6)

Figure 2.4: ORTEP[153] representation of the molecular structure of the Zn(II) tetramer **(2.6)** showing the labelling scheme. Thermal ellipsoids are plotted at 50% probability. Hydrogen atoms and solvent molecules have been omitted for clarity.

The zinc complex crystallizes in the orthorhombic space group Cmca where 1/4 of the molecule, a water molecule, and three methanol molecules are crystallographically unique. The solvent molecules are disordered resulting in the lowest R1 = 0.0762. Applying the SQUEEZE command in the SHELX-97 software resulted in R1 = 0.0393.[151] This command removes the electron density from the disordered solvent molecules which in turn yields a better model of the crystallographic data. This is evident by the reported R1 values.

The zinc acetate complex is comprised of four Zn(II) ions and two carboxamide ligands. The metal to ligand ratio is thus 2:1. Each carboxamide ligand chelates in a *bis*-tridentate fashion through the bipyridine, amide and terminal pyridine nitrogen atoms

while the carbonyl oxygen atom remains unchelated. Two additional oxygen atoms, one from a methoxide ion and the other from an acetate molecule, complete the 5-coordinate geometry around the Zn(II) ions and balance the charge. The coordination geometry around the Zn(II) centres is best described as being intermediate between trigonal bipyramidal and square-based pyramidal. The ligand is twisted. The torsion angle between the best planes of the bipyridine rings is 43.8°. The terminal pyridine rings lie at an angle of 54.1° from the bipyridine (pyridine) ring to which each is directly attached and 77.7° to the opposite bipyridine (pyridine) ring. The distance between the Zn(II) ions in the same ligand molecule Zn(1)···Zn(1") is 6.269 Å, while the distance between the Zn(II) ions across the bridged acetate Zn(1)···Zn(1') is considerably shorter, 3.323 Å. Tables 2.3 and 2.4 summarize the selected bond lengths and bond angles around the Zn(II) metal centre of this complex. A full list of all bond lengths and angles for this complex can be found in the *Appendix* section of the thesis, Tables 6.1 and 6.2.

Table 2.3: Selected bond lengths [Å] for the zinc complex **(2.6)**.

Atoms	Bond [Å]	Atoms	Bond [Å]
Zn(1) - O(2)	2.0340(18)	Zn(1) - O(3)	1.9495(14)
Zn(1) - N(2)	2.033(2)	Zn(1) - N(3)	2.170(2)
Zn(1) - N(1')	2.173(2)		

Table 2.4: Selected bond angles [°] for the zinc complex **(2.6)**.

Atoms	Angle [°]	Atoms	Angle [°]
O(2) - Zn(1) - O(3)	97.77(9)	O(2) - Zn(1) - N(2)	154.24(8)
O(2) - Zn(1) - N(3)	84.12(8)	O(2) - Zn(1) - N(1')	94.73(8)
O(3) - Zn(1) - N(2)	106.87(9)	O(3) - Zn(1) - N(3)	122.43(10)
O(3) - Zn(1) - N(1')	111.90(9)	N(2) - Zn(1) - N(3)	76.49(8)
N(2) - Zn(1) - N(1')	83.15(7)	N(3) - Zn(1) - N(1')	125.34(8)

The UV-Vis spectrum of complex **(2.6)** has peaks centered at λ = 231, 257, 309, 341 nm that can be assigned to π-π^* and n-π^* ligand based electronic transitions. No additional bands are observed past 500 nm. The mass spectrometry data displays fragmentation ions at *m/z* = 1042 for $[Zn_3(\mathbf{L^1})_2OAc]^+$, *m/z* = 919 for $[Zn_2(\mathbf{L^1})_2]^+$, and *m/z* = 676 for $[Zn_2(\mathbf{L^1})(OAc)_2MeO]^+$. The IR spectrum shows the loss of the N-H_{str} while the C=O_{str} at 1674 cm^{-1} has not shifted. The spectrum also displays intense bands at 1562, 1513, 1463, and 1432 cm^{-1}. The first two bands can be assigned to the υ_{asym} (OCO) and the last two bands assigned to υ_{sym} (OCO) of the acetate.[115] These bands are consistent with the bidentate bridging mode of the acetate molecule. The CHN data is consistent for $[C_{50}H_{40}N_{12}O_{10}Zn_4]\cdot 3MeOH\cdot H_2O$ which is in complete agreement with the molecular structure of the complex determined by X-ray diffraction.

2.3.2 –Copper(II) Chloride Complex (1.27)[81] and Copper(II) Acetate Complex (2.7)

The reported data for copper complex **(1.27)** consists of the IR, MS, and CHN microanalysis along with the X-ray crystal structure.[81] The synthesis of this complex was repeated during the course of these studies and isolated as a green crystalline powder in 66% yield. All data matched the literature values.[81] The UV-Vis spectrum of the copper complex **(1.27)** has peaks centered at λ = 231, 258, 324, 370 nm assigned to π-π^* and n-π^* ligand based electronic transitions. The mass spectrometry data displays a parent peak at *m/z* = 593 for $[Cu_2(\mathbf{L^1})Cl_2]^+$ and fragmentation ions at *m/z* = 557 for $[Cu_2(\mathbf{L^1})Cl]^+$ and *m/z* = 457 for $[Cu(\mathbf{L^1})]^+$. The IR spectrum shows the loss of the N-H_{str} while the C=O_{str} has shifted from 1678 cm^{-1} for the uncoordinated ligand to 1623 cm^{-1} for complex **(1.27)**. This shift is of the same order of magnitude as that observed by Woollins

and co-workers, who prepared structurally similar pyridyl systems which coordinated through the amide nitrogen atoms rather than the carbonyl oxygen.[116] This weakening of the $C{=}O_{str}$ is consistent with structural studies of amide complexes of first row transition metal ions which typically show longer C=O bond lengths and shorter C-N bond lengths on coordination through a deprotonated amide nitrogen atom. The CHN data is consistent for $[C_{22}H_{14}N_6O_2Cu_2Cl_2]$ which is in agreement with the molecular structure of the complex reported in the literature.[81]

The copper(II) acetate complex **(2.7)** was obtained in 77% yield and isolated as a green crystalline powder. Recrystallization of the complex from a 1:1 solution of DCM:MeOH yielded green crystals suitable for X-ray diffraction. The molecular structure of the $[Cu_2(\mathbf{L^1})(OAc)_2]$ **(2.7)** complex is shown in Figure 2.5.

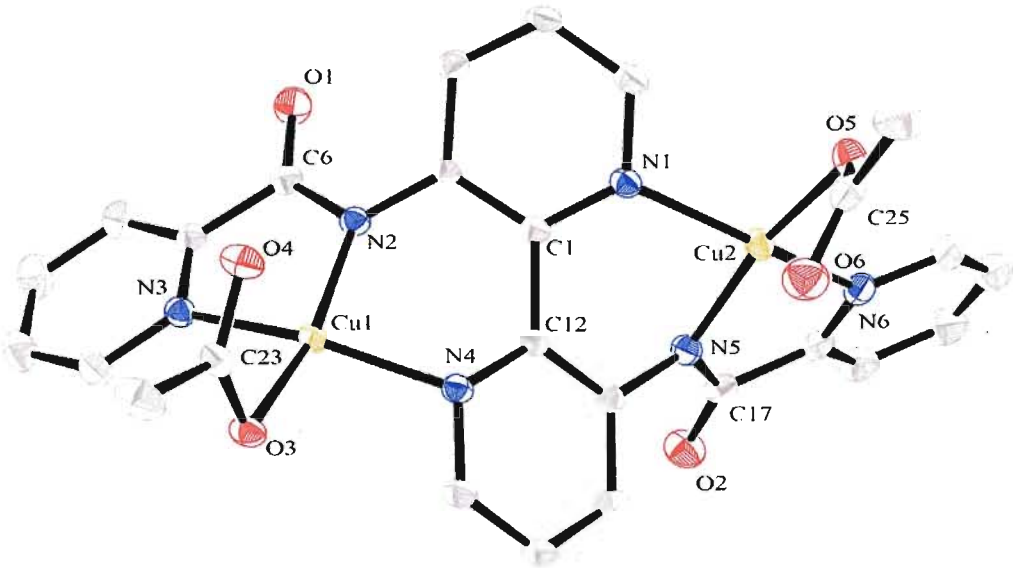

(2.7)

Figure 2.5: ORTEP[153] representation of the molecular structure of the $[Cu_2(\mathbf{L^1})(OAc)_2]$ complex **(2.7)**. Thermal ellipsoids are plotted at 50% probability. Hydrogen atoms and solvent molecules have been omitted for clarity.

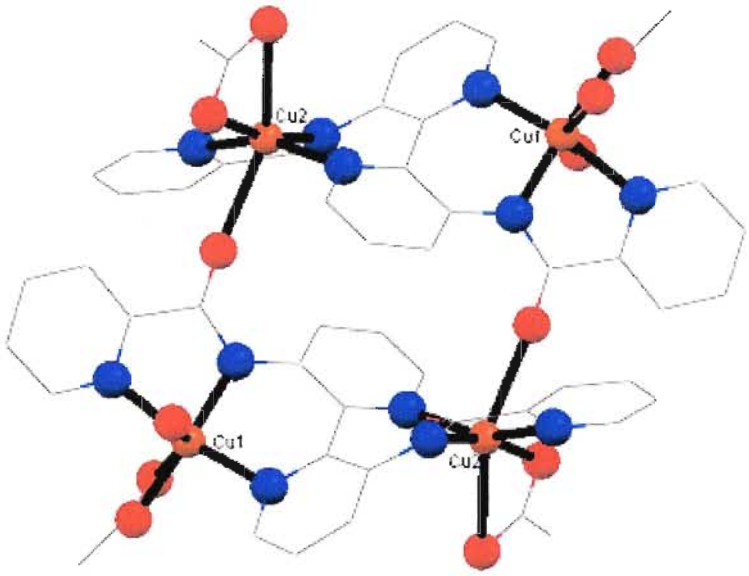

Figure 2.6: Mercury[152] view of the packing structure of the copper(II) acetate complex **(2.7)** showing the coordination geometry around each Cu(II) metal ion.

The copper(II) acetate complex **(2.7)** crystallises in the monoclinic space group C2/c. The complex is a tetramer where half of the tetramer is crystallographically unique. The metal to ligand ratio is thus 2:1. Each of the crystallographically independent Cu(II) centres exhibits an N_3O_3 coordination geometry. For Cu(1) this coordination geometry comprises of a tridentate N_3 donor set from the dianionic $\mathbf{L^1}$, two O atoms from a chelating μ_2-OAc ligand and a μ_2-η^2:η^1-OAc bridge to a crystallographically equivalent Cu(1') related by a 2_1 screw axis parallel to *b*. Cu(2) also has an N_3 donor set from the dianionic $\mathbf{L^1}$ and a chelating acetate while the final coordination site on Cu(2) is taken by one of the two carboxamide O atoms of the ligand. The torsion angle between the best planes of the bipyridine rings is 43.4°. The terminal pyridine rings lie at angles of 48.5° and 66.1° from the bipyridine (pyridine) ring to which each is directly attached and 63.7° and 61.6° to the opposite bipyridine (pyridine) ring. The intramolecular distance between Cu(1)···Cu(2) is 6.113 Å, while the distance between Cu(1)···Cu(2') is 6.490 Å. Tables 2.5

and 2.6 summarize the selected bond lengths and bond angles for the copper(II) acetate complex **(2.7)**.

Table 2.5: Selected bond lengths [Å] for the copper(II) acetate complex **(2.7)**.

Atoms	Bond [Å]	Atoms	Bond [Å]
Cu(1) - O(3)	1.9672(19)	Cu(1) - O(4)	2.4484(16)
Cu(1) - N(2)	1.927(2)	Cu(1) - N(3)	2.0006(19)
Cu(1) - N(4)	2.0077(18)	Cu(1) - O(4')	2.5298(15)
Cu(2) - O(1)	2.531(2)	Cu(2) - O(5)	1.9385(16)
Cu(2) - O(6)	2.692(2)	Cu(2) - N(1)	2.0455(17)
Cu(2) - N(5)	1.9104(17)	Cu(2) - N(6)	2.0240(17)

Table 2.6: Selected bond angles [°] for the copper(II) acetate complex **(2.7)**.

Atoms	Angle [°]	Atoms	Angle [°]
Cu(1) - O(4) - Cu(1')	139.77(8)	O(3) - Cu(1) - N(2)	161.70(7)
O(3) - Cu(1) - N(3)	94.22(7)	O(3) - Cu(1) - N(4)	97.04(8)
O(3) - Cu(1) - C(23)	29.97(6)	O(3) - Cu(1) - O(4')	98.81(6)
O(4) - Cu(1) - N(2)	103.06(7)	O(4) - Cu(1) - N(3)	91.32(7)
O(4) - Cu(1) - N(4)	111.84(7)	O(4) - Cu(1) - C(23)	28.89(6)
O(4) - Cu(1) - O(4')	154.06(5)	N(2) - Cu(1) - N(3)	83.19(8)
N(2) - Cu(1) - N(4)	92.05(8)	N(2) - Cu(1) - C(23)	131.77(7)
N(2) - Cu(1) - O(4')	98.19(7)	N(3) - Cu(1) - N(4)	156.83(7)
N(3) - Cu(1) - C(23)	91.58(8)	N(3) - Cu(1) - O(4')	76.51(6)
N(4) - Cu(1) - C(23)	108.14(8)	N(4) - Cu(1) - O(4')	81.79(6)
O(1) - Cu(2) - O(5)	82.42(7)	O(1) - Cu(2) - O(6)	135.19(6)
O(1) - Cu(2) - N(1')	87.34(7)	O(1) - Cu(2) - N(5')	111.76(8)
O(1) - Cu(2) - N(6')	76.10(7)	O(5) - Cu(2) - O(6)	54.30(7)
O(5) - Cu(2) - N(1)	96.19(7)	O(5) - Cu(2) - N(5)	165.19(10)
O(5) - Cu(2) - N(6)	98.77(7)	O(6) - Cu(2) - N(1)	86.51(7)
O(6) - Cu(2) - N(5)	112.46(8)	O(6) - Cu(2) - N(6)	117.57(7)
N(1) - Cu(2) - N(5)	89.00(7)	N(1) - Cu(2) - N(6)	155.91(8)

A full list of all bond lengths and angles for the $[Cu_2(\mathbf{L^1})(OAc)_2]$ complex **(2.7)** can be found in the *Appendix* section of the thesis, Tables 6.3 and 6.4.

For Cu(1) the Jahn-Teller distortion is manifested in an elongation along the O(4)Cu(1)O(4') axis and a similar distortion is observed for Cu(2) along the O(1)Cu(2)O(6) axis. The crystal packing of $[Cu_2(\mathbf{L^1})(OAc)_2]$ can be considered to be comprised of dinuclear $Cu_2(\mathbf{L^1})(OAc)_2$ units linked together via bridging carboxamide O atoms to form a centrosymmetric tetranuclear complex, Figure 2.6. These tetramers are then further linked via the μ_2-η^2:η^1-OAc bridges to form a polymeric chain-like structure, Figure 2.7.

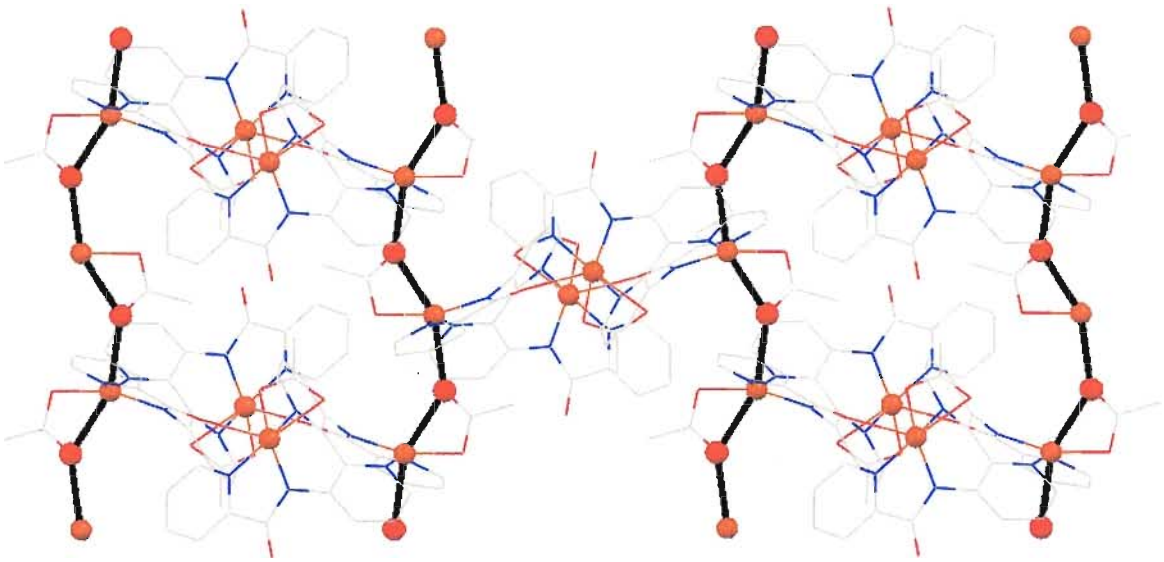

Figure 2.7: Crystal packing of tetramers showing the bridging of copper ions to form polymeric {Cu(1)-O(4)}$_\infty$ chains. Hydrogen atoms have been omitted for clarity.

The UV-Vis spectrum of the copper complex **(2.7)** has peaks centered at λ = 228, 256, 320, 363 nm assigned to π-π^* and n-π^* ligand based electronic transitions. An additional band at 667 nm is assigned to the d-d transitions. The mass spectrometry data displays a parent peak at m/z = 642 for $[Cu_2(\mathbf{L^1})(OAc)_2]^+$. Fragmentation ions are present

at m/z = 579 for $[Cu_2(\mathbf{L^1})OAc]^+$ and m/z = 520 for $[Cu_2(\mathbf{L^1})]^+$. The IR spectrum shows the loss of the N-H_{str} while the C=O_{str} is red shifted from 1678 cm^{-1} for the uncoordinated ligand to 1637 cm^{-1} for complex **(2.7)**. There are various bands from 1598 – 1344 cm^{-1} assigned to C-O stretches of the acetate groups in the complex. These bands are indicative of the bidentate and bridging coordination modes of the acetate molecules. The CHN data is consistent with the stoichiometry $[C_{26}H_{20}N_6O_6Cu_2]\cdot MeOH$.

Once characterized, the susceptibility of the copper(II) acetate complex was then measured to investigate its magnetic properties. A sample of 12.3 mg of **(2.7)** was measured on a Quantum Design SQUID magnetometer in an applied field of 1000 Oe between 5 and 300 K. The data were corrected for the sample holder and sample diamagnetism (Pascal's constants).[8] A plot of $1/\chi_M$ *vs.* T, Figure 2.9, showed the complex obeyed the Curie-Weiss law with C = 1.077 cm^3 K mol^{-1} and θ = -6.1 K consistent with two S = ½ ions with g = 2.40 and the presence of weak antiferromagnetic interactions between the Cu(II) ions. The g-value is typical of Cu^{II} ions in which second-order spin-orbit coupling leads to $g > g_e$.[117] This value of g was confirmed by the EPR measurements carried out in a DCM solution of the $[Cu_2(\mathbf{L^1})(OAc)_2]$ complex.

In order to generate an appropriate magnetic model for $[Cu_2(\mathbf{L^1})(OAc)_2]$, its molecular structure was examined for close Cu···Cu contacts and pathways for magnetic superexchange, Figure 2.8.

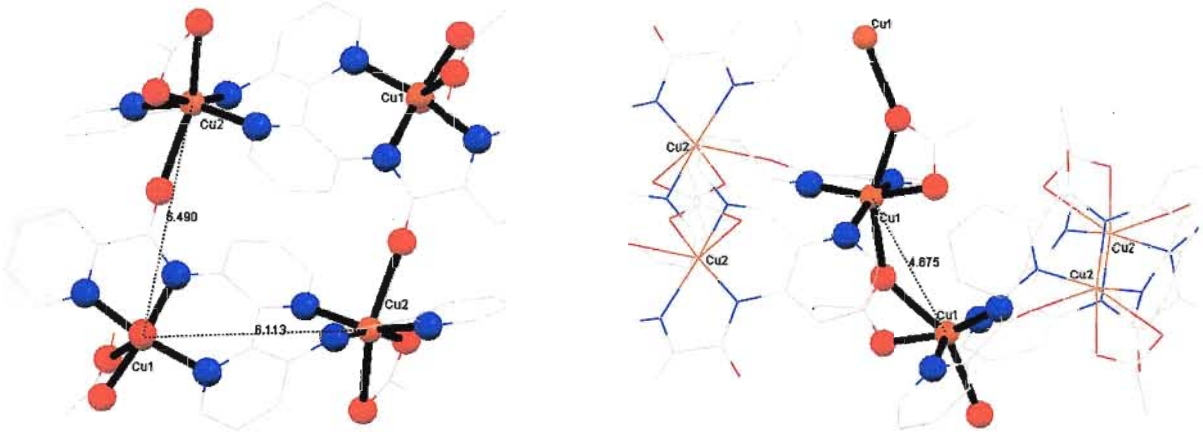

Figure 2.8: Mercury[152] view displaying copper-copper contacts in complex **(2.7)**. Distances are given in Å.

The closest Cu···Cu distances (4.675 Å) are between the tetramer units and are associated with the μ_2-η^2:η^1-acetate bridge (Cu-O-Cu = 139.77(8)°), linking Cu(1) atoms together to form the one-dimensional chain, Figure 2.7. The remaining through-bond interactions comprise a three-atom OCN bridge *via* the carboxamide linking Cu(1) and Cu(2') at 6.490 Å and *via* the four-atom NCCN unit of the 2,2′-bipyridyl sub-unit linking Cu(1) and Cu(2) at 6.113 Å, Figure 2.8. The large inter-nuclear contacts and multiple atom bridges suggested that the best magnetic model might therefore be a one-dimensional chain of interacting Cu(1) ions and isolated Cu(2) ions. As a consequence the magnetic susceptibility was fitted to a Heisenberg linear chain[118] with an additional term to account for the non-interacting Cu^{2+} ion:

$$\chi = \frac{Ng^2\beta^2}{kT} \cdot \frac{(0.25 + 0.14995x + 0.30094x^2)}{(1 + 1.9862x + 0.68854x^2 + 6.0626x^3)} + \frac{Ng^2\beta^2 S(S+1)}{3kT}$$

where $x = J/k\mathrm{T}$.

A fit of the susceptibility to this expression yielded g = 2.40 and J = -7.64 cm^{-1}. This model fit the observed data very well as indicated by the $\chi_M T$ *vs.* T graph, Figure 2.9.

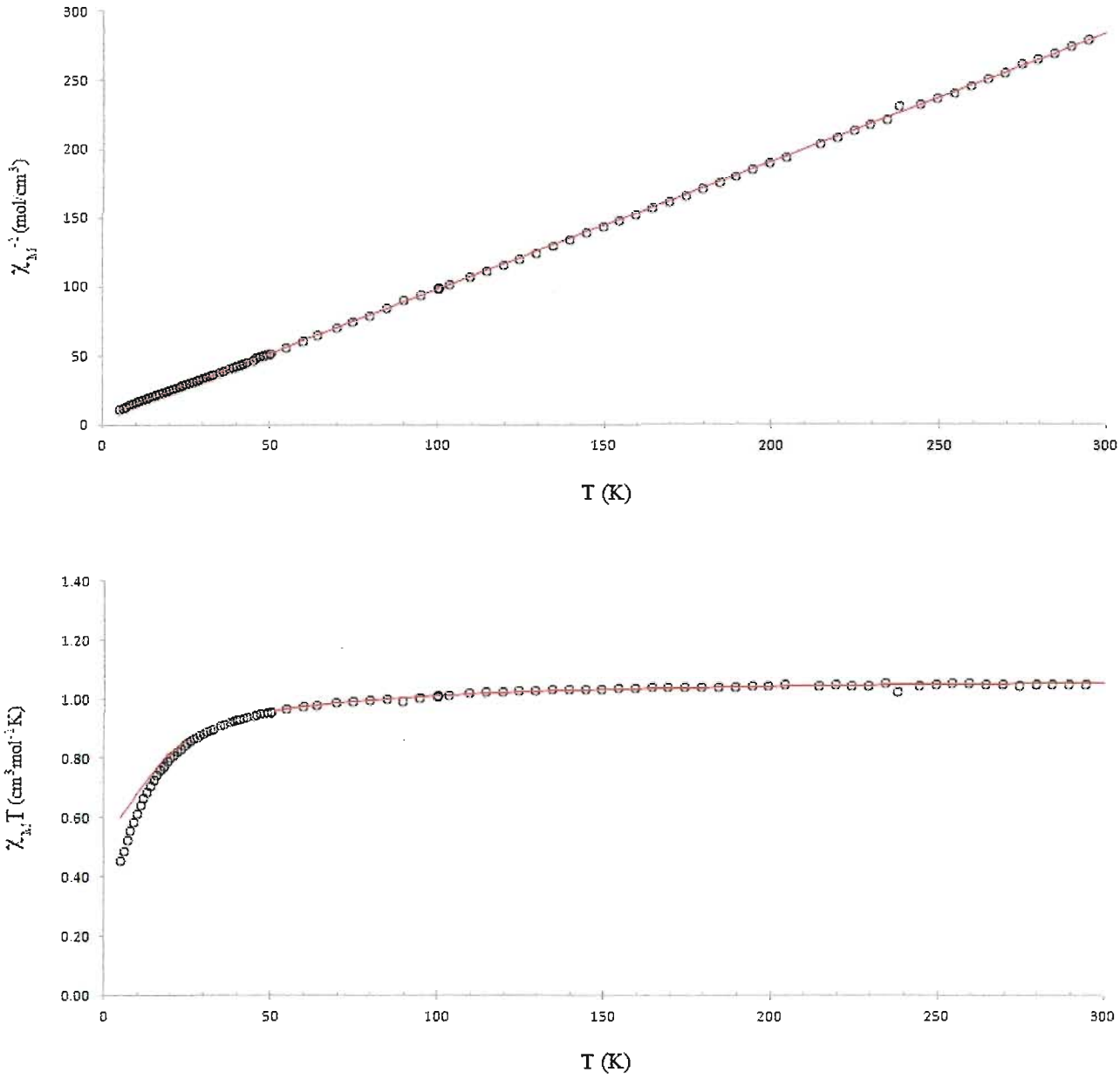

Figure 2.9: Graphs of $1/\chi_M$ *vs.* T and $\chi_M T$ *vs.* T for complex **(2.7)**. The open circles represent the experimental data and the solid red line represents the best model.

The overall magnetic interaction in the $[Cu_2(\mathbf{L^1})(OAc)_2]$ complex **(2.7)** is thus weakly antiferromagnetic.

Unlike the copper(II) acetate complex **(2.7)**, the previously reported $[Cu_2(\mathbf{L^1})Cl_2]$ **(1.27)** complex displayed both antiferromagnetic and ferromagnetic interactions. Complex **(2.7)** is not as interesting magnetically as it is structurally. A chain-like copper structure, similar to **(2.7)**, has been reported which displays alternating antiferromagnetic and ferromagnetic ordering.[119] Scientific interest is now focused on hetero-bimetallic chain-like structures ultimately leading to higher dimensional compounds.[119]

2.3.3 – Nickel(II) Trimers (2.8) and (2.9)

The next two complexes to crystallize were two Ni(II) trimers, which were synthesized via reaction of ligand **(2.1)** with nickel(II) chloride and nickel(II) acetate, respectively.

The reaction of nickel(II) chloride with the ligand **(2.1)** yielded a yellow powder. However, suitable single crystals for X-ray diffraction were grown via a slow liquid diffusion reaction that consisted of layering a methanol solution of $NiCl_2 \cdot 6H_2O$ over a solution of DCM containing triethylamine and the carboxamide ligand **(2.1)**. The isolated crystals were red cubes. The molecular structure of the nickel complex reveals that the molecule crystallizes as a trimer. The complex contains three nickel(II) centres, three carboxamide ligands, and six disordered water molecules. The metal to ligand ratio in the complex is 1:1. A view of the molecular structure of the nickel(II) trimer **(2.8)** is presented in Figure 2.10.

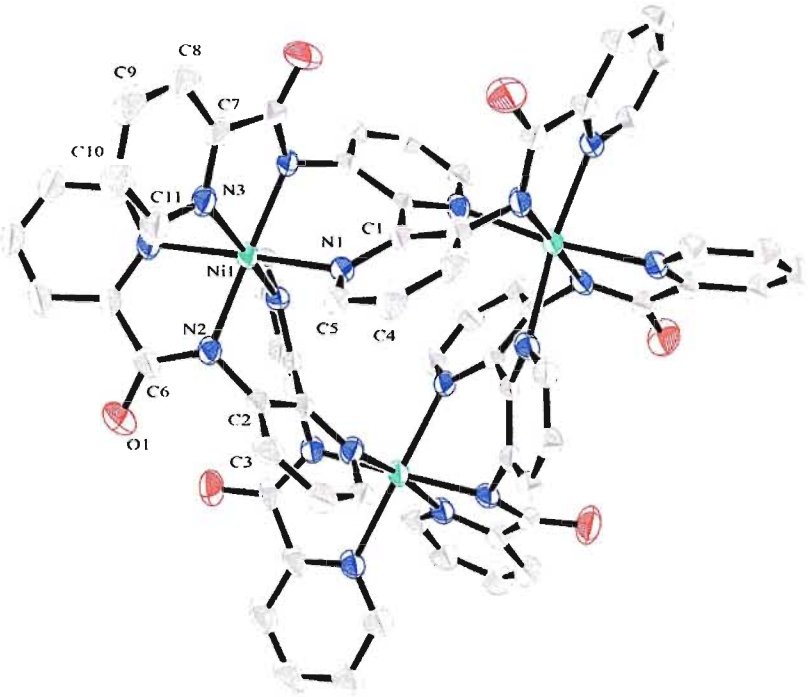

(2.8)

Figure 2.10: ORTEP[153] representation of the molecular structure of the Ni(II) trimer **(2.8)** showing the labelling scheme. Thermal ellipsoids are plotted at 50% probability. Hydrogen atoms have been omitted for clarity.

The nickel trimer **(2.8)** crystallizes in the trigonal space group R-3c where 1/6 of the molecule is crystallographically unique. Each carboxamide ligand is chelated in a *bis*-tridentate manner to two Ni(II) metal ions through the deprotonated amide nitrogen and the two pyridine nitrogen atoms, leaving the carbonyl oxygen atom unchelated. The complex is neutral and as such there are no counter ions present. The coordination geometry around each Ni(II) metal centre is best described as being a distorted octahedral N_6 environment. Tables 2.7 and 2.8 summarize the selected bond lengths and bond angles for the nickel(II) trimer complex **(2.8)**. The dihedral angle between the best planes of the two bipyridine rings is 43.9°. The terminal pyridine rings lie at an angle of 59.5° from the bipyridine (pyridine) ring to which each is directly attached and 82.6° to the opposite

bipyridine (pyridine) ring. The intramolecular Ni(II)···Ni(II) distances are all 6.097 Å. The cluster has a cavity of approximately 4 Å in diameter relative to the bipyridine rings. There is a disordered solvent molecule located in the central cavity. Since the disordered solvent could not be correctly modelled using crystallographic constraints and restrains a SQUEEZE function was performed using the SHELX-97 software.[151] As mentioned, this function eliminates the electron density from the disordered solvent and improves the final crystallographic model. The consequences are more accurate bond lengths and angles in the final structure.

Table 2.7: Selected bond lengths [Å] for the nickel(II) trimer complex **(2.8)**.

Atoms	Bond [Å]	Atoms	Bond [Å]
Ni(1) - N(2)	2.020(4)	Ni(1) - N(3)	2.120(4)
Ni(1) - N(1)	2.148(5)	Ni(1) - N(1')	2.148(4)
Ni(1) - N(2')	2.020(4)	Ni(1) - N(3')	2.120(5)

Table 2.8: Selected bond angles [°] for the nickel(II) trimer complex **(2.8)**.

Atoms	Angle [°]	Atoms	Angle [°]
N(2) - Ni(1) - N(3')	78.94(15)	N(2) - Ni(1) - N(1)	97.77(16)
N(2) - Ni(1) - N(1')	81.27(15)	N(2) - Ni(1) - N(2')	178.57(15)
N(2) - Ni(1) - N(3)	102.19(17)	N(3) - Ni(1) - N(1)	169.97(17)
N(3') - Ni(1) - N(1')	89.51(16)	N(3') - Ni(1) - N(2')	102.16(16)
N(3) - Ni(1) - N(3')	82.02(19)	N(1) - Ni(1) - N(1')	99.40(17)
N(1) - Ni(1) - N(2')	81.30(17)	N(1) - Ni(1) - N(3')	89.5(2)
N(1') - Ni(1) - N(2')	97.79(16)	N(1') - Ni(1) - N(3)	169.98(16)
N(2) - Ni(1) - N(3')	78.91(18)		

A full list of all bond lengths and angles for the Ni(II) trimer complex **(2.8)** can be found in the *Appendix* section of the thesis, Tables 6.5 and 6.6.

The UV-Vis spectrum of the nickel trimer **(2.8)** has absorption maxima at λ = 229, 262, and 331 nm assigned to π-π^* and n-π^* ligand based electronic transitions. No additional bands are observed beyond 500 nm. The mass spectrometry data displays fragmentation ions at *m/z* = 964 for $[Ni_3(\mathbf{L^1})_2]^+$, *m/z* = 511 for $[Ni_2(\mathbf{L^1})]^+$, and *m/z* = 452 for $[Ni(\mathbf{L^1})]^+$. The IR spectrum shows the loss of the N-H_{str} when compared to the free ligand while after chelation, the C=O_{str} is once again red shifted from 1678 cm^{-1} to 1614 cm^{-1}. A band at 3403 cm^{-1} is consistent with the O-H_{str} of the water molecules present in the crystal lattice. The CHN data is consistent for the trimer having stoichiometry $[C_{66}H_{42}N_{18}O_6Ni_3]\cdot 6H_2O$.

The next reaction was that of nickel(II) acetate with the ligand **(2.1)**. This reaction yielded a yellow powder much like the previous reaction. Attempts to crystallize the complex as before (liquid-liquid diffusion) did not result in suitable single crystals. However, a recrystallization of the isolated yellow powder from a 1:1 mixture of DCM:MeOH afforded deep red, cubic shaped single crystals suitable for X-ray diffraction. Investigation of the crystal structure revealed that this nickel complex crystallizes as a trimer and that the complex is structurally very similar to the previous nickel(II) trimer **(2.8)**. Tables 2.9 and 2.10 summarize the selected bond lengths and bond angles for the nickel(II) trimer complex **(2.9)**.

Table 2.9: Selected bond lengths [Å] for the nickel(II) trimer complex **(2.9)**.

Atoms	Bond [Å]	Atoms	Bond [Å]
Ni(1) - N(2)	2.020(5)	Ni(1) - N(3)	2.141(6)
Ni(1) - N(1)	2.136(7)	Ni(1) - N(1')	2.137(6)
Ni(1) - N(2')	2.020(5)	Ni(1) - N(3')	2.141(7)

Table 2.10: Selected bond angles [°] for the nickel(II) trimer complex **(2.9)**.

Atoms	Angle [°]	Atoms	Angle [°]
N(2) - Ni(1) - N(3')	77.51(18)	N(2) - Ni(1) - N(1)	95.6(2)
N(2) - Ni(1) - N(1')	81.4(2)	N(2) - Ni(1) - N(2')	175.3(2)
N(2) - Ni(1) - N(3)	106.2(2)	N(3) - Ni(1) - N(1)	166.3(2)
N(3') - Ni(1) - N(1')	91.26(18)	N(3') - Ni(1) - N(2')	106.2(2)
N(3) - Ni(1) - N(3')	79.7(3)	N(1) - Ni(1) - N(1')	99.4(2)
N(1) - Ni(1) - N(2')	81.4(2)	N(1) - Ni(1) - N(3')	91.2(3)
N(1') - Ni(1) - N(2')	95.6(2)	N(1') - Ni(1) - N(3)	166.37(18)
N(2) - Ni(1) - N(3')	77.5(2)		

A full list of all bond lengths and angles for the Ni(II) trimer complex **(2.9)** can be found in the *Appendix* section of the thesis, Tables 6.7 and 6.8.

The trimers **(2.8)** and **(2.9)** are not isostructural. Table 2.11 summarizes some of the data displaying these variations which are most likely caused by the water molecules affecting the packing of the trimers. In this respect, the CHN data agrees with the crystallographic structure refinement in that there are six disordered water molecules present in the crystal structure of **(2.8)** but only 4 for **(2.9)**.

Table 2.11: Comparison of the two Ni^{II} trimers prepared from ligand **(2.1)**.

	Ni^{II} Trimer (2.8)	**Ni^{II} Trimer (2.9)**
Ni(1)···Ni(1')	6.097 Å	6.156 Å
Dihedral angle (bipy)	43.9°	41.0°
Unit cell: V	11792 $Å^3$	10083 $Å^3$
Space Group	Trigonal: R-3c	Trigonal: R-3c
No. Water Molecules	6	4

The packing diagrams of the nickel trimers reveals that the intermolecular distances are quite long. Figures 2.11 and 2.12 show the intermolecular distances for the **(2.8)** trimer. The closest intermolecular distance is 9.177 Å. As previously mentioned, an isolated unit is a property necessary for single molecule magnet behaviour and the trimer **(2.8)** may fulfill this requirement.

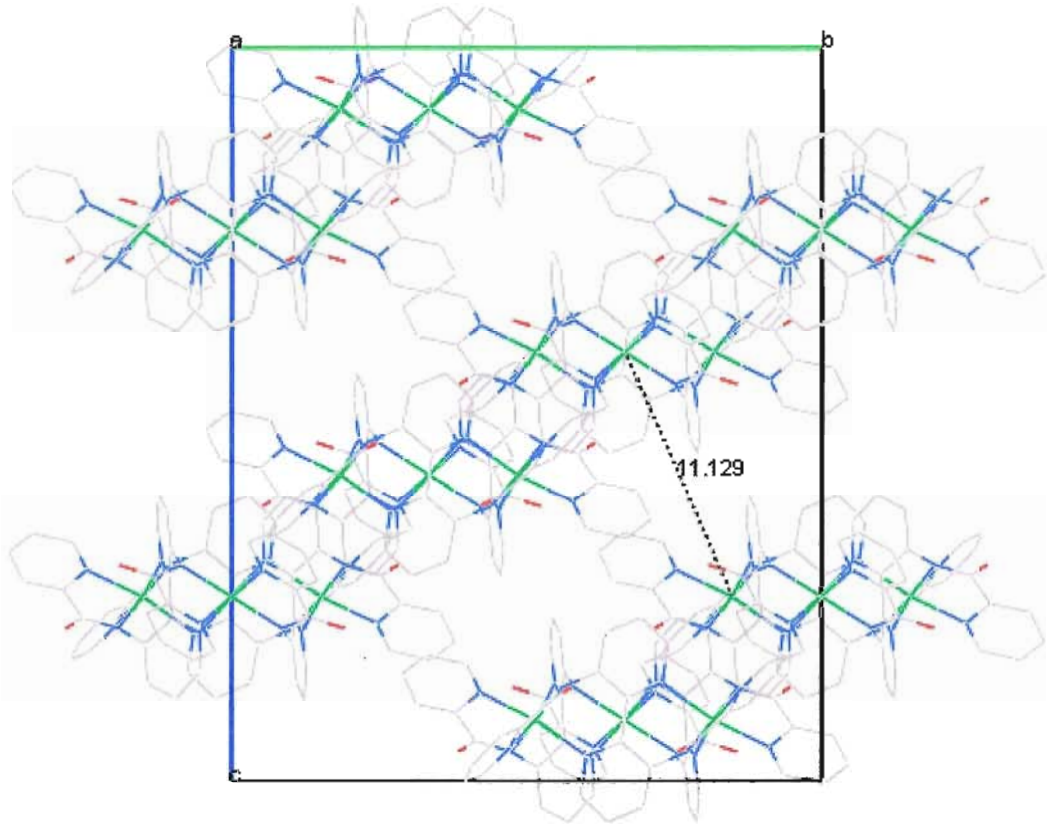

Figure 2.11: Packing diagram of complex **(2.8)**. View down the *a*-axis displaying the shortest intermolecular Ni(II)···Ni(II) contact of 11.129 Å. Hydrogen atoms have been omitted for clarity.

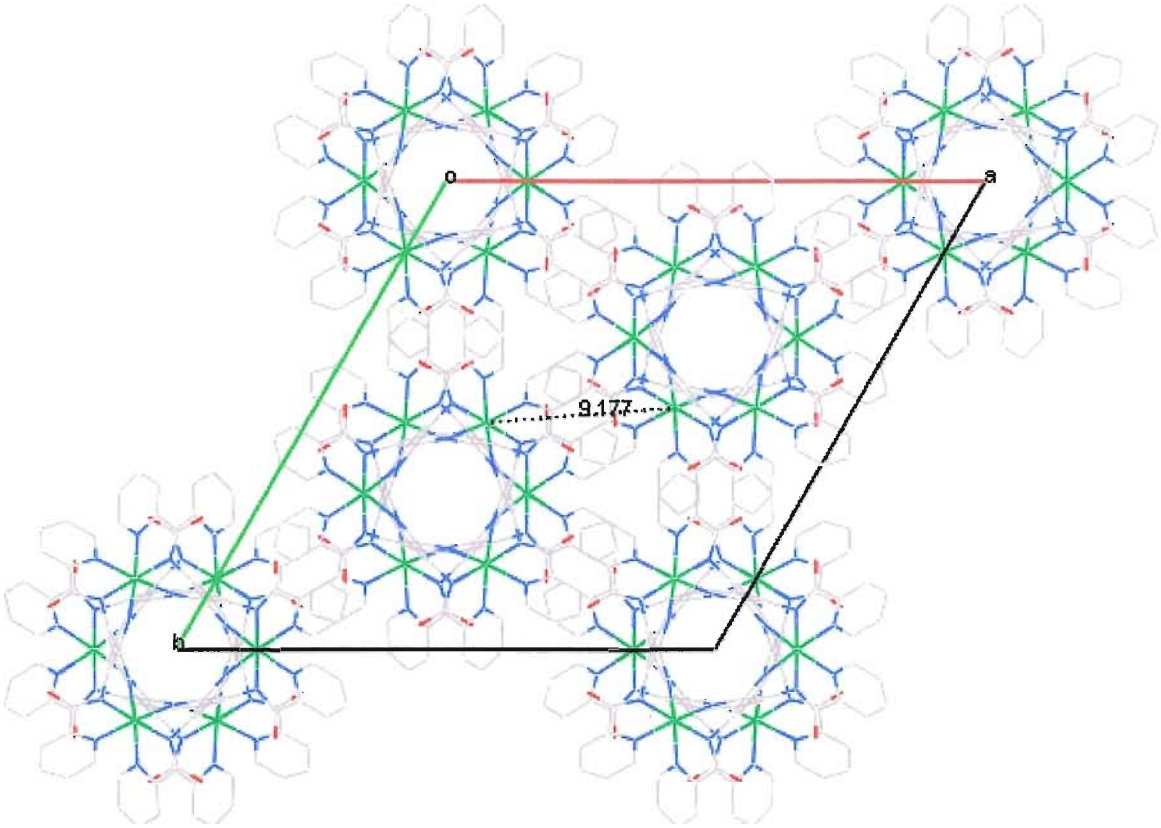

Figure 2.12: Packing diagram of complex **(2.8)**. View down the *c*-axis displaying shortest intermolecular Ni(II)···Ni(II) contact of 9.177 Å. Hydrogen atoms have been omitted for clarity.

Lippert and co-workers have indicated that the easiest way to assemble a molecular triangle is to use three 60° fragments and three linear ones.[120] However, the number of reported metal-containing molecular triangles is surprisingly small.[120,121] Examples of nickel triangular trimers are very scarce in the chemical literature and those reported normally consist of isosceles triangles bridged by oxides with angles of 80 – 90°.[121] Nickel is typically found in the octahedral coordination geometry. Therefore, it is the flexibility of the organic ligands that allows formation of the triangular structures. One of the first Ni(II) triangular trimers ever reported that contained octahedral

coordination geometry for the nickel ions as the corners was by Qing-jin and co-workers, Figure 2.13.[121] The authors were interested in the self-assembly properties associated with the ligand and as such did not measure the magnetic properties.

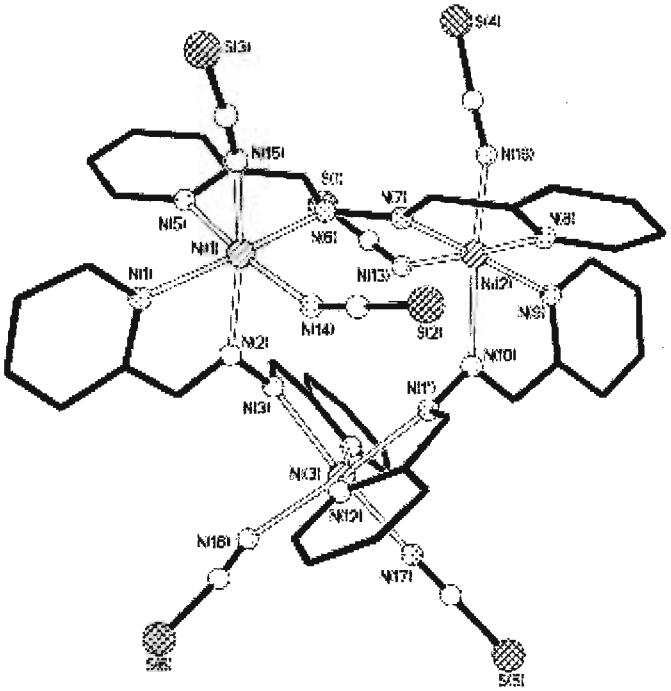

(2.10)

Figure 2.13: Nickel trimer **(2.10)** prepared by Qing-jin and co-workers. Reprinted with permission from reference 121. Copyright {2002} Royal Society of Chemistry.

Literature examples of nickel trimers in which the magnetic properties were studied have been reported.[122,123] The molecular structures of two examples are presented below in Figures 2.14 and 2.15. Unlike the trimers synthesized in this thesis they consist of closer Ni(II)···Ni(II) distances in the range of 2.819 - 3.164 Å and are linked via oxide bonds. These complexes were modelled with a two *J* system, indicating two couplings of spins.

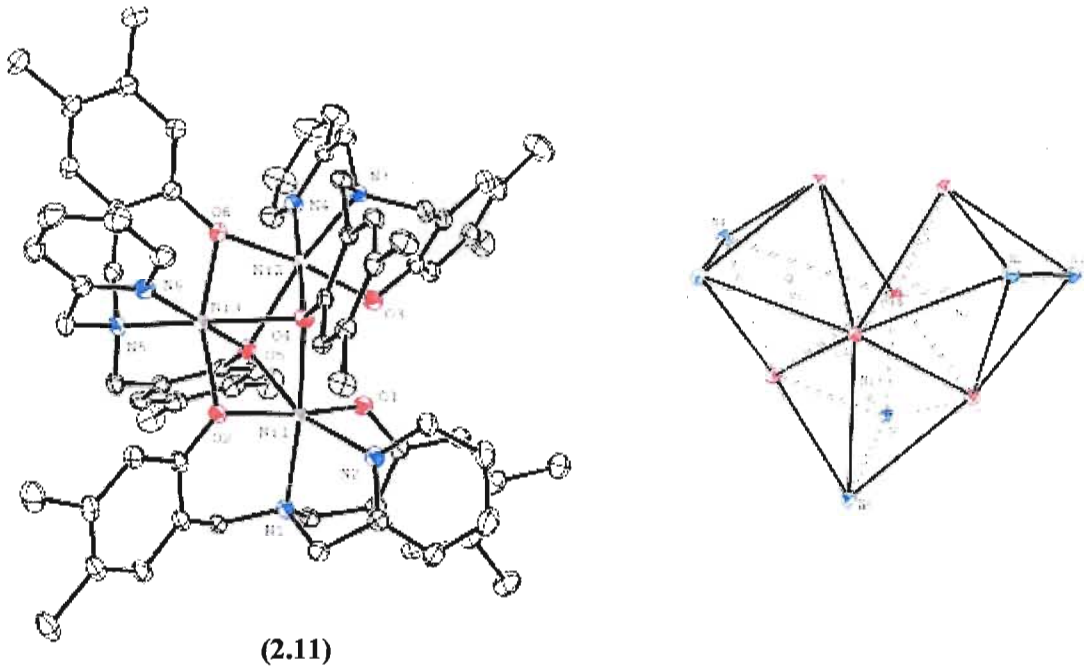

(2.11)

Figure 2.14: Nickel trimer **(2.11)**. The nickel centres are bridged via oxide linkers. Reprinted with permission from reference 122. Copyright {2009} Royal Society of Chemistry.

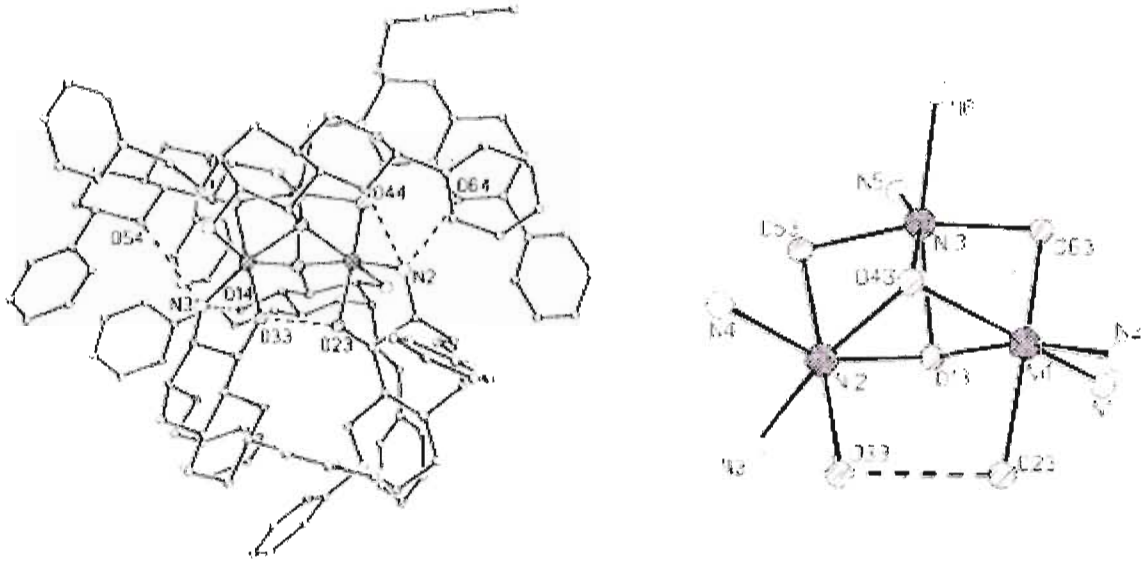

(2.12)

Figure 2.15: Nickel trimer **(2.12)**. The nickel centres are bridged via oxide linkers. Reprinted with permission from reference 123.

The $\chi_M T$ *vs.* T graph of the literature compound **(2.11)** indicates that the nickel centres are weakly antiferromagnetically coupled, Figure 2.16.

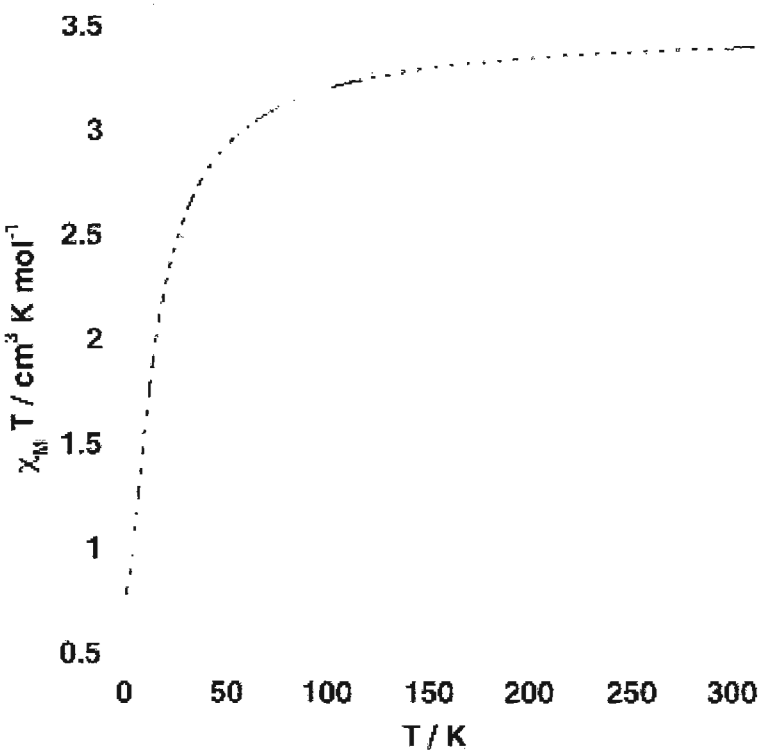

Figure 2.16: $\chi_M T$ *vs.* T graph of the literature compound **(2.11)**. Reprinted with permission from reference 122. Copyright {2009} Royal Society of Chemistry.

In contrast, complex **(2.12)** was reported to be the first triangular nickel(II) complex with an overall ferromagnetic interaction within the Ni_3 core.[123] The $\chi_M T$ *vs.* T graph of this literature compound **(2.12)** is shown in Figure 2.17. For triangular systems generally an antiferromagnetic interaction is observed, independent of the molecular symmetry for isosceles and equilateral Ni_3 triangles.[123,124,125]

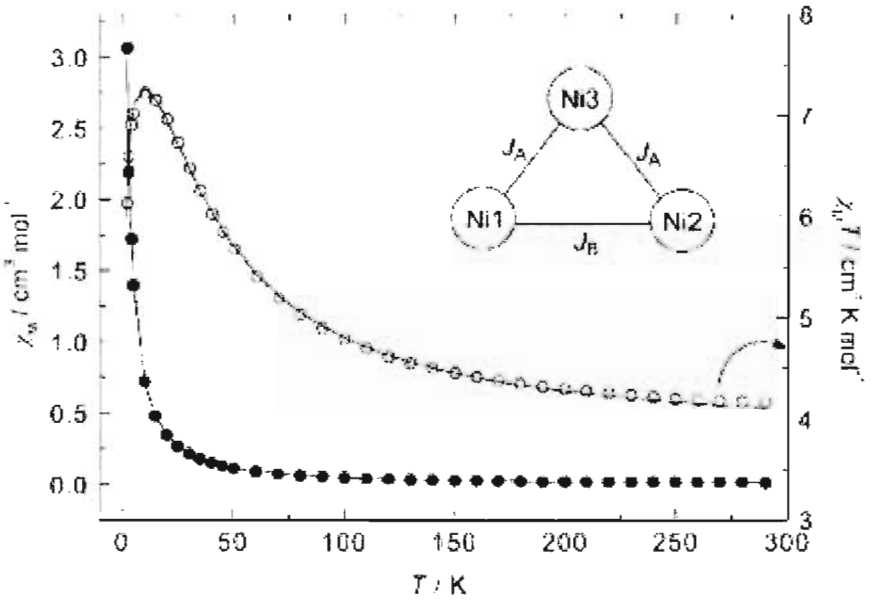

Figure 2.17: χ_M *vs.* T and $\chi_M T$ *vs.* T graphs of the literature compound **(2.12)**. Reprinted with permission from reference 123.

The observed ferromagnetic coupling within the Ni_3 core of **(2.12)** is consistent with magnetization measurements at 2 K shown in Figure 2.18, which confirmed a ferromagnetic $S = 3$ ground state for the complex.

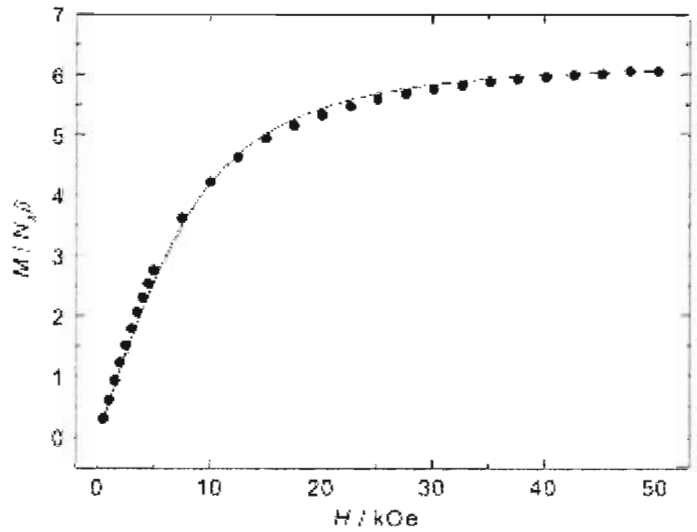

Figure 2.18: Magnetic saturation displaying the ground state of the literature compound **(2.12)**. Reprinted with permission from reference 123.

A sample of 8.1 mg of the Ni(II) trimer **(2.8)** was measured on a Quantum Design SQUID magnetometer in an applied field of 5000 Oe between 5 and 300 K. The data were corrected for the sample holder and sample diamagnetism (Pascal's constants).[8] A plot of $1/\chi_M$ *vs.* T, Figure 2.20, showed the sample obeyed Curie-Weiss law with C = 3.700 cm^3 K mol^{-1} and θ = +4.2 K consistent with three S = 1 ions with g = 2.19 and the presence of weak ferromagnetic interactions between the Ni(II) metal ions.

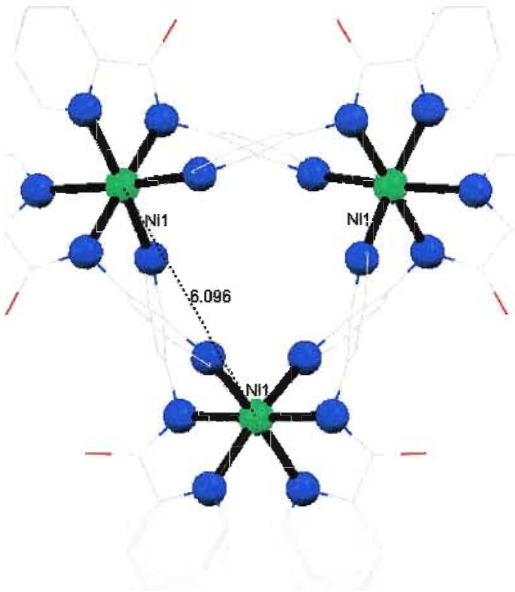

(2.8)

Figure 2.19: Mercury[152] view of the Ni(II) trimer **(2.8)** displaying the intramolecular Ni···Ni distances in Å.

Initially the $\chi_M T$ data for **(2.8)** at 300 K is 3.60 cm^3 K mol^{-1} which is indicative of three non-interacting Ni(II) ions with $S = 1$ ($g = 2.19$). Upon cooling the $\chi_M T$ data reaches a maximum of 4.77 cm^3 K mol^{-1}. The decrease of the $\chi_M T$ values below 11 K can be attributed to zero-field splitting (ZFS) or antiferromagnetic intermolecular interactions of the nickel(II) ions.[124] The nickel trimer **(2.8)**, because of the aforementioned symmetry,

can be treated as an equilateral triangle with three equivalent pairwise interactions, Figure 2.19. As a consequence the magnetic susceptibility was fitted to the following expression:

$$\chi_M = \frac{2N\beta^2 g^2}{kT} \frac{3expA + 10expB + 14expC}{1 + 9expA + 10expB + 7expC}$$

where, A = J/kT, B = $3J/k$T, and C = $6J/k$T.[124]

A fit of the susceptibility to this expression yielded g = 2.19 and J = 2.78 cm^{-1}. This model fit the observed data well as indicated by the $\chi_M T$ *vs.* T graph, Figure 2.20.

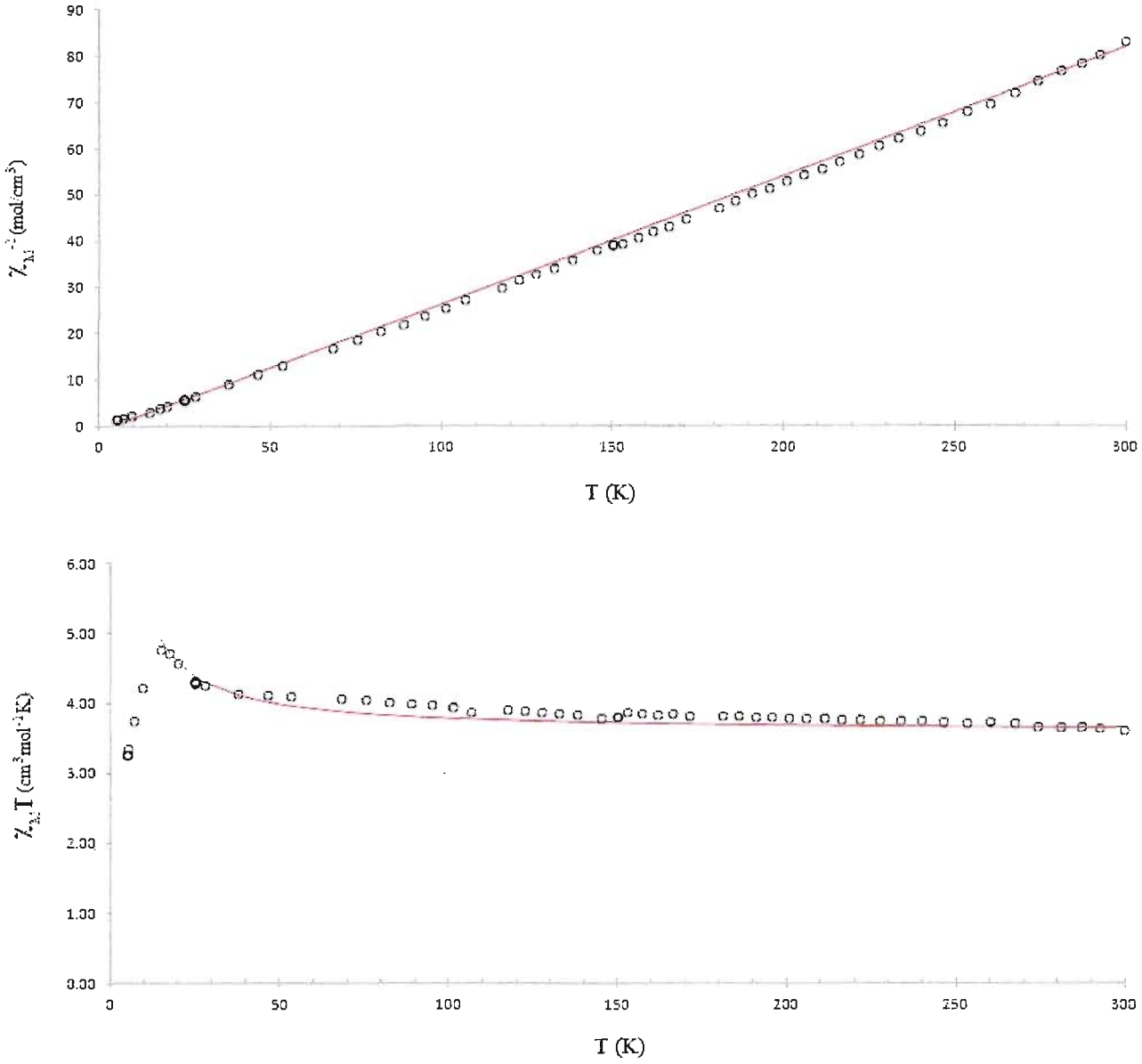

Figure 2.20: Graphs of $1/\chi_M$ *vs.* T and $\chi_M T$ *vs.* T for complex **(2.8)**. The open circles represent the experimental data and the solid red line represents the best model.

The observed ferromagnetic coupling within the Ni_3 core of **(2.8)** is consistent with magnetization measurements at 3 K shown in Figure 2.21. Although the measurement did not reach saturation it can be used to suggest the $S = 3$ ground state.

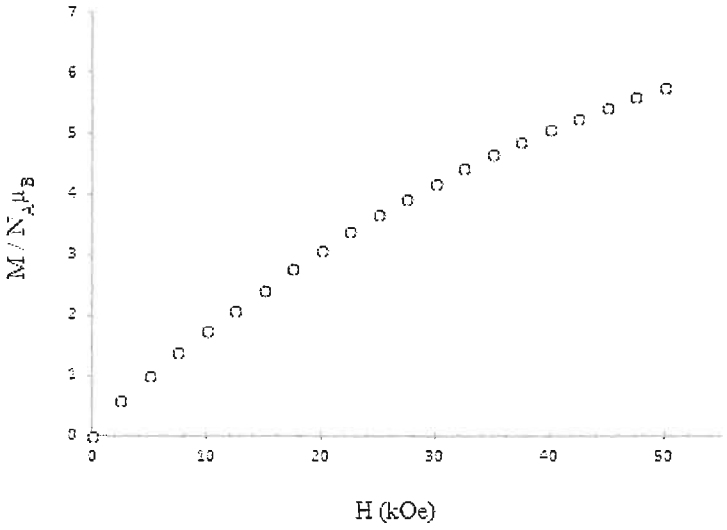

Figure 2.21: Magnetic saturation of the Ni(II) trimer **(2.8)**.

AC susceptibility measurements can be used to determine whether or not single molecule magnet behaviour is present in the sample. These measurements can determine if the relaxation is of molecular origin which is the fingerprint of single molecule magnet behaviour. In this respect, AC susceptibility measurements of complex **(2.8)** did not indicate any out-of-phase signals. Therefore, **(2.8)** did not display any single molecule magnet behaviour.

The remaining compounds synthesized from ligand **(2.1)** did not crystallize during the course of this work. Crystallization is one of the main challenges associated with this area of research. However, UV-Vis, IR, MS, and CHN data were used to confirm the coordination of the ligand and suggest possible molecular structures of the complexes. A summary of the UV-Vis, IR, MS, and CHN data for these complexes is presented in Table 2.12.

Table 2.12: Summary of the UV-Vis, IR, MS and CHN data for the coordination complexes prepared from ligand H_2L^1 **(2.1)**.

Compound	UV-Vis, λ_{max} (nm)	IR, N-H_{str}, C=O_{str} (cm^{-1})	MS (*m/z*)	CHN
H_2L^1 **(2.1)**	232, 292, 336	3449, 1678	396 [M^+]	$C_{22}H_{16}N_6O_2$ calcd: C 66.65%, H 4.07%, N 21.20% found: C 66.74%, H 3.72%, N 20.80%
$[Cu_2(L^1)Cl_2]$ **(1.27)**	231, 258, 324, 370	---, 1623	593 $[Cu_2(L^1)Cl_2]^+$ 557 $[Cu_2(L^1)Cl]^+$	$C_{22}H_{14}N_6O_2Cu_2Cl_2$ calcd: C 44.61%, H 2.38%, N 14.19% found: C 44.80%, H 2.45%, N 14.24%
$[Cu_2(L^1)(OAc)_2]$ **(2.7)**	228, 256, 320, 363, 667	---, 1637	642 $[Cu_2(L^1)(OAc)_2]^+$ 579 $[Cu_2(L^1)(OAc)]^+$	$C_{26}H_{20}N_6O_6Cu_2 \cdot MeOH$ calcd: C 48.29%, H 3.60%, N 12.41% found: C 48.39%, H 3.67%, N 11.97%
$[Ni(L^1)]_3$ **(2.8)**	229, 262, 331	---, 1614	964 $[Ni_3(L^1)_2]^+$ 511 $[Ni_2(L^1)]^+$	$C_{66}H_{42}N_{18}O_6Ni_3 \cdot 6H_2O$ calcd: C 54.02%,H 3.71%, N 17.18% found: C 53.79%,H 3.67%, N 17.15%
$[Ni(L^1)]_3$ **(2.9)**	230, 261, 331	---, 1612	964 $[Ni_3(L^1)_2]^+$ 510 $[Ni_2(L^1)]^+$	$C_{66}H_{42}N_{18}O_6Ni_3 \cdot 4H_2O$ calcd: C 55.38%, H 3.52%, N 17.61% found: C 55.14%, H 3.67%, N 17.38%
$[Mn_2(L^1)Cl_2]$ **(2.13)**	229, 266, 339	---, 1623	576 $[Mn_2(L^1)Cl_2]^+$ 540 $[Mn_2(L^1)Cl]^+$	$C_{22}H_{14}N_6O_2Mn_2Cl_2 \cdot 3.6MeOH$ calcd: C 44.53%, H 4.15%, N 12.17%. found: C 44.67%, H 4.65%, N 12.68%
$[Mn_2(L^1)(OAc)_2]$ **(2.14)**	227, 250, 333	---, 1637	624 $[Mn_2(L^1)(OAc)_2]^+$ 565 $[Mn_2(L^1)(OAc)]^+$	$C_{26}H_{20}N_6O_6Mn_2 \cdot 1.95MeOH \cdot 1.75H_2O$ calcd: C 46.86%, H 4.40%, N 11.73% found: C 46.51%, H 4.04%, N 11.37%
$[Co_2(L^1)Cl_2]$ **(2.15)**	231, 262	---, 1635	581 $[Co_2(L^1)Cl_2]^+$ 546 $[Co_2(L^1)Cl]^+$	found: C 45.23%, H 5.53%, N 12.02%
$[Co_2(L^1)(OAc)_2]$ **(2.16)**	236, 260	---, 1637	571 $[Co_2(L^1)(OAc)]^+$ 513 $[Co_2(L^1)]^+$	$C_{26}H_{20}N_6O_6Co_2 \cdot 3.5MeOH \cdot 2.85H_2O$ calcd: C 44.63%, H 5.04%, N 10.59% found: C 44.39%, H 4.70%, N 10.24%
$[Zn_2(L^1)(OAc)(MeO)]_2$ **(2.6)**	231, 257, 309, 341	---, 1674	1042 $[Zn_3(L^1)_2OAc]^+$ 919 $[Zn_2(L^1)_2]^+$	$C_{50}H_{40}N_{12}O_{10}Zn_4 \cdot 3MeOH \cdot H_2O$ calcd: C 47.34%, H 4.05%, N 12.50% found: C 47.02%, H 3.79%, N 12.34%

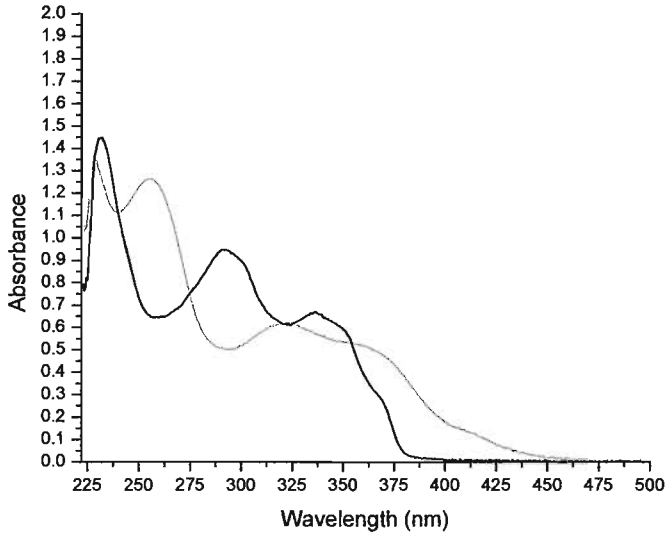

Figure 2.22: UV-Vis spectra of the copper(II) acetate complex **(2.7)** (green line) compared to that of the unchelated ligand **(2.1)** (black line).

All of the compounds contain a band in their UV-Vis spectra at around λ = 232 nm which is consistent with the high energy π-π^* transition of the bipyridine of ligand **(2.1)**. The UV-Vis spectrum of the copper acetate complex **(2.7)** is shown in Figure 2.22. It is clear that when compared to that of the free ligand shown by the black line in Figure 2.22 the absorption bands are shifted indicating a change in the electronic structure of the molecule. MLCT bands for these complexes were not observed for they are most likely masked by the high energy bands associated with the ligand. *d-d* transitions are normally observed at longer wavelengths and are very weak. Complex **(2.7)** is the only one that displays a *d-d* transition at 667 nm. These transitions are normally forbidden and therefore are not observed for the other complexes. The IR spectra of all complexes also display a loss of the $N\text{-}H_{str}$ associated with the amide as well as a shift of the $C{=}O_{str}$ to lower wavenumbers.

2.3.4 – Manganese(II) Chloride (2.13) and Manganese(II) Acetate (2.14) Complexes

Reaction of manganese(II) chloride and 2,2'-bipyridine-3,3'-(2-pyridinecarboxamide) **(2.1)** in the presence of triethylamine afforded a brown powder. The major bands observed in the UV-Vis spectrum are summarized in Table 2.12. No additional bands were observed beyond 500 nm. The MS data for **(2.13)** displays peaks at m/z = 576 assigned to $[Mn_2(\mathbf{L^1})Cl_2]^+$ and m/z = 540 assigned to $[Mn_2(\mathbf{L^1})Cl]^+$. This data suggests that the manganese has coordinated with the dianionic ligand. The IR spectrum also displays the loss of the N-H_{str} while the carbonyl peak is red shifted by 55 wavenumbers to 1623 cm^{-1}. The UV-Vis, IR, and MS data are consistent with the complex containing one dianionic ligand and two Mn(II) metal ions. The elemental analysis data was an acceptable fit to a 2:1 metal to ligand complex of stoichiometry $[C_{22}H_{14}N_6O_2Mn_2Cl_2]\cdot 3.6MeOH$. Given these results it is probable that the molecular structure of complex **(2.13)** is isostructural with the copper complex **(1.27)**. A proposed molecular structure for complex **(2.13)** is shown in Figure 2.23.

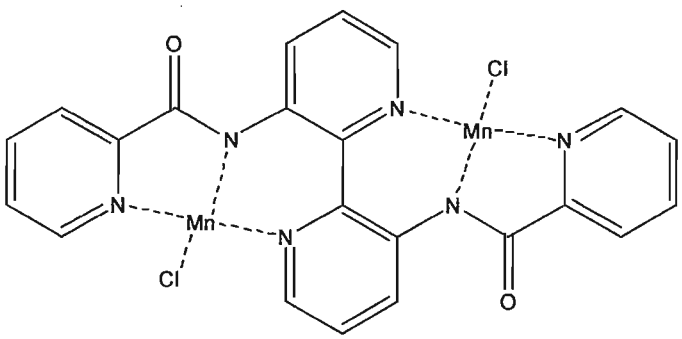

Figure 2.23: Proposed structure of manganese complex **(2.13)**. Additional coordination sites of the metal ion may be taken by solvent molecules.

Reaction of manganese(II) acetate and 2,2'-bipyridine-3,3'-(2-pyridinecarboxamide) **(2.1)** in the presence of triethylamine afforded a beige powder. The

UV-Vis spectrum of this manganese complex is summarized in Table 2.12. Once again no additional bands were observed beyond 500 nm. The MS data displays peaks at m/z = 624 for $[Mn_2(\mathbf{L^1})(OAc)_2]^+$, m/z = 565 for $[Mn_2(\mathbf{L^1})(OAc)]^+$, and m/z = 506 for $[Mn_2(\mathbf{L^1})]^+$. This data suggests that the manganese has coordinated with the dianionic ligand. The IR spectrum also displays the loss of the N-H_{str} while the carbonyl peak is red shifted by 41 wavenumbers to 1637 cm^{-1}. A broad band at 3421 cm^{-1} is observed for O-H_{str} of either methanol or water in the complex. Additional bands between 1571 – 1463 cm^{-1} are indicative of the aforementioned bidentate bridging mode of the acetate molecules. The UV-Vis, IR, and MS data are consistent with the complex containing one dianionic ligand and two Mn(II) metal ions. The elemental analysis data was fit to a 2:1 metal to ligand complex of stoichiometry $[C_{26}H_{20}N_6O_6Mn_2]\cdot 2MeOH\cdot 1.75H_2O$. Therefore, a proposed structure of **(2.14)** is presented in Figure 2.24.

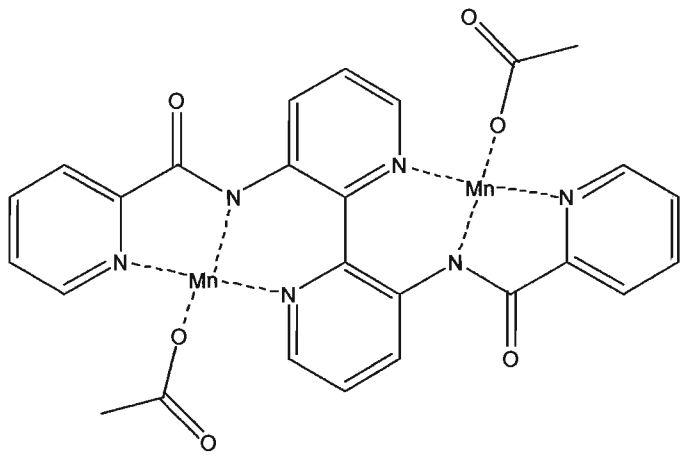

Figure 2.24: Proposed structure of manganese complex **(2.14)**. Additional coordination sites of the metal ion may be taken by solvent molecules.

2.3.5 – Cobalt(II) Chloride Complex (2.15) and Cobalt(II) Acetate Complex (2.16)

Reaction of cobalt(II) chloride and 2,2'-bipyridine-3,3'-(2-pyridinecarboxamide) **(2.1)** in the presence of triethylamine afforded a red/brown powder. The absorption maxima of the UV-Vis spectrum of the cobalt complex are summarized in Table 2.12. The MS data displays peaks at m/z = 581 for $[Co_2(\mathbf{L^1})Cl_2]^+$, m/z = 546 for $[Co_2(\mathbf{L^1})Cl]^+$ and m/z = 453 for $[Co(\mathbf{L^1})]^+$. This data is suggestive that a coordination complex has formed. In addition the N-H_{str} in the ligand is now absent and the C=O_{str} is once again red shifted when compared with the spectrum of the free ligand. A broad band at 3419 cm^{-1}, assigned to the O-H_{str} of either methanol or water, is consistent with solvent in the compound. The UV-Vis, IR, and MS data are consistent with the complex containing one dianionic ligand and two Co(II) metal ions. The structure of complex **(2.15)** may therefore be that display in Figure 2.25.

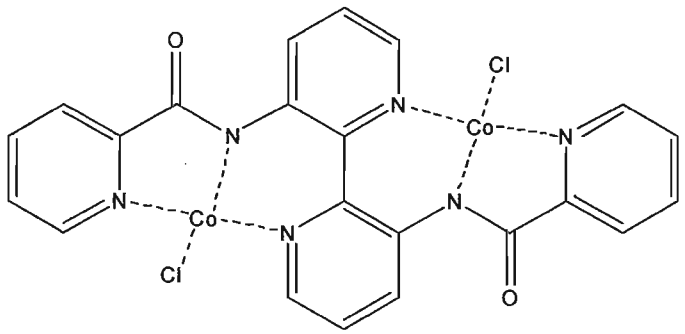

Figure 2.25: Proposed structure of cobalt complex **(2.15)**. Additional coordination sites of the metal ion may be taken by solvent molecules.

Reaction of cobalt(II) acetate and 2,2'-bipyridine-3,3'-(2-pyridinecarboxamide) **(2.1)** in the presence of triethylamine afforded a brown crystalline solid. The absorption maxima of the UV-Vis spectrum of this cobalt complex **(2.16)** are summarized in table 2.12. The MS data displays peaks at m/z = 571 for $[Co_2(\mathbf{L^1})(OAc)]^+$, m/z = 513 for

$[Co_2(L^1)]^+$, and m/z = 454 for $[Co(L^1)]^+$. This data suggests that the cobalt has coordinated with the dianionic ligand. The IR spectrum also displays the loss of the N-H_{str} while the carbonyl peak is red shifted by 41 wavenumbers to 1637 cm^{-1}. A broad band at 3423 cm^{-1} is consistent with the O-H_{str} of solvent water or methanol in the compound. The UV-Vis, IR, and MS data are consistent with the complex containing one dianionic ligand and two Co(II) metal ions. Any additional coordination sites of the metal are most likely satisfied by coordinating solvent molecules. The elemental analysis data was fit to a 2:1 metal to ligand complex of stoichiometry $[C_{26}H_{20}N_6O_6Co_2]\cdot 3.5MeOH\cdot 2.85H_2O$. A proposed molecular structure is presented in Figure 2.26.

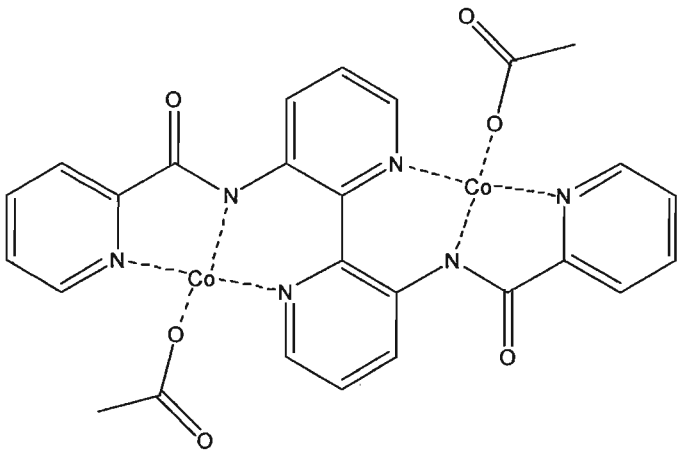

Figure 2.26: Proposed structure of cobalt complex **(2.16)**. Additional coordination sites of the metal ion may be taken by solvent molecules.

The magnetic susceptibility of complexes **(2.13)-(2.16)** were not measured since we were not able to absolutely determine their molecular structures by X-ray crystallography. Not knowing the absolute structure makes the modelling of the magnetic data problematic.

Moving forward with this project, a second bipyridine ligand was targeted which would introduce more nitrogen coordination sites into the ligand via pyrazine arms. We proposed that the pyrazine functionality of this ligand might favour the assembly of polymetallic chains or extended networks rather than the dimers, trimers and tetramers as observed for ligand **(2.1)**.

2.4 – 2,2'-Bipyridine-3,3'-(2-Pyrazinecarboxamide) (H_2L^2) (2.2)

The synthetic procedure initially followed for the preparation of ligand **(2.2)** was to follow the same strategy that was successful for ligand **(2.1)**. Therefore, the strategy involved reacting 3,3'-diamino-2,2'-bipyrdine **(1.17)** together with pyrazinoic acid chloride. Unfortunately, this resulted in a very low yield of **(2.2)** (12%). In order to increase the yield, a new method was adapted from a procedure by Woollins and Bhattacharyya.[116] Pyrazinoic acid could be reacted directly with 3,3'-diamino-2,2'-bipyrdine **(1.17)** using this procedure. The synthetic outline followed is shown in Scheme 2.2.

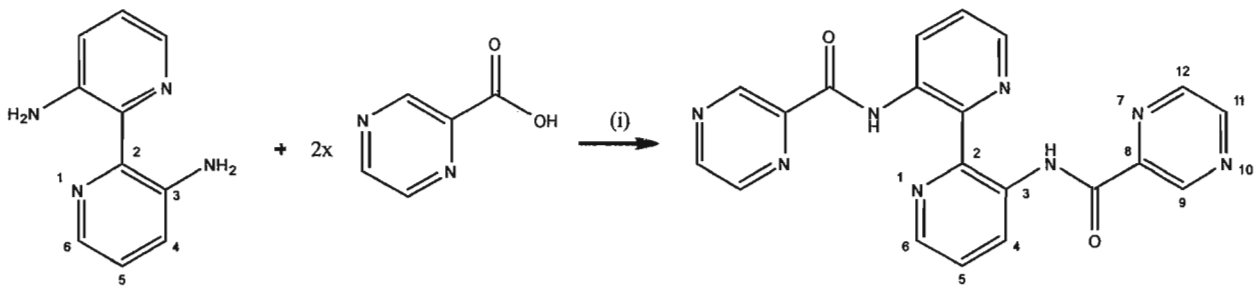

(1.17) **(2.2)**

Scheme 2.2: Synthetic route for the synthesis of 2,2'-bipyridine-3,3'-(2-pyrazinecarboxamide) **(H_2L^2) (2.2)**. Reagents and conditions: (i) a) pyridine, 40 °C, 45 mins, b) triphenylphosphite, 95 °C, 5 hrs.

In this respect, the use of triphenylphosphite resulted in a one-pot synthesis of the target ligand **(2.2)** (76% yield). In fact, repeating the synthesis of 2,2'-bipyridine-3,3'-(2-

pyridinecarboxamide) ($\mathbf{H_2L^1}$) **(2.1)** from 3,3'-diamino-2,2'-bipyrdine **(1.17)** and picolinic acid following this new synthetic procedure increased the yield from 52% to 93%.

The structure of the new ligand, 2,2'-bipyridine-3,3'-(2-pyrazinecarboxamide) **(2.2)**, was confirmed by ^{1}H-NMR, ^{13}C-NMR, mass spectrometry (EI), UV-Vis and IR spectroscopy.

The 300 MHz ^{1}H-NMR spectrum of the ligand ($\mathbf{H_2L^2}$) **(2.2)** confirms the structure. The amide peak is observed as a singlet at 15.08 ppm. The second peak, a doublet, at 9.52 ppm is attributed to the 12-H of the terminal pyrazine rings. The next peak, a doublet of doublets, at 9.40 ppm corresponds to the 6-H of the bipyridine. Following this, a doublet at 8.84 ppm is attributed to the 11-H of the terminal pyrazine rings. The next peak, a triplet, at 8.76 ppm corresponds to the 4-H of the bipyridine. The next peak, a doublet of doublets, at 8.64 ppm is attributed to the C_{12} protons of the pyrazine rings. The final doublet of doublets at 7.52 ppm is attributed to the protons located on the C_5 position of the ligand. All peaks integrate with the correct ratios for the appropriate number of protons.

The 75 MHz ^{13}C-NMR spectrum for the ligand **(2.2)** shows a peak for the amide carbonyl at 164.2 ppm. The remaining peaks have been assigned to the aromatic carbons of the bipyridine and pyrazine rings: 146.3 (12-C), 144.8 (8-C), 144.4 (11-C), 144.2 (9-C), 143.0 (2-C), 141.0 (6-C), 135.8 (3-C), 129.3 (4-C), 123.9 (5-C).

The IR spectrum of this ligand has an intense band at 1672 cm^{-1} attributed to the C=O stretch of the amide carbonyl. A sharp band corresponding to the N-H stretch is seen at 3425 cm^{-1}. An observed absorption band at 2960 cm^{-1} is consistent with aromatic C-H stretches of the bipyridine and pyrazine rings.

UV-Vis absorptions at $\lambda = 230$, 267, and 353 nm can be assigned to π-π^* and n-π^* transitions of the ligand (230 nm π-π^* bipyridine, 267 nm N(n)-π^* bipyridine, 353 nm N(n)-π^* amide). The high resolution EI mass spectrum of the ligand has a parent ion peak at m/z = 398.1236 which is in close agreement with the calculated value of m/z = 398.1240 for $C_{20}H_{14}N_8O_2$. Furthermore, the CHN data are all within the acceptable ± 0.4% limit for $C_{20}H_{14}N_8O_2$.

Single crystals of this ligand were grown via slow evaporation of a supersaturated dichloromethane solution at room temperature. The ligand crystallizes in the monoclinic space group $P2_1/c$ with two independent molecules per unit cell where half of each is crystallographically unique. An ORTEP[153] view of the molecular structure of one molecule along with the atom-numbering scheme is shown in Figure 2.27.

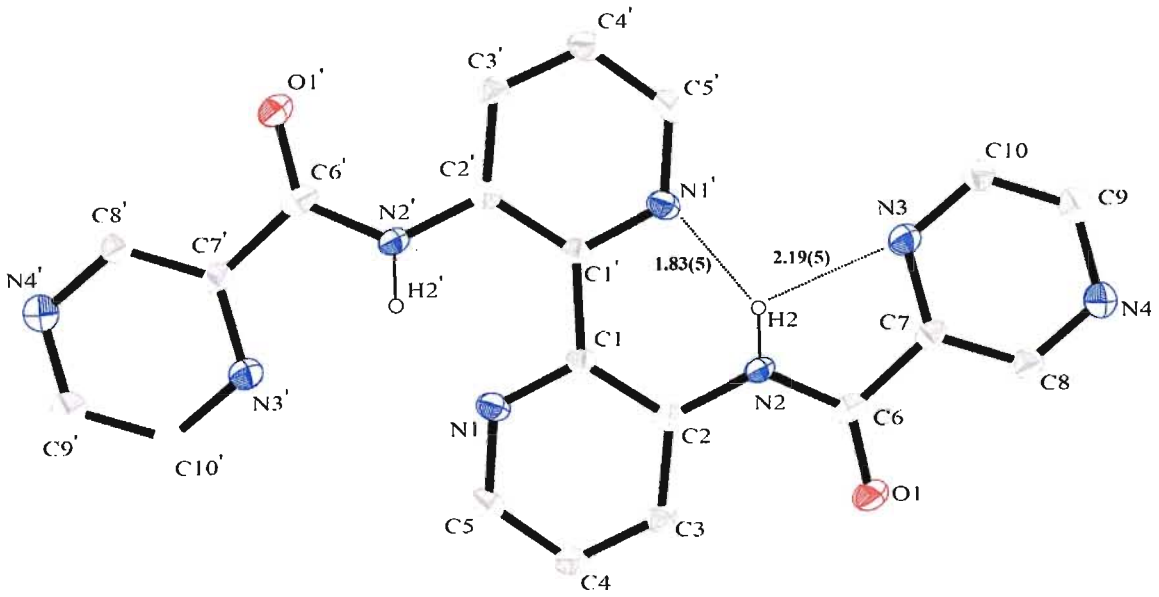

(2.2)

Figure 2.27: ORTEP[153] representation of the molecular structure of the **(H_2L^2)** ligand showing the labelling scheme for molecule A. Thermal ellipsoids are plotted at 50% probability. Aromatic hydrogen atoms have been omitted for clarity. Intramolecular H-bonds are represented by dashed lines and are reported in Å.

The ligand crystallizes in the *trans* configuration with respect to its bipyridine rings. The terminal pyrazine rings are planar with respect to the best plane of the two bipyridine rings resulting in a completely flat molecule. The amide hydrogen atom forms an intramolecular H-bond with the bipyridine nitrogen (N-H2···N1 = 1.83 Å) and a longer H-bond with the nitrogen of the terminal pyrazine (N-H2···N3 = 2.19 Å) stabilizing the *trans* configuration. There is also extensive hydrogen bonding between molecules; between the terminal pyrazine rings (2.66 Å) and between the carbonyl oxygen and terminal pyrazine rings (2.45 and 2.71 Å), Figure 2.28. This extensive hydrogen bonding accounts for the limited solubility of this ligand in conventional organic solvents.

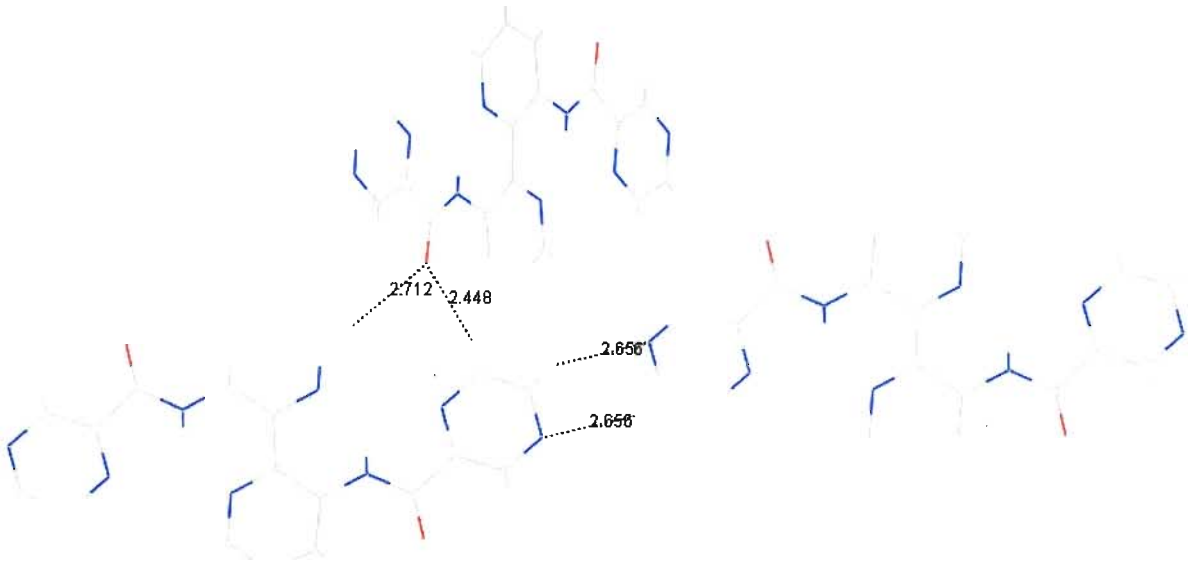

Figure 2.28: Mercury[152] view of the extensive hydrogen bonding within the crystal structure of the 2,2'-bipyridine-3,3'-(2-pyrazinecarboxamide) ligand **(2.2)**. Distances are in Å.

A view down the *c*-axis of the unit cell reveals that the molecules are π-π stacked in a zigzag arrangement, Figure 2.29. The separation of 3.48 Å between molecules is ideal for π-π interactions as determined by Hunter and Sanders.[114]

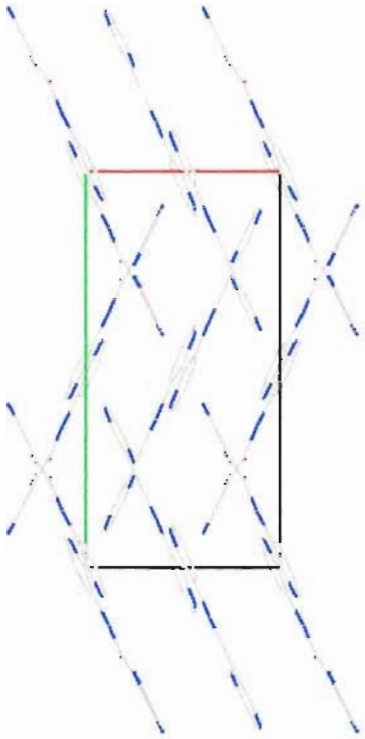

Figure 2.29: Mercury[152] view of the packing of ligand **(2.2)**. Hydrogen atoms have been omitted for clarity. View down the *c*-axis.

Tables 2.13 and 2.14 summarize the selected bond lengths and bond angles for 2,2'-bipyridine-3,3'-(2-pyrazinecarboxamide) **(2.2)**.

Table 2.13: Selected bond lengths [Å] for ligand **(2.2)**, molecule A.

Atoms	Bond [Å]	Atoms	Bond [Å]
O(1) - C(6)	1.221(5)	N(4) - C(9)	1.340(5)
N(1) - C(1)	1.346(5)	C(1) - C(2)	1.423(5)
N(1) - C(5)	1.330(5)	C(1) - C(1')	1.496(4)
N(2) - C(2)	1.399(5)	C(2) - C(3)	1.394(6)
N(2) - C(6)	1.350(5)	C(3) - C(4)	1.367(6)
N(3) - C(7)	1.338(5)	C(4) - C(5)	1.377(6)
N(3) - C(10)	1.336(5)	C(6) - C(7)	1.516(6)
N(4) - C(8)	1.337(5)	C(7) - C(8)	1.382(6)
N(2) - H(2)	0.86(2)	C(9) - C(10)	1.381(6)

Table 2.14: Selected bond angles [°] for ligand **(2.2)**, molecule A.

Atoms	Angle [°]	Atoms	Angle [°]
C(1) - N(1) - C(5)	121.4(3)	C(3) - C(4) - C(5)	118.4(4)
C(2) - N(2) - C(6)	128.7(3)	N(1) - C(5) - C(4)	121.9(4)
C(7) - N(3) - C(10)	115.4(4)	O(1) - C(6) - N(2)	127.5(4)
C(8) - N(4) - C(9)	115.5(4)	O(1) - C(6) - C(7)	119.9(4)
N(1) - C(1) - C(2)	119.7(3)	N(2) - C(6) - C(7)	112.6(4)
N(1) - C(1) - C(1')	115.3(3)	N(3) - C(7) - C(6)	118.0(4)
C(2) - C(1) - C(1')	125.0(3)	N(3) - C(7) - C(8)	122.4(4)
N(2) - C(2) - C(1)	120.1(3)	C(6) - C(7) - C(8)	119.7(4)
N(2) - C(2) - C(3)	122.6(3)	N(4) - C(8) - C(7)	122.2(4)
C(1) - C(2) - C(3)	117.3(3)	N(4) - C(9) - C(10)	122.2(4)
C(2) - C(3) - C(4)	121.4(3)	N(3) - C(10) - C(9)	122.4(4)

A full list of all bond lengths and angles can be found in the *Appendix* section of the thesis, Tables 6.9 and 6.10.

Once ligand **(2.2)** had been prepared and fully characterized, the next objective was to investigate its coordination chemistry with the aforementioned paramagnetic divalent transition metals ions.

2.5 – Coordination Chemistry of Ligand (2.2)

2,2'-Bipyridine-3,3'-(2-pyrazinecarboxamide) **(2.2)** was predicted to contain four coordination sites: two tridentate binding pockets located within the amide structure and two coordination sites located at the terminal pyrazine nitrogen atoms. As a consequence, a typical experiment required reacting 4.1 equivalents of a respective metal salt together with one equivalent of the ligand **(2.2)**. As previously discussed, two equivalents of triethylamine were added to facilitate the deprotonation of the amide moiety of the

ligand. As mentioned, the solubility of this ligand in conventional organic solvents was limited, therefore, this reaction series required heating (reflux, approx. 60 °C) in order to increase ligand solubility. All reactions were carried out at 60 °C in a 7:1 mixture of DCM:MeOH.

A summary of the selected UV-Vis, IR, MS, and CHN data of all of the complexes prepared from ligand **(2.2)** is presented in Table 2.15.

Table 2.15: Summary of the UV-Vis, IR, MS and CHN data for the coordination complexes prepared from ligand $\mathbf{H_2L^2}$ **(2.2)**.

Compound	UV-Vis, λ_{max} (nm)	IR, N-H_{str}, C=O_{str} (cm^{-1})	MS (*m/z*)	CHN
$\mathbf{H_2L^2}$ **(2.2)**	230, 267, 353	3425, 1672	398 $[M^+]$	$C_{20}H_{14}N_8O_2$ calcd: C 60.30%, H 3.54%, N 28.13% found: C 60.54%, H 3.50%, N 28.00%
$[Cu_2(\mathbf{L^2})Cl_2]$ **(2.18)**	231, 258, 340	---, 1625	594 $[Cu_2(\mathbf{L^2})Cl_2]^+$ 558 $[Cu_2(\mathbf{L^2})Cl]^+$	found: C 40.69%, H 5.02%, N 11.46%
$[Cu_3(\mathbf{L^2})(OAc)_3MeO]$ **(2.17)**	228, 270, 358, 686	---, 1637	981 $[Cu_2(\mathbf{L^2})_2OAc]^+$ 583 $[Cu_2(\mathbf{L^2})OAc]^+$	$C_{27}H_{24}N_8O_9Cu_3$ calcd: C 40.78%, H 3.04%, N 14.09% found: C 41.12%, H 3.35%, N 14.34%
$[Ni_2(\mathbf{L^2})Cl_2]$ **(2.19)**	230, 252, 335	---, 1625	584 $[Ni_2(\mathbf{L^2})Cl_2]^+$ 526 $[Ni_2(\mathbf{L^2})Cl]^+$	found: C 41.41%, H 6.76%, N 13.58%
$[Ni_3(\mathbf{L^2})(OAc)_4MeO]$ **(2.20)**	228, 256, 350	---, 1633	631 $[Ni_2(\mathbf{L^2})(OAc)_2]^+$ 572 $[Ni_2(\mathbf{L^2})OAc]^+$	$C_{29}H_{27}N_8O_{11}Ni_3 \cdot 3MeOH \cdot 3H_2O$ calcd: C 38.83%, H 4.58%, N 11.32% found: C 38.68%, H 4.22%, N 11.01%
$[Mn_2(\mathbf{L^2})Cl_2]$ **(2.21)**	229, 250, 342	---, 1615	505 $[Mn_2(\mathbf{L^2})]^+$ 450 $[Mn(\mathbf{L^2})]^+$	found: C 40.07%, H 4.49%, N 10.00%
$[Mn_3(\mathbf{L^2})(OAc)_4MeO]$ **(2.22)**	221, 245, 352	---, 1637	961 $[Mn_2(\mathbf{L^2})_2OAc]^+$ 567 $[Mn_2(\mathbf{L^2})OAc]^+$	$C_{29}H_{27}N_8O_{11}Mn_3 \cdot 3MeOH \cdot 3H_2O$ calcd: C 39.28%, H 4.64%, N 11.45% found: C 39.47%, H 4.96%, N 11.41%
$[Co_2(\mathbf{L^2})Cl_2]$ **(2.23)**	229, 265	---, 1625	549 $[Co_2(\mathbf{L^2})Cl]^+$ 514 $[Co_2(\mathbf{L^2})]^+$	No CHN data
$[Co_3(\mathbf{L^2})(OAc)_3MeO]$ **(2.24)**	228, 260	---, 1642	573 $[Co_2(\mathbf{L^2})OAc]^+$ 513 $[Co_2(\mathbf{L^2})]^+$	$C_{27}H_{24}N_8O_9Co_3 \cdot 2H_2O$ calcd: C 39.68%, H 3.45%, N 13.71% found: C 39.36%, H 3.76%, N 14.01%

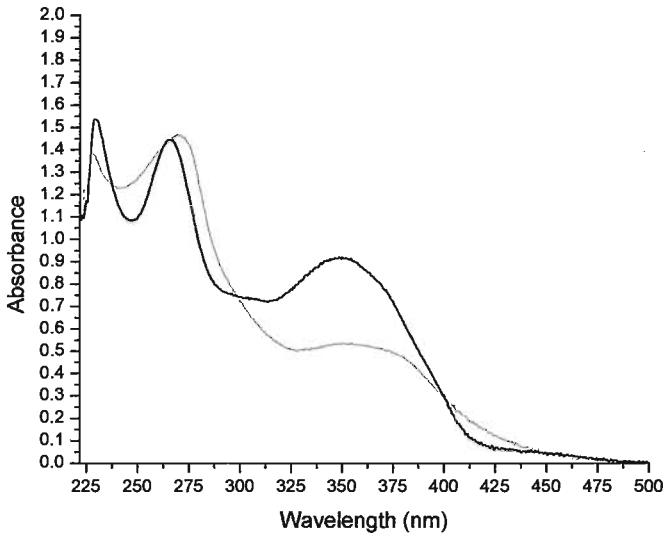

Figure 2.30: UV-Vis spectrum of the copper(II) acetate complex **(2.17)** (green line) compared to that of the unchelated ligand **(2.2)** (black line).

All of the compounds contain a maximum in their UV-Vis spectra centered around 230 nm which is consistent with the high energy π-π^* transition of the ligand. Two other absorption maxima are present centered around 260 and 350 nm. As observed in Figure 2.30 the UV-Vis spectrum of the coordination complex is not significantly shifted when compared to that of the free ligand. In this respect it is difficult to tell just by examining the UV-Vis spectrum whether or not coordination had taken place. A summary of the UV-Vis data is presented in Table 2.15. The IR spectra of the complexes are also summarized in Table 2.15. Once again the $N\text{-}H_{str}$ of the uncoordinated ligand is now absent and the amide $C{=}O_{str}$ in the complexes is red shifted when compared to the free ligand. Once again in order to investigate the magnetic properties of these complexes their structural characterization via X-ray crystallography was first targeted. In this respect, reaction of the ligand with two copper salts afforded two new complexes, one of which yielded suitable single crystals for X-ray diffraction.

2.5.1 – Copper(II) Chloride (2.18) and Copper(II) Acetate (2.17) Complexes

Reaction of copper(II) acetate and ligand **(2.2)** in the presence of triethylamine afforded the copper(II) acetate complex **(2.17)** in 62% yield as a green crystalline powder. The UV-Vis spectrum of the copper complex **(2.17)** is summarized in Table 2.15. For this complex there is an additional band at 686 nm which is consistent with *d-d* transitions of the complex. The MS data displays fragmentation ions at *m/z* = 981 *m/z* for $[Cu_2(\mathbf{L^2})_2OAc]^+$, *m/z* = 583 for $[Cu_2(\mathbf{L^2})OAc]^+$, and *m/z* = 303 for $[Cu_2(OAc)_3]^+$. Once again no $N\text{-}H_{str}$ is observed in the IR spectrum of this complex and its $C{=}O_{str}$ is red shifted when compared to the free ligand. There are a number of intense bands from 1562 – 1411 cm^{-1} consistent with the presence of coordinated acetate molecules in the complex. The CHN data is an excellent fit for a 3:1 metal to ligand complex of stoichiometry $[C_{27}H_{24}N_8O_9Cu_3]$.

Suitable single crystals of complex **(2.17)** for X-ray diffraction were grown via the slow vapour diffusion of diethyl ether into a cold (4 °C) 1:1 MeOH:DCM solution of the previously isolated green crystalline solid. The complex crystallizes as a 1-D chain of stoichiometry $[Cu_3(\mathbf{L^2})(OAc)_3MeO]_n$. An ORTEP[153] representation of the crystallographically unique part of the chain is shown in Figure 2.31.

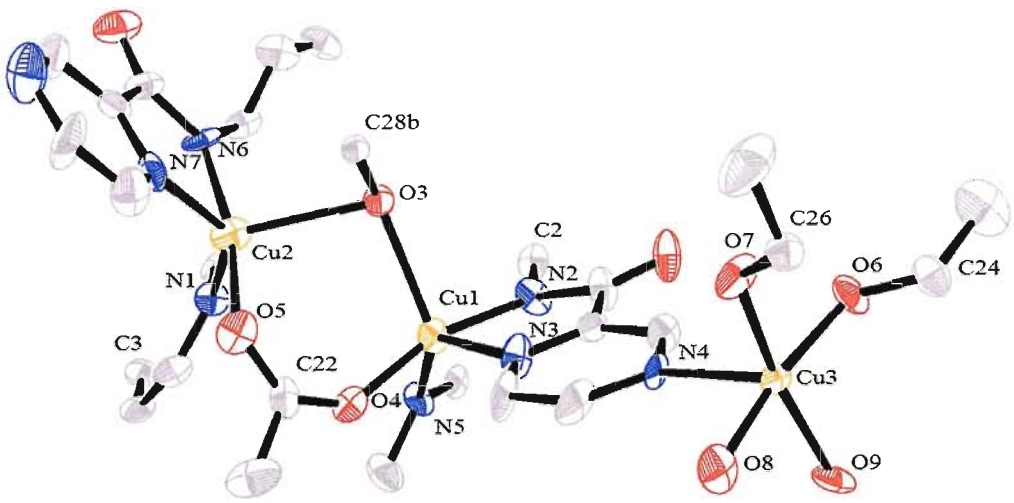

(2.17)

Figure 2.31: ORTEP[153] representation of the $[Cu_3(\mathbf{L^2})(OAc)_3MeO]$ complex **(2.17)**. Thermal ellipsoids are plotted at 50% probability. Hydrogen atoms have been omitted for clarity.

Two of the crystallographically independent Cu(II) centres (Cu(1) and Cu(2)) exhibit an N_3O_2 coordination geometry. For both copper(II) centres this comprises a tridentate N_3 donor set from the dianionic $\mathbf{L^2}$ ligand, one oxygen atom from a bridging μ_2-η^1:η^1-OAc ligand and another oxygen from a disordered bridging methoxide (C(28a) and C(28b)). This results in a distorted square pyramidal geometry for both metal centres. The Cu(3) environment is best described as being very similar to the native copper(II) acetate structure, which consists of four chelating oxygen atoms from four acetate molecules.[126] The torsion angle between the best planes of the bipyridine rings of the ligand is 39.0°. The terminal pyrazine ring lies at angle of 56.2° from the bipyridine (pyridine) ring to which it is directly attached and 67.9° to the opposite bipyridine (pyridine) ring.

Tables 2.16 and 2.17 summarize the selected bond lengths and bond angles for the copper(II) acetate complex **(2.17)**.

Table 2.16: Selected bond lengths [Å] for the copper(II) acetate complex **(2.17)**.

Atoms	Bond [Å]	Atoms	Bond [Å]
Cu(1) - O(3)	2.395(6)	Cu(1) - O(4)	1.942(9)
Cu(1) - N(2)	1.930(11)	Cu(1) - N(3)	2.141(11)
Cu(1) - N(5)	2.069(8)	Cu(2) - N(1)	2.113(10)
Cu(2) - N(6)	1.931(9)	Cu(2) - N(7)	2.062(10)
Cu(2) - O(3)	2.417(7)	Cu(2) - O(5)	1.945(9)
Cu(3) - O(6)	1.961(9)	Cu(3) - O(7)	1.941(8)
Cu(3) - O(8)	1.946(10)	Cu(3) - O(9)	1.965(8)
Cu(3) - N(4)	2.200(11)		

Table 2.17: Selected bond angles [°] for the copper(II) acetate complex **(2.17)**.

Atoms	Angle [°]	Atoms	Angle [°]
O(3) - Cu(1) - O(4)	98.9(3)	O(3) - Cu(1) - N(2)	95.4(3)
O(3) - Cu(1) - N(5)	126.3(3)	O(4) - Cu(1) - N(2)	162.8(4)
O(4) - Cu(1) - N(5)	92.3(4)	N(2) - Cu(1) - N(3)	79.5(4)
N(3) - Cu(1) - N(5)	130.8(4)	N(1) - Cu(2) - N(6)	84.9(4)
N(1) - Cu(2) - O(3)	105.7(4)	N(1) - Cu(2) - O(5)	97.8(4)
N(6) - Cu(2) - O(3)	93.9(4)	N(6) - Cu(2) - O(5)	167.7(5)
N(7) - Cu(2) - O(5)	89.6(4)	O(3) - Cu(2) - O(5)	96.9(4)
O(6) - Cu(3) - O(8)	169.6(4)	O(6) - Cu(3) - O(9)	88.0(4)
O(7) - Cu(3) - O(8)	89.1(4)	O(7) - Cu(3) - O(9)	169.1(4)
O(8) - Cu(3) - O(9)	90.1(4)	O(8) - Cu(3) - N(4)	93.3(4)
O(3) - Cu(1) - N(3)	102.1(3)	N(7) - Cu(2) - O(3)	117.6(3)
O(4) - Cu(1) - N(3)	88.0(4)	O(6) - Cu(3) - O(7)	90.8(4)
N(2) - Cu(1) - N(5)	87.0(4)	O(6) - Cu(3) - N(4)	97.1(4)
N(1) - Cu(2) - N(7)	134.9(5)	O(7) - Cu(3) - N(4)	94.9(4)
N(6) - Cu(2) - N(7)	80.1(4)	O(9) - Cu(3) - N(4)	96.0(4)
Cu(1) - O(3) - Cu(2)	99.8(2)		

A list of all bond lengths and angles for the $[Cu_3(\mathbf{L^2})(OAc)_3MeO]$ complex **(2.17)** can be found in the *Appendix* section of the thesis, Tables 6.11 and 6.12.

The packing diagram of the complex is shown in Figure 2.32. As suggested by the $C{=}O_{str}$ in the IR spectrum, a complete copper acetate structure is present coordinated through one of the terminal pyrazine units of the ligand. Four copper ions (Cu(1), Cu(1'), Cu(2), and Cu(2')) form a central core tetramer which is linked via the copper acetate units of Cu(3) and Cu(3') essentially producing a 1-D chain-like structure, Figure 2.32.

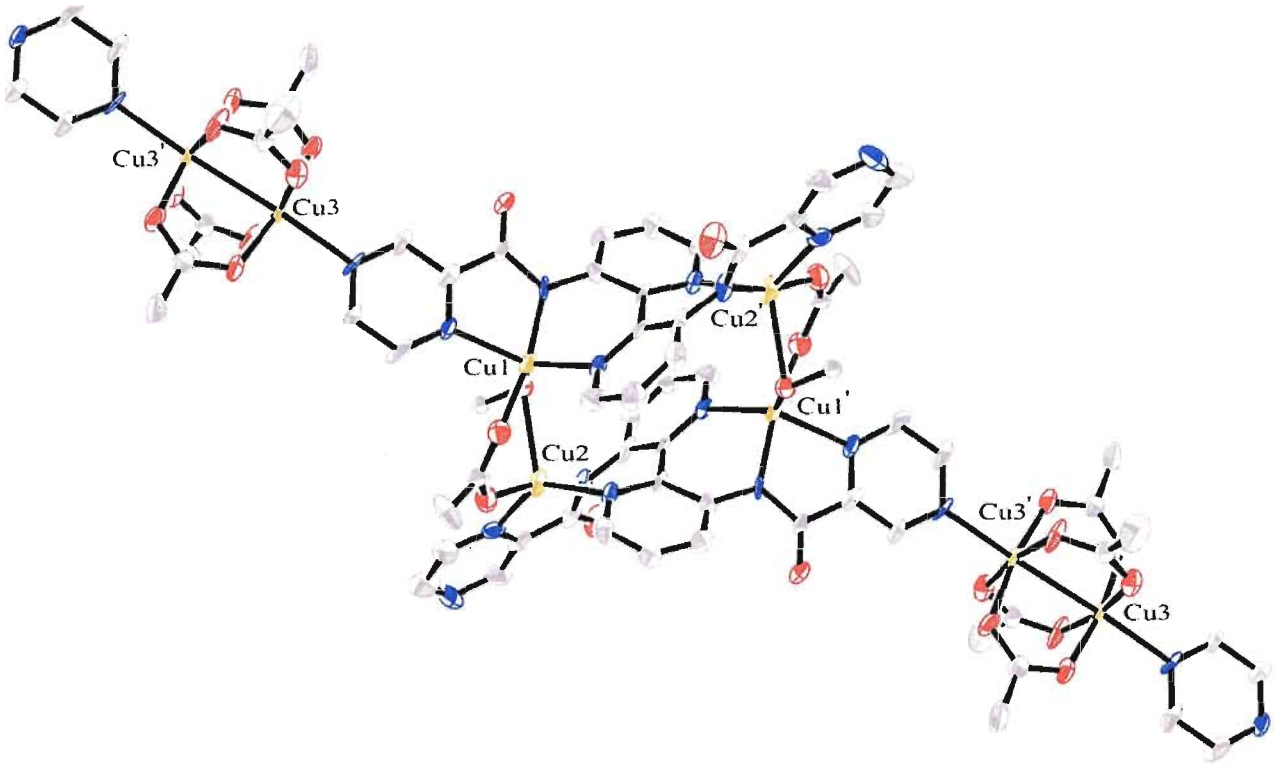

Figure 2.32: ORTEP[153] representation of the packing model of the $[Cu_3(\mathbf{L^2})(OAc)_3MeO]$ complex. Thermal ellipsoids are plotted at 50% probability. Hydrogen atoms have been omitted for clarity.

Once characterized the magnetic properties of complex **(2.17)** were studied. A sample of 14.8 mg of the complex was measured on a Quantum Design SQUID magnetometer in an applied field of 1000 Oe between 5 and 300 K. The data were

corrected for the sample holder and sample diamagnetism (Pascal's constants).[8] A plot of $1/\chi_M$ *vs.* T showed the sample obeyed Curie-Weiss law with C = 1.237 cm^3 K mol^{-1} and θ = -24.9 K consistent with three S = ½ ions with g = 2.230 and the presence of both strong and weak antiferromagnetic interactions between ions. The g-value is typical of Cu^{II} ions in which second-order spin-orbit coupling leads to $g > g_e$.[117] This value of g was confirmed by the EPR measurements carried out in a DCM solution of the complex.

In order to generate an appropriate magnetic model for the complex, the structure was examined for close Cu···Cu contacts and pathways for magnetic superexchange, Figure 2.33. The distances between the copper metal centres are: 3.681 Å for Cu(1)···Cu(2), 6.154 Å for Cu(1)···Cu(2'), and 2.596 Å for Cu(3)···Cu(3').

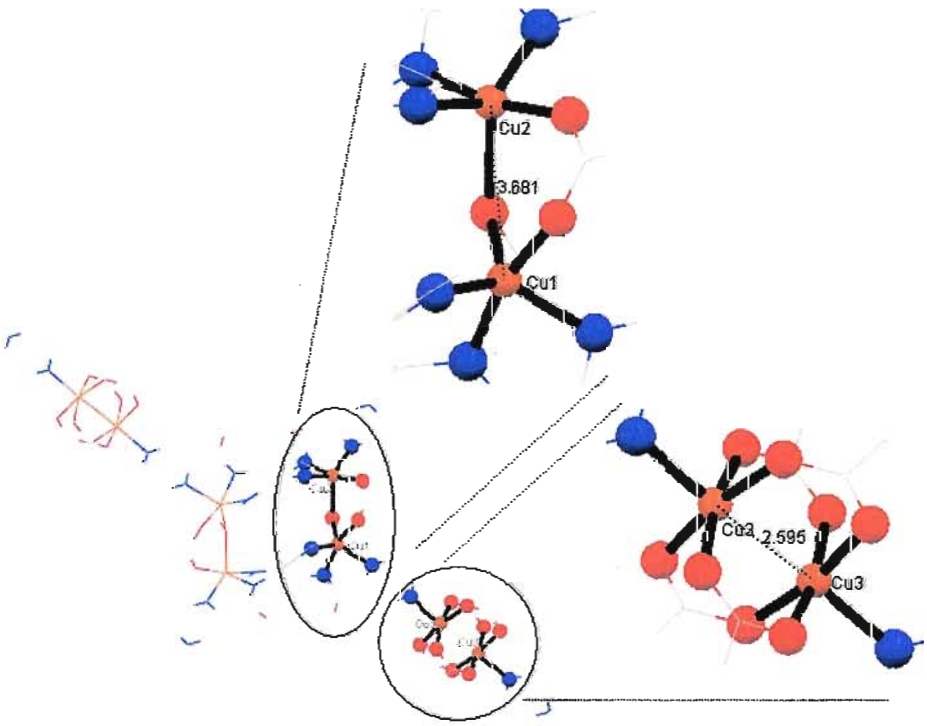

Figure 2.33: Mercury[152] view of the copper acetate complex **(2.17)**. The Cu···Cu interactions are displayed as dashed lines. Distances are in Å.

The closest Cu···Cu distance is located within the copper acetate dimer (2.596 Å) between Cu(3) and Cu(3'). Bleaney and Bowers studied the magnetic properties of the copper acetate dimer and determined that the complex was strongly antiferromagnetically coupled. This work was one of the first examples of magnetic modelling.[127] Piovesana and co-workers prepared a complex that contained the native copper acetate structure and determined that it was strongly antiferromagnetically coupled with a J value of -145.8 cm^{-1}.[128] The complex prepared from their work is shown in Figure 2.34. Their data shows a steady decrease in susceptibility from 300 K to ~80 K, where the final value is appropriate for two S = ½ uncorrelated spins, 0.8 cm^3 K mol^{-1} (i.e. two non-interacting Cu^{II} metal ions). At approximately 10 K the susceptibility tends to zero, indicating antiferromagnetic exchange between the other two copper ions.

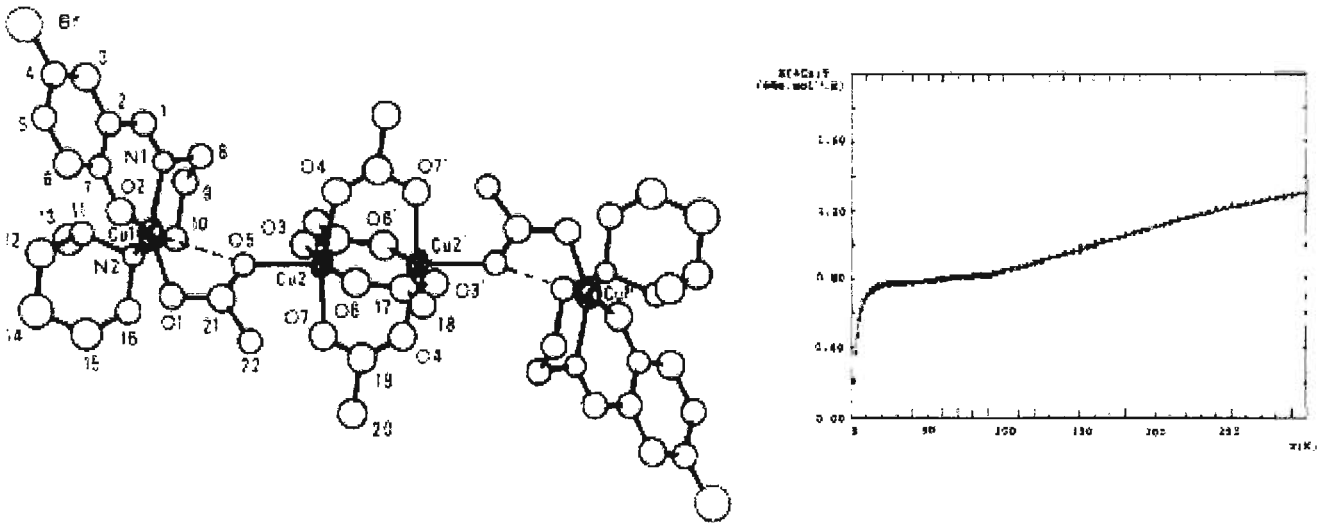

Figure 2.34: Molecular structure of the copper acetate complex prepared by Piovesana *et al.* and its measured and modelled magnetic susceptibility. Reprinted with permission from reference 128. Copyright {1993} American Chemical Society.

This was used to model the magnetic data from the copper acetate structure in complex **(2.17)**, however, only half of the susceptibility was used since the molecular structure only contains half of the native copper acetate structure:

$$\chi_M = \frac{3g^2}{8T} \cdot \frac{2exp2J/kT}{1+3exp2J/kT} \cdot \frac{1}{2} \qquad \text{(A)}$$

The distance between Cu(1) and Cu(2) is 3.685 Å and was expected to be weakly coupled. Therefore, the model also used two interacting ½ spin copper ions (dimer).

$$\chi_M = \frac{3g^2}{8T} \cdot \frac{2exp2J/kT}{1+3exp2J/kT} \qquad \text{(B)}$$

Adding the two values from (A) and (B) generated a model that fit the observed data well as indicated by the $\chi_M T$ *vs.* T graph, Figure 2.34. This yielded a $g = 2.23$ and J values of -145.8 cm^{-1} for the copper acetate dimer between Cu(3) and Cu(3') and -4.24 cm^{-1} for the dimer between Cu(1) and Cu(2).

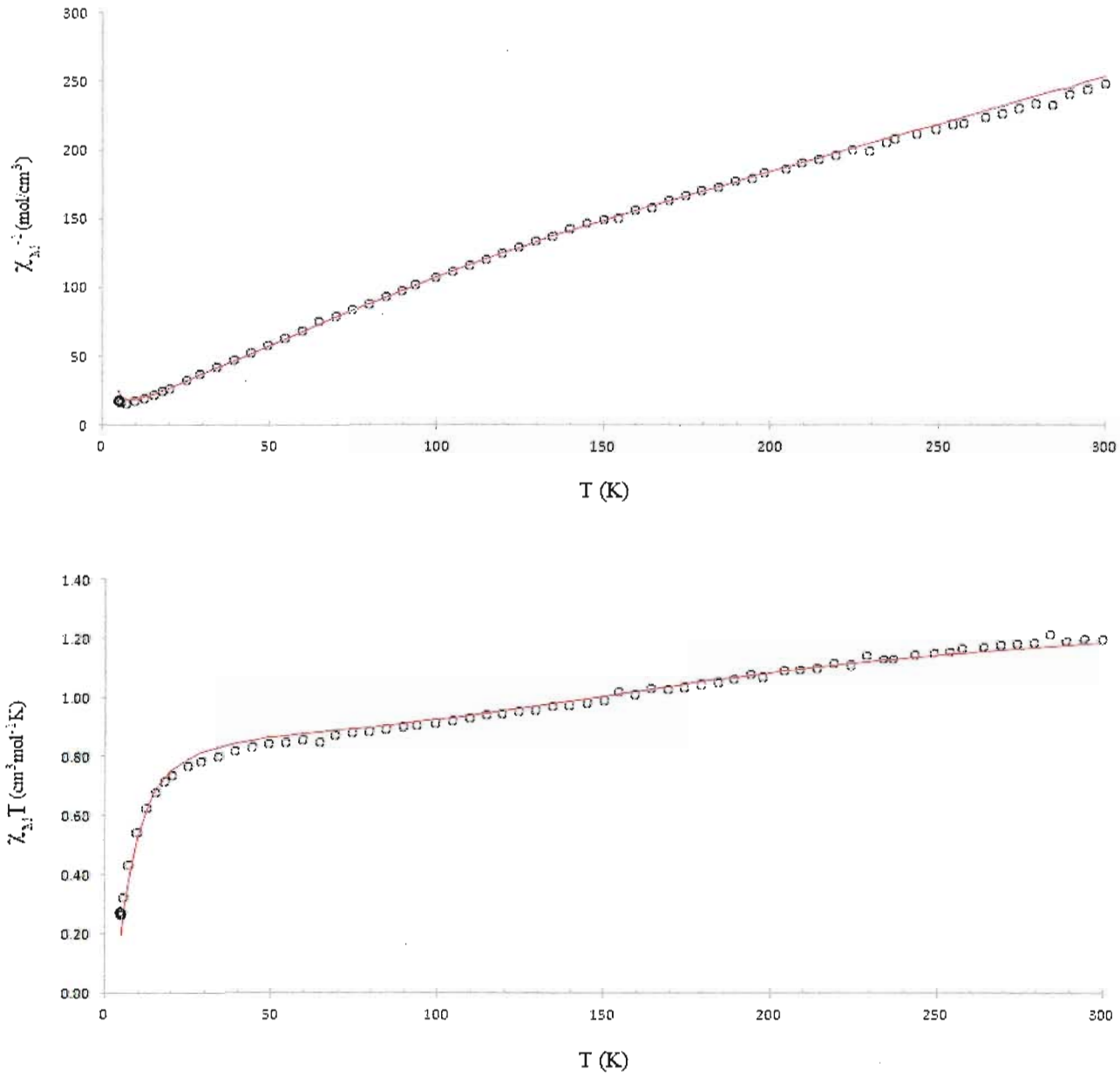

Figure 2.35: Graphs of $1/\chi_M$ *vs.* T and $\chi_M T$ *vs.* T for complex **(2.17)**. The open circles represent the experimental data and the solid red line represents the best model.

It was also determined that an interaction between Cu(1) and Cu(3) could be possible which would result in a tetramer linking Cu(1), Cu(3), Cu(3'), and Cu(1'), Figure 2.36.

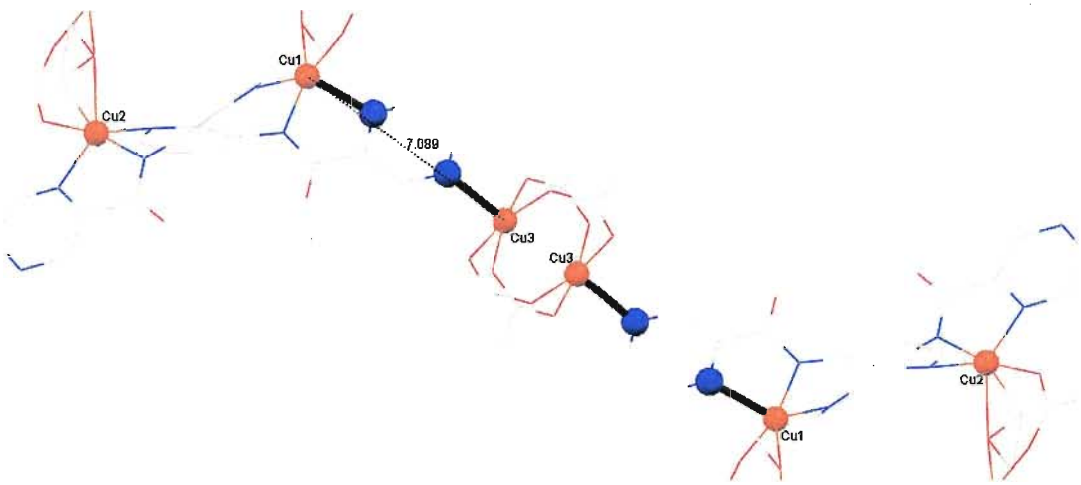

Figure 2.36: Mercury view of the copper acetate complex **(2.17)** displaying the possible tetrameric interaction among Cu(1), Cu(3), Cu(3'), and Cu(1'). Distance is in Å.

If this second model is applied, a non interacting $S = ½$ spin would result in a susceptibility that does not drop below 0.375 cm^3 K mol^{-1}. However, as observed experimentally the susceptibility drops to 0.279 cm^3 K mol^{-1} at 5 K. In this respect the experimental data supports a second antiferromagnetic coupling. This cannot occur in the second tetrameric model and thus this model was rejected. It seems reasonable to suggest that the first model is more appropriate to account for the magnetic susceptibility data of this complex namely that the overall magnetic interaction is both strongly and weakly antiferromagnetic.

Reaction of copper(II) chloride and 2,2'-bipyridine-3,3'-(2-pyrazinecarboxamide) **(2.2)** in the presence of triethylamine afforded a green crystalline powder. The absorption maxima of the UV-Vis spectrum of the copper compound are summarized in Table 2.15. The MS data displays peaks at m/z = 594 for $[Cu_2(\mathbf{L^2})Cl_2]^+$, m/z = 558 for $[Cu_2(\mathbf{L^2})Cl]^+$, and m/z = 523 for $[Cu_2(\mathbf{L^2})]^+$. This data suggests the formation of a coordination complex. The IR spectrum also displays the loss of the N-H_{str} while the carbonyl peak is

red shifted by 47 wavenumbers to 1625 cm^{-1}. Although this data is suggestive of the formation of the copper(II) chloride complex **(2.18)** it is not definitive. Unfortunately, CHN data could not be fit to a reasonable structure for this complex.

2.5.2 – Chloride Complexes (2.19), (2.21), and (2.23)

The exact same elemental analysis data fitting problem for complex **(2.18)** was encountered for the following complexes: nickel(II) chloride complex **(2.19)**, manganese(II) chloride complex **(2.21)**, and cobalt(II) chloride complex **(2.23)**. Since no suitable single crystals of these complexes could be obtained the use of a reference structure was hard to establish. Therefore, the molecular structures of these complexes could not definitively be determined by the available UV-Vis, IR, and MS data which are summarized in Table 2.15.

On the other hand, the remaining acetate complexes, even though they also did not yield suitable single crystals for X-ray diffraction, could be compared to the copper(II) acetate complex **(2.17)**.

2.5.3 – Acetate Complexes (2.20), (2.22), and (2.24)

Reaction of the respective acetate salt with ligand **(2.2)** in the presence of triethylamine afforded the acetate complexes. The nickel(II) acetate complex **(2.20)** was isolated a yellow powder in 52% yield, the manganese(II) acetate complex **(2.22)** was isolated as a brown crystalline powder in 48% yield, and the cobalt(II) acetate complex **(2.24)** was isolated as a brown crystalline powder in 69% yield. A summary of the UV-Vis, IR, MS, and CHN data of these complexes are presented in Table 2.15.

For the nickel(II) acetate complex **(2.20)** the CHN data is consistent with a 3:1 metal to ligand complex of stoichiometry $[C_{29}H_{27}N_8O_{11}Ni_3]\cdot 3MeOH\cdot 3H_2O$, which is indicative of a structure similar to that of the copper(II) acetate complex **(2.17)**. The CHN data for the manganese(II) acetate complex **(2.22)** and the cobalt(II) acetate complex **(2.24)** are consistent with stoichiometries of $[C_{29}H_{27}N_8O_{11}Mn_3]\cdot 3MeOH\cdot 3H_2O$ and $[C_{27}H_{24}N_8O_9Co_3]\cdot 2H_2O$, respectively. These divalent metal ions are known to bridge through acetate molecules where the acetates can adopt various coordination modes.[129] Therefore, from the available data for the aforementioned acetate complexes the structures may be similar to that of the copper(II) acetate complex whose crystal structure was elucidated by X-ray diffraction. Proposed structures of these complexes are presented in Figure 2.37.

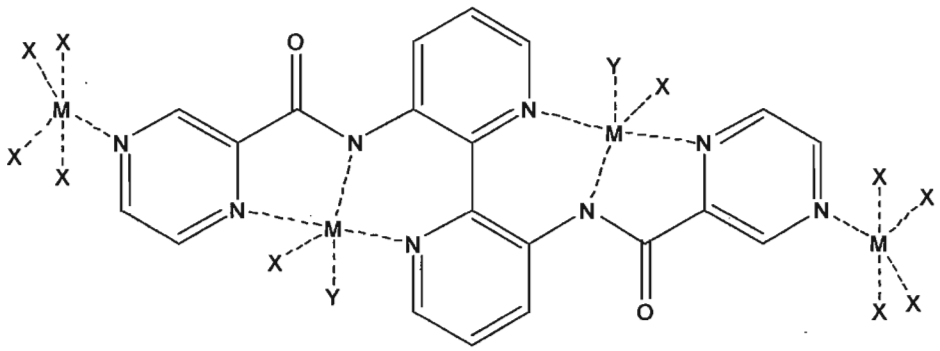

Figure 2.37: Proposed molecular structures for the acetate complexes **(2.20)**, **(2.22)**, and **(2.24)**. M = Ni(II), Mn(II), Co(II). X = OAc. Y = MeO. Bridging may occur through the acetate and methoxide ligands. Additional coordination sites may be taken by solvent molecules.

The next ligand targeted was 2,2'-bipyridine-3,3'-(ethyl-2-aminoacetate) **(H_2L^3)** **(2.3)**.

2.6 – 2,2'-Bipyridine-3,3'-(Ethyl-2-Aminoacetate) (H_2L^3) (2.3)

A third ligand with more flexible arms was targeted in order to continue our investigation. The longer term objective was to prepare heterocyclic oxadiazole derivatives of 3,3'-diamino-2,2'-bipyridine, Figure 2.38. Oxadiazole ligands are known to form multimetallic systems with various coordination modes.[131]

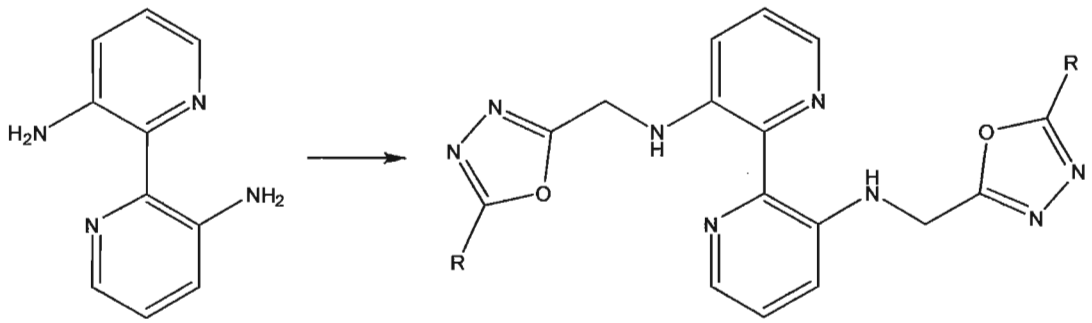

Figure 2.38: The targeted oxadiazole derivatives starting from 3,3'-diamino-2,2'-bipyridine. R = SH, NH_2, 2-pyridyl.

In order to reach the long term objective an effective synthetic strategy for the preparation of the various oxadiazole derivatives was prepared. Following Scheme 2.3 the synthesis of a bipyridine ethoxy derivative **(2.3)** was targeted first. This could then be converted into a hydrazide derivative **(2.4)** which could then be converted into the various oxadiazole derivatives. The synthetic intermediates **(2.3)** and **(2.4)** were investigated in regard to their suitability for the preparation of molecule-based magnetic materials. As such their coordination chemistry with the aforementioned paramagnetic divalent transition metal ions was targeted.

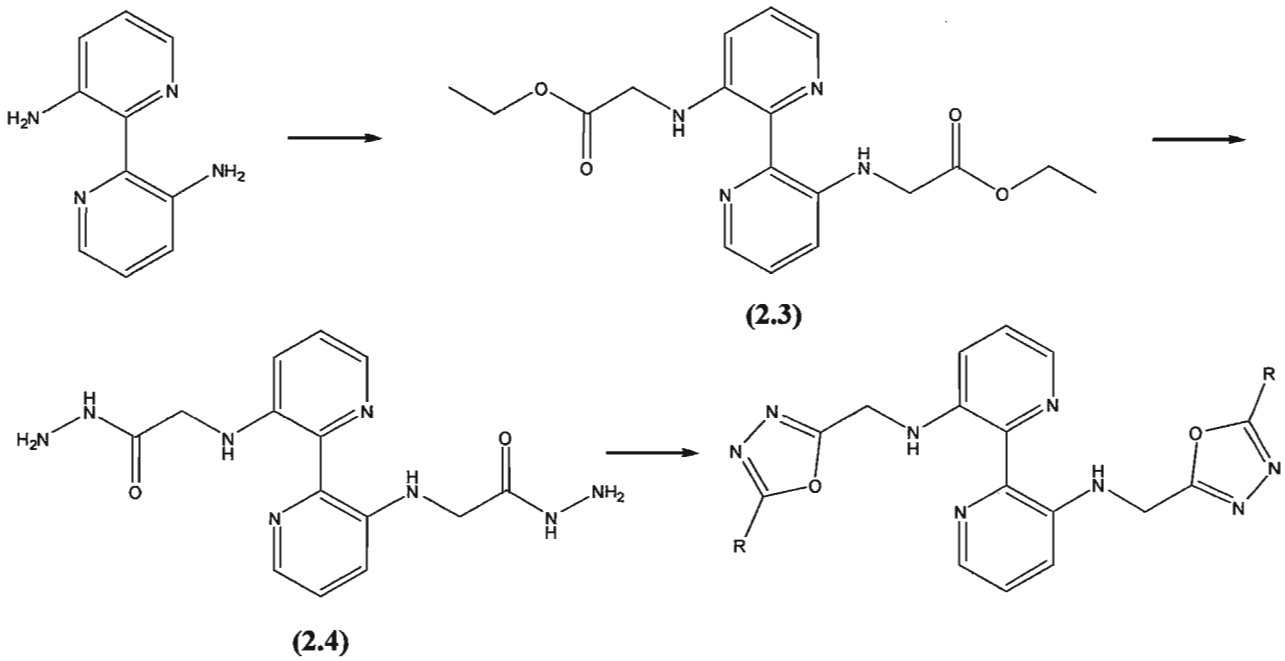

Scheme 2.3: Overview of the synthetic outline for the preparation of the oxadiazole derivatives.

Therefore, an overview of the synthetic pathway followed for the preparation of **(2.3)** is shown in Scheme 2.4.[130]

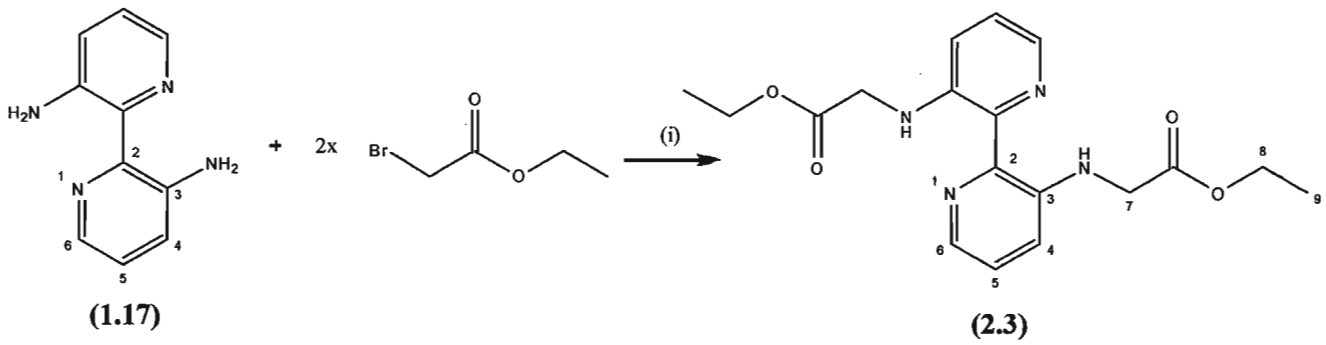

Scheme 2.4: Synthetic route for the synthesis of 2,2'-bipyridine-3,3'-(ethyl-2-aminoacetate) (H_2L^3) **(2.3)**. Reagents and conditions: (i) a) MeCN / DIEA, 60 °C, 30 mins, b) Ethyl bromoacetate, 60 °C, 5 hrs.

An excess of Hünig's base (*N*,*N*-diisopropylethylamine) was used to facilitate the deprotonation of 3,3'-diamino-2,2'-bipyridine **(1.17)** which was reacted with exactly two equivalents of ethyl bromoacetate. The diisopropylethylamine hydrogen bromide salt was

removed by washing with water during work up. Ligand **(2.3)** was obtained in a 54% yield. The structure of 2,2'-bipyridine-3,3'-(ethyl-2-aminoacetate) **(2.3)** was confirmed by ^{1}H-NMR, ^{13}C-NMR, mass spectrometry (EI), UV-Vis and IR spectroscopy.

The ^{1}H-NMR spectrum of the ligand **(2.3)** displays the amine peak as a very broad singlet at 10.16 ppm. The second peak, a doublet, at 8.02 ppm is assigned to the 6-H of the bipyridine. The next peak, a doublet, at 7.15 ppm is assigned to the 5-H of the bipyridine. Following this, a doublet at 6.90 ppm is assigned to the 4-H of the bipyridine. The next peak, a quartet, at 4.28 ppm is assigned to the 8-H of the terminal arm. The next peak, a singlet, at 4.04 ppm is assigned to the 7-H of the terminal arm. The final peak, a triplet, at 1.33 ppm is assigned to the protons located on the C_9 position of the ligand. All peaks integrate with the correct ratios for the appropriate number of protons.

The ^{13}C-NMR spectrum for the ligand **(2.3)** displays a peak for the ester carbonyl at 170.7 ppm. The remaining peaks have been assigned to the following carbons: 144.2 ppm (2-C), 140.4 ppm (3-C), 133.7 ppm (6-C), 123.1 ppm (4-C), 117.6 ppm (5-C), 61.3 ppm (8-C), 45.3 ppm (7-C), 14.2 ppm (9-C).

The IR spectrum of this ligand has an intense band at 1745 cm^{-1} attributed to the C=O stretch of the ester carbonyl. A band corresponding to the N-H stretch is seen at 3450 cm^{-1}. Observed bands from 3043 cm^{-1} to 2836 cm^{-1} are consistent with aromatic and aliphatic C-H stretches of the bipyridine and terminal arms.

The UV-Vis spectrum of ligand **(2.3)** shows three maxima at λ = 231, 269, and 383 nm that can be assigned to π-π^* and n-π^* transitions of the ligand (231 nm π-π^* bipyridine, 269 nm N(n)-π^* bipyridine, 383 nm N(n)-π^*, NH). The high resolution EI mass spectrum has a parent ion peak at *m/z* = 358.1640 which is in close agreement with

the calculated value of m/z = 358.1641 for $C_{18}H_{22}N_4O_4$. The CHN data are all within the acceptable ± 0.4% limit for $C_{18}H_{22}N_4O_4$.

Single crystals of **(2.3)** suitable for X-ray diffraction were obtained via the slow evaporation of a chloroform solution of the ligand at room temperature. The diffraction data indicated that the crystals were highly twinned which made the refinement of the data problematic. A tentative molecular structure of the ligand is presented in Figure 2.39. It should be noted that to-date the structure has not been fully refined.

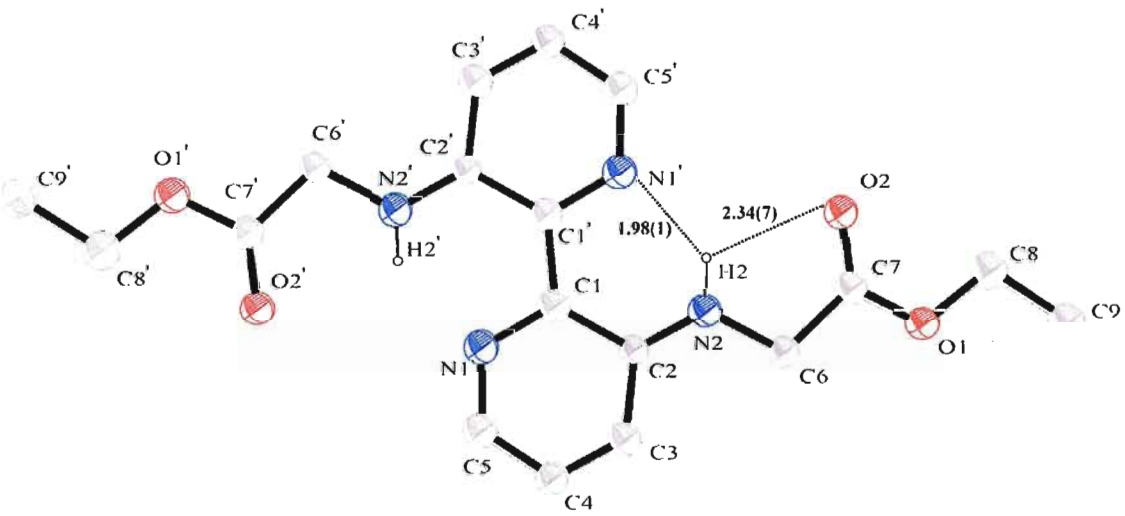

(2.3)

Figure 2.39: ORTEP[153] representation of the molecular structure of **(H_2L^3) (2.3)** showing the labelling scheme. Thermal ellipsoids are plotted at 30% probability. Select hydrogen atoms have been omitted for clarity.

The ligand crystallizes in the monoclinic space group $P2_1/c$ with two molecules per unit cell. An ORTEP[153] view of the molecular structure of one independent ligand molecule along with the atom-numbering scheme is shown in Figure 2.39. The ligand crystallizes in the *trans* configuration with respect to its bipyridine rings. The amine hydrogen atom forms an intramolecular H-bond with the bipyridine nitrogen (N-H2···N1

= 1.98 Å) and a longer H-bond with the oxygen of the ester carbonyl (N-H2···O2 = 2.35 Å), Figure 2.38. This bonding stabilizes the *trans* configuration of the ligand. A view down the *b*-axis of the unit cell reveals that the molecules are π-π stacked, Figure 2.40. The separation of 3.39 Å between molecules is ideal for π-π interactions as determined by Hunter and Sanders.[114]

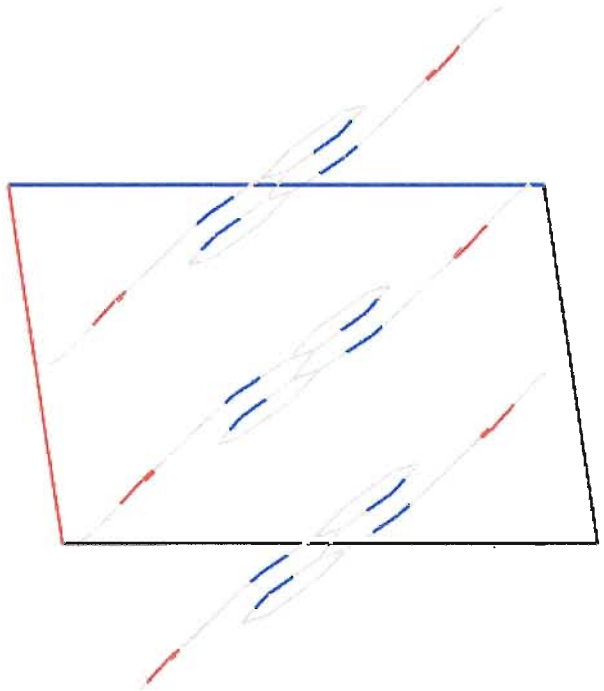

Figure 2.40: Mercury[152] view of the packing of **(2.3)**. View down the *b*-axis.

Once ligand **(2.3)** had been prepared and fully characterized, the next objective was to investigate its coordination chemistry with the aforementioned divalent transition metal ions.

2.7 – Coordination Chemistry of Ligand (H_2L^3) (2.3)

Ligand **(2.3)** was expected to either coordinate in a *cis* or *trans* configuration with respect to its bipyridine rings. As previously shown in the *Introduction* section of the thesis the bipyridine moiety can easily adopt a *cis* configuration and coordination to a metal ion can occur through the bipyridine nitrogen atoms. The ligand could also coordinate in the *trans* configuration where it would contain two tridentate binding pockets. To test this coordination capability no base was added to the reaction series. Furthermore, glycine derivatives are capable of coordinating through the nitrogen atom regardless if they are protonated or not.

In a typical experiment, 2.1 equivalents of a metal salt were reacted together with one equivalent of the ligand **(2.3)**. All reactions were carried out at room temperature in a 3:1 mixture of DCM:MeOH. The ligand was soluble in DCM, whereas the salts were soluble in MeOH.

Multiple crystallization experiments have been carried out on this particular series of coordination complexes: liquid-liquid diffusions, vapour diffusions, and slow evaporations of reaction mixtures or isolated products redissolved in various solvents. Unfortunately, to-date no single crystals of any of these coordination complexes have been obtained. A summary of the selected UV-Vis, IR, MS, and CHN data for the complexes is presented in Table 2.18.

All of the compounds contain an absorption maximum in their UV-Vis spectra centered on 232 nm. This is consistent with the high energy π-π^* transition of the ligand. The complexes also display two additional absorption bands, however, they are not shifted as compared to the free ligand **(2.3)**. The intensity of the second band in each UV-

Vis spectrum of the coordination complexes differs in intensity as compared to the uncoordinated ligand **(2.3)**. As an example the spectrum of the copper(II) acetate complex **(2.25)** is compared to the spectrum of the uncoordinated ligand in Figure 2.41.

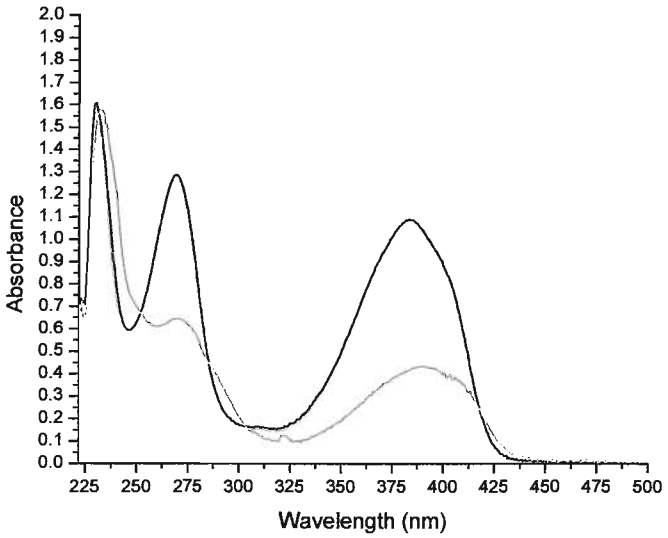

Figure 2.41: UV-Vis spectrum of the copper(II) acetate complex **(2.25)** (green line) compared to that of the unchelated ligand **(2.3)** (black line).

Table 2.18: Summary of the UV-Vis, IR, MS and CHN data for the coordination complexes prepared from ligand H_2L^3 **(2.3)**.

Compound	UV-Vis, λ_{max} (nm)	IR, N-H_{str}, C=O_{str} (cm^{-1})	MS (*m/z*)	CHN
H_2L^3 (2.3)	231, 269, 383	3450, 1745	358 [M^+]	$C_{18}H_{22}N_4O_4$ calcd: C 60.32%, H 6.19%, N 15.63% found: C 60.13%, H 6.04%, N 15.63%
[Cu(H_2L^3)Cl_2] **(2.27)**	243, 283, 391	3448, 1740	456 [Cu(H_2L^3)Cl]$^+$ 421 [Cu(H_2L^3)]$^+$	found: C 35.08%, H 4.89%, N 8.48%
[Cu(H_2L^3)$(OAc)_2$] **(2.25)**	234, 271, 392, 742	3421 w, 1735	480 [Cu(H_2L^3)OAc]$^+$ 421 [Cu(H_2L^3)]$^+$	$C_{22}H_{28}N_4O_8Cu{\cdot}4H_2O$ calcd: C 43.17%, H 5.93%, N 9.15% found: C 43.43%, H 5.73%, N 9.32%
[Ni(H_2L^3)Cl_2] **(2.28)**	233, 273, 392	3450, 1745	451 [Ni(H_2L^3)Cl]$^+$ 416 [Ni(H_2L^3)]$^+$	No CHN data
[Ni(H_2L^3)$(OAc)_2$] **(2.29)**	231, 273, 389	3447, 1742	474 [Ni(H_2L^3)OAc]$^+$ 415 [Ni(H_2L^3)]$^+$	found: C 39.14%, H 5.18%, N 7.38%
[Mn(H_2L^3)Cl_2] **(2.30)**	234, 272, 394	3452, 1741	448 [Mn(H_2L^3)Cl]$^+$ 413 [Mn(H_2L^3)]$^+$	found: C 41.42%, H 6.54%, N 9.42%
[Mn(H_2L^3)$(OAc)_2$] **(2.31)**	234, 271, 394	3445, 1740	531 [Mn(H_2L^3) $(OAc)_2$]$^+$ 472 [Mn(H_2L^3) (OAc)]$^+$	found: C 38.50%, H 4.73%, N 5.97%
[Co(H_2L^3)Cl_2] **(2.26)**	235, 271, 394, 628, 665, 697	3445, 1742	452 [Co(H_2L^3)Cl]$^+$ 417 [Co(H_2L^3)]$^+$	$C_{18}H_{22}N_4O_4CoCl_2{\cdot}3H_2O{\cdot}3MeOH$ calcd: C 39.51%, H 6.32%, N 8.78% found: C 39.51%, H 6.19%, N 9.07%
[Co(H_2L^3)$(OAc)_2$] **(2.32)**	231, 275, 392	3449, 1739	476 [Co(H_2L^3)OAc]$^+$ 417 [Co(H_2L^3)]$^+$	found: C 37.94%, H 4.58%, N 5.92%

Suitable single crystals for X-ray diffraction could not be obtained for any of the complexes prepared from ligand **(2.3)**. However, two compounds could be fully characterized using UV-Vis, IR, MS and CHN data: a copper(II) acetate complex **(2.25)** and a cobalt(II) chloride complex **(2.26)**.

2.7.1 – Copper(II) Acetate Complex (2.25)

The reaction of copper(II) acetate with the ligand **(2.3)** afforded a bright green crystalline powder in 88% yield. The absorption maxima of the UV-Vis spectrum of the copper(II) acetate compound are summarized in Table 2.18. The peak centered at 271 nm (log ε = 4.08 $M^{-1}cm^{-1}$) for the copper complex as compared to the free ligand (log ε = 4.41 $M^{-1}cm^{-1}$) is considerably less intense, Figure 2.41. This suggests that the ligand is coordinating to the copper(II) metal centre through the nitrogen atoms of the bipyridine ring in a *cis*-conformation. A band at 742 nm is consistent with *d-d* transitions of the complex. Five-coordinate Cu(II) complexes that show *d-d* absorptions in the range of 588 – 769 nm typically tend to approximate a square-pyramidal geometry about the copper centre, while complexes with a trigonal-bipyramidal geometry show absorption bands at longer wavelengths.[132] Therefore, the geometry of the copper metal centre is more than likely trigonal-bipyramidal. The mass spectrometry data displays fragmentation ions at *m/z* = 480 for $[Cu(\mathbf{H_2L^3})OAc]^+$ and *m/z* = 421 for $[Cu(\mathbf{H_2L^3})]^+$. The IR spectrum shows a broad band at 3421 cm^{-1} which can be assigned to the $O\text{-}H_{str}$ of coordinated water solvent molecules which could be masking the $N\text{-}H_{str}$ of the ligand. The $C{=}O_{str}$ has not shifted for the copper(II) acetate complex indicating the non-involvement of the carbonyl oxygen atom. There is a band at 1565 cm^{-1} attributed to the υ_{asym} (OCO) of the acetate, while a

band at 1425 cm^{-1} is indicative of the υ_{sym} (OCO) of the acetate molecules. These bands indicate a monodentate coordination mode of the acetate molecules. This data suggests that the copper(II) is coordinated to the neutral ligand **(2.3)** in a 1:1 metal to ligand ratio. The coordination geometry of the metal ion is most likely satisfied by two acetate molecules together with a coordinating water molecule. Elemental analysis data is consistent with a 1:1 metal to ligand complex of stoichiometry $[C_{22}H_{28}N_4O_8Cu]\cdot 4H_2O$. A proposed structure of the complex is presented in Figure 2.42.

.

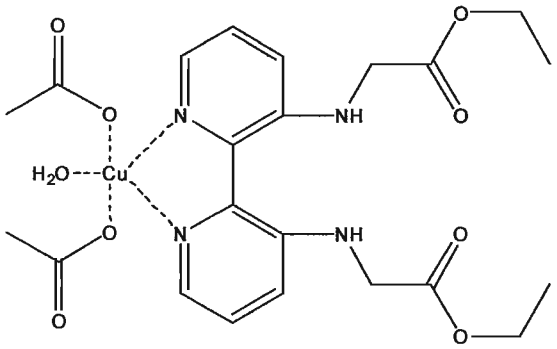

Figure 2.42: Proposed structure of the copper(II) acetate complex **(2.25)** prepared from ligand **(2.3)** and copper(II) acetate.

2.7.2 – Cobalt(II) Chloride Complex (2.26)

The reaction of cobalt(II) chloride with ligand **(2.3)** afforded a green crystalline powder in 77% yield. The absorption maxima of the UV-Vis spectrum are summarized in Table 2.18. The peak at 271 nm for the cobalt compound as compared to the free ligand is considerably less intense. This suggests that the ligand is coordinating to the cobalt(II) metal centre through the nitrogen atoms of the bipyridine ring in a *cis*-conformation. Three bands at 628, 665, and 697 nm are consistent with *d-d* transitions of the complex. These multiple bands indicate an octahedral geometry of the Co(II) metal centre.[132] The

mass spectrometry data displays fragmentation ions at m/z = 452 for $[Co(\mathbf{H_2L^3})Cl]^+$ and m/z = 417 for $[Co(\mathbf{H_2L^3})]^+$. The IR spectrum shows a sharp band at 3552 cm^{-1} which can be assigned to the $O\text{-}H_{str}$ of coordinated water solvent molecules. The $N\text{-}H_{str}$ of the compound is seen at 3445 cm^{-1} indicating the ligand is not deprotonated. The $C{=}O_{str}$ has not shifted for the cobalt(II) chloride complex indicating the non-involvement of the carbonyl oxygen atom in coordination. This data suggests that the cobalt(II) is coordinated to the neutral **(2.3)** ligand in a 1:1 metal to ligand ratio. The coordination sites of the metal ion are most likely satisfied by two chloride molecules together with two coordinating water molecules. The CHN data is consistent with a 1:1 metal to ligand complex of stoichiometry $[C_{18}H_{22}N_4O_4CoCl_2]\cdot 3H_2O\cdot 3MeOH$. A proposed structure of the complex is presented in Figure 2.43.

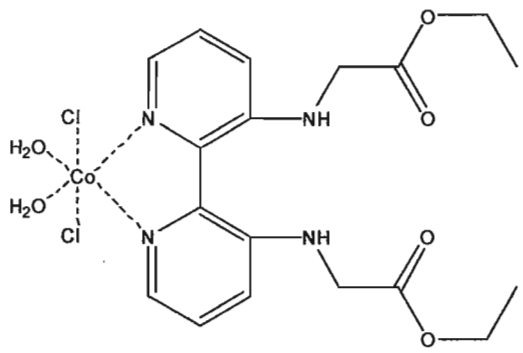

Figure 2.43: Proposed structure of the cobalt(II) chloride complex **(2.26)** prepared from ligand **(2.3)**.

2.7.3 – Other Coordination Complexes

The UV-Vis, IR, and MS data of the various complexes prepared using copper(II) chloride, nickel(II) chloride, nickel(II) acetate, manganese(II) chloride, manganese(II) acetate, and cobalt(II) acetate with ligand **(2.3)** are summarized in Table 2.18. As previously mentioned the UV-Vis data is consistent with coordination through the

nitrogen atoms of the bipyridine rings. All of the compounds prepared displayed MS peaks at $[M(\mathbf{H_2L^3})X]$, M = Cu(II), Ni(II), Mn(II), Co(II) and X = Cl^-, OAc^-. The six compounds prepared also displayed IR bands for the N-H_{str} ranging from 3450 – 3421 cm^{-1}. The C=O_{str} is also visible for the compounds ranging from 1745 – 1735 cm^{-1}. This is indicative of the non-involvement in coordination of either the amine nitrogen atom or carbonyl oxygen atom. Therefore, it can be suggested that the compounds prepared from these metal salts yielded a 1:1 metal to ligand ratio however this is not definitive. The CHN data of these complexes could not be fit to a reasonable structure.

2.8 – 2,2'-Bipyridine-3,3'-(2-Aminoacetohydrazide) (H_2L^4) (2.4)

The final ligand was synthesized in order to introduce more nitrogen atoms into the terminal arms which would then be used to synthesize the heterocyclic groups of the oxadiazole bipyridine derivatives, Figure 2.38.

The synthesis of ligand **(2.4)** was straightforward, utilizing a simple hydrazinolysis reaction of the previous ligand, 2,2'-bipyridine-3,3'-(ethyl-2-aminoacetate) **(2.3)**, Scheme 2.5.[130] An excess of hydrazine monohydrate was used to cleave the terminal ethoxy groups of the ligand.

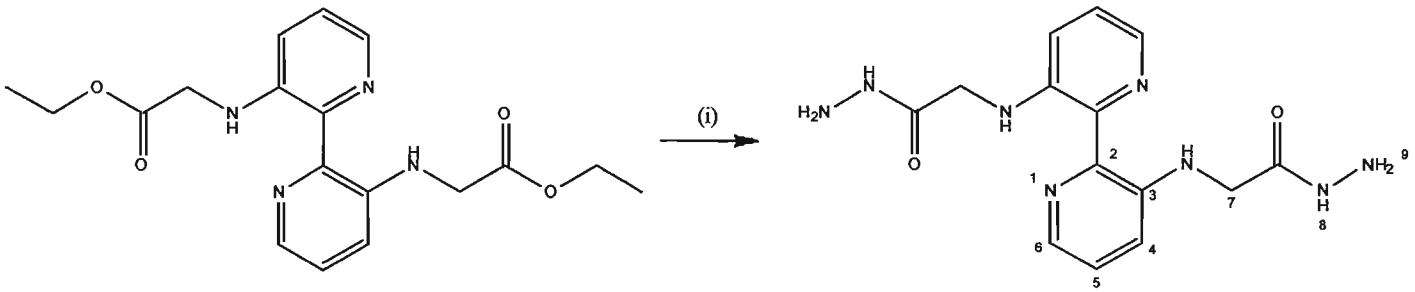

(2.3) **(2.4)**

Scheme 2.5: Synthetic route for the synthesis of 2,2'-bipyridine-3,3'-(2-aminoacetohydrazide) **(H_2L^4) (2.4)**. Reagents and conditions: (i) EtOH, hydrazine monohydrate, 75 °C, 12 hrs.

Ligand **(2.4)** was obtained in 62% yield. The molecular structure of the ligand was confirmed by ^{1}H-NMR, ^{13}C-NMR, mass spectrometry (EI), UV-Vis and IR spectroscopy.

The first peak of the ^{1}H-NMR spectrum of ligand **(2.4)**, a doublet of doublets, at 7.96 ppm is assigned to the 6-H of the bipyridine. The next peak, another doublet of doublets, at 7.32 ppm is assigned to the 5-H of the bipyridine. The last aromatic peak, a doublet of doublets, at 7.06 ppm is that of the 4-H of the bipyridine moiety. The singlet peak at 3.81 ppm is assigned to the 7-H of the terminal arm. The peaks for the protons of the nitrogen atoms are not seen (D_2O exchangeable).

The ^{13}C-NMR spectrum for ligand **(2.4)** has been obtained. It displays a peak for the carbonyl at 171.8 ppm. The remaining peaks have been assigned to the following carbons: 142.4 ppm (2-C), 140.0 ppm (3-C), 137.8 ppm (6-C), 125.4 ppm (4-C), 120.2 ppm (5-C), 45.3 ppm (7-C).

The IR spectrum of this ligand has an intense band at 1654 cm^{-1} attributed to the C=O stretch of the carbonyl. Bands corresponding to the NH stretches are seen at 3297 cm^{-1}, and 3124 cm^{-1}. Observed bands from 3012 cm^{-1} to 2873 cm^{-1} are consistent with aromatic and aliphatic C-H stretches. UV-Vis absorption maxima at 229, 265, and 385 nm can be assigned to π-π^* and n-π^* transitions of the ligand. The high resolution EI mass spectrum has a parent ion peak at m/z = 330.1553 which is in close agreement with the calculated value of m/z = 330.1549 for $C_{14}H_{18}N_8O_2$. The CHN data are all within the acceptable ± 0.4% limit for $C_{14}H_{18}N_8O_2$.

To-date no single crystals of **(2.4)** have been obtained for characterization of the molecular structure by X-ray crystallography. This is largely because of the poor solubility of this ligand in conventional organic solvents.

2.9 – Coordination Chemistry of Ligand (H_2L^4) (2.4)

A preliminary coordination experiment was carried out using copper(II) acetate and ligand **(2.4)**. The copper(II) acetate compound **(2.33)** was obtained as a green powder. The UV-Vis spectrum displays absorption maxima centered at 243, 287, and 417 nm, Figure 2.44. No observable band is seen past 500 nm. The IR spectrum of the copper(II) acetate compound displays a broad band at 3421 cm^{-1} assigned to the $O\text{-}H_{str}$ of solvent water molecules. This band masks the bands from the $N\text{-}H_{str}$ of the hydrazide and amine functionalities in the compound. The band for the $C{=}O_{str}$ has shifted from 1654 to 1637 cm^{-1}. Two bands for an acetate molecule are present at 1567 and 1427 cm^{-1} suggesting a monodentate coordination mode.

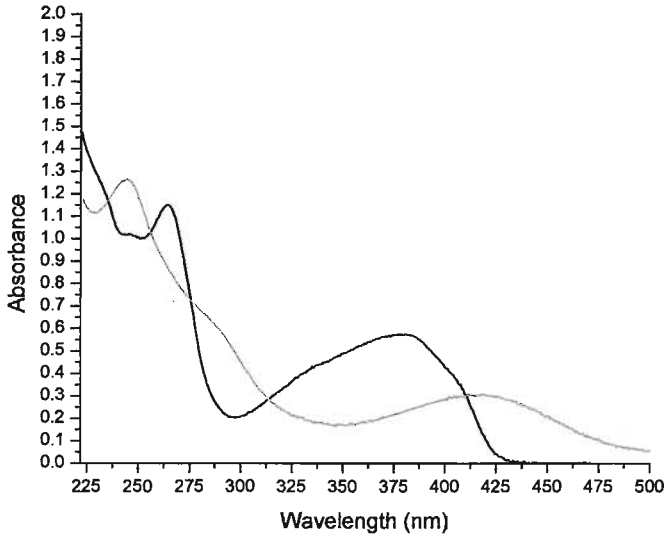

Figure 2.44: UV-Vis spectrum of the copper(II) acetate compound **(2.33)** (green line) compared to that of the unchelated ligand **(2.4)** (black line).

2.10 – Conclusion and Future Work

The objectives of project 1 were to design and synthesize a new family of bipyridine ligands and investigate their coordination chemistry with divalent transition metal ions. In this respect, the four ligands prepared in the first thesis project were 2,2'-bipyridine-3,3'-(2-pyridinecarboxamide) **(2.1)**, 2,2'-bipyridine-3,3'-(2-pyrazinecarboxamide) **(2.2)**, 2,2'-bipyridine-3,3'-(ethyl-2-aminoacetate) **(2.3)**, and 2,2'-bipyridine-3,3'-(2-aminoacetohydrazide) **(2.4)**. The coordination chemistry of these ligands with various divalent first row transition metal ions was investigated.

Suitable single crystals of four coordination complexes prepared from ligand **(2.1)** were obtained and their molecular structures elucidated via X-ray crystallography. Complex $[Zn_2(\mathbf{L^1})(OAc)(MeO)]_2$ **(2.6)** crystallized as a tetramer. Complex $[Cu_2(\mathbf{L^1})(OAc)_2]$ **(2.7)** crystallized as a dimer that was linked to form tetramers that were further organized into a 1-D chain-like structure. This complex displayed an overall antiferromagnetic interaction. Two nickel compounds **(2.8)** and **(2.9)**, that were trimeric polymorphs, of stoichiometry $[Ni(\mathbf{L^1})]_3$ were also obtained. Reports of triangular nickel trimers in the chemical literature are very scarce and those that are reported are normally antiferromagnetically coupled. The magnetic data of nickel trimer **(2.8)** indicated an overall ferromagnetic interaction.

The new pyrazine carboxamide ligand **(2.2)** was synthesized in order to introduce more coordination sites in the terminal arms of the bipyridine moiety. This was expected to yield complexes that preferentially crystallized as 1-D chains which is what occurred for complex $[Cu_3(\mathbf{L^2})(OAc)_3MeO]$ **(2.17)**. The molecular structure of this complex, as determined by X-ray crystallography, revealed that the chain consisted of an alternating

tetrameric structure and the native dimeric copper acetate structure. The magnetic data of this chain-like structure revealed that the native dimeric copper acetate was strongly antiferromagnetically coupled. The magnetic data also indicated that the tetrameric structure was also antiferromagnetically coupled.

Two new ligands **(2.3)** and **(2.4)** with more flexible arms that could ultimately be synthetically converted to heterocycles such as oxadiazole based compounds were prepared and characterized. Although a series of coordination complexes were prepared, no single crystals of these complexes have been obtained to-date to fully elucidate the coordination preferences of these two ligands.

Future work includes continued crystallization attempts of the various complexes to obtain suitable single crystals for X-ray diffraction. Although preliminary coordination data was inconclusive for ligand **(2.4)** the ligand has the capability to be future synthetically modified to yield various derivatives, specifically oxadiazole based compounds, Figure 2.45. These considerations will hopefully be investigated in the near future.

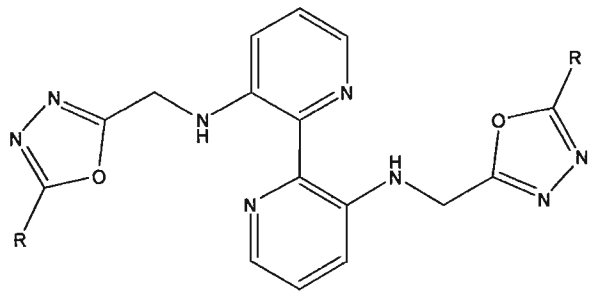

Figure 2.45: Possible 1,3,4-oxadiazole derivatives starting from the hydrazide ligand **(2.4)**. R = SH, NH_2, 2-pyridyl.

Chapter 3 – Results and Discussion – Project 2

Synthesis and Study of Porphyrinic Triol Ligands

3.1 – Introduction

The organization and addressability of single molecule magnets remains at the forefront of scientific interest for materials science.[96] Efforts have been made to study single molecule magnets at the single-molecule level by placing them on surfaces to examine their conductive properties.[96] Determining the exact position and dispersion of the molecules can be difficult. When photoluminescent ligands are appended to single molecule magnets it may be possible to ascertain the exact positions and concentration of molecules.[96] Moreover, if the photoexcited state of the ligands couples directly with the magnetic moment of the single molecule magnet (below T_B) this may provide a tool for studying the fundamental quantum behaviour exhibited by SMMs.[96] As mentioned in the *Introduction* section of this thesis, porphyrins have been used as photoluminescent ligands since they have strong absorption and long lived excited states. However, they have yet to be appended to single molecule magnets. To this end, the goal of the second project was to confirm in the solid state the attachment of porphyrinic units to a tetrairon^{III} single molecule magnet **(1.4)**.

The tetrairon^{III} single molecule magnet of stoichiometry $[Fe_4(OMe)_6(dpm)_6]$ (**(1.4)**, Hdpm = dipivaloylmethane) has been studied for the past decade, Figure 3.1.[35] The cluster displays the remarkable ability to undergo an exchange of all six of the methoxide bridges within the core of the cluster, $[Fe_4(\mathbf{OMe})_6(dpm)_6]$. As previously stated in the *Introduction* section of this thesis the exchange was carried out with various derivatives of 2-(hydroxymethyl)propane-1,3-diol, $RC(CH_2OH)_3$. Therefore, two triol

ligands would replace six methoxide bridges within the cluster to form the resulting compounds of stoichiometry $[Fe_4(\mathbf{RC(CH_2O)_3})_2(dpm)_6]$ (R = CH_3, Ph, CH_2Br).[48] We proposed to exploit this selective replacement as a synthetic strategy to append porphyrin molecules to a tetrairon^{III} single molecule magnet. Therefore, the design of the porphyrin ligands must include a triol unit of stoichiometry $RC(CH_2OH)_3$ in order to facilitate the selective exchange.

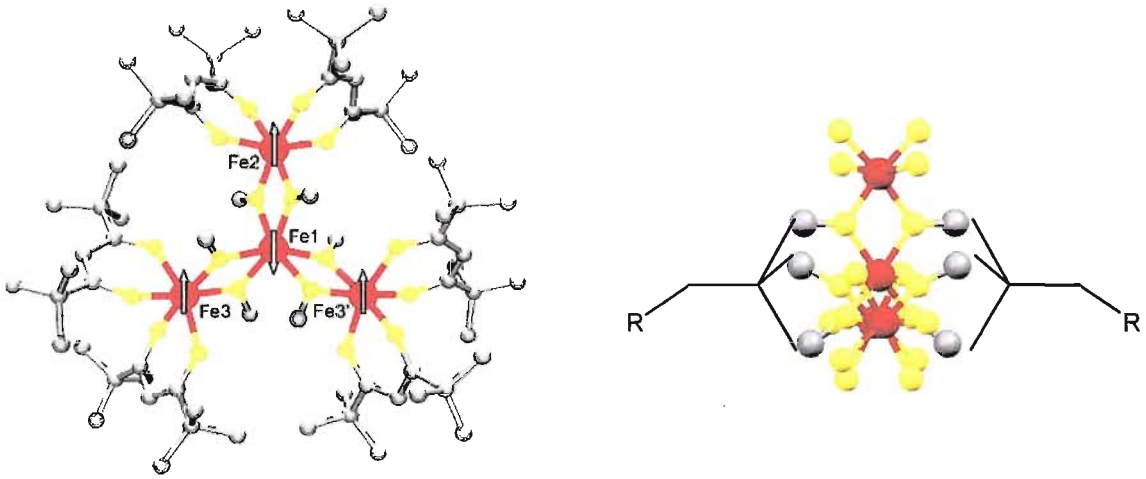

(1.4)

Figure 3.1: Molecular structure of the tetrairon^{III} single molecule magnet **(1.4)**. Reprinted with permission from reference 35. Copyright {1999} American Chemical Society. Representation of the exchanged tetrairon^{III} cluster. R = H for **(3.22b)**, Ph for **(3.23b)**, and Br **(3.7b)**. Note that the outer dpm ligands have been removed for clarity and the SMM has been rotated 90°. Adapted from reference 48. Copyright {2006} American Chemical Society.

In order to address these objectives, the first step of this research was to design, synthesize and characterize the triol appended porphyrin molecules which could then be exchanged for the methoxide bridges in the tetrairon^{III} single molecule magnet **(1.4)**. In this regard three porphyrin triol molecules were targeted, Figure 3.2. The first compound contained a *meso*-positioned triol **(3.1)** while the second and third porphyrin molecules had *axial*-positioned triol units, **(3.2)** and **(3.3)**. The second objective of the project was to

synthesis the tetrairon^{III} single molecule magnet **(1.4)** and to investigate the conditions for ligand exchange.[35,48] The final objectives were to exchange the porphyrin triol molecules with the methoxide bridges within the tetrairon^{III} single molecule magnet **(1.4)** and to characterize the molecular structures of these complexes **((3.4)-(3.6))** by X-ray crystallography, Figure 3.3.

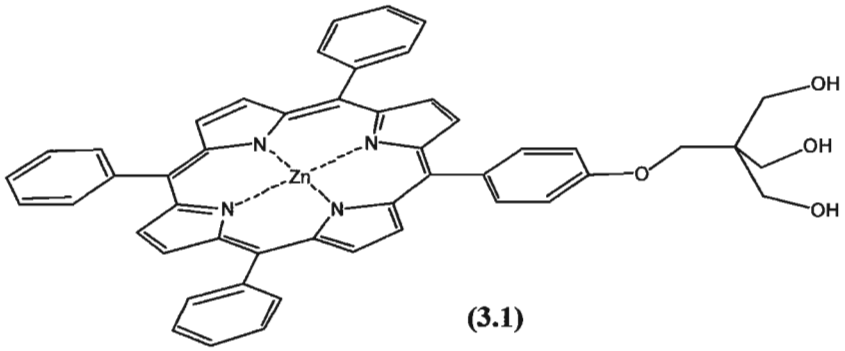

(3.1)

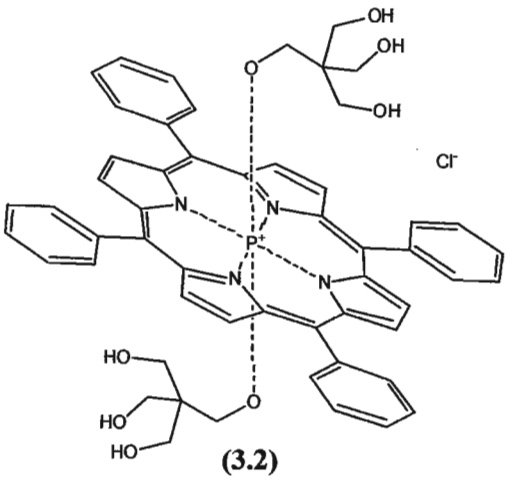

(3.2)

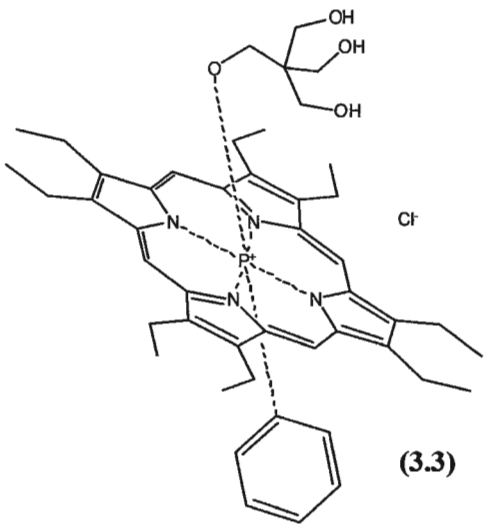

(3.3)

Figure 3.2: Porphyrin triol molecules: $[Zn(HPTPP\text{-}CH_2C(CH_2OH)_3)]$ **(3.1)**, $[P(TPP)(OCH_2C(CH_2OH)_3)_2]^+Cl^-$ **(3.2)**, and $[P(OEP)(C_6H_5)(OCH_2C(CH_2OH)_3)]^+Cl^-$ **(3.3)**.

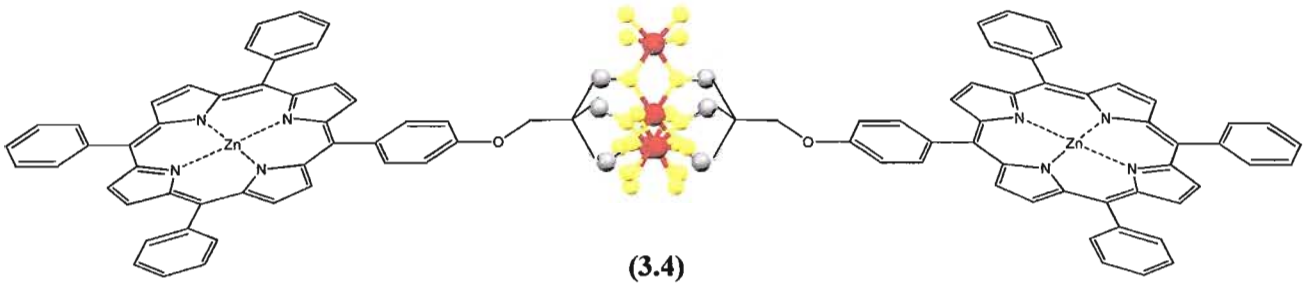

(3.4)

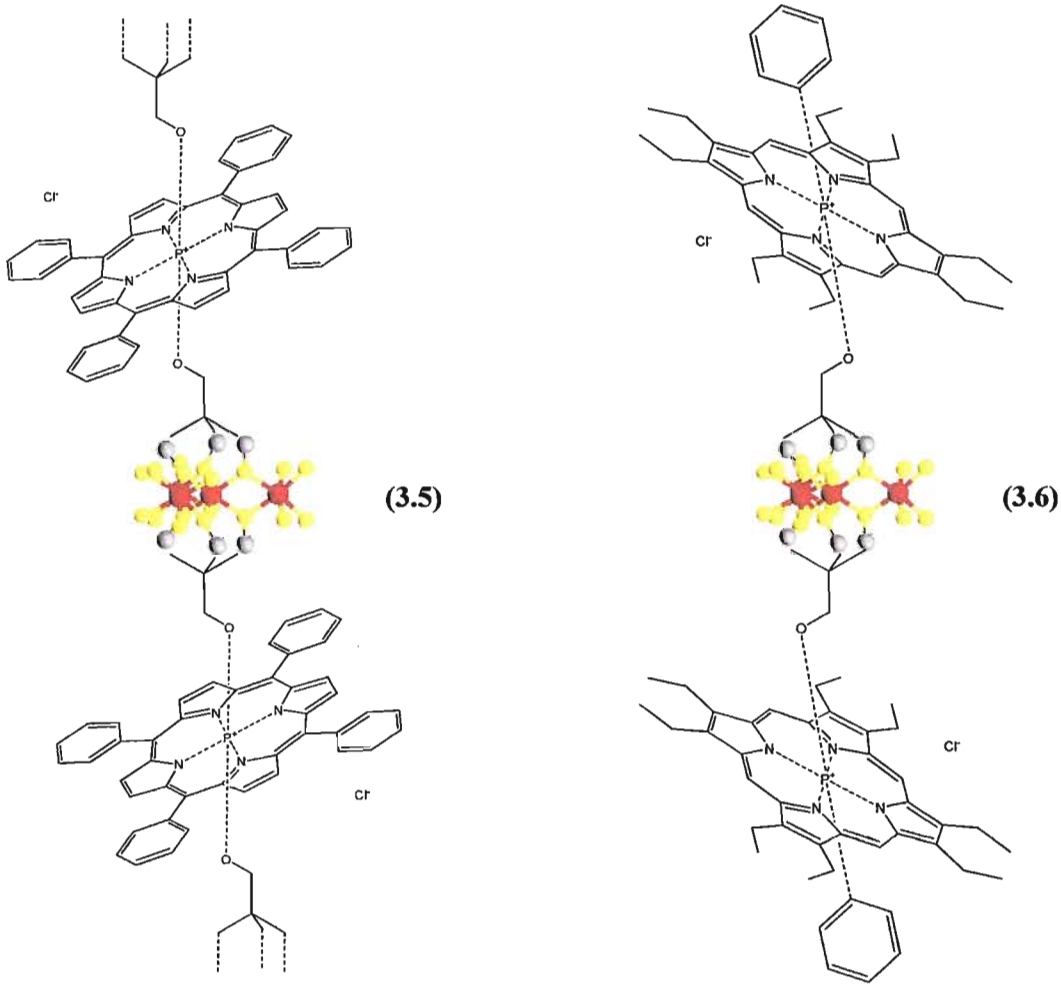

(3.5)

(3.6)

Figure 3.3: Molecular structures of the proposed target molecules for project 2. **(3.4)** contains two *meso*-coordinated zinc porphyrinic units appended to one tetrairon^{III} cluster. **(3.5)** contains an alternating chain of *axially*-coordinated phosphorus porphyrinic units and the tetrairon^{III} cluster. **(3.6)** contains two *axially*-coordinated phosphorus porphyrinic units to one tetrairon^{III} cluster.

3.2 – Design, Synthesis and Characterization of Porphyrin Triols: [Zn(HPTPP-$CH_2C(CH_2OH)_3$)] (3.1), $[P(TPP)(OCH_2C(CH_2OH)_3)_2]^+Cl^-$ (3.2), and $[P(OEP)(C_6H_5)(OCH_2C(CH_2OH)_3)]^+Cl^-$ (3.3)

3.2.1 Introduction

As mentioned in the *Introduction* section of this thesis, zinc and phosphorus are among the most common elements inserted into porphyrin macrocycles. Each element has a great effect on the electronic properties of the resulting porphyrin derivative. Zinc porphyrin units are electron donors.[105] For the porphyrin macrocycle, zinc is commonly reported as having a five coordinate square-pyramidal geometry.[105] The equatorial positions are chelated by the nitrogen atoms of the porphyrin macrocycle whereas one axial position is normally occupied by a solvent molecule.[105,133] Zinc porphyrins are among the most stable of the group 12 elements, however, complete demetallation can occur in the presence of dilute acid (0.01 N HCl).[105] Phosphorus is the smallest element to have been inserted into porphyrins and as a consequence the porphyrin structures are severely ruffled. Unlike the zinc porphyrins, phosphorus porphyrins are electron acceptors.[105] The phosphorus atom is commonly seen in an octahedral coordination geometry that is often distorted. Phosphorus also has a high affinity for oxygen and as such can form strong *axial* P-O bonds with various oxygen containing molecules.[134] Countless zinc and phosphorus porphyrins have been extensively studied in the chemical literature which further supports the use of such compounds in this thesis. They are known to have long lived excited states and have been studied for their electrochemical properties.[105]

The porphyrins used in this thesis are 5,10,15,20-tetraphenylporphyin (TPP), 5-

(hydroxyphenyl)-10,15,20-(triphenylporphyrin) (HPTPP) and 2,3,7,8,12,13,17,18-octaethylporphyrin (OEP), which are among the most commonly used porphyrin macrocycles in the chemical literature.

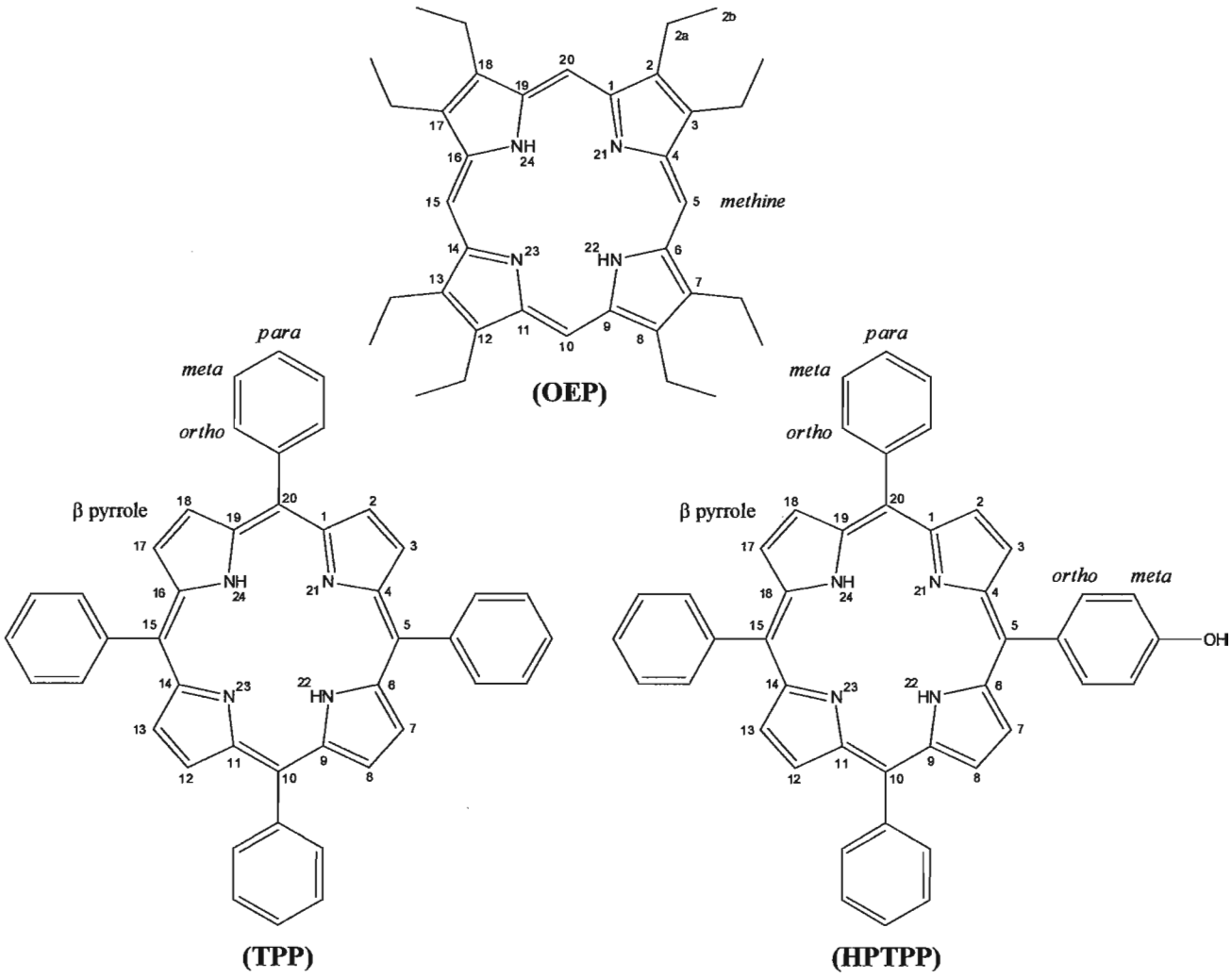

Figure 3.4: Molecular structures of 5,10,15,20-tetraphenylporphyin **(TPP)**, 5-(hydroxyphenyl)-10,15,20-(triphenylporphyrin) **(HPTPP)** and 2,3,7,8,12,13,17,18-octaethylporphyrin **(OEP)**.

TPP and OEP can accommodate a large variety of atoms in their central macrocyclic cavity which can potentially allow for *axial* coordinated ligands to the central atom. As such in this project phosphorus was inserted into TPP and OEP to allow for the formation of strong *axial* P-O bonds of pentaerythritol ($C(CH_2OH)_4$). The

chemical literature states that if a large excess of a diol or triol is used then only one oxygen atom of the molecule coordinates *axially* to the phosphorus centre.[135] Zinc insertion into TPP and OEP was disregarded as zinc does not readily form strong bonds with *axially* coordinated ligands. On the other hand, HPTPP was synthetically modified to introduce a *meso*-positioned triol. Zinc was inserted into HPTPP-$CH_2C(CH_2OH)_3$ to yield the [Zn(HPTPP-$CH_2C(CH_2OH)_3$)] **(3.1)** triol since zinc insertion into porphyrin molecules is more mild compared to phosphorus insertion. From a synthetic point of view it is highly unlikely that phosphorus could be inserted into the central cavity of the HPTPP-$CH_2C(CH_2OH)_3$ triol as the phosphorus would potentially coordinate to the triol instead of inserting into the cavity of the porphyrin macrocycle.

3.2.2 Porphyrin Triol [Zn(HPTPP-$CH_2C(CH_2OH)_3$)] (3.1)

The synthetic outline followed for the synthesis of the [Zn(HPTPP-$CH_2C(CH_2OH)_3$)] **(3.1)** triol is shown in scheme 3.2. The first step required the synthesis of 5-(hydroxyphenyl)-10,15,20-(triphenylporphyrin) (HPTPP). This was carried out via the Ruthemond procedure, Scheme 3.1.[136] This method yields a mixture of products, two of which are the desired TPP and HPTPP. The separation of the two porphyrins was carried out on basic alumina. TPP was eluted with chloroform (R_f = 0.88), while HPTPP was eluted with chloroform containing 5% methanol (R_f = 0.34). The structures of TPP and HPTPP were confirmed by ^{1}H-NMR, MS (FAB), and UV-Vis all matching literature data.[136] The overall yield of TPP was 5.1% and HPTPP was 3.3%. These yields are typical following this type of procedure as many by-products are formed during the course of the reaction which drastically decreases the isolated yield of the desired

products. Following the synthesis of HPTPP the attachment of the triol was targeted next.

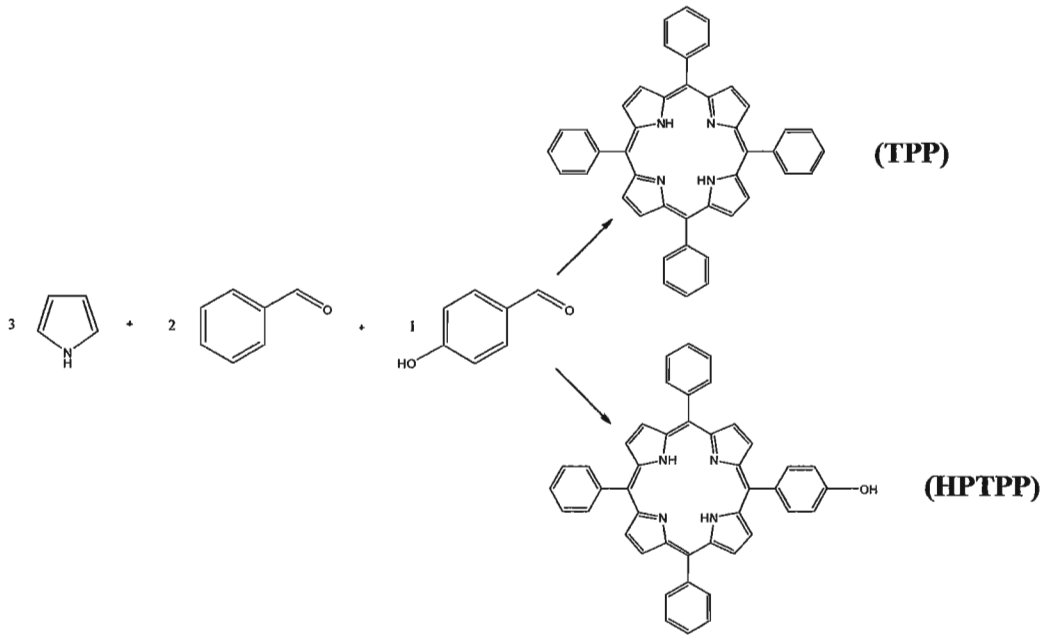

Scheme 3.1: Synthesis of TPP and HPTPP following a modified Ruthemond procedure.[136] Reagents and conditions: (i) propionic acid, 145 °C, 45 mins.[85]

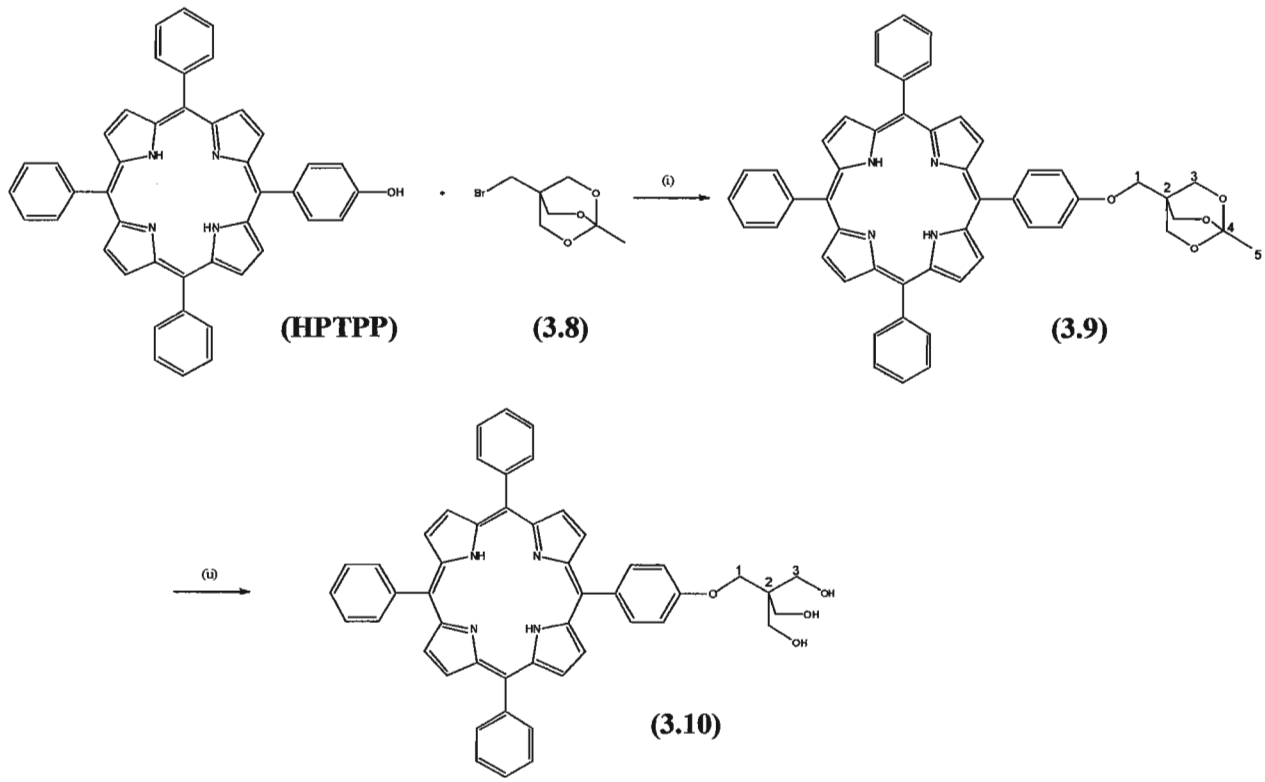

Scheme 3.2: Synthetic outline followed for the attachment of the triol to HPTPP. Reagents and conditions: (i) DMF, NaH, 70 °C, 24 hrs. (ii) a) 0.01N HCl, MeOH, reflux, 3 hrs. b) $NaHCO_3$, RT, 3 hr.

Attachment of the triol on HPTPP followed a modified literature procedure.[137] This required the synthesis of bromopentaerythritol **(3.7a)** from pentaerythritol followed by a protection reaction, Scheme 3.3,[138,139] and finally a tethering reaction to append the protected triol onto HPTPP, Scheme 3.2.

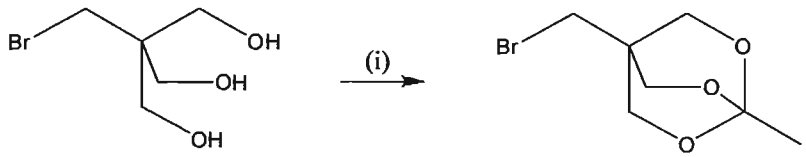

(3.7a) **(3.8)**

Scheme 3.3: Protection reaction of bromopentaerythritol. Reagents and conditions: (i) a) Toluene, triethyl orthoacetate, trace: p-toluenesulphonic acid, 90 °C, 12 hrs. b) 60 °C, sublimation.[139]

The protection of bromopentaerythritol **(3.7a)** used triethyl orthoacetate as the protecting unit, Scheme 3.3. Sublimation resulted in pure protected compound, 4-bromomethyl-1-methyl-2,6,7-trioxabicyclo[2.2.2]octane **(3.8)**. As stated in the literature bicyclic ortho esters not only simultaneously mask three triol groups but can be easily cleaved to regenerate the triol under mild conditions.[139]

The tethering reaction between HPTPP and 4-bromomethyl-1-methyl-2,6,7-trioxabicyclo[2.2.2]octane **(3.8)** was carried out in anhydrous DMF. NaH was added to react with the *meso*-hydroxyl group of HPTPP to yield the corresponding Na^+ salt which was used to react with the protected triol **(3.8)** resulting in compound **(3.9)**, Scheme 3.2. Purification of **(3.9)** was achieved via chromatography on basic alumina. Unreacted **(3.8)** was eluted with EtOAc:Hexane (1:9) (R_f = 0.42), compound **(3.9)** was then eluted with EtOAc:Hexane (9:1) (R_f = 0.49), whereas unreacted HPTPP remained at the origin. After purification compound **(3.9)** was isolated as purple solid in 75% yield. The molecular structure of **(3.9)** was confirmed by ^{1}H- and ^{13}C-NMR, MS (FAB), UV-Vis and CHN

data. The ^{1}H-NMR spectrum is shown in Figure 3.5 and is assigned as follows: 8.87 (m, 8H, β-H), 8.24 (d, 6H, J = 7.2 Hz, H_{ortho}), 8.15 (d, 2H, J = 7.2 Hz, H_{ortho}-OH), 7.78 (m, 9H, H_{meta}, H_{para}), 7.25 (d, 2H, J = 7.2 Hz, H_{meta}-OH), 4.34 (s, 6H, 3-H), 4.06 (s, 2H, 1-H), 1.57 (s, 3H, 5-H), -2.76 (s, 2H, N-H). The peaks at 4.34, 4.06, and 1.57 ppm confirm the attachment of the protected triol to the porphyrin macrocycle. The mass spectrometry data also displays a parent peak at m/z = 773. UV-Vis data displays a Soret band at λ = 419 nm. The Q-bands are observed at 516, 551, 591, and 646 nm. The CHN data is consistent with a stoichiometry of $[C_{51}H_{40}N_4O_4]$.

The cleavage of the bicyclic ortho ester of **(3.9)** took place in a mixture of methanol and water with the addition of 0.01 N HCl to allow for hydrolysis to the triol **(3.10)**. However, attempts to completely hydrolyze the bicyclic ortho ester failed. As evident by the ^{1}H-NMR, two hydroxyl groups were generated whereas the third remained protected, Figure 3.5. This same problem has been encountered in the literature where an acetate molecule is the remaining protecting group.[139] 4-bromomethyl-1-methyl-2,6,7-trioxabicyclo[2.2.2]octane **(3.8)** could in fact be cleaved to the diol and acetate group by the addition of MeOH and HCl. In the literature the addition of $NaHCO_3$ normally cleaves the acetate group, however, in these cases the R groups are simple alkyl chains.[139,140] The addition of $NaHCO_3$ to the **(3.11)** porphyrin compound did not cleave the acetate group as evident by the ^{1}H-NMR spectrum. NaOH or NaOMe was added in order to cleave the acetate group, however, this resulted in either no effect or cleavage of the ether linkage as evident by the reappearance of pentaerythritol units in the ^{1}H-NMR spectrum. Furthermore, continued heating had no effect on cleaving the acetate of **(3.11)**.

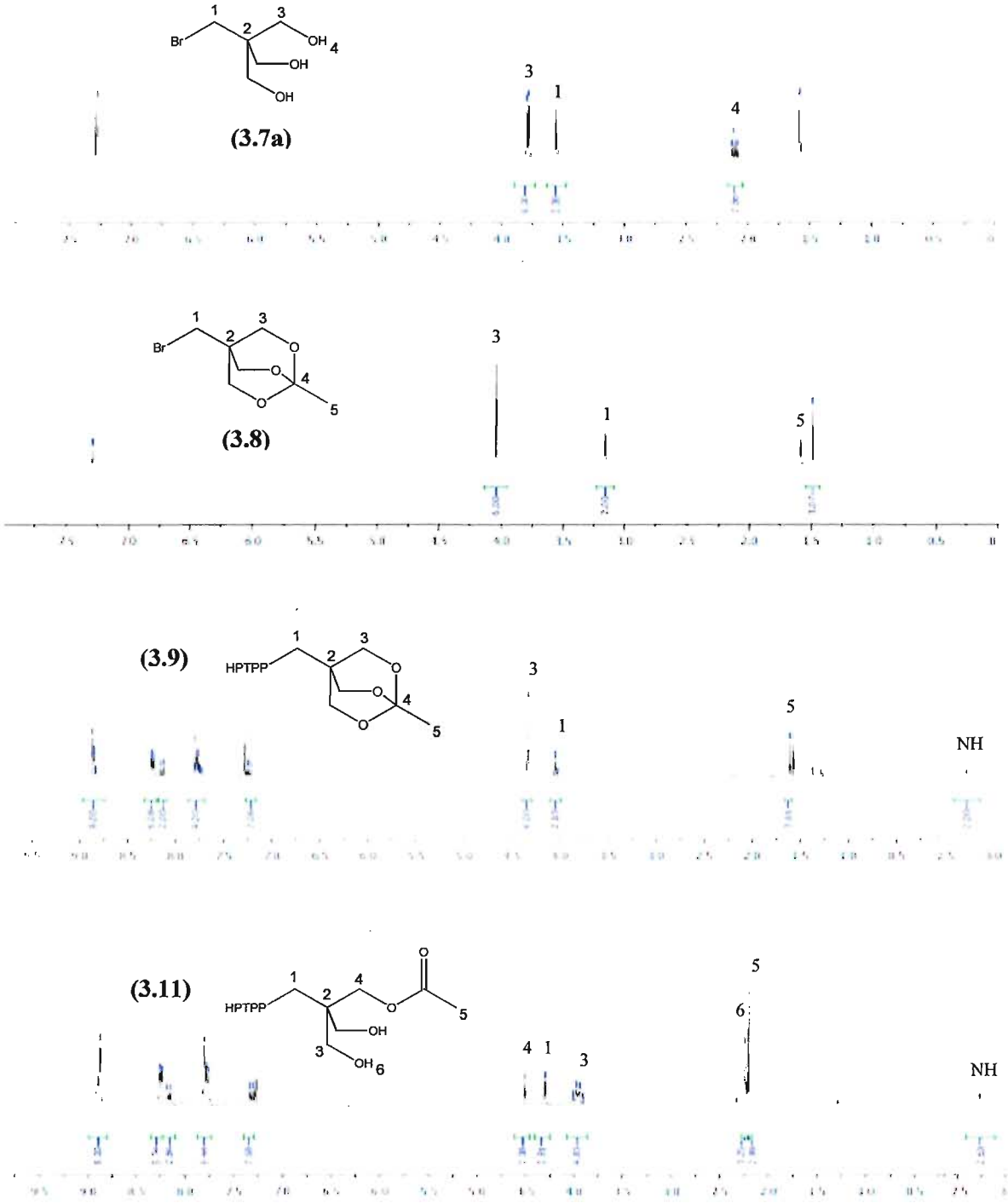

Figure 3.5: 300 MHz ^{1}H-NMR spectra of **(3.7a)**, **(3.8)**, **(3.9)** and **(3.11)**. The peaks corresponding to the bicyclic ortho ester and hydroxyl groups have been labeled accordingly.

During the course of this work the crystal structure of **(3.11)** was obtained. Suitable single crystals for X-ray diffraction were grown via the slow evaporation of the reaction mixture obtained during the deprotection of the bicyclic ortho ester protecting group. The molecular structure of **(3.11)** is shown in Figure 3.6. A disordered 2-propanal molecule has been removed by applying the SQUEEZE command in the SHELX-97 software.[151]

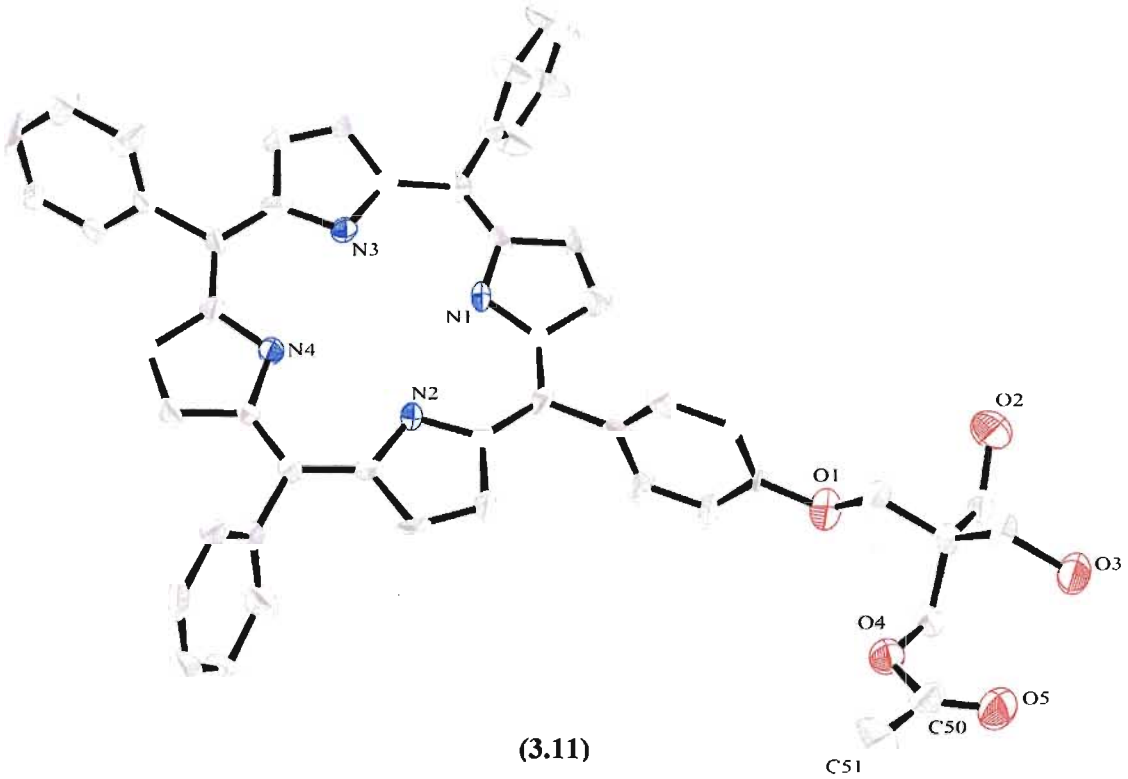

(3.11)

Figure 3.6: ORTEP[153] representation of the molecular structure of **(3.11)**. Thermal ellipsoids are plotted at 50% probability.

The molecular structure of **(3.11)** clearly shows the bound acetate unit at O4, while O2 and O3 are hydroxyl groups and have been deprotected. The ether linkage at O1 confirmed the attachment of the protected triol to the HPTPP porphyrin molecule. The porphyrin crystallizes in the triclinic P-1 space group. Porphyrins normally crystallize in

the triclinic P-1 space group because of stabilizing π-π interactions between neighbouring macrocycles.[105] There are two molecules in the unit cell related by an inversion centre shown as a red dot in the centre of the unit cell in Figure 3.7. The porphyrin macrocycles are separated by a distance of 4.05 Å relative to the pyrrole units of the porphyrin structure. A full list of all bond lengths and angles for complex **(3.11)** can be found in the *Appendix* section of the thesis, Tables 6.13 and 6.14.

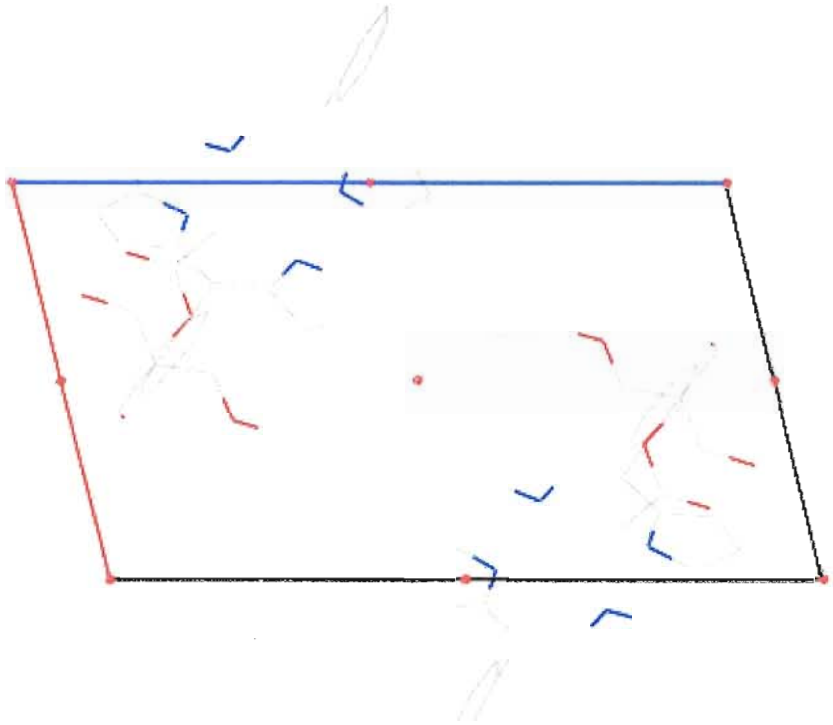

Figure 3.7: Mercury representation of **(3.11)** displaying the inversion centre.

In order to allow complete hydrolysis of the protected bicyclic ortho ester, triethyl orthoformate was used as the protecting ortho group, Scheme 3.4. According to the literature heating this bicyclic ortho ester in water under mild acidic conditions followed by carbonate addition allows for complete hydrolysis to the triol.[141] The cleavage still proceeds through a diol, however, the additional protecting group is a formate which is

more easily removed than an acetate.[141] The preparation of 4-bromomethyl-2,6,7-trioxabicyclo[2.2.2]octane **(3.12)** required higher temperatures and was less stable than the previous bicyclic ortho ester **(3.8)**. The conditions for the protection are outlined in Scheme 3.4.

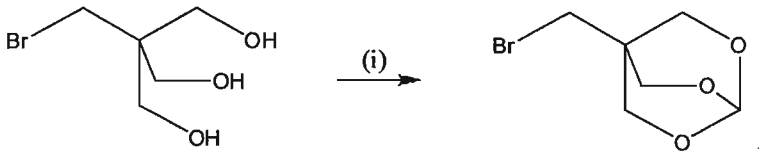

(3.7a) **(3.12)**

Scheme 3.4: Protection reaction of bromopentaerythritol. Reagents and conditions: (i) a) Dioctyl phthalate, triethyl orthoformate, trace: p-toluenesulphonic acid, 90 °C, 12 hrs. b) 120 °C, sublimation.[141]

The same procedure for the attachment of the previous bicyclic ortho ester **(3.9)** to HPTPP was used for the attachment of **(3.12)** to HPTPP, Scheme 3.5. The attachment of 4-bromomethyl-2,6,7-trioxabicyclo[2.2.2]octane **(3.12)** to HPTPP was achieved in relatively high yield (62%). Purification of **(3.13)** was achieved via chromatography on basic alumina. Unreacted **(3.12)** was eluted with EtOAc:Hexane (1:9) (R_f = 0.42), compound **(3.13)** was then eluted with EtOAc:Hexane (9:1) (R_f = 0.50), whereas unreacted HPTPP remained at the origin.

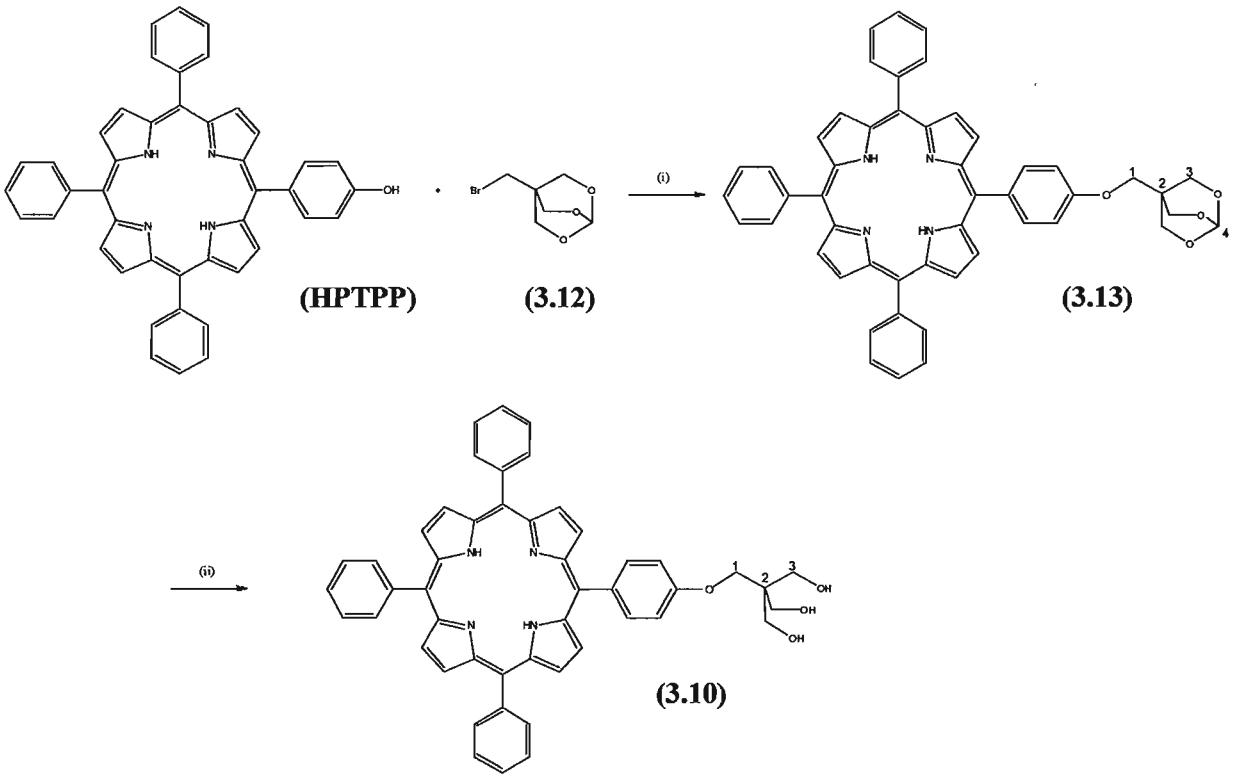

Scheme 3.5: Synthetic outline followed for the attachment of the triol to HPTPP. Reagents and conditions: (i) DMF, NaH, 70 °C, 24 hrs. (ii) a) 0.01N HCl, MeOH, reflux, 3 hrs. b) $NaHCO_3$, RT, 3 hr.

The cleavage of the bicyclic ortho ester to afford compound **(3.10)** was achieved in high yield (98%). The molecular structure of this compound was confirmed via ^{1}H- and ^{13}C-NMR, MS (FAB), IR, and CHN elemental analysis. The ^{1}H-NMR spectrum displayed a peak at 2.38 ppm assigned to the three hydrogen atoms of the triol. A singlet peak at 4.35 ppm was assigned to the hydrogen atoms of O-CH_2-C (1-H), while a doublet peak at 4.06 ppm was assigned to the hydrogen atoms of -CH_2-OH (3-H). MS data displays a peak at m/z = 748 for M^+. The IR spectrum displays a band at 3421 cm^{-1} for the O-H_{str} of the triol and a band at 3309 cm^{-1} which is consistent with the N-H_{str} of a porphyrin macrocycle. The CHN data was within ±0.4% for $C_{49}H_{40}N_4O_4$.

Once the HPTPP-$CH_2C(CH_2OH)_3$ triol **(3.10)** was synthesized and characterized

the insertion of zinc into the central cavity of the porphyrin macrocycle was targeted. Refluxing the porphyrin with a zinc acetate salt in DMF for 30 mins afforded the desired triol **(3.1)** with stoichiometry [Zn(HPTPP-$CH_2C(CH_2OH)_3$)], Figure 3.8.

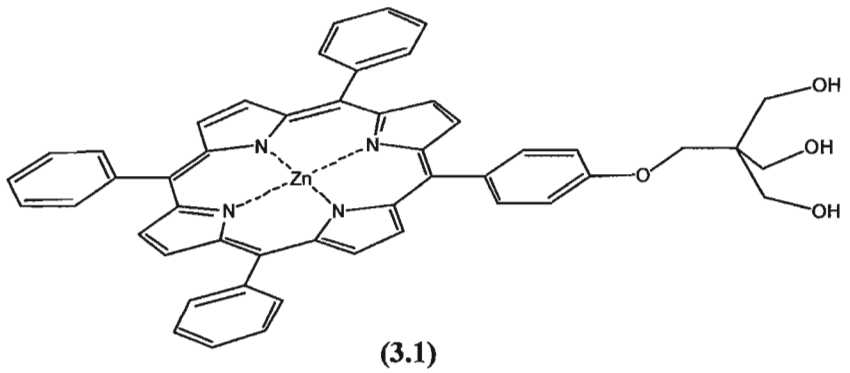

(3.1)

Figure 3.8: First porphyrin unit **(3.1)** prepared from the free base porphyrin **(3.10)**. The triol is located on the *meso*-position of the HPTPP sub unit.

The confirmation of zinc insertion into porphyrin **(3.10)** can clearly be seen by the comparison of the UV-Vis spectra of **(3.10)** and **(3.1)**, Figure 3.9. In this respect, the free base porphyrin **(3.10)** contains four Q-bands in the visible spectrum whereas the zinc porphyrin **(3.1)** contains only two. This is caused by the change in the electronic properties of the porphyrin associated with the insertion of zinc into the central cavity.[103] The ^{1}H-NMR spectra also displayed a loss of the signal for the N-H protons of the HPTPP macrocycle. The MS (FAB) spectrum shows a parent peak at m/z = 813. The IR spectrum of **(3.1)** also displays a band at 3415 cm^{-1} for the O-H_{str} of the triol while a band for an N-H_{str} is not observed. The CHN data is within ±0.4% for $C_{49}H_{38}N_4O_4Zn$.

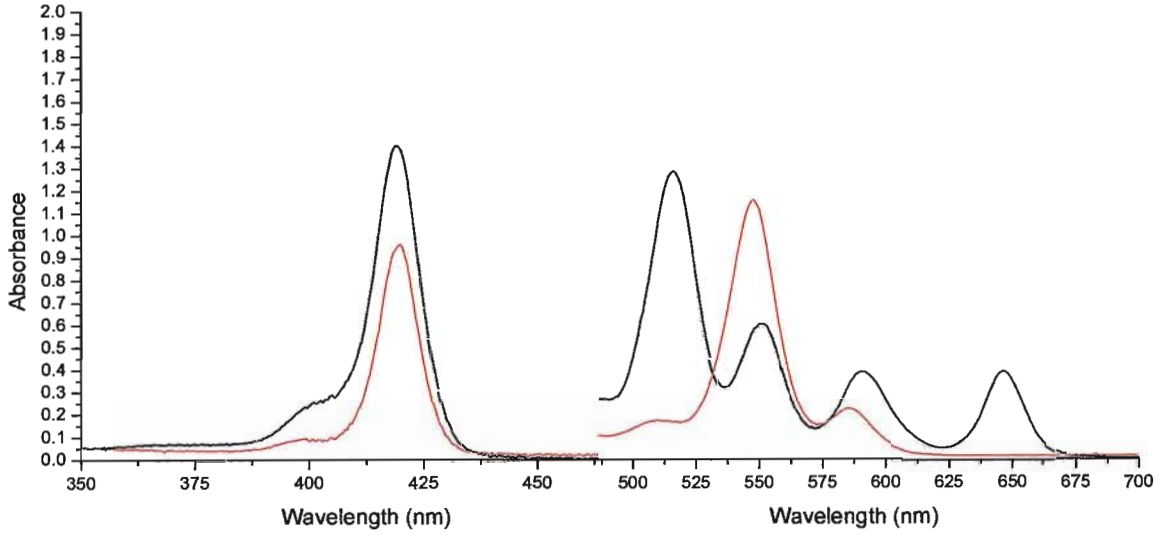

Figure 3.9: UV-Vis spectra of HPTPP-$CH_2C(CH_2OH)_3$ triol **(3.10)** (black line) and [Zn(HPTPP-$CH_2C(CH_2OH)_3$)] triol **(3.1)** (red line).

The next porphyrin complex targeted was $[P(TPP)(OCH_2C(CH_2OH)_3)_2]^+Cl^-$ **(3.2)**, Figure 3.10.

3.2.3 Porphyrin Triol $[P(TPP)(OCH_2C(CH_2OH)_3)_2]^+Cl^-$ (3.2)

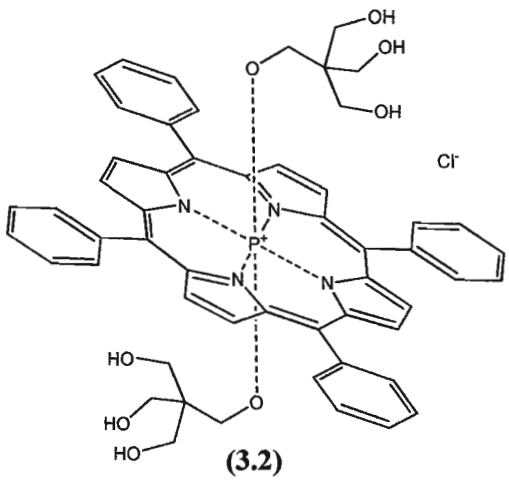

(3.2)

Figure 3.10: Molecular structure of $[P(TPP)(OCH_2C(CH_2OH)_3)_2]^+Cl^-$ **(3.2)**.

The synthetic outline followed to prepare $[P(TPP)(OCH_2C(CH_2OH)_3)_2]^+Cl^-$ **(3.2)** is shown in Scheme 3.6. The synthesis of TPP has previously been shown in Scheme 3.2.

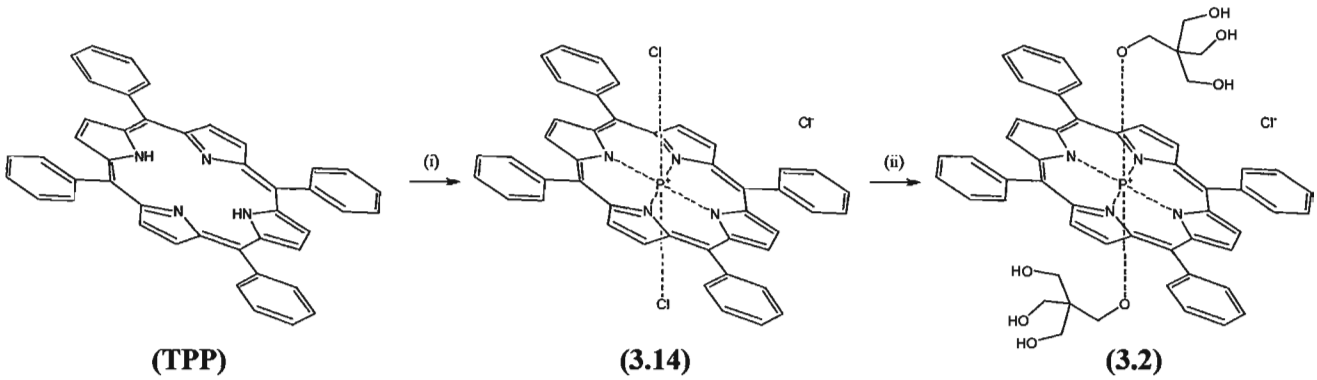

(TPP) **(3.14)** **(3.2)**

Scheme 3.6: Synthetic outline followed for the insertion of phosphorus into TPP and axial ligand exchange. Reagents and conditions: (i) pyridine, $POCl_3$, 125 °C, 24 hrs. (ii) pyridine, pentaerythritol, 125 °C, 48 hrs.

The insertion of phosphorus into a porphyrin requires specific reagents depending on the particular porphyrin type. P^{III} reagents (such as PCl_3) are not effective for phosphorus insertion into TPP, therefore $POCl_3$ was used in this thesis following literature methodology.[142] The insertion of phosphorus into TPP was carried out in refluxing pyridine with the addition of $POCl_3$. After reducing the mixture to dryness the resulting product $[P(TPP)Cl_2]^+Cl^-$ **(3.14)** was purified via column chromatography on neutral alumina. Unreacted TPP was eluted with DCM (R_f = 0.82). $[P(TPP)Cl_2]^+Cl^-$ **(3.14)** was eluted with DCM containing 5% methanol (R_f = 0.58). The overall yield of the intermediate $[P(TPP)Cl_2]^+Cl^-$ **(3.14)** was 12%. The structure of $[P(TPP)Cl_2]^+Cl^-$ **(3.14)** was confirmed by UV-Vis, ^{1}H-NMR, ^{31}P-NMR and MS (FAB) data. All data matched literature values for this compound.[142] The UV-Vis spectrum displayed peaks that were indicative of the P^V compound.[143] A comparison of the UV-Vis spectra of TPP and $[P(TPP)Cl_2]^+Cl^-$ **(3.14)** is shown in Figure 3.11. The ^{1}H-NMR spectrum displays a loss of

the signal from the NH protons of the macrocycle. The ^{31}P-NMR spectrum has a single peak at -229.0 ppm matching literature data for $[P(TPP)Cl_2]^+Cl^-$ **(3.14)**.[142]

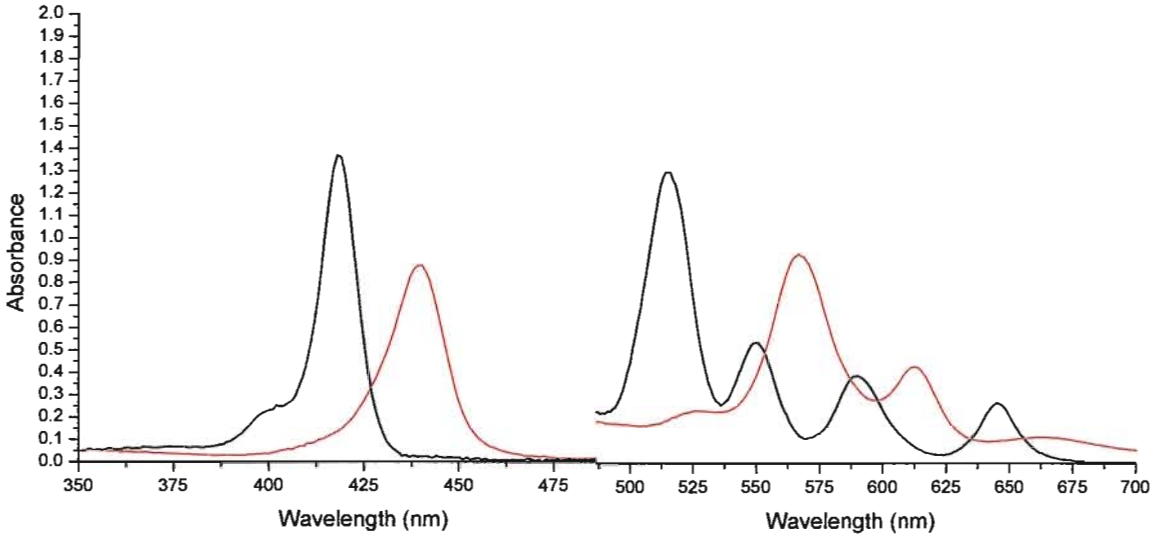

Figure 3.11: UV-Vis spectra of (TPP) (black line) and $[P(TPP)Cl_2]^+Cl^-$ **(3.14)** (red line).

The next step towards the synthesis of the desired porphyrin triol **(3.2)** was the exchange of the *axial* chloro ligands of $[P(TPP)Cl_2]^+Cl^-$ **(3.14)** with triol units. The reaction was carried out in refluxing pyridine with the addition of a large excess of pentaerythritol, $C(CH_2OH)_4$. The resulting slurry was refluxed for 2 days. The mixture was brought to dryness and the residue copiously washed with water, dried, extracted into anhydrous methanol, evaporated, and dried under vacuum to yield $[P(TPP)(OCH_2C(CH_2OH)_3)_2]^+Cl^-$ **(3.2)** (62%).

The exchange of the chloro ligands of **(3.14)** with pentaerythritol caused a shift of the protons attached to the pentaerythritol unit (-CH_2-, 3.62 ppm), Figure 3.12. The signal for the protons of the P-OCH_2- is shifted to -2.41 ppm. The signal for C-CH_2-OH protons is shifted to 1.07 ppm. These shifts occur because of the ring current effect associated with the π electrons of the porphyrin macrocycle.[135] The closer the proton is to the P-O

bond the further upfield the signal is shifted.[135] The ^{31}P-NMR spectra for **(3.2)** displayed a single peak for the central P atom at -177.0 ppm. This is indicative of an octahedral coordination geometry about the P atom.[143] MS (FAB) displayed a peak for the parent ion at *m/z* = 950 and a second fragmentation ion at *m/z* = 915 for [M^+-Cl]. A comparison of the UV-Vis spectra of $[P(TPP)Cl_2]^+Cl^-$ **(3.14)** and $[P(TPP)(OCH_2C(CH_2OH)_3)_2]^+Cl^-$ **(3.2)** is shown in Figure 3.13. The data does not indicate a large a shift of the peaks, however, it does indicate that the coordination about the P atom is symmetrical. The IR spectrum also displayed a band for the P-O_{str} at 819 cm^{-1} which is in the reported range for this type of bond.[143] Elemental analysis data for $[P(TPP)(OCH_2C(CH_2OH)_3)_2]^+Cl^-$ **(3.2)** was also within ± 0.4% for $C_{54}H_{50}N_4O_8PCl$.

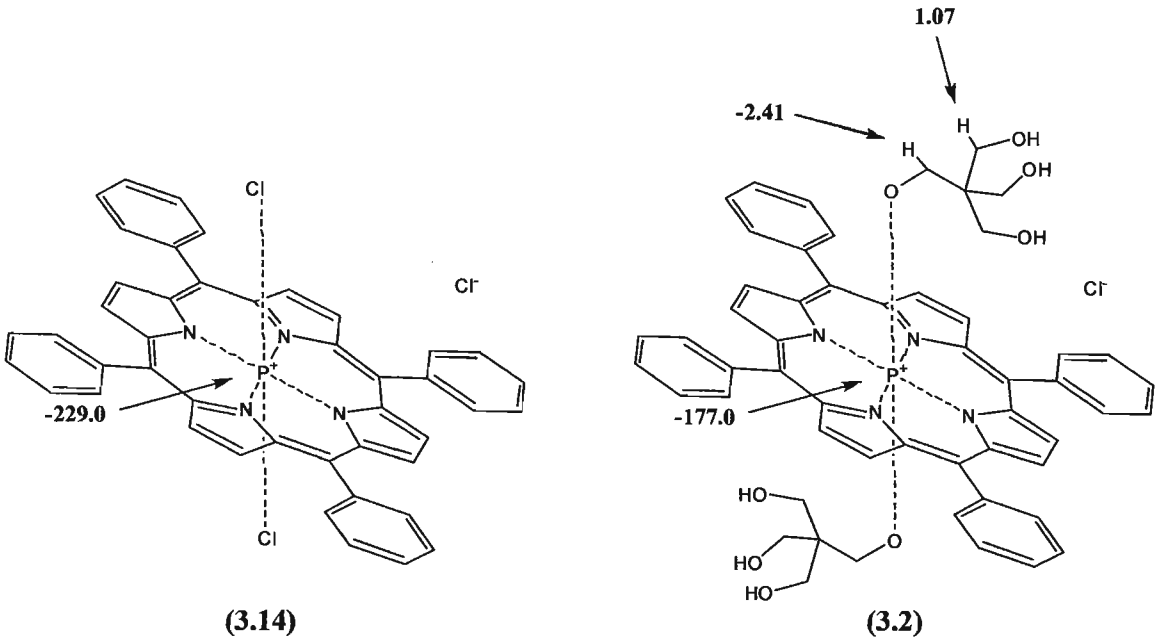

Figure 3.12: $[P(TPP)Cl_2]^+Cl^-$ **(3.14)** and $[P(TPP)(OCH_2C(CH_2OH)_3)_2]^+Cl^-$ **(3.2)** displaying the shifts of the central phosphorus and select hydrogen atoms. The large shift of the protons is because of the ring current effect of the porphyrinic unit.

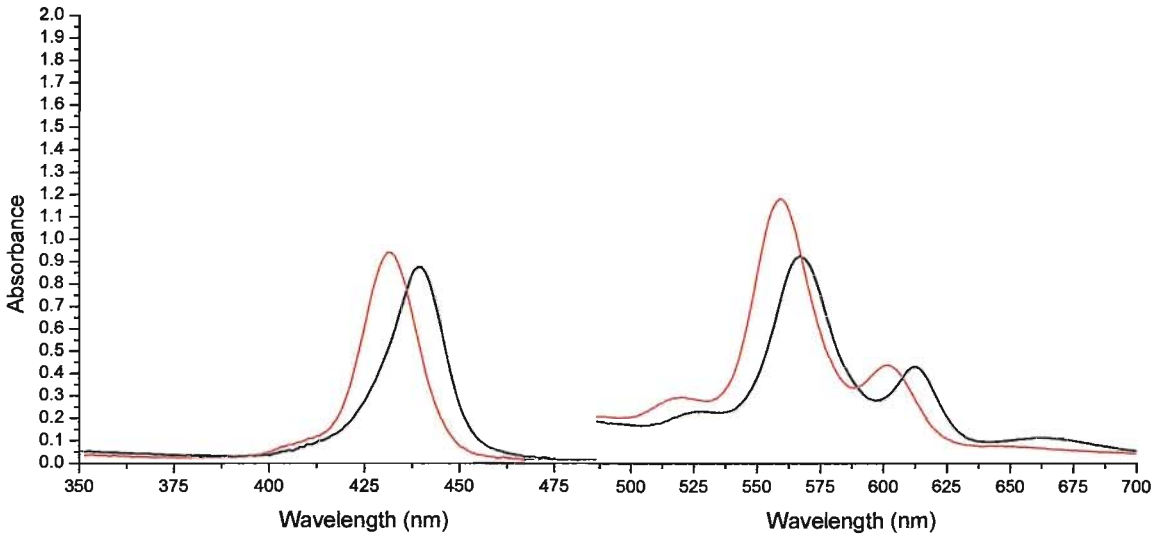

Figure 3.13: UV-Vis spectra of $[P(TPP)Cl_2]^+Cl^-$ **(3.14)** (black line) and $[P(TPP)(OCH_2C(CH_2OH)_3)_2]^+Cl^-$ **(3.2)** (red line).

The next porphyrin complex targeted was $[P(OEP)(C_6H_5)(OCH_2C(CH_2OH)_3)]^+Cl^-$ **(3.3)**, Figure 3.14.

3.2.4 Porphyrin Triol $[P(OEP)(C_6H_5)(OCH_2C(CH_2OH)_3)]^+Cl^-$ (3.3)

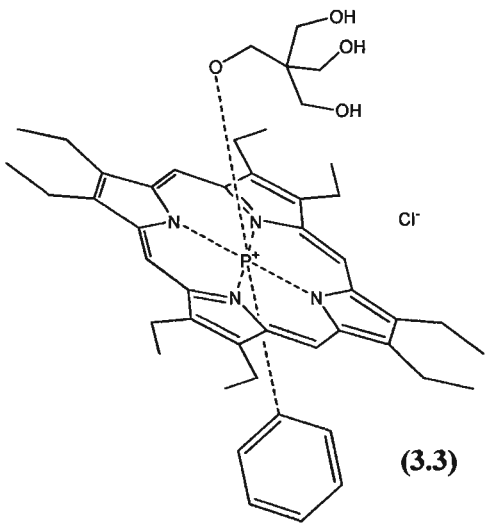

(3.3)

Figure 3.14: Molecular structure of $[P(OEP)(C_6H_5)(OCH_2C(CH_2OH)_3)]^+Cl^-$ **(3.3)**.

The synthetic route followed to prepare compound **(3.3)** is shown in Scheme 3.7.

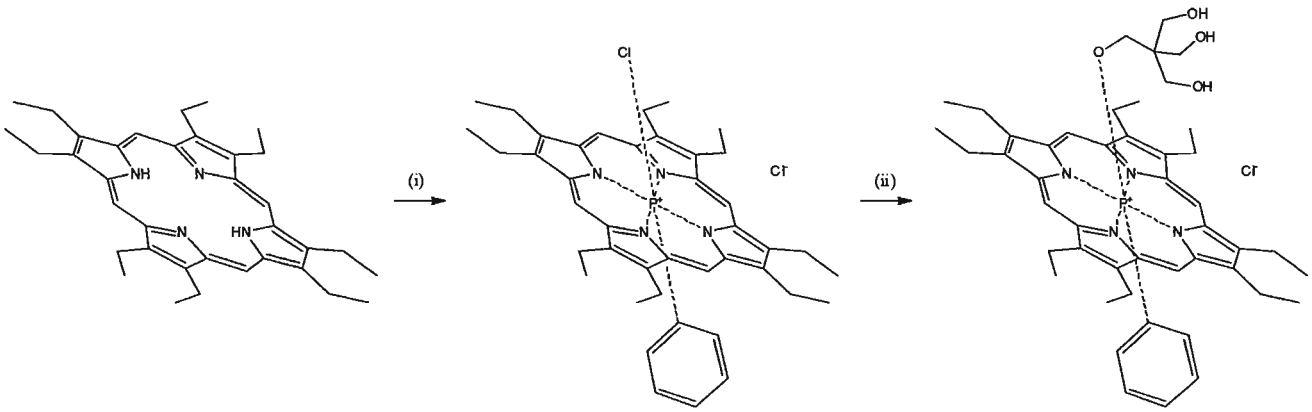

(OEP) **(3.15)** **(3.3)**

Scheme 3.7: Synthetic outline followed for the insertion of phosphorus into OEP and axial ligand exchange. Reagents and conditions: (i) DCM / 2,6-dimethylpyridine, $PhPCl_2$, 36 hrs. (ii) DCM, pentaerythritol, 25 °C, 2 hrs.

The synthesis of OEP was non-trivial and required multiple steps. OEP was synthesized following the synthetic strategy presented in Scheme 3.9. The overall yield of OEP was 10%, five percent below the best yield reported in the literature.[144]

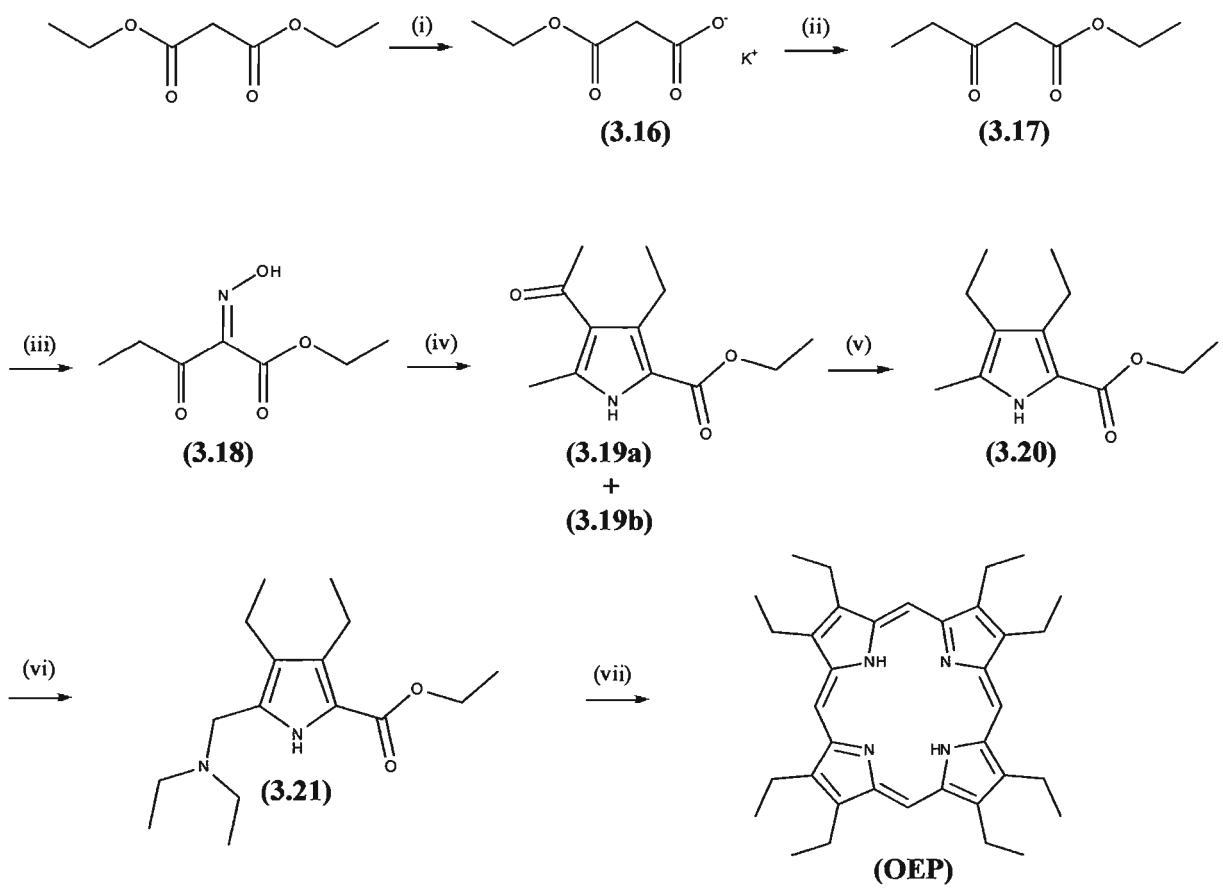

Scheme 3.8: Synthetic outline of **OEP**. Reagents and conditions: (i) EtOH, KOH, 24 hrs. (ii) a) EtOAc, Et_3N, $MgCl_2$, propionyl chloride, 12 hrs. b) 2 N HCl. (iii) sodium nitrite, H_2O. (iv) acetic acid, acetylacetone, zinc dust. (v) a) THF, $NaBH_4$, $BF_3{\cdot}Et_2O$, 10 °C, 1 hr. b) acetic acid, H_2O. (vi) a) Et_2O, Br_2, DCM, 20 mins. b) diethylamine, 30 mins, H_2O. (vii) a) 95% EtOH, KOH, H_2O, 100 °C, 3 hrs. b) H_2O, 0 °C, acetic acid, 100 °C, 1 hr, MeOH.

The first step of the synthesis of OEP required the conversion of diethyl malonate into its monopotassium salt **(3.16)**.[145] This was then converted into ethyl propionylacetate **(3.17)** via a magnesium enolate intermediate.[146] **(3.17)** was then converted into 4-acetyl-2-ethoxycarbonyl-3-ethyl-5-methylpyrrole **(3.19a)** through an oxime intermediate **(3.18)** via the Paal-Knorr pyrrole synthesis.[147] This procedure yielded a by-product, 2-ethoxycarbonyl-3,5-dimethylpyrrole **(3.19b)**, via the Fischer-Fink side reaction.[147] This impurity was removed by its conversion into 2-ethoxycarbonyl-4-

N,N-diethylaminomethyl-3,5-dimethylpyrrole **(3.19c)** which was then removed via acid extraction, Scheme 3.9.

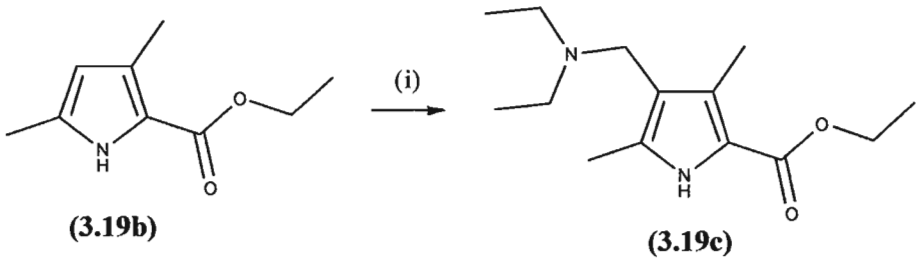

(3.19b) **(3.19c)**

Scheme 3.9: Conversion of 2-ethoxycarbonyl-3,5-dimethylpyrrole **(3.19b)** to 2-ethoxycarbonyl-4-*N,N*-diethylaminomethyl-3,5-dimethylpyrrole **(3.19c)**. Reagents and conditions: (i) diethylamine, 37% aqueous formaldehyde, conc. HCl, 100 °C, 12 hrs.

The reduction of **(3.19a)** to 2-ethoxycarbonyl-3,4-diethyl-5-methylpyrrole **(3.20)** was carried out via *in situ* diborane.[147] 5-*N,N*-diethylaminomethyl-2-ethoxycarbonyl-3,4-diethylpyrrole **(3.21)** was synthesized via the bromination of **(3.20)** which generated a sensitive α-bromomethylpyrrole which was not isolated, but immediately quenched with diethylamine.[144,147] Saponification of the ester function of **(3.21)** gave the labile carboxylate salt which was treated with acetic acid for conversion into 2,3,7,8,12,13,17,18-octaethylporphyrin (OEP).[144,147] OEP was isolated as a purple crystalline solid after washing with MeOH and drying under reduced pressure. NMR, MS (FAB), IR, and UV-Vis data all matched the literature values.[147,148] The next step in the synthesis of $[P(OEP)(C_6H_5)(OCH_2C(CH_2OH)_3)]^+Cl^-$ **(3.3)** required the insertion of phosphorus into the central cavity of OEP.

Phosphorus insertion into OEP is normally carried out with P^{III} reagents. OEP also has the ability to allow for unsymmetrical axial coordination, i.e. two different ligands can coordinate to the central P atom.[149] This can be achieved by the careful selection of the phosphorus reagent. Commercial availability of these particular P^{III}

reagents is limited and as such $PhPCl_2$ was used for phosphorus insertion in OEP. The insertion of phosphorus into OEP was carried out in a mixture of refluxing DCM and 2,6-dimethylpyridine (lutidine) with the addition of *P,P*-dichlorophenylphosphine ($PhPCl_2$).[149] The resulting compound, $[P(OEP)(C_6H_5)Cl]^+Cl^-$ **(3.15)** was not air stable in solution or in the solid state and as such was not purified. The ^{1}H-NMR and ^{31}P-NMR were obtained for this complex which matched literature data.[149] The ^{1}H-NMR spectrum displays a loss of the signal from the N-H protons of the macrocycle which indicates insertion of phosphorus has occurred. The ^{31}P-NMR spectrum displays a peak for the central P atom at -212.9 ppm which matches the literature data.[149] Care was taken not to expose $[P(OEP)(C_6H_5)Cl]^+Cl^-$ **(3.15)** to any moisture, otherwise it would convert into the hydroxide of formula $[P(OEP)(C_6H_5)OH]^+Cl^-$.

The next step towards the synthesis of the desired porphyrin triol **(3.3)** was the exchange of the *axial* chloro ligand of $[P(OEP)(C_6H_5)Cl]^+Cl^-$ **(3.15)** with a triol unit. The reaction was carried out in DCM with the addition of an excess of pentaerythritol. The resulting mixture was stirred at room temperature for 2 hrs. Removal of the solvent yielded the crude porphyrin as a purple solid. The residue was washed copiously with water, dried, and extracted into anhydrous methanol. Filtration followed by evaporation of the methanol solvent yielded the porphyrin triol **(3.3)**. Therefore, the chloro group in $[P(OEP)(C_6H_5)Cl]^+Cl^-$ **(3.15)** was exchanged for pentaerythritol $C(CH_2OH)_4$ to yield $[P(OEP)(C_6H_5)(OCH_2C(CH_2OH)_3)]^+Cl^-$ **(3.3)**.

The exchange of the chloro ligand of **(3.15)** with pentaerythritol caused a shift of the protons attached to the pentaerythritol unit (-CH_2-, 3.62 ppm), Figure 3.15. The signal for the protons of the P-OCH_2- is shifted to -2.90 ppm. The signal for C-CH_2-OH protons

is shifted to 0.09 ppm. These shifts occur because of the aforementioned ring current effect.[135] No signal is observed for the hydroxyl hydrogen atoms. The ^{31}P-NMR spectra for **(3.3)** displayed a single peak for the central P atom at -189.6 ppm, indicative of an octahedral environment of the P atom. MS (FAB) displayed a fragmentation ion at *m/z* = 777 for $[M^+\text{-Cl}]$. A comparison of the UV-Vis spectra of OEP and $[P(OEP)(C_6H_5)(OCH_2C(CH_2OH)_3)]^+Cl^-$ **(3.3)** is shown in Figure 3.16. The data displays two peaks for the Q-bands of $[P(OEP)(C_6H_5)(OCH_2C(CH_2OH)_3)]^+Cl^-$ **(3.3)**, while free-base OEP has four bands. The ratio of the two Q-bands in the $[P(OEP)(C_6H_5)(OCH_2C(CH_2OH)_3)]^+Cl^-$ **(3.3)** indicates a stable coordination about the P atom. The IR spectrum of $[P(OEP)(C_6H_5)(OCH_2C(CH_2OH)_3)]^+Cl^-$ **(3.3)** displayed a band at 800 cm^{-1} for the $P\text{-}O_{str}$. The CHN data is consistent with stoichiometry $[C_{47}H_{60}N_4O_4P]^+Cl^-$.

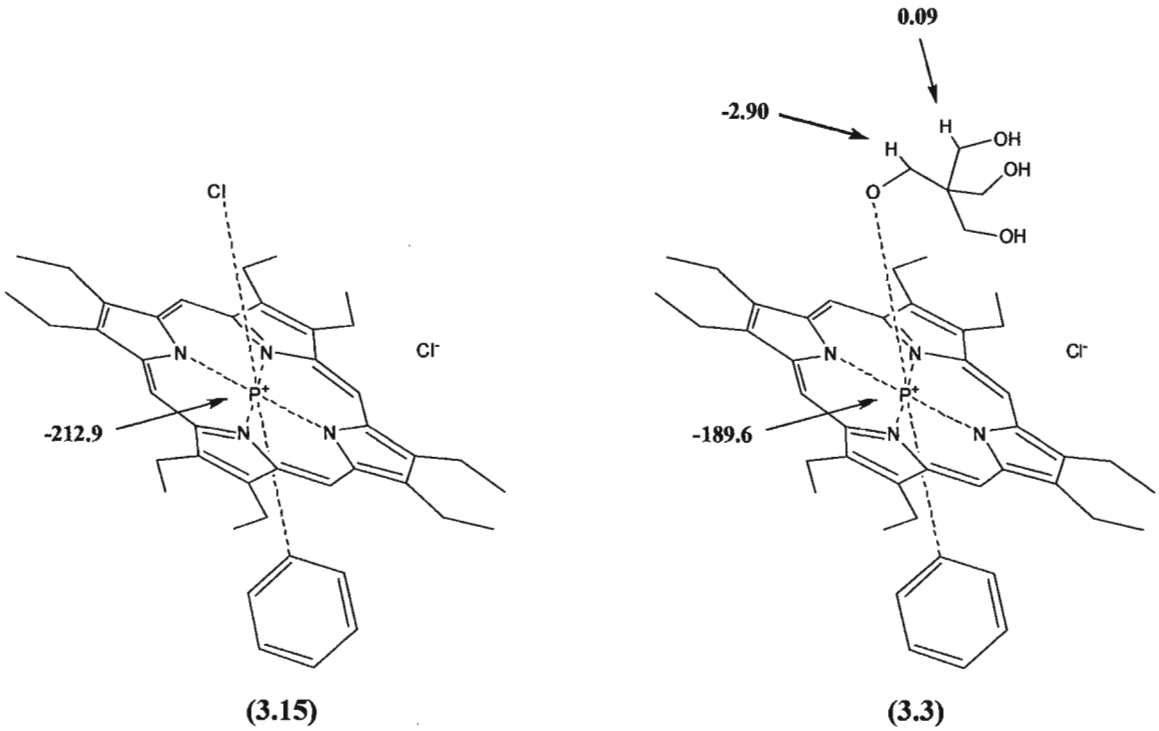

(3.15) **(3.3)**

Figure 3.15: $[P(OEP)(C_6H_5)Cl]^+Cl^-$ **(3.15)** and $[P(OEP)(C_6H_5)(OCH_2C(CH_2OH)_3)]^+Cl^-$ **(3.3)** displaying the shifts of the central phosphorus and select hydrogen atoms. The large shift of the protons is because of the ring current effect of the porphyrinic unit.

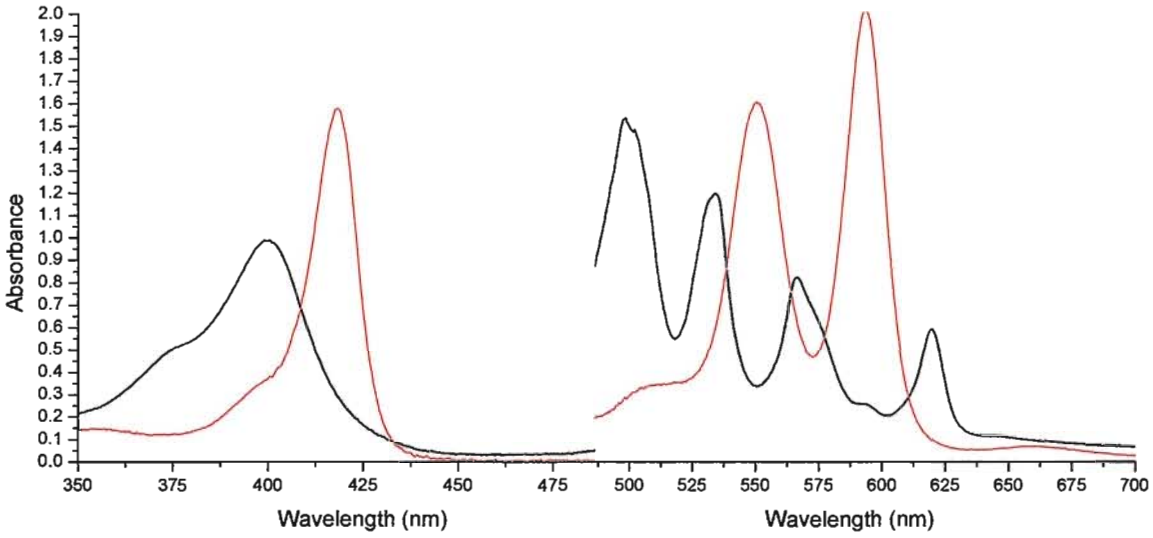

Figure 3.16: UV-Vis spectra of OEP (black line) and $[P(OEP)(C_6H_5)(OCH_2C(CH_2OH)_3)]^+Cl^-$ **(3.3)** (red line).

After the porphyrin triols **(3.1)**, **(3.2)**, and **(3.3)** had been synthesized and characterized the exchange of the methoxide bridges within the tetrairon^{III} single molecule magnet **(1.4)** was targeted. This required the preparation of the $[Fe_4(\mathbf{OMe})_6(dpm)_6]$ cluster as well as the preparation of the previously reported derivatives of stoichiometry $[Fe_4(\mathbf{RC(CH_2O)_3})_2(dpm)_6]$ (R = CH_3, Ph, CH_2Br). The derivatives were prepared in order to test the ease of exchangeability as well as to determine the optimum experimental conditions required for the ligand exchange.

3.3 – Synthesis of the Tetrairon^{III} Cluster and Derivatives

As mentioned, the next step in the project required the synthesis of the tetrairon^{III} cluster $[Fe_4(OMe)_6(dpm)_6]$ **((1.4)**, Hdpm = dipivaloylmethane) commonly known as a ferric star, Figure 3.17.[35] The cluster was synthesized via the reaction of anhydrous $FeCl_3$ with Hdpm and NaOMe in a mixture of anhydrous methanol and diethyl ether. A

dimeric intermediate was isolated as reported in the literature.[48] This dimer was reacted with additional NaOMe and $FeCl_3$ to form the tetrairon^{III} cluster. Crystals suitable for X-ray diffraction were grown either by the slow evaporation of the reaction mixture or the slow vapour diffusion of methanol into the reaction mixture. The molecular structure of **(1.4)** was confirmed via single crystal X-ray diffraction and CHN microanalysis, which matched the literature data.[48]

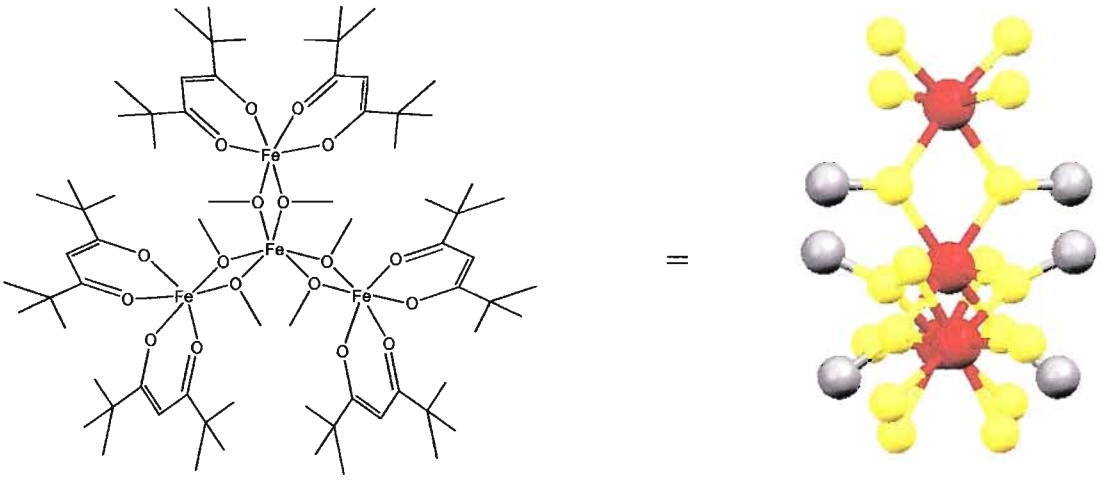

(1.4) (b)

Figure 3.17: Molecular structure of the tetrairon^{III} cluster **(1.4)**. b) A side view of the cluster displaying the methoxide units (the outer dpm units have been omitted for clarity). Note that yellow = oxygen, red = iron, and grey = carbon. Adapted from reference 35. Copyright {1999} American Chemical Society.

The exchange of the triol ligands **(3.22a)**, **(3.23a)**, and **(3.7a)** with the methoxide bridges of the tetrairon^{III} cluster was repeated in order to test how reproducible this process was, Figure 3.18.[48]

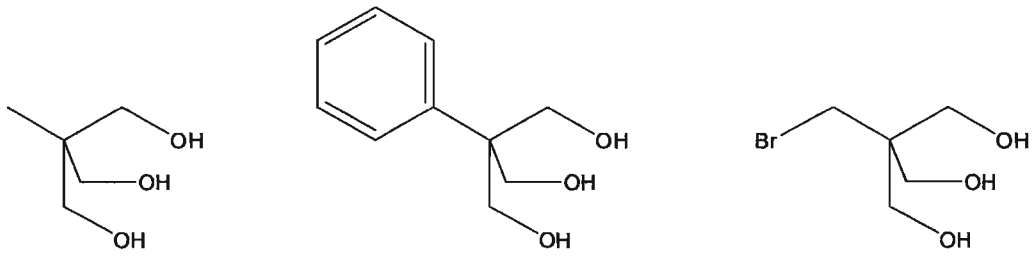

(3.22a) **(3.23a)** **(3.7a)**

Figure 3.18: Triol ligands exchanged with the methoxide bridges in the tetrairon^{III} cluster.

Ligand **(3.22a)** was commercially available from Aldrich whereas ligands **(3.23a)** and **(3.7a)** had to be synthesized. The synthetic procedure followed for the preparation of ligand **(3.23a)** is shown in Scheme 3.10.[150] It required reacting phenylacetaldehyde with paraformaldehyde in THF in the presence of $Ca(OH)_2$. After four days the crude product was isolated via filtration as a very viscous slightly yellow oil. Upon sitting in anhydrous diethyl ether the pure product precipitated as a white powder which was isolated via filtration. ^{1}H-NMR data of the isolated product matched the literature data.[150] 2-(bromomethyl)-2-(hydroxymethyl)-1,3-propanediol, [bromopentaerythritol] **(3.7a)** was prepared from pentaerythritol following the literature procedure, Scheme 3.11.[138] The product was isolated as a white powder in 30% yield. ^{1}H- and ^{13}C-NMR data matched the literature values for this compound.[138]

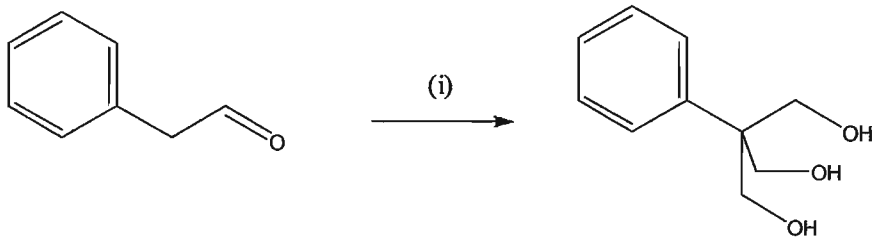

(3.23a)

Scheme 3.10: Synthetic procedure for the preparation of ligand (**3.23a**). Reagents and conditions: (i) THF, paraformaldehyde, $Ca(OH)_2$, 60 °C, 4 d.[150]

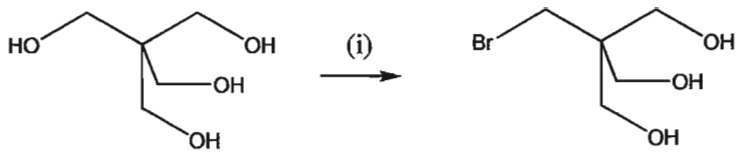

(3.7a)

Scheme 3.11: Synthetic procedure for the preparation of 2-(bromomethyl)-2-(hydroxymethyl)-1,3-propanediol, [bromopentaerythritol] **(3.7a)**. Reagents and conditions: (i) acetic acid, hydrobromic acid, reflux.

Once ligands **(3.22a)**, **(3.23a)**, and **(3.7a)** were obtained the exchange of these ligands for the methoxide bridges in the tetrairon^{III} cluster was carried out. All of the exchange reactions were carried out via the addition of the ligand to an anhydrous diethyl ether solution of the cluster.[48] The ratio of tetrairon^{III} cluster to triol ligand was 1:2 in each experiment. Crystallizations were carried out at room temperature by either the slow diffusion of methanol directly into the reaction mixture or via the slow evaporation of the diethyl ether from the reaction mixtures.[48] Both procedures yielded single crystals suitable for X-ray diffraction. Suitable single crystals of the tetrairon^{III} triol derivative **(3.7b)** were not obtained during the course of these studies. However, the CHN data for the resulting product was indicative of ligand exchange.

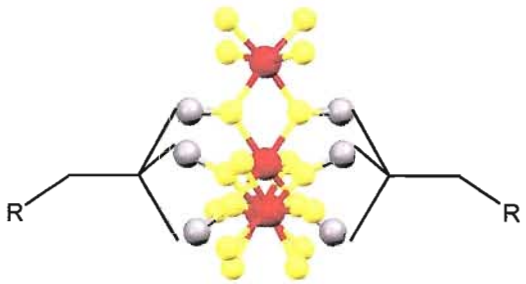

Figure 3.19: Representation of the exchanged tetrairon^{III} cluster derivatives. R = H for **(3.22b)**, Ph for **(3.23b)**, and Br **(3.7b)**. Adapted from reference 48. Copyright {2006} American Chemical Society.

Yields of the crystallized clusters were in the range of 76 to 78%. The unit cell of each exchanged complex was measured and found to match literature data, Table 3.1.[48] The CHN data was also in agreement, Table 3.1.[35,48]

Table 3.1: Summary of the CHN elemental analysis and crystallographic data obtained for compounds **(1.4)**, **(3.22b)**, **(3.23b)**, and **(3.7b)**.

Compound	CHN	Unit Cell	
(1.4)	$C_{72}H_{132}Fe_4O_{18}$·MeOH calc: C 56.89%, H 8.89% found: C 56.49%, H 8.89%	*a = 29.217 Å, α = 90° *b = 15.996 Å, β = 94.965° *c = 18.244 Å, γ = 90°	a = 29.220 Å, α = 90° b = 16.011 Å, β = 94.645° c = 18.221 Å, γ = 90°
(3.22b)	$C_{76}H_{132}Fe_4O_{18}$ calc: C 58.62%, H 8.54% found: C 58.69%, H 8.19%	*a = 16.189 Å, α = 90° *b = 16.189 Å, β = 90° *c = 56.712 Å, γ = 120°	a = 16.210 Å, α = 90° b = 16.210 Å, β = 90° c = 56.370 Å, γ = 120°
(3.23b)	N/A	*a = 16.289 Å, α = 90° *b = 16.289 Å, β = 90° *c = 54.712 Å, γ = 120°	a = 16.275 Å, α = 90° b = 16.275 Å, β = 90° c = 54.700 Å, γ = 120°
(3.7b)	$C_{76}H_{130}Fe_4O_{18}Br_2$ calc: C 53.22%, H 7.64% found: C 53.10%, H 7.82%	N/A	

*literature data from reference 48.

The exchangeability of the triol ligands for the methoxide bridges in the tetrairon^{III} cluster was found to occur rather easily in the previous examples, resulting in high yields of the exchanged tetrairon^{III} derivatives **(3.22b)**, **(3.23b)**, and **(3.7b)**. It should be noted that the success of this approach is reliant on being able to obtain single crystals of the final products directly from the reaction mixtures.

The final step of this research was to exchange the synthesized porphyrin triol molecules **(3.1)**, **(3.2)**, and **(3.3)** with the methoxide bridges of the tetrairon^{III} single molecule magnet.

3.4 – Target Complexes for Project 2

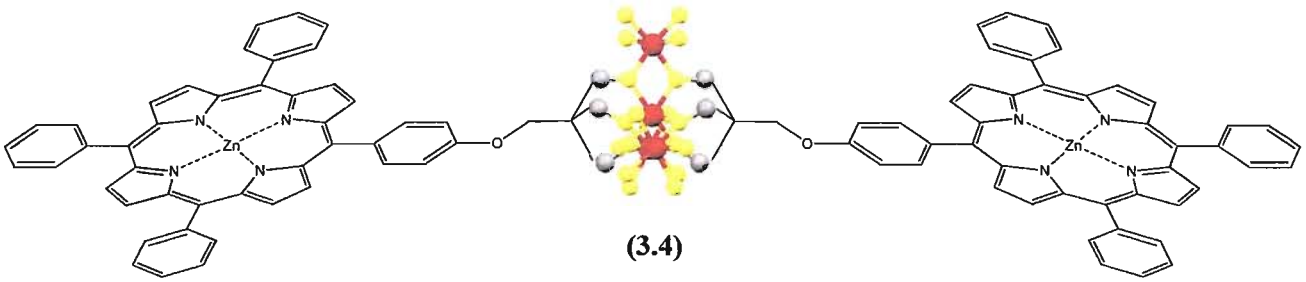

(3.4)

Figure 3.20: The **(3.4)** target contains two *meso*-coordinated zinc porphyrinic units to one tetrairon^{III} cluster.

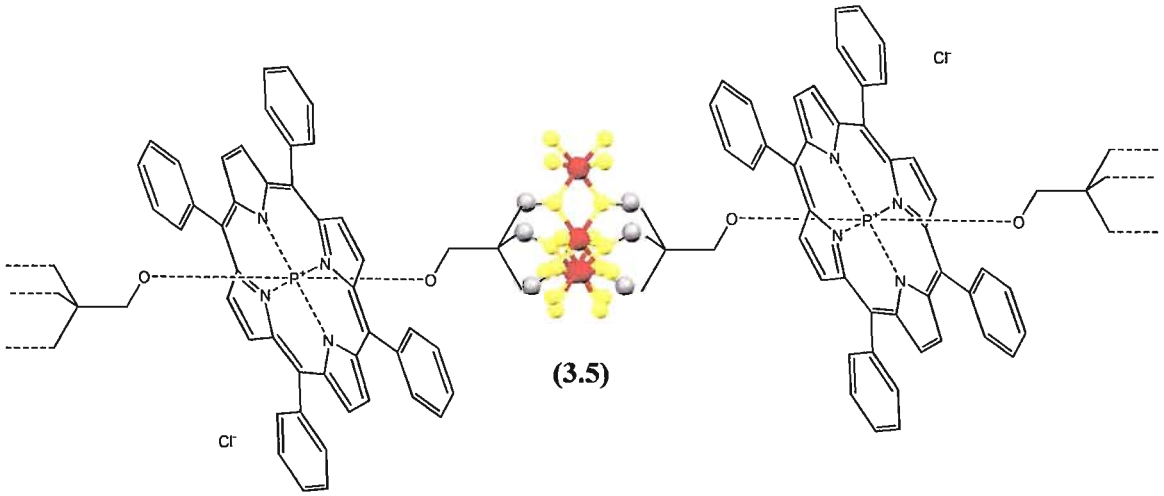

(3.5)

Figure 3.21: The **(3.5)** target contains an alternating chain of *axial*-coordinated phosphorus porphyrinic units **(3.2)** and the tetrairon^{III} cluster.

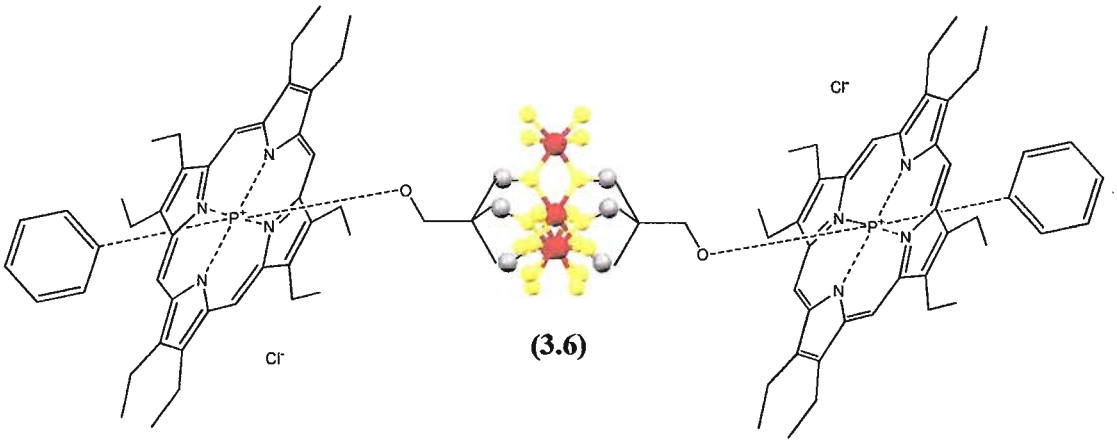

(3.6)

Figure 3.22: The **(3.6)** target contains two *axial*-coordinated phosphorus porphyrinic units **(3.3)** to one tetrairon^{III} cluster.

The first target **(3.4)** sought to append two porphyrin triol molecules of **(3.1)** to one tetrairon^{III} cluster **(1.4)**, Figure 3.20. The ratio of cluster:porphyrin is thus 1:2. The exchange reaction was carried out in a mixture of anhydrous diethyl ether and methanol. The addition of methanol was required since the porphyrin triol **(3.1)** was not very soluble in diethyl ether. The mixture was stirred at room temperature for one day. The growth of suitable single crystals for X-ray diffraction was targeted and various crystallization experiments were carried out. Unfortunately, to-date no single crystals of this compound have been obtained.

The next target **(3.5)** required the reaction of porphyrin **(3.2)** with the tetrairon^{III} cluster **(1.4)**, Figure 3.21. The ratio of cluster:porphyrin is thus 1:1 which could allow for the formation of a chain-like structure of alternating units of porphyrin and cluster. The exchange reaction was carried out in a mixture of anhydrous diethyl ether and methanol. The addition of methanol was required to dissolve the porphyrin triol **(3.2)** since it had limited solubility in diethyl ether. The mixture was stirred at room temperature for one day and various attempts to grow suitable single crystals of any products have been unsuccessful to-date.

The final target **(3.6)** required the reaction of porphyrin **(3.3)** with the tetrairon^{III} cluster **(1.4)**, Figure 3.22. The ratio of cluster:porphyrin of this experiment is thus 1:2. The exchange reaction was carried out once again in a mixture of anhydrous diethyl ether and methanol because of the porphyrin triol solubility. The mixture was stirred at room temperature for one day. The growth of suitable single crystals for X-ray diffraction was targeted and as such various crystallization experiments were carried out. Unfortunately, to-date this compound has not crystallized.

Each of the aforementioned exchange reactions were repeated with the substitution of acetone for methanol. These experiments did not yield suitable single crystals for X-ray diffraction.

During the course of this work an alternative approach for the preparation of **(3.4)** was used. The tetrairon^{III} cluster derivative **(3.7b)** $[Fe_4(RC(CH_2O)_3)_2(dpm)_6]$ (R = CH_2Br) was reacted together with ZnHPTPP **(3.24)**, Figure 3.23. The use of KOH was used to facilitate the deprotonation of the hydroxyl functionality which would exchange with the Br of **(3.24)** which could append the porphyrin to the single molecule magnet. Slow evaporation of the reaction mixture resulted in a thick purple residue that contained small purple crystals. The crystals were not well formed, but nevertheless were suitable for X-ray diffraction. The molecular structure of the isolated compound is shown in Figure 3.24. The molecular structure reveals that the isolated compound is the HPTPP porphyrin macrocycle with a coordinated zinc metal ion in the central cavity. The zinc ion also has an *axially* bound oxetane structure with a Zn-O distance of 2.171 Å. This resulting structure may have resulted via the degradation of the cluster and thus rearrangement of the bromopentaerythritol could occur. This rearranged compound would have then coordinated to the zinc of HPTPP.

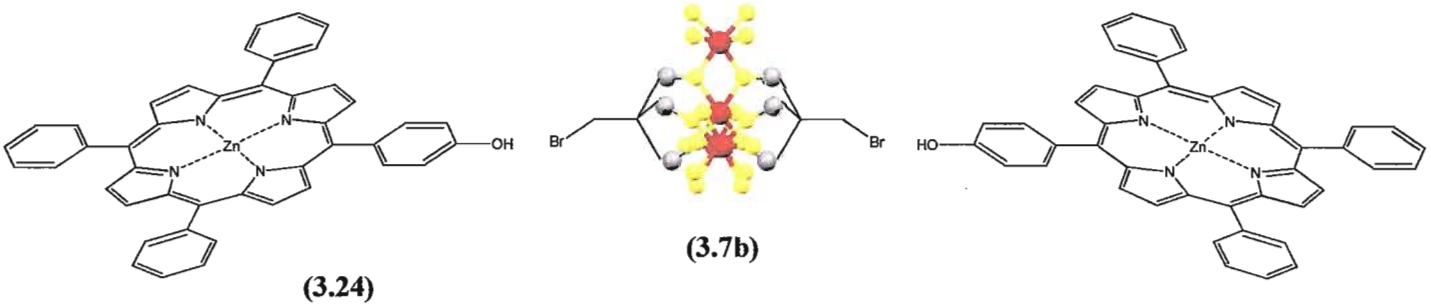

(3.24) **(3.7b)**

Figure 3.23: Attachment idea of **(3.24)** and **(3.7b)**. Reagents and conditions: DMF, KOH.

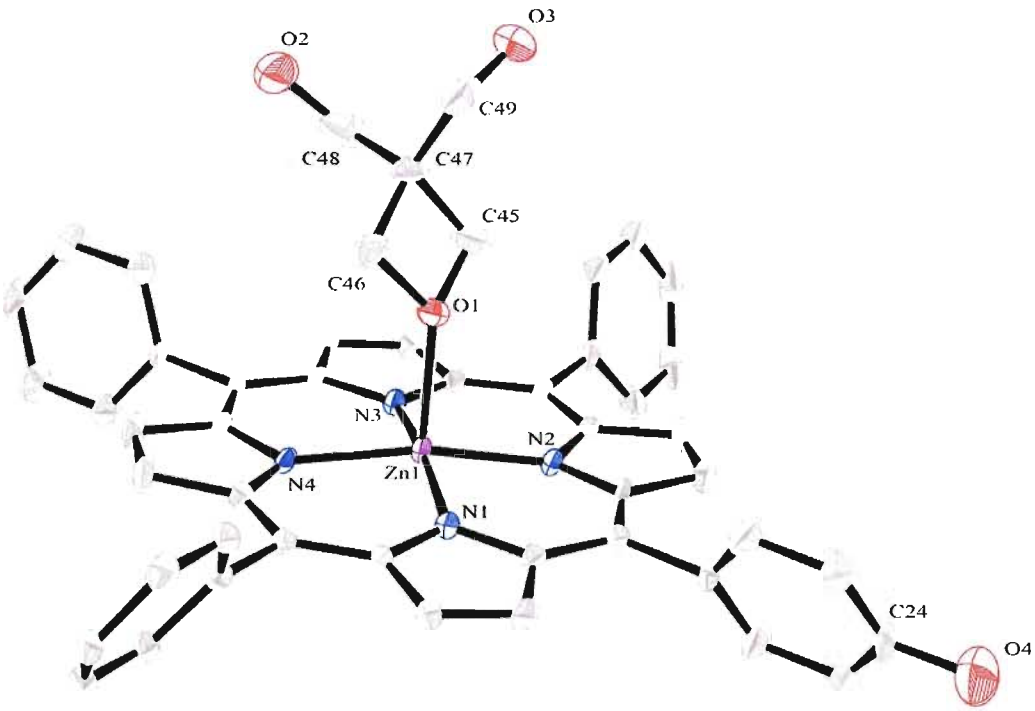

(3.25)

Figure 3.24: ORTEP representation of the molecular structure of the ZnHPTPP oxetane complex **(3.25)**. Thermal ellipsoids are plotted at 50% probability.

The complex **(3.25)** crystallizes in the triclinic P-1 space group. There are no solvent molecules in the crystal lattice. The geometry around the zinc ion is square-pyramidal with an N_4O binding mode. The porphyrin macrocycles are separated by a distance of 4.43 Å relative to the pyrrole units of the macrocycle. A full list of all bond lengths and angles for complex **(3.25)** can be found in the *Appendix* section of the thesis, Tables 6.15 and 6.16.

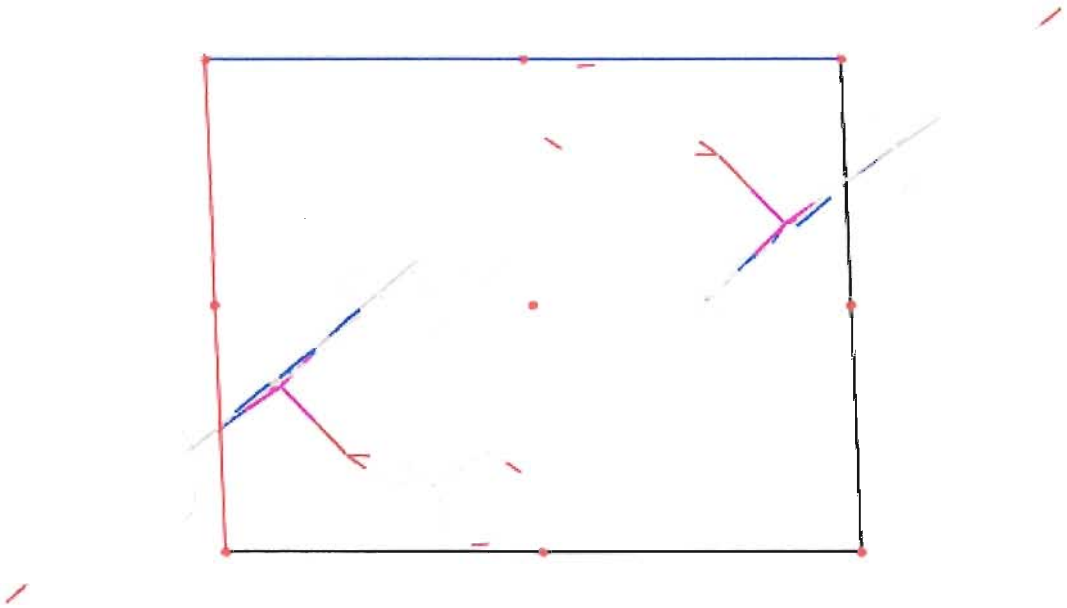

Figure 3.25: Mercury representation of **(3.25)** displaying the inversion centre.

To-date the proposed complexes **(3.4)**, **(3.5)** and **(3.6)** have not crystallized. In order to obtain pure products from the exchange reactions it is necessary to find appropriate experimental conditions that facilitate the growth of single crystals of the products. The use of UV-Vis, IR, and MS data was inconclusive in establishing whether or not the exchange reactions had taken place. It was not possible to determine if the tested samples contained one product or a mixture of products.

3.5 – Conclusion and Future Work

In project two, the synthetic strategies for the preparation of 3 new porphyrin derivatives with triol functionality **(3.1)**-**(3.3)** have been devised and these compounds have been prepared and characterized. It has become apparent that following literature procedures it is possible to substitute the labile MeO bridges of the tetrairon^{III} cluster for

triol ligands but that the experimental conditions heavily rely on the products crystallizing out of the reaction mixture. Unfortunately, given the limited solubility of the porphyrin building blocks in diethyl ether changing the solvent conditions was not favourable for the growth of single crystals. An alternative attempt to tether the cluster directly onto the porphyrin was also unsuccessful since the cluster was not stable to the basic conditions required for deprotonation and subsequent nucleophilic substitution. Within the timeframe of the project a large portion of time was invested working towards the synthesis and purification of the appropriate functionalized porphyrin derivatives. In the future, time needs to be invested in repeating the exchange reactions modifying the experimental conditions that favour the growth of single crystals.

What is clear from this work is that the ligand replacement reactions work well for one particular family of compounds but that its applicability to target more complex, larger systems is somewhat problematic. In hindsight the attachment of the porphyrin building blocks to the cluster is an ambitious goal, it might be more appropriate to target a more simple class of photoluminescent ligands such as anthracene that can be prepared with much less synthetic effort. In this respect more effort can be focused on establishing the optimum experimental conditions for the purification and characterization of these systems.

Chapter 4 – Experimental

4.1 – General Information

All reagents were purchased from commercial suppliers (Sigma-Aldrich, Alfa Aesar, Fluka, Acros, and Strem). Unless stated otherwise, all reactions were carried out under an inert atmosphere of nitrogen using standard Schlenk line procedures. All extractions and work-up procedures used reagent grade solvents. Distilled water was used for all aqueous work-ups. Anhydrous dichloromethane (DCM), diethyl ether (Et_2O), and tetrahydrofuran (THF) were obtained from a Puresolve PS MD-4 solvent purification system and stored over 3 or 4 Å molecular sieves. Anhydrous dimethylformamide (DMF) and methanol (MeOH) were purchased from Sigma-Aldrich and used as received. Thionyl chloride ($SOCl_2$) was simple distilled and stored over 3 Å molecular sieves. Ethanol (EtOH) was dried over powdered 3 Å molecular sieves, distilled, and stored over 3 Å molecular sieves. Pyridine was dried over CaH_2 and distilled right before use. Any transportation of solvents used air sensitive methods. Unless otherwise stated coordination chemistry was generally carried out using reagent grade solvents in air at room temperature. Thin layer chromatography (TLC) was carried out on either Merck pre-coated aluminum oxide or silicon oxide aluminum sheets that were 0.2 mm thick and 20 mm wide by 40 mm long.

4.2 – Instrumentation

Melting Point (m.p.)

Melting points of solids were measured using a Stuart Scientific SMP 10 melting point apparatus.

Nuclear Magnetic Resonance (NMR)

^{1}H-NMR, ^{13}C-NMR, and ^{31}P-NMR were obtained on a Bruker Advance AV 300 Digital NMR spectrometer with deuterated chloroform ($CDCl_3$) as the solvent unless otherwise stated. ^{1}H-NMR, ^{13}C-NMR, and ^{31}P-NMR experiments were carried out with spectrometer frequencies of 300, 75, and 121 MHz, respectively. Data acquisition and analysis were carried out using the Bruker TOPSPIN 2.1 PL6 software. Data acquisition on a 600 MHz Bruker Advance AV 600 Digital NMR spectrometer was carried out by Razvan Simionescu.

Mass Spectrometry (MS)

Mass spectra (EI, FAB, MALDI) were recorded on a Carlo Ebra/Kratos GCMS Concept 1S double focusing mass spectrometer interfaced to a Kratos DART acquisition system and a Sun SPARC workstation. Sample preparation and measurements were performed by Tim Jones.

Fourier Transformation Infrared Spectroscopy (FT-IR)

Spectra were recorded on a ThermoMattson RS-1 spectrometer with the WinFirst data acquisition system. Samples were prepared as potassium bromide (KBr) pellets and were recorded at approximately 295 K from 400 to 4000 cm^{-1}.

Ultraviolet Visible Spectroscopy (UV-Vis)

Spectra were recorded on a ThermoSpectronic/Unicam UV-4 spectrometer with the Vision data acquisition system. Samples were prepared to either 0.1 mM, 0.05 mM, 0.025 mM, or 0.00156 mM. Samples were recorded at approximately 295 K from 200 to 900 nm.

Elemental Analysis

The CHN data were collected by Atlantic Microlab, *Inc.* Norcross, GA, USA.

X-ray Crystallography

X-ray data were collected on an APEX II CCD Kappa diffractometer with Mo K_α graphite monochromated radiation (λ = 0.71073 Å) and an Oxford low temperature device. Single crystals were suspended in paraffin oil and mounted on either nylon or MiTeGen loops and flash cooled. The data were processed using the Bruker SHELXTL[151] software package. Structures were solved by Direct Methods using SHELXS-97 and refined using SHELX-97. PLATON/SQUEEZE was used to correct the data for disordered solvent. Mercury[152] and ORTEP[153] programs were used to generate

graphics of the molecular structures and packing diagrams. The single crystal data were collected, solved and refined by Prof. M. Pilkington and Nicholas J. Hurley.

Magnetic Susceptibility

Measurements were carried out on a Quantum Design SQUID magnetometer MPMS in applied fields of 1000, 2000 or 5000 Oe between 5 and 300 K. Magnetic saturation was carried out at 3 K between 0 and 50,000 Oe. The data were corrected for the sample holder and sample diamagnetism (Pascal's constants).[8]

Electron Paramagnetic Resonance (EPR)

The samples were prepared in quartz tubes as solids or solutions. The spectra were recorded on a Bruker Elexysys E580 pulsed and a CW X-band (9 GHz) spectrometer. The EPR data was modelled by Sam Mula using Easy Spin 3.1.7 simulation software.

Project 1

4.3 – Synthesis of 3,3'-Diamino-2,2'-Bipyridine (1.17)[67]

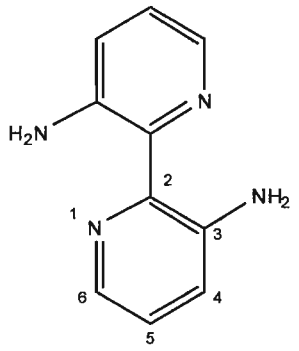

(1.17)

4.3.1 Activation of Copper Powder

25 g of copper powder (1-3 μm) was stirred in a solution of 2% iodine (5 g) in acetone (250 mL) for approximately 1 hr until a pale yellow coloured mixture was obtained. The mixture was then filtered resulting in a grayish pink coloured residue which was transferred to a solution of 38% hydrochloric acid:acetone (1:1, 125 mL) and stirred for 1 hr. The mixture was filtered and the resulting copper powder was washed several times with acetone (3 x 100 mL). The pink copper powder was allowed to dry after which time it was used directly in the next step **(4.3.2)**. The remaining copper powder was stored in a desiccator.

4.3.2 3,3'-Dinitro-2,2'-Bipyridine (4.1)[67]

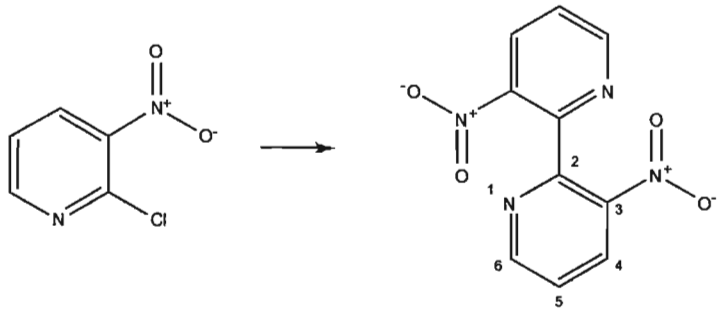

(4.1)

2-Chloro-3-nitropyridine (3.00 g, 18.9 mmol) was dissolved in anhydrous DMF (60 mL). Freshly activated copper powder (3.00 g) **(4.3.1)** was then added. The mixture was heated to 150 °C and stirred for approximately 2.5 hrs. The progress of the reaction was monitored by TLC (Al_2O_3, CH_2Cl_2). After approximately 2 hrs no more starting material was observed on the TLC plate. The mixture was then cooled via the addition of ice water (60 mL) which precipitated the crude product as a brownish/orange solid. The solid was collected by filtration, washed with 28% ammonium hydroxide (2 x 30 mL), and the resulting greenish-brown residue extracted into boiling 1,4-dioxane (225 mL). The mixture was boiled for 30 minutes and then cooled to room temperature. Removal of the solvent under vacuum afforded a brown solid which was transferred into boiling ethanol (500 mL). The hot solution was immediately filtered and the yellow filtrate was reduced to approximately 150 mL. The solution was left to cool at 4 °C overnight affording pale yellow crystals of 3,3'-dinitro-2,2'-bipyridine which were isolated via filtration. Yield 1.53 g (66%), m.p. 205 °C.

^{1}H-NMR ($CDCl_3$, ppm): 8.90 (dd, 2H, J = 4.8, J = 1.2 Hz, 6-H), 8.60 (dd, 2H, J = 8.2, J = 1.2 Hz, 4-H), 7.67 (dd, 2H, J = 8.4, J = 4.8 Hz, 5-H).

^{13}C-NMR ($CDCl_3$, ppm): 152.9 (6-C), 150.7 (2-C), 144.0 (3-C), 133.1 (4-C), 124.6 (5-C).

MS (EI, *m/z*): 246 $[M]^+$ (2.2%), 200 ($[M]^+$ - NO_2) (100%).

4.3.3 3,3'-Diamino-2,2'-Bipyridine (1.17)[67]

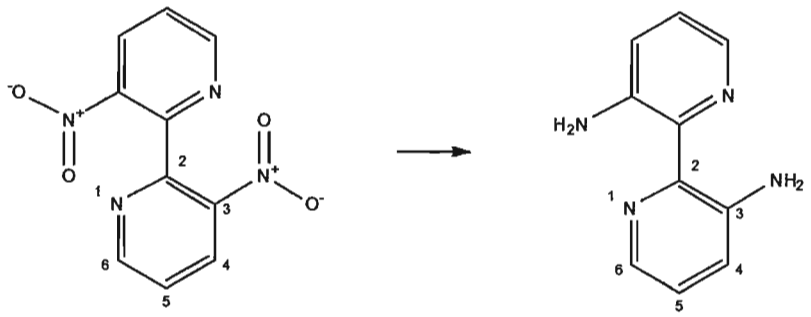

(4.1) **(1.17)**

3,3'-Dinitro-2,2'-bipyridine **(4.1)** (1.60 g, 6.50 mmol) was dissolved in a hot solution (80 °C) of $SnCl_2$ (11.2 g, 59.1 mmol) in 38% hydrochloric acid (28 mL) and refluxed for 45 mins. The pH of the solution was then adjusted to ~ 7 with the drop-wise addition of aqueous 5 M NaOH solution while still keeping the reaction mixture hot (care was taken not to let the solution cool down before the pH was adjusted otherwise an insoluble green precipitate is formed and the reaction fails). After adjustment of the pH the yellow reaction mixture was allowed to cool after which time it was extracted into chloroform and dried over sodium sulphate. The solvent was then removed under vacuum to yield 3,3'-diamino-2,2'-bipyridine as a bright-yellow powder. Yield 1.17 g (97%), m.p. 133-134°C.

^{1}H-NMR ($CDCl_3$, ppm): 8.00 (dd, 2H, J = 3.8, J = 2.4 Hz, 6-H), 7.06 (m, 4H, 4-H and 5-H), 6.30 (s, 4H, 2 NH_2).

^{13}C-NMR ($CDCl_3$, ppm): 143.8 (3-C), 140.6 (2-C), 135.7 (6-C) 123.9 (4-C),

122.9 (5-C).

MS (EI, *m/z*): 186 $[M]^+$ (98%), 170 ($[M]^+$ - NH_2) (100%).

UV-Vis (DCM, λ_{max} (nm)), {log ε}: 230 {4.27}, 267 {4.19}, 374 {4.21}.

4.4 – Synthesis of 2,2'-Bipyridine-3,3'-(2-Pyridinecarboxamide) (H_2L^1) (2.1)[81]

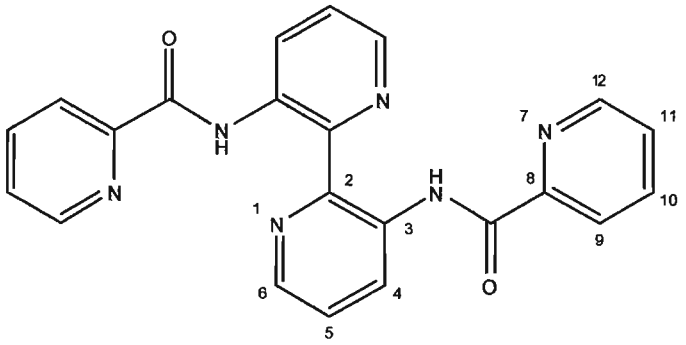

(2.1)

Method A – Two Step Synthesis[81]

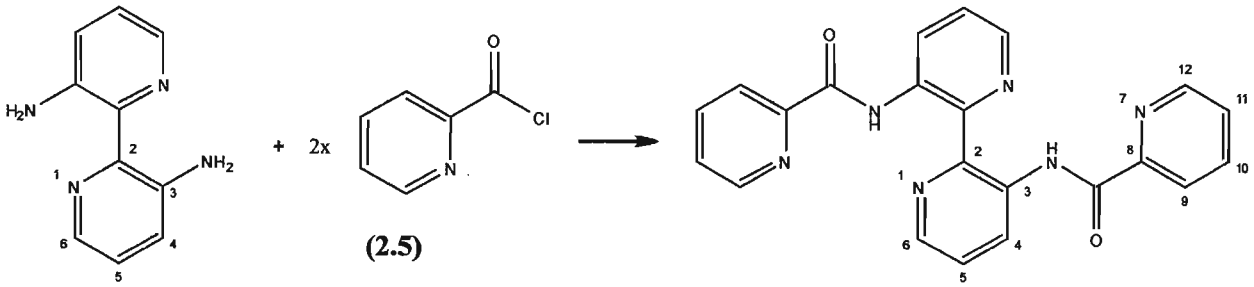

(1.17) **(2.5)** **(2.1)**

4.4.1 Preparation of 2-Pyridine Carbonyl Chloride (2.5)[81]

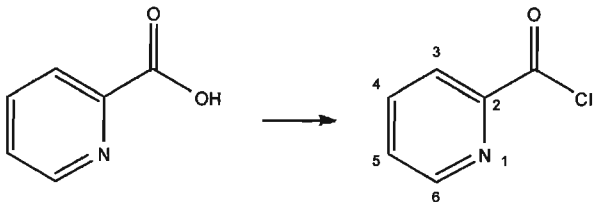

(2.5)

Picolinic acid (1.04 g, 8.41 mmol) was dissolved in freshly distilled thionyl chloride (25 mL). Dry DMF was then added (3 drops) and the green solution was refluxed at 90 °C for 15 hrs resulting in a light orange solution. Excess thionyl chloride was removed via vacuum affording the product as a green solid. Yield 1.19 g (100%). This product was used directly in the next step **(4.4.2)** without any further purification.

^{1}H-NMR ($CDCl_3$, ppm): 8.84 (m, 1H, 6-H), 8.14 (m, 1H, 3-H), 7.92 (m, 1H, 4-H), 7.60 (m, 1H, 5-H).

MS (EI, *m/z*): 106 ($[M]^+$ - Cl).

IR (KBr, cm^{-1}): 3094, 1734 (C=O), 1611, 1460, 1407, 1258, 1087, 750.

4.4.2 2,2'-Bipyridine-3,3'-(2-Pyridinecarboxamide) (H_2L^1) (2.1)[81]

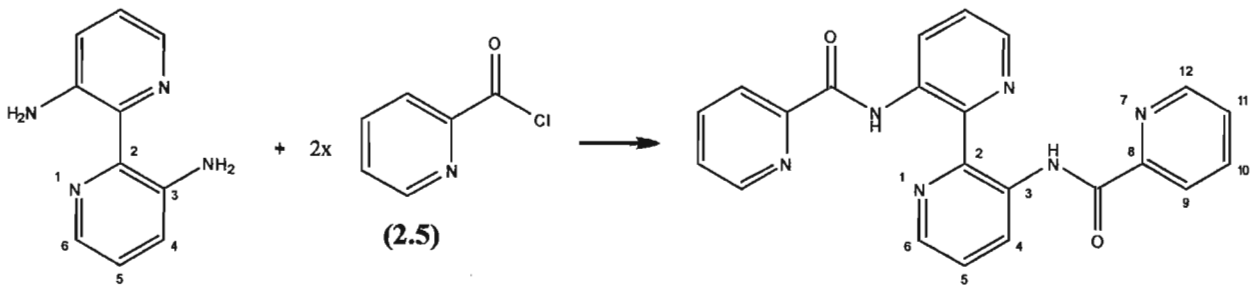

2-Pyridine carbonyl chloride **(2.5)** (1.19 g, 8.41 mmol) was dissolved in anhydrous DCM (24 mL) and cooled to 0 °C. 3,3'-diamino-2,2'-bipyridine **(1.17)** (0.78 g, 4.20 mmol) was added followed by triethylamine (1.76 mL, 12.60 mmol) in two equal portions. The solution was allowed to stir at 0 °C for 2 hrs. Following this, the mixture was refluxed at 50 °C for approximately 15 hrs. After cooling, a crude brown solid was isolated by filtration. The crude product was washed with saturated sodium bicarbonate solution and extracted into DCM (100 mL). This solution was washed with saturated

sodium bicarbonate solution (300 mL), dried over sodium sulphate, and evaporated to dryness to afford a greenish-yellow solid. The crude product was washed with acetone and diethyl ether to afford the product as a pale yellow solid. Yield 0.86 g (52%). m.p. 218°C.

Characterization following method B

Method B – One Step Synthesis[116]

4.4.3 2,2'-Bipyridine-3,3'-(2-Pyridinecarboxamide) (H_2L^1) (2.1)

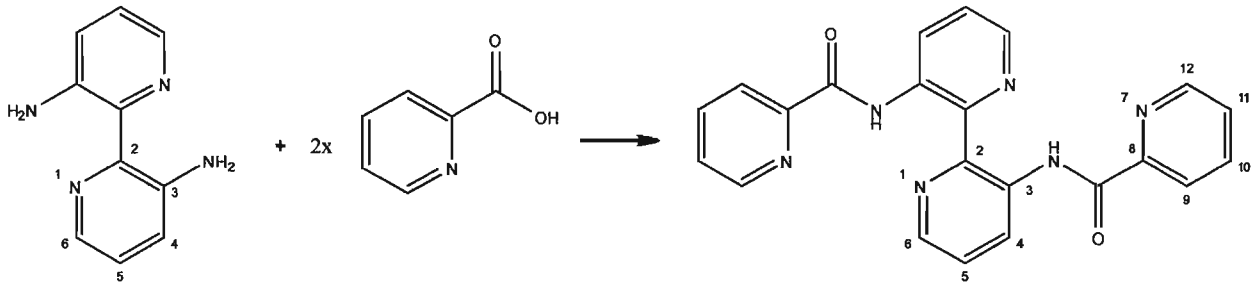

(1.17) **(2.1)**

3,3'-Diamino-2,2'-bipyridine **(1.17)** (0.466 g, 2.50 mmol) was dissolved in freshly distilled pyridine (3.5 mL). To this was added picolinic acid (0.650 g, 5.28 mmol) in one portion. This mixture was allowed to stir at 45 °C for 45 mins. Triphenylphosphite (1.31 mL, 5.00 mmol) was then added via syringe over a 5 minute period. The solution was taken to 95 °C and stirred for 4 hrs. The resulting thick beige slurry was cooled to room temperature and filtered. The residue was washed with water (3 x 15 mL), acetone (3 x 15 mL) and finally diethyl ether (20 mL) to yield the pure product as a light beige solid. Yield 0.90 g (92%). m.p. 218 °C.

^{1}H-NMR ($CDCl_3$, δ ppm): 14.84 (s, 2H, CONH), 9.38 (dd, 2H, J = 8.4, J = 1.5 Hz, 6-H), 8.79 (d, 2H, J = 4.2 Hz, 4-H), 8.65 (dd, 2H, J = 4.5, J

= 1.5 Hz, 12-H), 8.29 (d, 2H, J = 7.8 Hz, 9-H), 7.92 (t, 2H, J = 7.4 Hz, 10-H), 7.52 (m, 4H, 5-H, 11-H).

^{13}C-NMR ($CDCl_3$, δ ppm): 164.0 (C=O), 150.8 (8-C), 148.5 (12-C), 143.3 (2-C), 141.5 (6-C), 137.4 (10-C), 136.0 (3-C), 129.7 (4-C), 126.3 (11-C), 123.9 (5- C), 122.7 (9-C).

MS (EI, *m/z*): 396 $[M]^+$.

HRMS (EI, *m/z*): $C_{22}H_{16}N_6O_2$ calcd: 396.1335; found: 396.1332.

IR (KBr, cm^{-1}): 3449 (N-H), 2925, 2362, 1678 (C=O) sh, 1562, 1513, 1434, 1386, 1296, 1226 sh, 1140, 1087, 997, 904, 804, 740, 694.

UV-Vis (DCM, λ_{max} (nm)), {log ε}: 232 {4.46}, 292 {4.28}, 336 {4.13}.

CHN $C_{22}H_{16}N_6O_2$ calcd: C 66.65%, H 4.07%, N 21.20%.
found: C 66.74%, H 3.72%, N 20.80%.

4.5 – Coordination of 2,2'-Bipyridine-3,3'-(2-Pyridinecarboxamide) (H_2L^1) (2.1)

4.5.1 Coordination with $CuCl_2 \cdot 2H_2O$ (1.27)

2,2'-Bipyridine-3,3'-(2-pyridinecarboxamide) **(2.1)** (50.0 mg, 0.126 mmol) was dissolved in DCM (15 mL) and triethylamine (0.018 mL, 0.126 mmol). To this solution was added $CuCl_2 \cdot 2H_2O$ (45.2 mg, 0.265 mmol) dissolved in methanol (5 mL). The mixture was stirred at room temperature for 15 hrs. Removal of the solvents under vacuum afforded a green solid which was washed with water (15 mL) and diethyl ether (15 mL) and finally dried under vacuum to yield the complex as a green crystalline powder. Yield 49.3 mg (66%).

MS (FAB, *m/z*): 593 $[Cu_2(\mathbf{L^1})Cl_2]^+$ (7.8%), 557 $[Cu_2(\mathbf{L^1})Cl]^+$ (34%), 457 $[Cu_2(\mathbf{L^1})Cl]^+$ (100%).

IR (KBr, cm^{-1}): 3070, 2672, 2362, 1623 (C=O) sh, 1594, 1523, 1467, 1434, 1405, 1348, 1299, 1230, 1155, 1081, 1022, 887, 812, 748, 682, 640.

UV-Vis (DCM, λ_{max} (nm)): 231, 258, 324, 370.

CHN: $C_{22}H_{14}N_6O_2Cu_2Cl_2$
calcd: C 44.61%, H 2.38%, N 14.19%.
found: C 44.80%, H 2.45%, N 14.24%.

4.5.2 Coordination with $Cu(OAc)_2 \cdot H_2O$ (2.7)

2,2'-Bipyridine-3,3'-(2-pyridinecarboxamide) (**2.1**) (50.0 mg, 0.126 mmol) was dissolved in DCM (15 mL) and triethylamine (0.018 mL, 0.126 mmol). To this solution was added $Cu(OAc)_2 \cdot H_2O$ (52.9 mg, 0.265 mmol) dissolved in methanol (5 mL). The mixture was stirred at room temperature for 15 hrs. Removal of the solvents under vacuum afforded a green oil which was washed with water (15 mL) and diethyl ether (15 mL) and finally dried under vacuum to yield the complex as a green crystalline powder. Yield 62.3 mg (77%).

Suitable single crystals for X-ray diffraction were grown at room temperature via the slow evaporation of a DCM/methanol solution (1:1) of the isolated green powder.

MS (FAB, *m/z*): 642 $[Cu_2(\mathbf{L^1})(OAc)_2]^+$ (11%), 579 $[Cu_2(\mathbf{L^1})(OAc)]^+$ (59%), 520 $[Cu_2(\mathbf{L^1})]^+$ (38%).

IR (KBr, cm^{-1}): 3072, 2981, 2360, 1637 (C=O) sh, 1598, 1569, 1421, 1344, 1301, 1226, 1155, 1022, 954, 858, 808, 757, 688, 649.

UV-Vis (DCM, λ_{max} (nm)): 228, 256, 320, 363, 667.

CHN: $C_{26}H_{20}N_6O_6Cu_2 \cdot MeOH$
calcd: C 48.29%, H 3.60%, N 12.41%.
found: C 48.39%, H 3.67%, N 11.97%.

4.5.3 Coordination with $NiCl_2 \cdot 6H_2O$ (2.8)

2,2'-Bipyridine-3,3'-(2-pyridinecarboxamide) **(2.1)** (50.0 mg, 0.126 mmol) was dissolved in DCM (15 mL) and triethylamine (0.018 mL, 0.126 mmol). To this solution was added $NiCl_2 \cdot 6H_2O$ (63.0 mg, 0.265 mmol) dissolved in methanol (5 mL). The mixture was stirred at room temperature for 15 hrs. Removal of the solvents under vacuum afforded a yellow solid which was washed with water (15 mL) and diethyl ether (15 mL) and finally dried under vacuum to yield the complex as a yellow powder. Yield 46.3 mg (75%).

Suitable single crystals for X-ray diffraction were grown via liquid-liquid diffusion of a methanol solution of $NiCl_2 \cdot 6H_2O$ over a DCM solution of **(2.1)** and Et_3N.

MS (FAB, *m/z*): 964 $[Ni_3(\mathbf{L^1})_2]^+$ (10%), 511 $[Ni_2(\mathbf{L^1})]^+$ (6.1%), 452 $[Ni(\mathbf{L^1})]^+$ (51%).

IR (KBr, cm^{-1}): 3403 w, 3070, 2946, 2356, 1614 (C=O) sh, 1563, 1515, 1436, 1384, 1294, 1226, 1118, 1087, 1018, 904, 804, 740, 694, 638.

UV-Vis (DCM, λ_{max} (nm)): 229, 262, 331.

CHN: $C_{66}H_{42}N_{18}O_6Ni_3 \cdot 6H_2O$
calcd: C 54.02%, H 3.71%, N 17.18%.
found: C 53.79%, H 3.67%, N 17.15%.

4.5.4 Coordination with $Ni(OAc)_2 \cdot 4H_2O$ (2.9)

2,2'-Bipyridine-3,3'-(2-pyridinecarboxamide) **(2.1)** (50.0 mg, 0.126 mmol) was dissolved in DCM (15 mL) and triethylamine (0.018 mL, 0.126 mmol). To this solution was added $Ni(OAc)_2 \cdot 4H_2O$ (66.0 mg, 0.265 mmol) dissolved in methanol (5 mL). The mixture was stirred at room temperature for 15 hrs. Removal of the solvents under

vacuum afforded a yellow solid which was washed with water (15 mL) and diethyl ether (15 mL) and finally dried under vacuum to yield the complex as a yellow powder. Yield 40.3 mg (65%).

Suitable single crystals for X-ray diffraction were grown at room temperature via the slow evaporation of a DCM/methanol solution (1:1) of the previously isolated compound.

MS (FAB, *m/z*): 964 $[Ni_3(\mathbf{L^1})_2]^+$ (7.2%), 510 $[Ni_2(\mathbf{L^1})]^+$ (12%), 453 $[Ni(\mathbf{L^1})]^+$ (11%).

IR (KBr, cm^{-1}): 3403 w, 3068, 2985, 2686, 2493, 2360, 1860, 1612 (C=O) sh, 1589, 1556, 1438, 1411, 1346, 1292, 1089, 1020, 910, 804, 761, 694.

UV-Vis (DCM, λ_{max} (nm)): 230, 261, 331.

CHN: $C_{66}H_{42}N_{18}O_6Ni_3 \cdot 4H_2O$
calcd: C 55.38%, H 3.52%, N 17.61%.
found: C 55.14%, H 3.67%, N 17.38%.

4.5.5 Coordination with $MnCl_2$ (2.13)

2,2'-Bipyridine-3,3'-(2-pyridinecarboxamide) **(2.1)** (50.0 mg, 0.126 mmol) was dissolved in DCM (15 mL) and triethylamine (0.018 mL, 0.126 mmol). To this solution was added $MnCl_2$ (33.4 mg, 0.265 mmol) dissolved in methanol (5 mL). The mixture was stirred at room temperature for 15 hrs. Removal of the solvents under vacuum afforded a brown solid which was washed with water (15 mL) and diethyl ether (15 mL) and finally dried under vacuum to yield the complex as a brown powder. Yield 46.5 mg (64%).

MS (FAB, *m/z*): 576 $[Mn_2(\mathbf{L^1})Cl_2]^+$ (18%), 540 $[Mn_2(\mathbf{L^1})Cl]^+$ (53%).

IR (KBr, cm^{-1}): 3070, 2672, 2362, 1623 (C=O) sh, 1594, 1523, 1467, 1434, 1405, 1348, 1299, 1230, 1155, 1081, 1022, 887, 812, 748, 682, 640.

UV-Vis (DCM, λ_{max} (nm)): 229, 266, 339.

CHN: $C_{22}H_{14}N_6O_2Mn_2Cl_2 \cdot 3.6MeOH$
calcd: C 44.53%, H 4.15%, N 12.17%.
found: C 44.67%, H 4.65%, N 12.68%.

4.5.6 Coordination with $Mn(OAc)_2 \cdot 4H_2O$ (2.14)

2,2'-Bipyridine-3,3'-(2-pyridinecarboxamide) **(2.1)** (50.0 mg, 0.126 mmol) was dissolved in DCM (15 mL) and triethylamine (0.018 mL, 0.126 mmol). To this solution was added $Mn(OAc)_2 \cdot 4H_2O$ (65.0 mg, 0.265 mmol) dissolved in methanol (5 mL). The mixture was stirred at room temperature for 15 hrs. Removal of the solvents under vacuum afforded a beige solid which was washed with water (15 mL) and diethyl ether (15 mL) and finally dried under vacuum to yield the complex as a beige powder. Yield 42.5 mg (54%).

MS (FAB, *m/z*): 624 $[Mn_2(\mathbf{L^1})(OAc)_2]^+$ (7.6%), 565 $[Mn_2(\mathbf{L^1})(OAc)]^+$ (11%), 506 $[Mn_2(\mathbf{L^1})]^+$ (91%).

IR (KBr, cm^{-1}): 3421 w, 3072, 2981, 2360, 1637 (C=O) sh, 1571, 1532, 1494, 1463, 1421, 1344, 1301, 1226, 1155, 1022, 954, 858, 808, 757, 688, 649.

UV-Vis (DCM, λ_{max} (nm)): 227, 250, 333.

CHN: $C_{26}H_{20}N_6O_6Mn_2 \cdot 1.95MeOH \cdot 1.75H_2O$
calcd: C 46.86%, H 4.40%, N 11.73%.
found: C 46.51%, H 4.04%, N 11.37%.

4.5.7 Coordination with $CoCl_2 \cdot 6H_2O$ (2.15)

2,2'-Bipyridine-3,3'-(2-pyridinecarboxamide) (**2.1**) (50.0 mg, 0.126 mmol) was dissolved in DCM (15 mL) and triethylamine (0.018 mL, 0.126 mmol). To this solution was added $CoCl_2 \cdot 6H_2O$ (63.1 mg, 0.265 mmol) dissolved in methanol (5 mL). The mixture was stirred at room temperature for 15 hrs. Removal of the solvents under vacuum afforded a brown solid which was washed with water (15 mL) and diethyl ether (15 mL) and finally dried under vacuum to yield the complex as a red/brown powder. Yield 56.2 mg.

MS (FAB, *m/z*): 581 $[Co_2(\mathbf{L^1})Cl_2]^+$ (2.1%), 546 $[Co_2(\mathbf{L^1})Cl]^+$ (26%), 453 $[Co(\mathbf{L^1})]^+$ (29%).

IR (KBr, cm^{-1}): 3419 w, 3072, 2977, 2603, 2495, 2360, 1635 (C=O) sh, 1600, 1560, 1340, 1155, 1033, 806, 763, 684.

UV-Vis (DCM, λ_{max} (nm)): 231, 262.

CHN: found: C 45.23%, H 5.53%, N 12.02%.

4.5.8 Coordination with $Co(OAc)_2 \cdot 4H_2O$ (2.16)

2,2'-Bipyridine-3,3'-(2-pyridinecarboxamide) (**2.1**) (50.0 mg, 0.126 mmol) was dissolved in DCM (15 mL) and triethylamine (0.018 mL, 0.126 mmol). To this solution was added $Co(OAc)_2 \cdot 4H_2O$ (66.0 mg, 0.265 mmol) dissolved in methanol (5 mL). The mixture was stirred at room temperature for 15 hrs. Removal of the solvents under vacuum afforded a brown solid which was washed with water (15 mL) and diethyl ether (15 mL) and finally dried under vacuum to yield the complex as a brown crystalline solid. Yield 45.3 mg (57%).

MS (FAB, *m/z*): 571 $[Co_2(\mathbf{L^1})(OAc)]^+$ (100%), 513 $[Co_2(\mathbf{L^1})]^+$ (54%),

454 $[Co(\mathbf{L^1})]^+$ (81%).

IR (KBr, cm^{-1}): 3423 w, 3075, 2983, 2682, 2489, 2360, 1637 (C=O) sh, 1600, 1417, 1334, 1297, 1160, 995, 802, 757, 657.

UV-Vis (DCM, λ_{max} (nm)): 236, 260.

CHN: $C_{26}H_{20}N_6O_6Co_2 \cdot 3.5MeOH \cdot 2.85H_2O$
calcd: C 44.63%, H 5.04%, N 10.59%.
found: C 44.39%, H 4.70%, N 10.24%.

4.5.9 Coordination with $Zn(OAc)_2 \cdot 2H_2O$ (2.6)

2,2'-Bipyridine-3,3'-(2-pyridinecarboxamide) **(2.1)** (50.0 mg, 0.126 mmol) was dissolved in DCM (15 mL) and triethylamine (0.018 mL, 0.126 mmol). To this solution was added $Zn(OAc)_2 \cdot 2H_2O$ (58.2 mg, 0.265 mmol) dissolved in methanol (5 mL). The mixture was stirred at room temperature for 15 hrs. Removal of the solvents under vacuum afforded a beige solid which was washed with water (15 mL) and diethyl ether (15 mL) and finally dried under vacuum to yield the complex as a beige powder. Yield 46.3 mg (60%). Suitable single crystals for X-ray diffraction were grown at room temperature via the slow evaporation of a DCM/methanol solution (1:1) of the previously isolated compound.

MS (FAB, *m/z*): 1042 $[Zn_3(\mathbf{L^1})_2OAc]^+$ (3.9%), 919 $[Zn_2(\mathbf{L^1})_2]^+$ (3.2%), 676 $[Zn2(\mathbf{L^1})(OAc)_2MeO]^+$ (16%).

IR (KBr, cm^{-1}): 3403 w, 3075, 2983, 2682, 2489, 2360, 1637 (C=O) sh, 1600, 1417, 1334, 1297, 1160, 995, 802, 757, 657.

UV-Vis (DCM, λ_{max} (nm)): 231, 257, 309, 341.

CHN: $C_{50}H_{40}N_{12}O_{10}Zn_4 \cdot 3MeOH \cdot H_2O$
calcd: C 47.34%, H 4.05%, N 12.50%.
found: C 47.02%, H 3.79%, N 12.34%.

4.6 – Synthesis of 2,2'-Bipyridine-3,3'-(2-Pyrazinecarboxamide) (H_2L^2) (2.2)

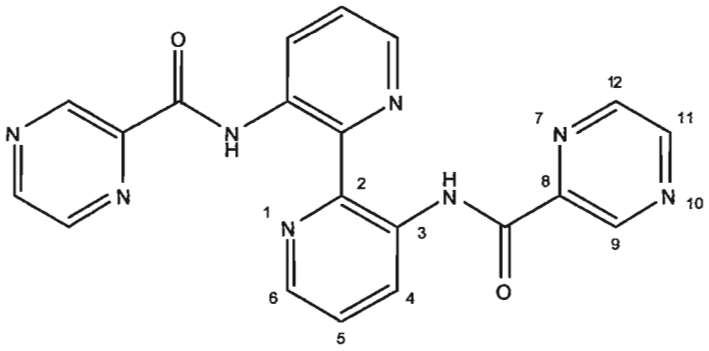

(2.2)

4.6.1 2,2'-Bipyridine-3,3'-(2-Pyrazinecarboxamide) (H_2L^2) (2.2)[116]

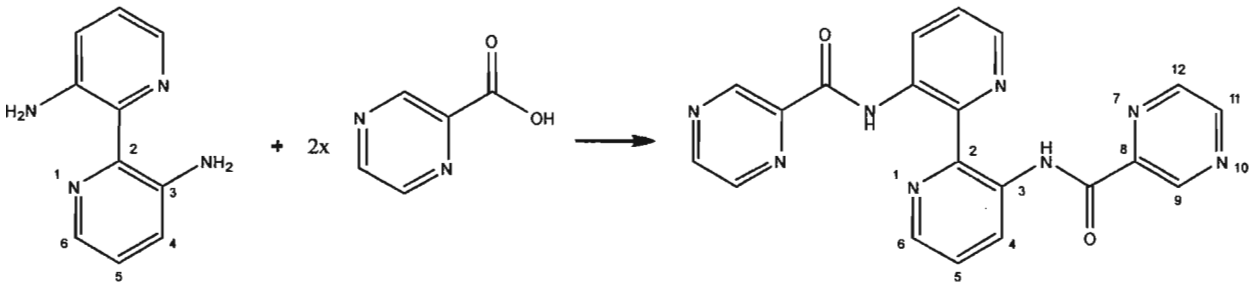

(1.17) **(2.2)**

3,3'-Diamino-2,2'-bipyridine **(1.17)** (0.466 g, 2.50 mmol) was dissolved in freshly distilled pyridine (3.5 mL). To this was added solid pyrazinoic acid (0.655 g, 5.28 mmol) in one portion. This mixture was allowed to stir at 45 °C for 45 mins. Triphenylphosphite (1.31 mL, 5.00 mmol) was then added over a 5 minute period. The solution was taken to 95 °C and stirred for 4 hrs. The resulting thick yellow slurry was cooled to room temperature and filtered. The residue was washed with water (3 x 15 mL), methanol (3 x 15 mL) and finally diethyl ether (20 mL) to yield the pure product as a pale-yellow solid. Yield 0.757 g (76%). m.p. >300 °C.

^{1}H-NMR ($CDCl_3$, δ ppm): 15.08 (s, 2H, CONH), 9.52 (d, 2H, J = 1.1 Hz, 9-H), 9.40 (dd, 2H, *J* = 8.7, *J* = 1.5 Hz, 6-H), 8.84 (d, 2H, *J* = 2.3 Hz,

	11-H), 8.76 (t, 2H, J = 1.9 Hz, 4-H), 8.64 (dd, 2H, J = 4.7, J = 1.7 Hz, 12-H), 7.52 (dd, 2H, J = 8.7, J = 4.5 Hz, 5-H).
^{13}C-NMR ($CDCl_3$, δ ppm):	164.2 (C=O), 146.3 (12-C), 144.8 (8-C), 144.4 (11-C), 144.2 (9-C), 143.0 (2-C), 141.0 (6-C), 135.8 (3-C), 129.3 (4-C), 123.9 (5-C).
MS (EI, *m/z*):	398 $[M]^+$.
HRMS (EI, *m/z*):	$C_{20}H_{14}N_8O_2$ calcd: 398.1240; found: 398.1236.
IR (KBr, cm^{-1}):	3425 (N-H), 2960, 2925, 2362, 1672 (C=O) sh, 1562, 1513, 1434, 1386, 1296, 1226, 1140, 1087, 997, 904, 804, 740, 694.
UV-Vis (DCM, λ_{max} (nm)), {log ε}:	230 {4.49}, 267 {4.46}, 353 {4.26}.
CHN	$C_{20}H_{14}N_8O_2$ calcd: C 60.30%, H 3.54%, N 28.13%. found: C 60.54%, H 3.50%, N 28.00%.

4.7 – Coordination of 2,2'-Bipyridine-3,3'-(2-Pyrazinecarboxamide) (H_2L^2) (2.2)

4.7.1 Coordination with $CuCl_2 \cdot 2H_2O$ (2.18)

2,2'-Bipyridine-3,3'-(2-pyrazinecarboxamide) **(2.2)** (50.0 mg, 0.126 mmol) was placed into DCM (35 mL) and triethylamine (0.018 mL, 0.126 mmol). To this was added a solution of $CuCl_2 \cdot 2H_2O$ (88.2 mg, 0.518 mmol) dissolved in methanol (5 mL). The mixture was heated to reflux (60 °C) and stirred for 15 hrs. After this time the solvents were removed to afford a green oil. The crude product was precipitated and dried via the addition of diethyl ether (15 mL). Collection by filtration, washing with water, and drying under vacuum yielded the compound as a green crystalline powder. Yield 69.2 mg.

MS (FAB, *m/z*): 594 $[Cu_2(\mathbf{L^2})Cl_2]^+$ (7.1%), 558 $[Cu_2(\mathbf{L^2})Cl]^+$ (42%), 523 $[Cu_2(\mathbf{L^2})]^+$ (76%).

IR (KBr, cm^{-1}): 3471, 3070, 2672, 2362, 1625 (C=O) sh, 1594, 1523, 1467, 1434, 1405, 1348, 1299, 1230, 1155, 1081, 1022, 887, 812, 748, 682, 640.

UV-Vis (DCM, λ_{max} (nm)): 231, 258, 340.

CHN: found: C 40.69%, H 5.02%, N 11.46%.

4.7.2 Coordination with $Cu(OAc)_2 \cdot H_2O$ (2.17)

2,2'-Bipyridine-3,3'-(2-pyrazinecarboxamide) **(2.2)** (50.0 mg, 0.126 mmol) was placed into DCM (35 mL) and triethylamine (0.018 mL, 0.126 mmol). To this was added a solution of $Cu(OAc)_2 \cdot H_2O$ (103 mg, 0.518 mmol) dissolved in methanol (5 mL). The mixture was heated to reflux (60 °C) and stirred for 15 hrs. After this time the solvents were removed to afford a green oil. The crude product was precipitated and dried via the addition of diethyl ether (15 mL). Collection by filtration, washing with water, and drying under vacuum yielded the compound as a green crystalline powder. Yield 64.3 mg (62%).

Suitable single crystals for X-ray diffraction were grown via the slow vapour diffusion of diethyl ether into a cooled (4 °C) MeOH:DCM (1:1) solution of the previously isolated solid.

MS (FAB, *m/z*): 981 $[Cu_2(\mathbf{L^2})_2OAc]^+$ (9.6%), 583 $[Cu_2(\mathbf{L^2})OAc]^+$ (10%), 303 $[Cu_2(OAc)_3]^+$ (57%).

IR (KBr, cm^{-1}): 3072, 2981, 2360, 1637 (C=O) sh, 1562, 1549, 1501, 1421, 1411, 1344, 1301, 1226, 1155, 1022, 954, 858, 808, 757, 688, 649.

UV-Vis (DCM, λ_{max} (nm)): 228, 270, 358, 686.

CHN $C_{27}H_{24}N_8O_9Cu_3$
calcd: C 40.78%, H 3.04%, N 14.09%.
found: C 41.12%, H 3.35%, N 14.34%.

4.7.3 Coordination with $NiCl_2 \cdot 6H_2O$ (2.19)

2,2'-Bipyridine-3,3'-(2-pyrazinecarboxamide) **(2.2)** (50.0 mg, 0.126 mmol) was placed into DCM (35 mL) and triethylamine (0.018 mL, 0.126 mmol). To this was added a solution of $NiCl_2 \cdot 6H_2O$ (123 mg, 0.518 mmol) dissolved in methanol (5 mL). The mixture was heated to reflux (60 °C) and stirred for 15 hrs. After this time the solvents were removed to afford a yellow oil. The crude product was precipitated and dried via the addition of diethyl ether (15 mL). Collection by filtration, washing with water, and drying under vacuum yielded the compound as a yellow powder. Yield 66.3 mg.

MS (FAB, *m/z*): 584 $[Ni_2(\mathbf{L^2})Cl_2]^+$ (17%), 526 $[Ni_2(\mathbf{L^2})Cl]^+$ (19%).

IR (KBr, cm^{-1}): 3388, 3045, 2687, 2362, 1625 (C=O) sh, 1594, 1523, 1467, 1434, 1405, 1348, 1299, 1230, 1155, 1081, 1019, 887, 812, 748, 684, 641.

UV-Vis (DCM, λ_{max} (nm)): 230, 252, 335.

CHN: found: C 41.41%, H 6.76%, N 13.58%.

4.7.4 Coordination with $Ni(OAc)_2 \cdot 4H_2O$ (2.20)

2,2'-Bipyridine-3,3'-(2-pyrazinecarboxamide) **(2.2)** (50.0 mg, 0.126 mmol) was placed into DCM (35 mL) and triethylamine (0.018 mL, 0.126 mmol). To this was added a solution of $Ni(OAc)_2 \cdot 4H_2O$ (129 mg, 0.518 mmol) dissolved in methanol (5 mL). The mixture was heated to reflux (60 °C) and stirred for 15 hrs. After this time the solvents

were removed to afford a yellow oil. The crude product was precipitated and dried via the addition of diethyl ether (15 mL). Collection by filtration, washing with water, and drying under vacuum yielded the compound as a yellow powder. Yield 65.2 mg (52%).

MS (FAB, *m/z*): 631 $[Ni_2(\mathbf{L^2})(OAc)_2]^+$ (13%), 572 $[Ni_2(\mathbf{L^2})OAc]^+$ (11%), 515 $[Ni_2(\mathbf{L^2})]^+$ (34%).

IR (KBr, cm^{-1}): 3400 w, 3015, 2981, 2360, 1633 (C=O) sh, 1598, 1569, 1421, 1344, 1301, 1226, 1155, 1022, 954, 858, 808, 757, 688, 647.

UV-Vis (DCM, λ_{max} (nm)): 228, 256, 350

CHN $C_{29}H_{27}N_8O_{11}Ni_3 \cdot 3MeOH \cdot 3H_2O$
calcd: C 38.83%, H 4.58%, N 11.32%.
found: C 38.68%, H 4.22%, N 11.01%.

4.7.5 Coordination with $MnCl_2$ (2.21)

2,2'-Bipyridine-3,3'-(2-pyrazinecarboxamide) **(2.2)** (50.0 mg, 0.126 mmol) was placed into DCM (35 mL) and triethylamine (0.018 mL, 0.126 mmol). To this was added a solution of $MnCl_2$ (65.1 mg, 0.518 mmol) dissolved in methanol (5 mL). The mixture was heated to reflux (60 °C) and stirred for 15 hrs. After this time the solvents were removed to afford a beige oil. The crude product was precipitated and dried via the addition of diethyl ether (15 mL). Collection by filtration, washing with water, and drying under vacuum yielded the compound as a beige powder. Yield 56.3 mg.

MS (FAB, *m/z*): 505 $[Mn_2(\mathbf{L^2})]^+$ (13%), 450 $[Mn(\mathbf{L^2})]^+$ (41%).

IR (KBr, cm^{-1}): 3445, 3045, 2867, 2670, 2362, 1615 (C=O) sh, 1594, 1523, 1467, 1434, 1405, 1348, 1299, 1230, 1155, 1081, 1022, 887, 812, 748, 633.

UV-Vis (DCM, λ_{max} (nm)): 229, 250, 342.
CHN: found: C 40.07%, H 4.49%, N 10.00%.

4.7.6 Coordination with $Mn(OAc)_2 \cdot 4H_2O$ (2.22)

2,2'-Bipyridine-3,3'-(2-pyrazinecarboxamide) **(2.2)** (50.0 mg, 0.126 mmol) was placed into DCM (35 mL) and triethylamine (0.018 mL, 0.126 mmol). To this was added a solution of $Mn(OAc)_2 \cdot 4H_2O$ (127 mg, 0.518 mmol) dissolved in methanol (5 mL). The mixture was heated to reflux (60 °C) and stirred for 15 hrs. After this time the solvents were removed to afford a brown oil. The crude product was precipitated and dried via the addition of diethyl ether (15 mL). Collection by filtration, washing with water, and drying under vacuum yielded the compound as a brown crystalline powder. Yield 49.8 mg (48%).

MS (FAB, *m/z*): 961 $[Mn_2(\mathbf{L^2})_2OAc]^+$ (4.3%), 567 $[Mn_2(\mathbf{L^2})OAc]^+$ (17%).

IR (KBr, cm^{-1}): 3421 w, 3072, 2981, 2360, 1637 (C=O) sh, 1598, 1569, 1421, 1344, 1301, 1226, 1155, 1022, 954, 858, 808, 757, 688, 649.

UV-Vis (DCM, λ_{max} (nm)): 221, 245, 352.

CHN $C_{29}H_{27}N_8O_{11}Mn_3 \cdot 3MeOH \cdot 3H_2O$
calcd: C 39.28%, H 4.64%, N 11.45%.
found: C 39.47%, H 4.96%, N 11.41%.

4.7.7 Coordination with $CoCl_2 \cdot 6H_2O$ (2.23)

2,2'-Bipyridine-3,3'-(2-pyrazinecarboxamide) **(2.2)** (50.0 mg, 0.126 mmol) was placed into DCM (35 mL) and triethylamine (0.018 mL, 0.126 mmol). To this was added a solution of $CoCl_2 \cdot 6H_2O$ (123 mg, 0.518 mmol) dissolved in methanol (5 mL). The mixture was heated to reflux (60 °C) and stirred for 15 hrs. After this time the solvents

were removed to afford a red oil. The crude product was precipitated and dried via the addition of diethyl ether (15 mL). Collection by filtration, washing with water, and drying under vacuum yielded the compound as a red/brown crystalline powder. Yield 62.5 mg.

MS (FAB, *m/z*): 549 $[Co_2(\mathbf{L^2})Cl]^+$ (17%), 514 $[Co_2(\mathbf{L^2})]^+$ (52%).

IR (KBr, cm^{-1}): 3471, 3070, 2672, 2362, 1625 (C=O) sh, 1594, 1523, 1467, 1434, 1405, 1348, 1299, 1230, 1155, 1081, 1022, 887, 812, 748, 682, 630.

UV-Vis (DCM, λ_{max} (nm)): 229, 265.

4.7.8 Coordination with $Co(OAc)_2 \cdot 4H_2O$ (2.24)

2,2'-Bipyridine-3,3'-(2-pyrazinecarboxamide) **(2.2)** (50.0 mg, 0.126 mmol) was placed into DCM (35 mL) and triethylamine (0.018 mL, 0.126 mmol). To this was added a solution of $Co(OAc)_2 \cdot 4H_2O$ (129 mg, 0.518 mmol) dissolved in methanol (5 mL). The mixture was heated to reflux (60 °C) and stirred for 15 hrs. After this time the solvents were removed to afford a brown oil. The crude product was precipitated and dried via the addition of diethyl ether (15 mL). Collection by filtration, washing with water, and drying under vacuum yielded the compound as a brown crystalline powder. Yield 68.3 mg (69%).

MS (FAB, *m/z*): 573 $[Co_2(\mathbf{L^2})OAc]^+$ (19%), 513 $[Co_2(\mathbf{L^2})]^+$ (62%).

IR (KBr, cm^{-1}): 3400, 3072, 2981, 2360, 1642 (C=O) sh, 1598, 1569, 1421, 1344, 1301, 1226, 1155, 1022, 954, 858, 808, 757, 688.

UV-Vis (DCM, λ_{max} (nm)): 228, 260.

CHN $C_{27}H_{24}N_8O_9Co_3 \cdot 2H_2O$
calcd: C 39.68%, H 3.45%, N 13.71%.
found: C 39.36%, H 3.76%, N 14.01%.

4.8 – Synthesis of 2,2'-Bipyridine-3,3'-(Ethyl-2-Aminoacetate) (H_2L^3) (2.3)

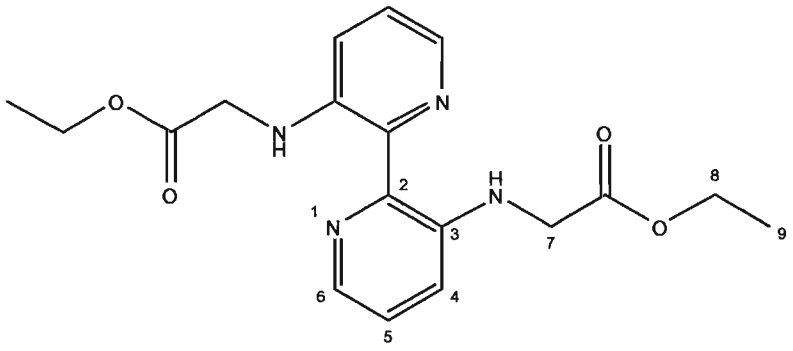

(2.3)

4.8.1 2,2'-Bipyridine-3,3'-(Ethyl-2-Aminoacetate) (H_2L^3)[130]

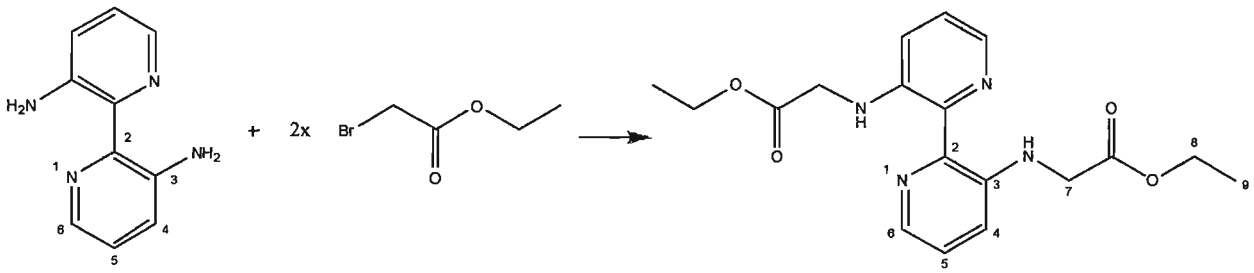

(1.17) **(2.3)**

3,3'-Diamino-2,2'-bipyridine **(1.17)** (0.466 g, 2.50 mmol) was dissolved in anhydrous acetonitrile (6.5 mL). *N,N*-Diisopropylethylamine (DIEA) (1.80 mL, 10.31 mmol) was added and the solution brought to 60 °C. Ethyl bromoacetate (0.553 mL, 5.00 mmol) was then added to the rapidly stirred solution over a 30 minute period. The resulting solution was stirred at 60 °C for 5 hrs. The solution was cooled to room temperature at which time the product precipitated and was collected by filtration. The crude product was washed with water (3 x 50 mL) and diethyl ether (3 x 50 mL) to yield the product as a bright-yellow light powder. Yield 0.487 g (54%). m.p. 189 °C.

^{1}H-NMR ($CDCl_3$, δ ppm): 10.16 (s, 2H, N-H), 8.02 (d, 2H, J = 3.6 Hz, 6-H), 7.15 (d, 2H, J = 2.5 Hz, 5-H), 6.90 (d, 2H, J = 1.5 Hz, 4-H), 4.28 (q, 4H, 8-H), 4.04 (s, 4H, 7-H), 1.33 (t, 6H, 9-H).

^{13}C-NMR ($CDCl_3$, δ ppm):	170.7 (C=O), 144.2 (2-C), 140.4 (3-C), 133.7 (6-C), 123.1 (4-C), 117.6 (5-C), 61.3 (8-C), 45.3 (7-C), 14.2 (9-C).
MS (EI, *m/z*):	358 $[M]^+$.
HRMS (EI, *m/z*):	$C_{18}H_{22}N_4O_4$ calcd: 358.1641; found: 358.1640.
IR (KBr, cm^{-1}):	3450 (N-H), 3043, 3040, 2985, 2939, 2890, 2836, 1745 (C=O) sh, 1585, 1486, 1432, 1403, 1365, 1213, 1149, 1027, 883, 846, 725, 632.
UV-Vis (DCM, λ_{max} (nm)), {log ε}:	231 {4.51}, 269 {4.41}, 383 {4.34}.
CHN	$C_{18}H_{22}N_4O_4$ calcd: C 60.32%, H 6.19%, N 15.63%. found: C 60.13%, H 6.04%, N 15.63%.

4.9 – Coordination of 2,2'-Bipyridine-3,3'-(Ethyl-2-Aminoacetate) (2.3)

4.9.1 Coordination with $CuCl_2 \cdot 2H_2O$ (2.27)

2,2'-Bipyridine-3,3'-(ethyl-2-aminoacetate) **(2.3)** (50.0 mg, 0.140 mmol) was dissolved in DCM (15 mL). To this solution was added $CuCl_2 \cdot 2H_2O$ (50.0 mg, 0.293 mmol) dissolved in methanol (5 mL). The mixture was stirred at room temperature for 15 hrs. Removal of the solvents under vacuum afforded a green solid which was washed with water (15 mL) and diethyl ether (15 mL) and finally dried under vacuum to yield the complex as a green crystalline powder. Yield 69.2 mg.

MS (FAB, *m/z*):	456 $[Cu(\mathbf{H_2L^3})Cl]^+$ (12%), 421 $[Cu(\mathbf{H_2L^3})]^+$ (32%).
IR (KBr, cm^{-1}):	3448 (N-H), 3071, 2652, 2322, 1740 (C=O) sh, 1564, 1523, 1467, 1434, 1405, 1348, 1299, 1225, 1155, 1081, 1022, 887, 812, 745, 670, 623.

UV-Vis (DCM, λ_{max} (nm)), {log ε}: 243 {4.50}, 283 {4.10}, 391 {3.93}.

CHN: found: C 35.08%, H 4.89%, N 8.48%.

4.9.2 Coordination with $Cu(OAc)_2 \cdot H_2O$ (2.25)

2,2'-Bipyridine-3,3'-(ethyl-2-aminoacetate) **(2.3)** (50.0 mg, 0.140 mmol) was dissolved in DCM (15 mL). To this solution was added $Cu(OAc)_2 \cdot H_2O$ (58.5 mg, 0.293 mmol) dissolved in methanol (5 mL). The mixture was stirred at room temperature for 15 hrs. Removal of the solvents under vacuum afforded a green solid which was washed with water (15 mL) and diethyl ether (15 mL) and finally dried under vacuum to yield the complex as a green crystalline powder. Yield 66.6 mg (88%).

MS (FAB, *m/z*): 480 $[Cu(\mathbf{H_2L^3})OAc]^+$ (30%), 421 $[Cu(\mathbf{H_2L^3})]^+$ (100%).

IR (KBr, cm^{-1}): 3421 w, 3117, 3050, 3040, 2985, 2939, 2890, 2836, 1735 (C=O) sh, 1565 sh, 1425 sh, 1400, 1365, 1213, 1149, 1037, 883, 846, 715, 602.

UV-Vis (DCM, λ_{max} (nm)), {log ε}: 234 {4.49}, 271 {4.08}, 392 {3.93}, 742 {2.92}.

CHN $C_{22}H_{28}N_4O_8Cu \cdot 4H_2O$
calcd: C 43.17%, H 5.93%, N 9.15%.
found: C 43.43%, H 5.73%, N 9.32%.

4.9.3 Coordination with $NiCl_2 \cdot 6H_2O$ (2.28)

2,2'-Bipyridine-3,3'-(ethyl-2-aminoacetate) **(2.3)** (50.0 mg, 0.140 mmol) was dissolved in DCM (15 mL). To this solution was added $NiCl_2 \cdot 6H_2O$ (69.7 mg, 0.293 mmol) dissolved in methanol (5 mL). The mixture was stirred at room temperature for 15 hrs. Removal of the solvents under vacuum afforded a yellow solid which was washed

with water (15 mL) and diethyl ether (15 mL) and finally dried under vacuum to yield the complex as a green/yellow powder. Yield 67.2 mg.

MS (FAB, *m/z*): 451 $[Ni(\mathbf{H_2L^3})Cl]^+$ (4.2%), 416 $[Ni(\mathbf{H_2L^3})]^+$ (6.5%).

IR (KBr, cm^{-1}): 3450 (N-H), 3116, 3060, 3040, 2985, 2939, 2890, 2836, 1745 (C=O) sh, 1585, 1486, 1432, 1403, 1365, 1213, 1149, 1027, 883, 846, 725, 632.

UV-Vis (DCM, λ_{max} (nm)), $\{\log \varepsilon\}$: 233 {4.51}, 273 {4.03}, 392 {3.92}.

4.9.4 Coordination with $Ni(OAc)_2 \cdot 4H_2O$ (2.29)

2,2'-Bipyridine-3,3'-(ethyl-2-aminoacetate) **(2.3)** (50.0 mg, 0.140 mmol) was dissolved in DCM (15 mL). To this solution was added $Ni(OAc)_2 \cdot 4H_2O$ (73.0 mg, 0.293 mmol) dissolved in methanol (5 mL). The mixture was stirred at room temperature for 15 hrs. Removal of the solvents under vacuum afforded a yellow solid which was washed with water (15 mL) and diethyl ether (15 mL) and finally dried under vacuum to yield the complex as a green/yellow powder. Yield 58.2 mg.

MS (FAB, *m/z*): 474 $[Ni(\mathbf{H_2L^3})OAc]^+$ (27%), 415 $[Ni(\mathbf{H_2L^3})]^+$ (100%).

IR (KBr, cm^{-1}): 3447 (N-H), 3126, 3059, 3039, 2985, 2939, 2890, 2836, 1742 (C=O) sh, 1585, 1485, 1430, 1403, 1365, 1213, 1149, 1027, 880, 845, 720, 630.

UV-Vis (DCM, λ_{max} (nm)), $\{\log \varepsilon\}$: 231 {4.48}, 273 {4.05}, 389 {3.92}.

CHN: found: C 39.14%, H 5.18%, N 7.38%.

4.9.5 Coordination with $MnCl_2$ (2.30)

2,2'-Bipyridine-3,3'-(ethyl-2-aminoacetate) **(2.3)** (50.0 mg, 0.140 mmol) was dissolved in DCM (15 mL). To this solution was added $MnCl_2$ (37.0 mg, 0.293 mmol) dissolved in methanol (5 mL). The mixture was stirred at room temperature for 15 hrs. Removal of the solvents under vacuum afforded a red solid which was washed with water (15 mL) and diethyl ether (15 mL) and finally dried under vacuum to yield the complex as a red crystalline powder. Yield 52.3 mg.

MS (FAB, *m/z*): 448 $[Mn(\mathbf{H_2L^3})Cl]^+$ (3.8%), 413 $[Mn(\mathbf{H_2L^3})]^+$ (15%).

IR (KBr, cm^{-1}): 3452 (N-H), 3126, 3045, 3040, 2975, 2929, 2889, 2836, 1741 (C=O) sh, 1585, 1486, 1432, 1413, 1355, 1213, 1149, 1017, 883, 845, 715.

UV-Vis (DCM, λ_{max} (nm)), {log ε}: 234 {4.52}, 272 {4.16}, 394 {3.91}.

CHN: found: C 41.42%, H 6.54%, N 9.42%.

4.9.6 Coordination with $Mn(OAc)_2 \cdot 4H_2O$ (2.31)

2,2'-Bipyridine-3,3'-(ethyl-2-aminoacetate) **(2.3)** (50.0 mg, 0.140 mmol) was dissolved in DCM (15 mL). To this solution was added $Mn(OAc)_2 \cdot 4H_2O$ (71.8 mg, 0.293 mmol) dissolved in methanol (5 mL). The mixture was stirred at room temperature for 15 hrs. Removal of the solvents under vacuum afforded a brown solid which was washed with water (15 mL) and diethyl ether (15 mL) and finally dried under vacuum to yield the complex as a beige powder. Yield 55.5 mg.

MS (FAB, *m/z*): 531 $[Mn(\mathbf{H_2L^3})(OAc)_2]^+$ (15%), 472 $[Mn(\mathbf{H_2L^3})OAc]^+$ (3.0%), 413 $[Mn(\mathbf{H_2L^3})]^+$ (4.2%).

IR (KBr, cm^{-1}): 3445 (N-H), 3120, 3060, 3040, 2985, 2939, 2890, 2836, 1740 (C=O) sh, 1585, 1486, 1422, 1413, 1365, 1213, 1149, 1127, 882, 836, 720.

UV-Vis (DCM, λ_{max} (nm)), {log ε}: 234 {4.50}, 271 {4.12}, 394 {3.90}.

CHN: found: C 38.50%, H 4.73%, N 5.97%.

4.9.7 Coordination with $CoCl_2 \cdot 6H_2O$ (2.26)

2,2'-Bipyridine-3,3'-(ethyl-2-aminoacetate) **(2.3)** (50.0 mg, 0.140 mmol) was dissolved in DCM (15 mL). To this solution was added $CoCl_2 \cdot 6H_2O$ (69.8 mg, 0.293 mmol) dissolved in methanol (5 mL). The mixture was stirred at room temperature for 15 hrs. Removal of the solvents under vacuum afforded a brown/green solid which was washed with water (15 mL) and diethyl ether (15 mL) and finally dried under vacuum to yield the complex as a green powder. Yield 52.3 mg (77%).

MS (FAB, *m/z*): 452 $[Co(\mathbf{H_2L^3})Cl]^+$ (17%), 417 $[Co(\mathbf{H_2L^3})]^+$ (6.3%).

IR (KBr, cm^{-1}): 3552 (O-H) sh, 3445 (N-H), 3116, 3060, 3040, 2985, 2939, 2890, 2836, 1742 (C=O) sh, 1585, 1486, 1432, 1403, 1365, 1213, 1149, 1027, 883, 846, 711.

UV-Vis (DCM, λ_{max} (nm)), {log ε}: 235 {4.52}, 271 {4.26}, 394 {4.11}, 628 {3.44}, 665 {3.47}, 697 {3.46}.

CHN $C_{18}H_{22}N_4O_4CoCl_2 \cdot 3H_2O \cdot 3MeOH$
calcd: C 39.51%, H 6.32%, N 8.78%.
found: C 39.51%, H 6.19%, N 9.07%.

4.9.8 Coordination with $Co(OAc)_2 \cdot 4H_2O$ (2.32)

2,2'-Bipyridine-3,3'-(ethyl-2-aminoacetate) **(2.3)** (50.0 mg, 0.140 mmol) was dissolved in DCM (15 mL). To this solution was added $Co(OAc)_2 \cdot 4H_2O$ (73.0 mg, 0.293 mmol) dissolved in methanol (5 mL). The mixture was stirred at room temperature for 15 hrs. Removal of the solvents under vacuum afforded a brown solid which was washed with water (15 mL) and diethyl ether (15 mL) and finally dried under vacuum to yield the complex as a brown powder. Yield 45.3 mg.

MS (FAB, *m/z*):	476 $[Co(\mathbf{H_2L^3})OAc]^+$ (1.6%), 417 $[Co(\mathbf{H_2L^3})]^+$ (54%).
IR (KBr, cm^{-1}):	3449 (N-H), 3116, 3060, 3040, 2985, 2939, 2890, 2836, 1739 (C=O) sh, 1585, 1486, 1432, 1403, 1365, 1213, 1149, 1027, 883, 846, 712.
UV-Vis (DCM, λ_{max} (nm)), {log ε}:	231 {4.50}, 275 {4.26}, 392 {3.96}.
CHN:	found: C 37.94%, H 4.58%, N 5.92%.

4.10 – Synthesis of 2,2'-Bipyridine-3,3'-(2-Aminoacetohydrazide) (H_2L^4) (2.4)

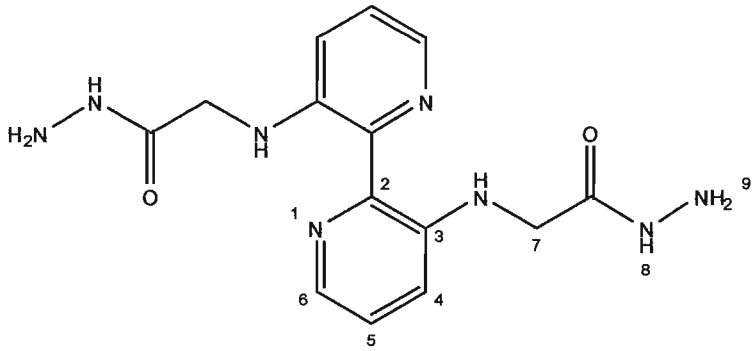

(2.4)

4.10.1 2,2'-Bipyridine-3,3'-(2-Aminoacetohydrazide) (H_2L^4) (2.4)[130]

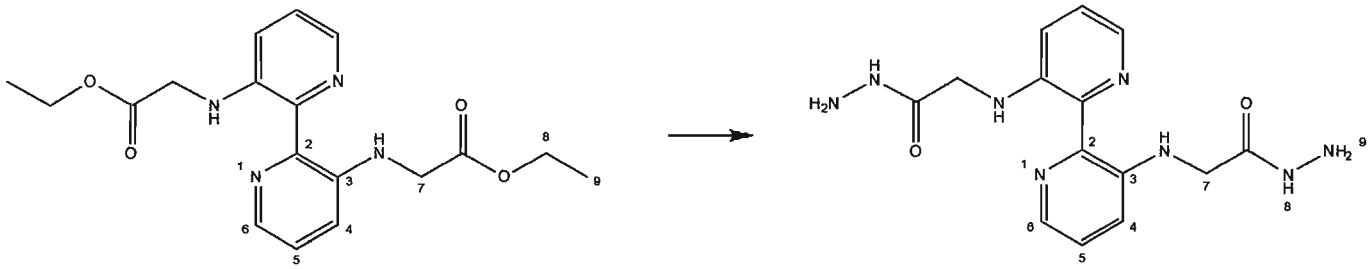

(2.3) **(2.4)**

2,2'-Bipyridine-3,3'-(ethyl-2-aminoacetate) (**2.3**) (0.179 g, 0.500 mmol) was dissolved in absolute ethanol (10 mL). To this was added hydrazine monohydrate (2 mL) and the yellow mixture heated to 75 °C for 12 hrs. The solution was brought to dryness via reduced pressure. The residue was washed with chloroform to yield the pure product as a light yellow powdery solid. Yield 0.102 g (62%). m.p. 245 °C.

^{1}H-NMR (D_2O, δ ppm): 7.96 (dd, 2H, J = 1.2 Hz, 6-H), 7.32 (dd, 2H, 5-H), 7.06 (dd, 2H, J = 2.5, 1.2 Hz, 4-H), 3.81 (s, 4H, 7-H).

^{13}C-NMR (D_2O, δ ppm): 171.8 (C=O), 142.4 (2-C), 140.0 (3-C), 137.8 (6-C), 125.4 (4-C), 120.2 (5-C), 45.3 (7-C).

MS (EI, *m/z*): 330 $[M]^+$.

HRMS (EI, *m/z*): $C_{14}H_{18}N_8O_2$ calcd: 330.1553; found: 330.1549.

IR (KBr, cm^{-1}):	3297 (N-H), 3124 (N-H), 3066, 3012, 2933, 2898, 2873, 1654 (C=O) sh, 1567, 1504, 1432, 1363, 1259, 1226, 1201, 1147, 1062, 973, 925, 800, 705, 601.
UV-Vis (MeOH, λ_{max} (nm)), {log ε}:	229 {4.40}, 265 {4.35}, 381 {4.06}.
CHN	$C_{14}H_{18}N_8O_2$ calcd: C 50.90%, H 5.49%, N 33.92%. found: C 50.51%, H 5.44%, N 33.63%.

4.11 – Coordination of 2,2'-Bipyridine-3,3'-(2-Aminoacetohydrazide) (H_2L^4) (2.4)

4.11.1 Coordination with $Cu(OAc)_2 \cdot H_2O$ (2.33)

2,2'-Bipyridine-3,3'-(2-aminoacetohydrazide) **(2.4)** (50.0 mg, 0.151 mmol) was dissolved in a mixture of MeOH (15 mL) and water (15 mL). To this solution was added $Cu(OAc)_2 \cdot H_2O$ (63.5 mg, 0.318 mmol) dissolved in methanol (5 mL). The mixture was stirred at room temperature for 15 hrs. Removal of the solvents under vacuum afforded a green/brown solid which was washed with water (15 mL) and diethyl ether (15 mL) and finally dried under vacuum to yield the complex as a green powder. Yield 66.3 mg.

MS (FAB, *m/z*):	531 $[Cu(\mathbf{H_2L^4})(OAc)_2H_2O]^+$ (10%), 392 $[Cu(\mathbf{H_2L^4})]^+$ (12%).
IR (KBr, cm^{-1}):	3421 w, 3050, 3040, 2983, 2935, 2890, 2836, 1637 (C=O) sh, 1567, 1427, 1328, 1205, 1159, 1018, 842, 809, 715, 680, 624.
UV-Vis (DCM, λ_{max} (nm)):	243, 287, 417.
CHN:	found: C 38.05%, H 5.11%, N 8.29%.

Project 2

4.12 – Synthesis of the Tetrairon^{III} Cluster and Tetrairon^{III} Cluster Derivatives

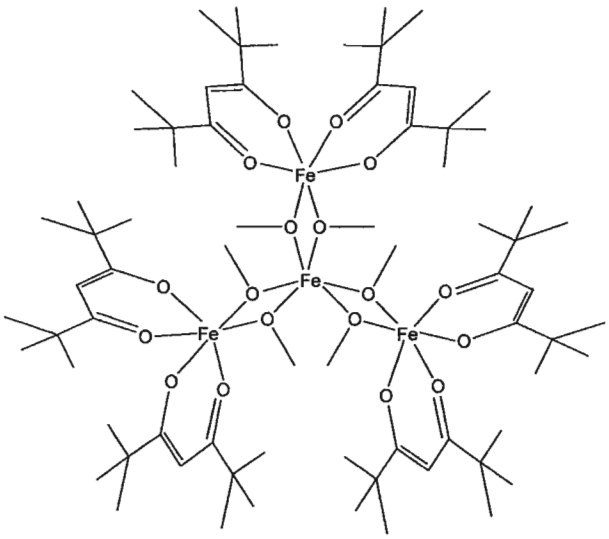

(1.4)

4.12.1 Synthesis of the Dimer iron^{III} compound (4.2)[48]

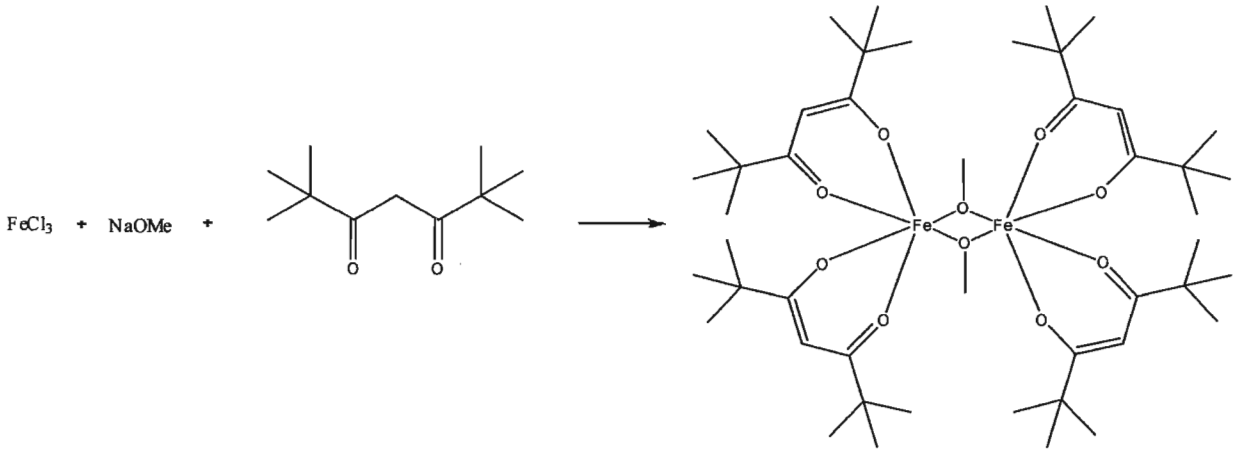

(4.2)

Preparation of NaOMe solution: To anhydrous methanol (8 mL) was added Na (0.544 g, 0.0237 mol) resulting in a 2.96 M solution. The addition of sodium was carried out *slowly* and *cautiously*.

$FeCl_3$ (0.519 g, 3.20 mmol) was dissolved in anhydrous methanol (40 mL) and stirred at room temperature for 15 mins. To this yellow solution was added drop-wise a

solution of 2.96 M NaOMe (4.00 mL, 11.8 mmol), Hdpm (1.37 mL, 6.40 mmol), and anhydrous methanol (10 mL). The resulting orange mixture was stirred at room temperature for 2 hrs. After this time the mixture was filtered and the residue washed with anhydrous methanol and dried under vacuum to yield the dimer iron^{III} compound. Yield 1.18 g (79%).

CHN $C_{46}H_{82}Fe_2O_{10}$ calcd: C 60.93%, H 9.11%.
found: C 61.01%, H 9.02%.

4.12.2 Synthesis of the Tetrairon^{III} Cluster (1.4)[48]

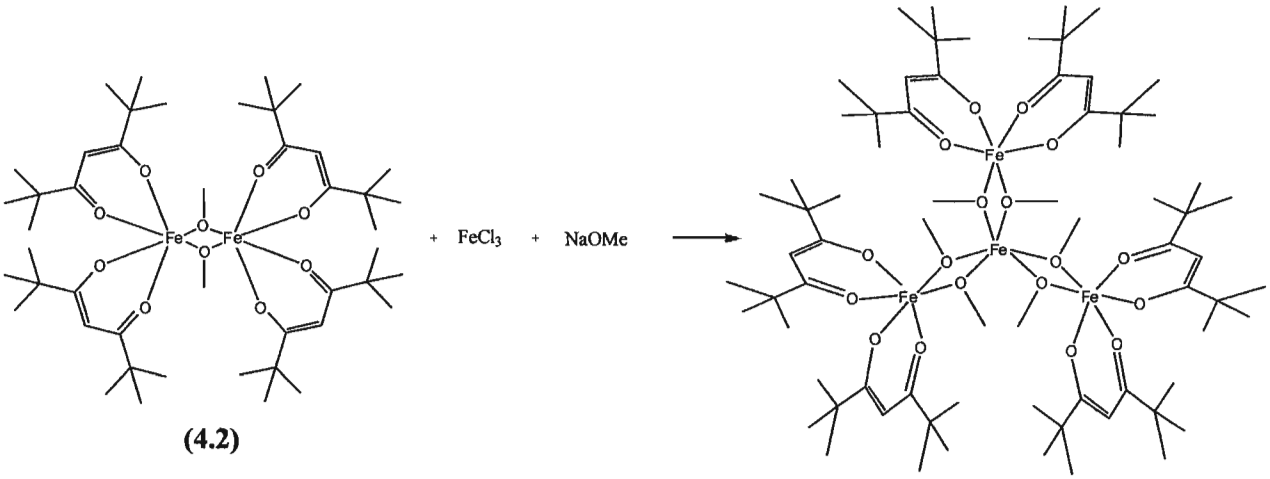

(4.2) **(1.4)**

The dimer iron^{III} compound **(4.2)** (0.500 g, 0.550 mmol) was dissolved in anhydrous MeOH:Et_2O (1:2, 46.5 mL). To this was added $FeCl_3$ (0.0595 g, 0.367 mmol) dissolved in anhydrous MeOH (5 mL). To this red mixture was then added 2.96 M NaOMe (0.375 mL, 1.10 mmol). The resulting yellow solution was stirred for 40 mins. The solution was then diluted with MeOH:Et_2O (1:4, 156 mL). The mixture was stirred for 15 mins and then filtered to remove formed NaCl. The resulting orange-yellow solution was partitioned into vials and either slow vapour diffusion of methanol in the

solution or slow evaporation of the solution resulted in yellow rod-like crystals of the tetrairon^{III} cluster.

CHN $C_{72}H_{132}Fe_4O_{18}$·MeOH: C 56.89%, H 8.89%.
found: C 56.49%, H 8.89%.

4.12.3 Tetrairon^{III} Cluster Derivative (3.22b)[48]

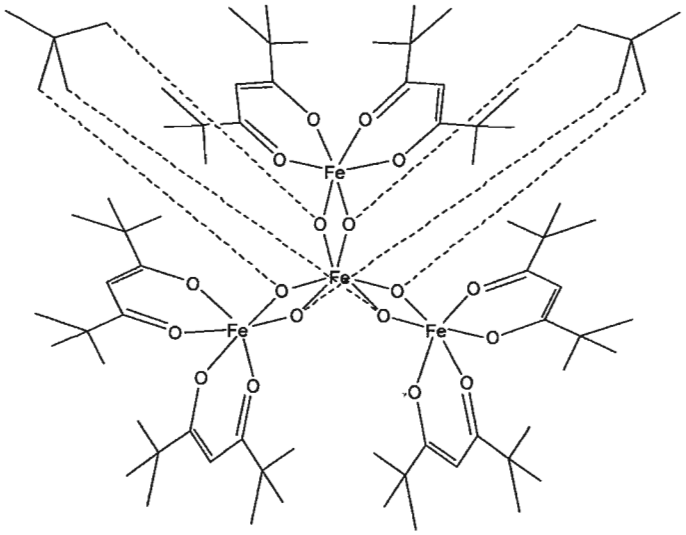

(3.22b)

The tetrairon^{III} cluster **(1.4)** (0.180 g, 0.119 mmol) was dissolved in anhydrous Et_2O (75 mL). This solution was treated with solid ligand **(3.22a)** (0.0350 g, 0.291 mmol). The solution was filtered and vapour diffusion of methanol resulted in the tetrairon^{III} cluster derivative as yellow-brown crystals. Yield 0.141 g (76%).

CHN $C_{76}H_{132}Fe_4O_{18}$ calcd: C 58.62%, H 8.54%.
found: C 58.69%, H 8.19%.

4.12.4 Tetrairon^{III} Cluster Derivative (3.23b)[48]

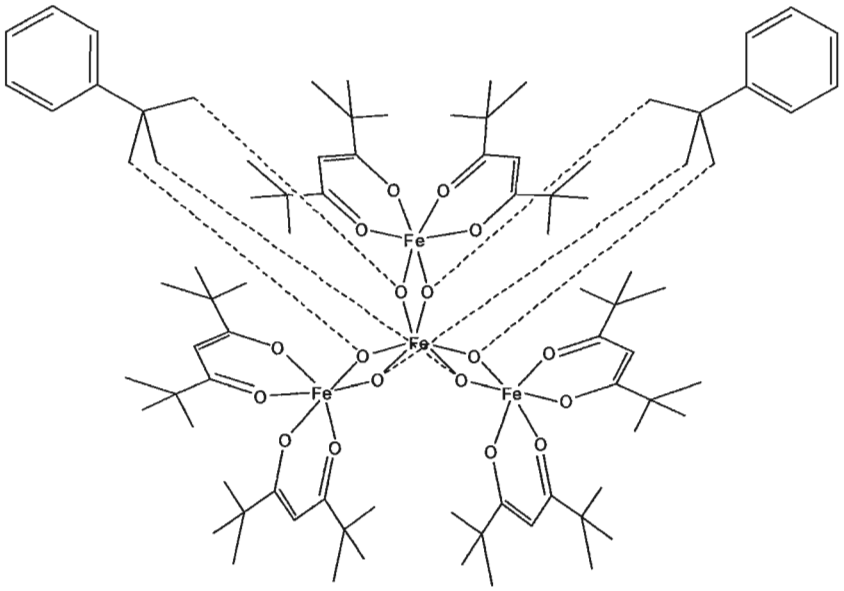

(3.23b)

The tetrairon^{III} cluster **(1.4)** (0.180 g, 0.119 mmol) was dissolved in anhydrous Et_2O (75 mL). This solution was treated with solid ligand **(3.23a)** (0.0587 g, 0.322 mmol). The solution was filtered and vapour diffusion of methanol resulted in the tetrairon^{III} cluster derivative as yellow-red crystals. Yield 0.162 g (78%). Crystals degraded when exposed to air.

4.12.5 Tetrairon^{III} Cluster Derivative (3.7b)[48]

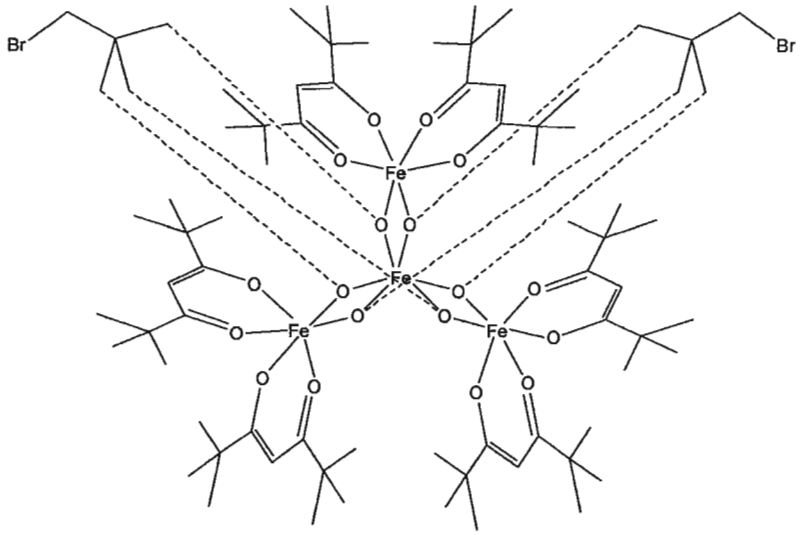

(3.7b)

The tetrairon^{III} cluster **(1.4)** (0.0400 g, 0.0265 mmol) was dissolved in anhydrous Et_2O (17 mL). This solution was treated with solid bromopentaerythritol **(3.7a)** (0.0145 g, 0.0728 mmol) and stirred for 30 mins. The solution was filtered and vapour diffusion of methanol resulted in the tetrairon^{III} cluster derivative as yellow-brown crystals. Yield 0.035 g (77%).

CHN $C_{76}H_{130}Fe_4O_{18}Br_2$ calcd: C 53.22%, H 7.64%.
found: C 53.10%, H 7.82%.

4.13 – Synthesis of Bromopentaerythritol (3.7a) and Protected Derivatives: 4-Bromomethyl-1-Methyl-2,6,7-Trioxabicyclo[2.2.2]octane (3.8) and 4-Bromomethyl-2,6,7-Trioxabicyclo[2.2.2]octane (3.12)

4.13.1 2-(Bromomethyl)-2-(Hydroxymethyl)-1,3-Propanediol, (Bromopentaerythritol) (3.7a)[138]

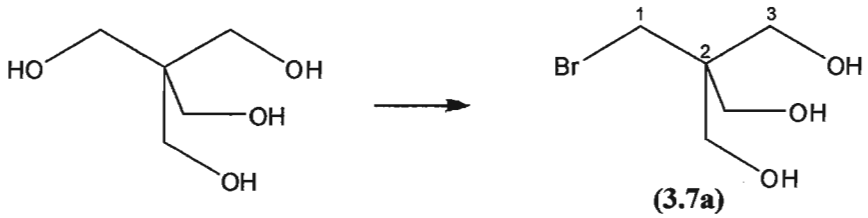

(3.7a)

Into a two neck 500 mL round bottom flask equipped with a condenser was added acetic acid (300 mL) and solid pentaerythritol (40.0 g, 0.294 mol). To this was added 48% hydrobromic acid (3.4 mL) and the mixture heated to reflux for 1 hr. Once the pentaerythritol was dissolved more 48% hydrobromic acid (34 mL) was added. The solution was refluxed at 100 °C for 3 hrs. After this time more 48% hydrobromic acid (19.2 mL) was added. The solution was again refluxed for 3 hrs. The solution was then allowed to cool to room temperature. The acetic acid was then removed as completely as possible via vacuum distillation. To the thick residue was added 95% ethanol (150 mL) and 48% hydrobromic acid (10 mL). The solution was then fractionally distilled to remove the ethanol/ethyl acetate azeotrope. Once 100 mL of distillate was collected another portion of 95% ethanol (150 mL) was added. The solution was again fractionally distilled until all of the solvent was removed. The residue was then placed under vacuum to completely remove the residual solvents. To the thick residue was added toluene (100 mL) which was distilled off at atmospheric pressure. This was repeated a second time. The very thick residue was then boiled for 5 hours in anhydrous diethyl ether (100 mL)

with frequent shaking (it was found advisable to break up any solid pieces with a glass rod). Once the mixture became white and granular it was filtered and the filtrate washed with cold diethyl ether (2 x 50 mL). The crude filtered product was recrystallized from chloroform/ethyl acetate (3:2) to yield the pure product as a white crystalline solid. Yield 17.5 g, (30%). m.p. 76 °C.

^{1}H-NMR ($CDCl_3$, δ ppm): 3.79 (d, 6H, J = 5.7 Hz, 3-H), 3.55 (s, 2H, 1-H), 2.10 (t, 3H, J = 5.4 Hz, O-H).

^{13}C-NMR ($CDCl_3$, δ ppm): 68.2 (3-C), 41.3 (2-C), 29.6 (1-C).

MS (EI, *m/z*): 200 $[M]^+$.

4.13.2 4-Bromomethyl-1-Methyl-2,6,7-Trioxabicyclo[2.2.2]octane (3.8)[139]

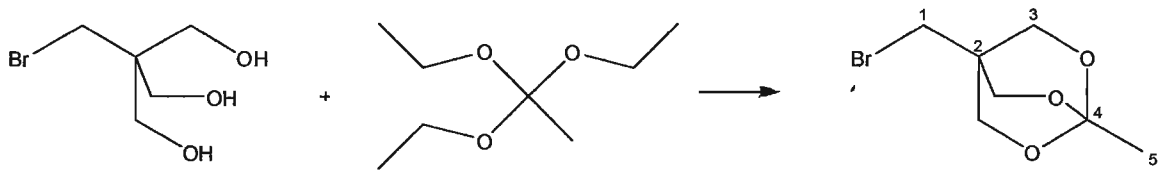

(3.7a) **(3.8)**

Bromopentaerythritol **(3.7a)** (1.00 g, 5.02 mmol) and a trace of *p*-toluenesulphonic acid (~14 mg) were dissolved in anhydrous toluene (5 mL). To this was added triethyl orthoacetate (0.93 mL, 5.07 mmol). The clear and colourless solution was heated to 95 °C for 12 hrs and the yielded ethanol was removed via simple distillation. The toluene was then removed via reduced pressure. The product was purified by sublimation (60 °C, 0.1 mmHg). The pure product was collected as sharp white crystals. Yield 0.560 g (50%). m.p. 51 °C.

^{1}H-NMR ($CDCl_3$, δ ppm): 4.04 (s, 6H, 3-H), 3.15 (s, 2H, 1-H), 1.49 (s, 3H, 5-H).

^{13}C-NMR ($CDCl_3$, δ ppm): 141.2 (4-C), 69.4 (3-C), 41.2 (2-C), 31.0 (1-C), 23.5 (5-C).

4.13.3 4-Bromomethyl-2,6,7-Trioxabicyclo[2.2.2]octane (3.12)[141]

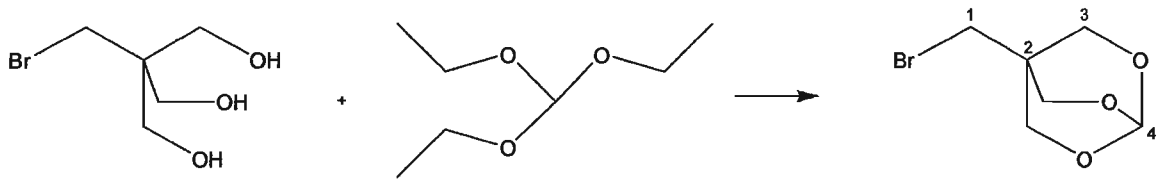

(3.7a) **(3.12)**

Bromopentaerythritol **(3.7a)** (1.00 g, 5.02 mmol) and a trace of *p*-toluenesulphonic acid (~14 mg) were dissolved in dioctyl phthalate (5 mL). To this was added anhydrous triethyl orthoformate (0.84 mL 5.07 mmol). The clear and colourless solution was heated to 95 °C for 12 hrs and the yielded ethanol was removed via simple distillation. The product was purified by sublimation (120 °C, 0.1 mmHg). The pure product was collected via a cold finger as a white crystalline powder. Yield 0.420 g (40%). m.p. 82 °C.

^{1}H-NMR ($CDCl_3$, δ ppm): 5.58 (s, 1H, 4-H), 4.05 (s, 6H, 3-H), 3.15 (s, 2H, 1-H).

^{13}C-NMR ($CDCl_3$, δ ppm): 120.4 (4-C), 69.9 (3-C), 40.2 (2-C), 31.2 (1-C).

4.14 – Porphyrin Syntheses: 5,10,15,20-Tetraphenylporphyin (TPP), 5-(Hydroxyphenyl)-10,15,20-(Triphenylporphyrin) (HPTPP), and 2,3,7,8,12,13,17,18-Octaethylporphyrin (OEP)

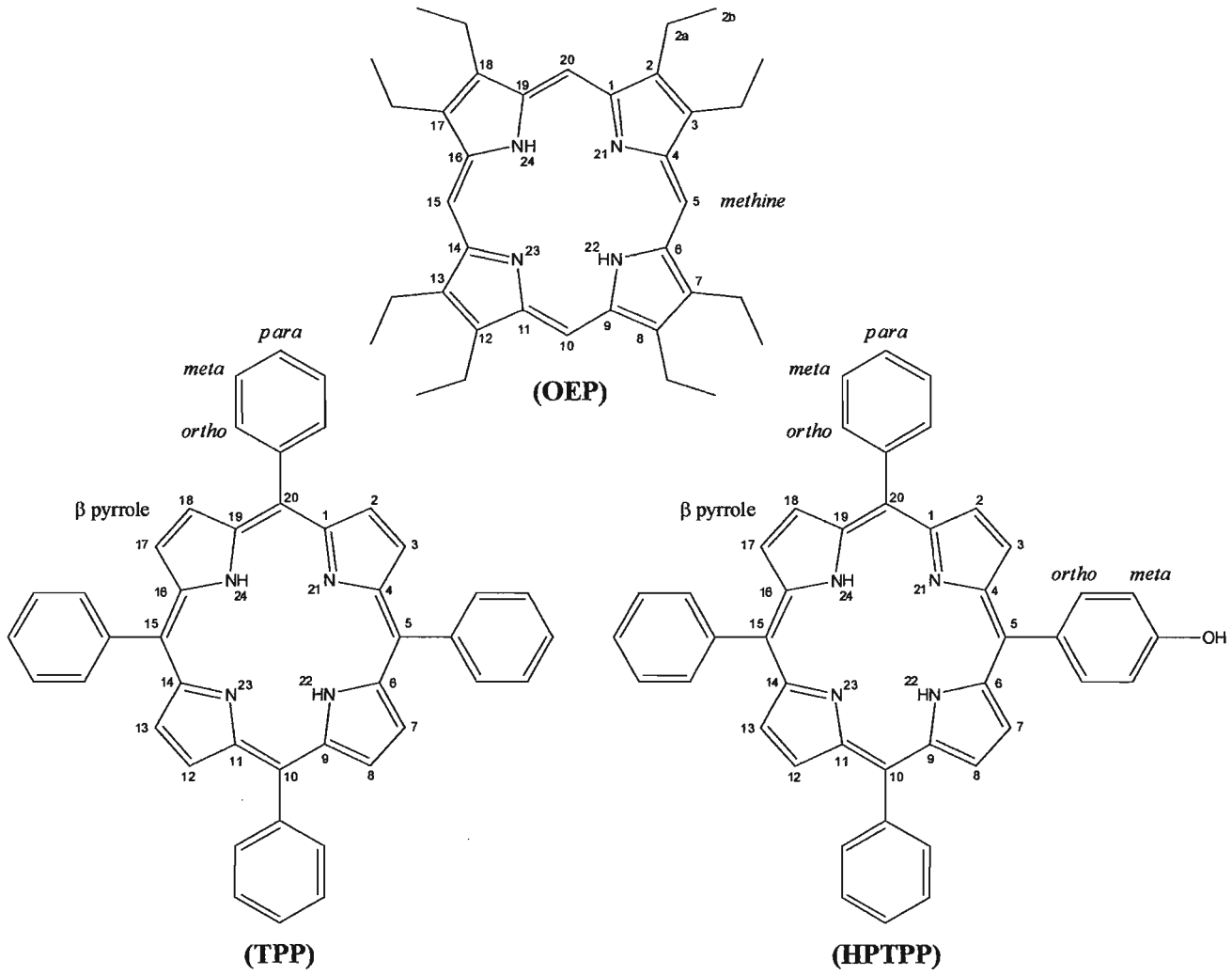

4.14.1 5,10,15,20-Tetraphenylporphyin (TPP) and 5-(Hydroxyphenyl)-10,15,20-(Triphenylporphyrin) (HPTPP)[136]

In air, 4-hydroxybenzaldehyde (4.07 g, 33.3 mmol) was dissolved in propionic acid (250 mL). Benzaldehyde (6.79 mL, 66.7 mmol) was added and the solution was heated to 125 °C. Pyrrole (6.94 mL, 99.9 mmol) was added and the mixture refluxed at 145 °C for 45 mins. The black mixture was then allowed to cool slightly (approx. 15

mins). Ethanol (40 mL) was then added and the solution was allowed to reach room temperature. The tarry liquid was then Buchner filtered and the resulting purple solid washed with ethanol (40 mL). The crude product was allowed to dry in air overnight. The crude product was purified via column chromatography on neutral alumina. The first cut was TPP eluted with chloroform (R_f = 0.88). HPTPP was eluted next with chloroform containing 5% methanol(R_f = 0.34). Crude porphyrin yield 2.20 g: TPP 0.781 g (5.1%); HPTPP 0.509 g (3.3%).

TPP;

^{1}H-NMR ($CDCl_3$, δ ppm): 8.86 (s, 8H, β-H), 8.24 (dd, 8H, H_{ortho}), 7.79 (m, 12H, H_{meta}, H_{para}), -2.76 (s, 2H, N-H).

MS (FAB, *m/z*): 614 $[M]^+$.

UV-Vis (DCM, λ_{max} (nm)): {log ε}: 419 {5.34}, 515 {4.41}, 551 {4.03}, 590 {3.89}, 647 {3.73}.

HPTPP;

^{1}H-NMR ($CDCl_3$, δ ppm): 8.89 (m, 8H, β-H), 8.24 (dd, 6H, H_{ortho}), 8.09 (d, 2H, H_{ortho}-OH), 7.76 (m, 9H, H_{meta}, H_{para}), 7.22 (d, 2H, H_{meta}-OH), -2.78 (s, 2H, N-H).

MS (FAB, *m/z*): 630 $[M]^+$.

UV-Vis (DCM, λ_{max} (nm)): {log ε}: 418 {5.35}, 516 {4.41}, 550 {4.08}, 589 {3.89}, 647 {3.89}.

4.14.2 2,3,7,8,12,13,17,18-Octaethylporphyrin (OEP)[144-148]

4.14.2.1 Synthesis of Potassium Ethyl Malonate (3.16)[145]

(3.16)

Diethyl malonate (50 g, 0.312 mol) was dissolved in absolute ethanol (200 mL). A solution of potassium hydroxide (17.5 g, 0.312 mol) in absolute ethanol (200 mL) was added drop-wise over one hour. Once the addition was complete the thick white slurry was allowed to stir overnight at room temperature. The solution was then evaporated to dryness and the residue washed with diethyl ether. The salt was collected via suction filtration and washed several times with ether (3 x 50 mL). The product was dried via vacuum and stored in a desiccator. Yield 45.6 g (85%).

^{1}H-NMR (D_2O, δ ppm): 4.06 (q, 2H), 3.15 (s, 2H), 1.12 (t, 3H).

4.14.2.2 Synthesis of Ethyl Propionylacetate (3.17)[146]

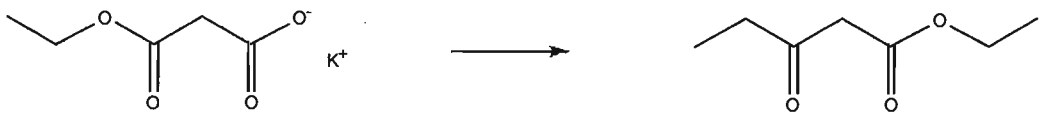

(3.16) **(3.17)**

Potassium ethyl malonate **(3.16)** (10 g, 58.7 mmol) was suspended in ethyl acetate (75 mL). The mixture was cooled in an ice bath and triethylamine (22.04 mL) was added. After stirring for 10 mins at 0 °C solid $MgCl_2$ (7.32 g) was added. The mixture was stirred at 0 °C for 2 hrs. After this time propionyl chloride (3.77 mL) was added drop-wise (care was taken not to let the temperature rise above 25 °C). The resulting mixture was stirred at room temperature for 12 hrs. The mixture was then placed into an ice bath.

HCl (2 N, 100 mL) was cautiously added, again not allowing the temperature to rise above 25 °C. The organic layer was separated and the aqueous layer back extracted with ethyl acetate. The combine organic layers were washed with HCl (2 N, 50 mL), water (2 x 100 mL), dried over Na_2SO_4, and evaporated to yield the product as clear and colourless oil. Yield 6.77 g (80%).

^{1}H-NMR ($CDCl_3$, δ ppm): 1.01 (K + E, t, 3H, J = 7 Hz), 1.23 (K + E, t, 3H, J = 7.5 Hz), 2.21 (E, q, 2H, J = 7.5 Hz), 2.54 (K, q, 2H, J = 7.5 Hz), 3.38 (K, s, 2H), 4.12 (K, q, 2H, J = 7.5 Hz), 4.15 (E, q, 2H, J = 7.5 Hz), 4.94 (E, s, 1H), 12.08 (E, br, OH).

K:E ratio approximately 9:1.

4.14.2.3 Synthesis of 4-Acetyl-2-Ethoxycarbonyl-3-Ethyl-5-Methylpyrrole (3.19a) Impurity: 2-Ethoxycarbonyl-3,5-Dimethylpyrrole (3.19b)[147]

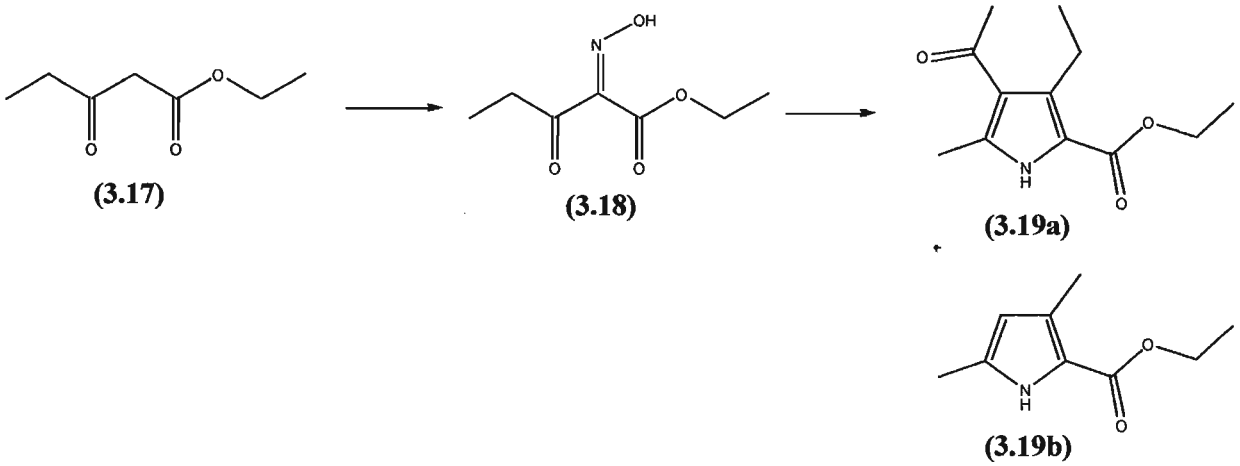

(3.17) **(3.18)** **(3.19a)** **(3.19b)**

A three neck flask equipped with two addition funnels, a condenser, and a gas inlet was setup and vacuum purged.

Ethyl propionylacetate **(3.17)** (6.00 g, 41.6 mmol) was dissolved in acetic acid (8.1 mL) in a round bottom flask. In a separate flask sodium nitrite (2.87 g, 41.6 mmol) was dissolved in water (4.5 mL). This sodium nitrite solution was added drop-wise to the

cooled ethyl propionylacetate solution (0 °C) at such a rate as to not allow the temperature to rise above 45 °C. Once the addition was complete this yielded the oxime **(3.18)** which was added to one of the addition funnels on the three neck flask. To the other funnel was added zinc dust (10.5 g, 0.161 mol) which was prepared into a thick slurry via the addition of water. To the three neck flask was added acetylacetone (6.08 mL, 59.5 mmol) and acetic acid (8.1 mL). The addition funnel of the oxime solution was opened and approximately 2 mL of solution was added to the main three neck flask. The addition of zinc from the other funnel resulted in an exothermic reaction. The reaction was allowed to proceed vigorously but not violently via the controlled addition from the two funnels. Half way through the addition more acetylacetone (2.03 mL, 20.0 mmol) and acetic acid (8.1 mL) were added. Once the reaction was complete the solution was immediately decanted while still hot and diluted to 4x its volume with water. The product oiled out then crystallized (approx. 3hrs). Once solid the crystals were filtered off with suction and washed copiously with water. The residue was dissolved in DCM and washed with water. The DCM solution was boiled and replaced with the addition of hexane. The pyrroles precipitated as white crystalline solids and were collected via filtration and washed with hexane. Yield 5.18 g (55%).

^{1}H-NMR ($CDCl_3$, δ ppm): 1.20 (t, 3H, J = 7.5 Hz), 1.38 (t, 3H, J = 7.5 Hz), 2.48 (s, 3H), 2.58 (s, 3H), 3.11 (q, 2H, J = 7.5 Hz), 4.36 (q, 2 H, J = 7.5 Hz), 10.58 (s, 1H).

Impurity, (3.19b)

^{1}H-NMR ($CDCl_3$, δ ppm): 1.36 (t, 3H, J = 7.5 Hz), 2.26 (s, 3H), 2.31 (s, 3H), 4.32 (q, 2H, J = 7.5 Hz), 5.78 (d, 1H, J = 3 Hz), 9.98 (s, 1H).

4.14.2.4 Synthesis of 2-Ethoxycarbonyl-3,4-Diethyl-5-Methylpyrrole (3.20)[147]

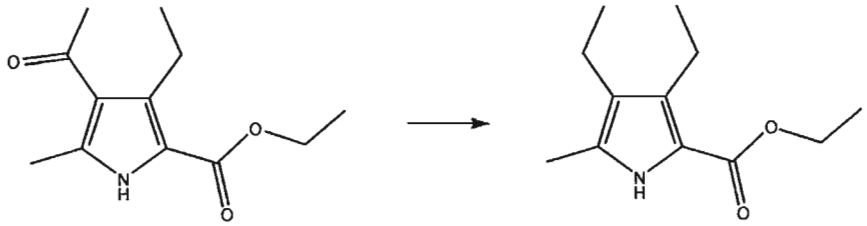

(3.19a) **(3.20)**

Into a three neck round bottom flask was placed crude 4-acetyl-2-ethoxycarbonyl-3-ethyl-5-methylpyrrole **(3.19a)** (contaminated with 2-ethoxycarbonyl-3,5-dimethylpyrrole **(3.19b)**) (1.5 g, 6.80 mmol) which was dissolved in anhydrous THF (10 mL). The solution was cooled to 0 °C before the addition of sodium borohydride (0.468 g, 12.4 mmol). The solution was stirred in the ice bath for 15 mins. After this time boron trifluoride etherate (2.4 g, 2.12 mL) was *slowly* added. The temperature of the reaction was kept below 10 °C. Once the addition was complete the mixture was stirred for 1 hr. The excess diborane was quenched with the cautious addition of acetic acid (6 mL) until gas evolution ceased. To the mixture was then added water (30 mL). The organic phase was separated, filtered and brought to dryness. The brown oil was dissolved in 95% ethanol (50 mL). To this was added diethylamine (0.38 mL), 37% aqueous formaldehyde (0.38 mL), and 1 drop of conc. HCl. The solution was refluxed for 12 hrs. The solution was then brought to dryness and dissolved in ether. The organic layer was washed with water (100 mL), 5% HCl acid (2x 100 mL), and finally water (100 mL). The ether solution was dried over Na_2SO_4 and brought to dryness to yield the pure reduced pyrrole. Yield 1.18 g (84%). m.p. 76 °C.

^{1}H-NMR ($CDCl_3$, δ ppm): 1.07 (t, 3H, J = 7.6 Hz), 1.14 (t, 3H, J = 7.6 Hz) 1.34 (t, 3H, J = 7.6 Hz), 2.21 (s, 3H) 2.36 (q, 2H, J = 7.6 Hz), 2.77 (q,

2H, J = 7.6 Hz), 4.29 (q, 2H, J = 7.6 Hz), 8.55 (br, 1H, N-H).

4.14.2.5 Synthesis of 5-*N*,*N*-Diethylaminomethyl-2-Ethoxycarbonyl-3,4-Diethylpyrrole (3.21)[144,147]

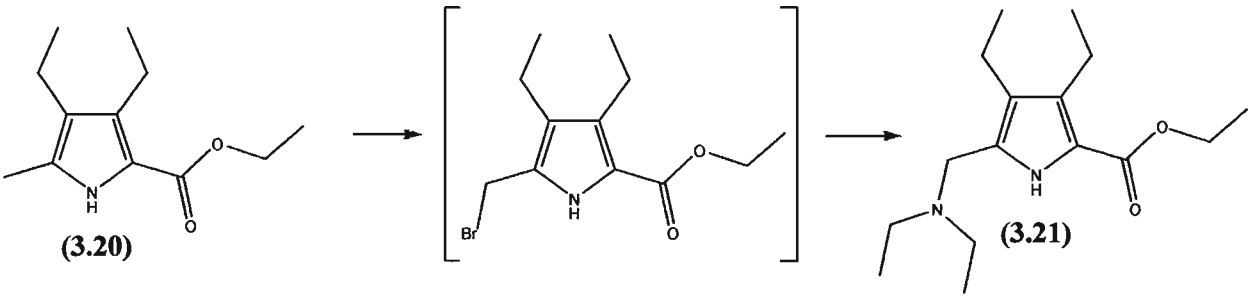

In a round bottom flask was added 2-ethoxycarbonyl-3,4-diethyl-5-methylpyrrole **(3.20)** (1.0 g, 4.78 mmol) dissolved in absolute ether (14 mL). To this was added drop-wise and rapidly a solution of bromine (0.705 g, 0.25 mL, 8.82 mmol) in anhydrous DCM (3 mL). The mixture refluxed. After the addition the solution was stirred for 20 mins. Diethylamine (1.6 mL, 15.5 mmol) in absolute ether (5 mL) was then added to the rapidly stirring solution. The mixture refluxed. Once added the solution was stirred for 30 mins. Water was then added and the organic phase separated. The organic phase was washed with water then excess crushed ice added. The product was extracted via the addition of ice-cold 3.7% HCl (10 mL), the aqueous phase was washed with ether then the product regenerated by the addition into 15% NH_4OH (25 mL). The product which immediately oiled out was extracted with petroleum ether, washed with water, and dried over Na_2SO_4 to yield the product as yellow oil. Yield 1.01 g (75%).

^{1}H-NMR ($CDCl_3$, δ ppm): 1.00 (t, 6H, J = 7.2 Hz), 1.05 (t, 3H, J = 7.5 Hz), 1.12 (t, 3H, J = 7.5 Hz), 1.32 (t, 3H, J = 7.5 Hz), 2.38 (q, 2H, J = 7.5 Hz), 2.48 (q, 4H, J = 7.2 Hz), 2.70 (q, 2H, J = 7.5 Hz), 3.48 (s, 2H), 4.26 (q, 2H, J = 7.5 Hz), 9.43 (br, 1H, N-H).

4.14.2.6 Synthesis of Octaethylporphyrin (OEP)[144,147]

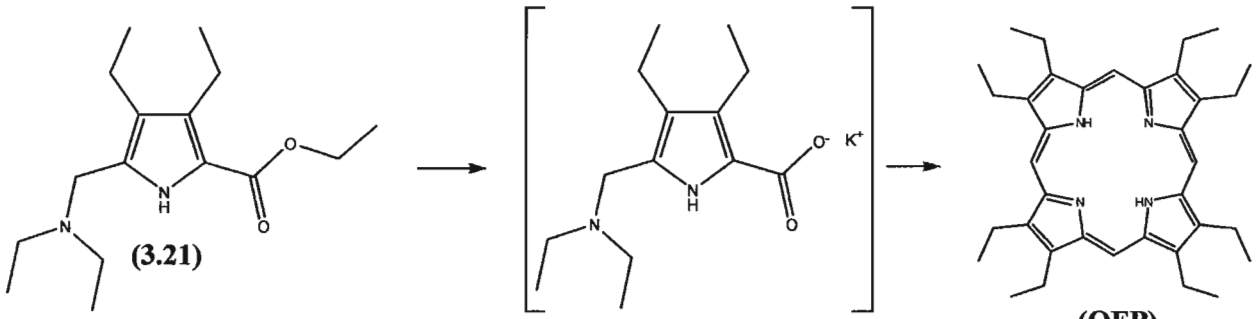

5-*N*,*N*-Diethylaminomethyl-2-ethoxycarbonyl-3,4-diethylpyrrole **(3.21)** (0.5 g, 1.78 mmol) was dissolved in 95% ethanol (3 mL). This solution was treated with KOH (0.236 g, 4.21 mmol) in water (1 mL). The mixture was stirred and heated at 100 °C for 3 hrs. The solution was then diluted to 5 mL with water and cooled in an ice bath. Acetic acid (3.5 mL) was then added and the mixture heated to reflux. When the solution had become very dark air was bubbled through the mixture. After boiling for 1 hr (after which time the volume was reduced by half) an equal volume of methanol was added. Once cool the product precipitated and was collected via filtration. The residue was washed with methanol to yield OEP. Yield 0.120 g (50%). m.p. >300 °C.

^{1}H-NMR ($CDCl_3$, δ ppm): 10.13 (s, 4H, $H_{methine}$), 4.15 (q, 16H, J = 8.4 Hz, 2a-H), 1.95 (t, 24H, J = 8.4 Hz, 2b-H), -3.70 (s, 2H, N-H).

^{13}C-NMR ($CDCl_3$, δ ppm): 120.2, 119.6, 118.3, 46.3, 25.3.

MS (FAB, *m/z*): 534 $[M]^+$.

IR (KBr, cm^{-1}): 3307 (N-H), 3070, 2964, 2869, 1459, 1211, 1105, 1056, 1008, 950, 819, 738, 667.

UV-Vis (DCM, λ_{max} (nm)): {log ε}: 400 {5.20}, 498 {4.32}, 534 {4.22}, 566 {4.06}, 620 {3.91}.

4.14.3 HPTPP Bicyclic Ortho Ester (3.9)

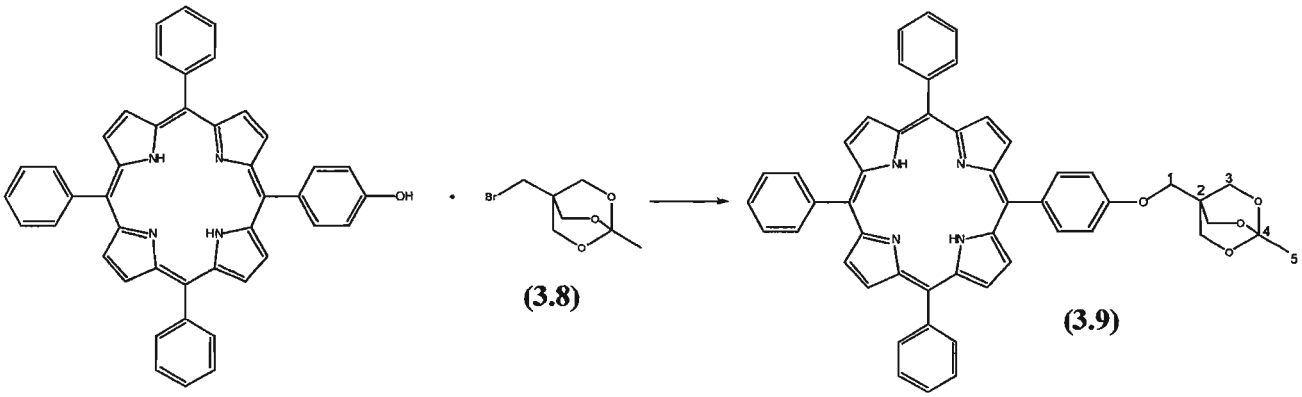

(HPTPP)

HPTPP (0.350 g, 0.555 mmol) was dissolved in anhydrous DMF (40 mL). To this was added solid NaH (0.0533 g, 2.22 mmol) and the mixture stirred at room temperature for 30 mins. Freshly sublimed 4-bromomethyl-1-methyl-2,6,7-trioxabicyclo[2.2.2]octane **(3.8)** (0.186 g, 0.832 mmol) was added and the mixture heated to 70 °C for 24 hrs. The solution was then cooled to room temperature. The solution was quenched with water and was then extracted with DCM and dried over sodium sulphate. Removal of the solvents (DCM via rotary and DMF via high vacuum) yielded the crude HPTPP bicyclic ortho ester **(3.9)** contaminated with unreacted 4-bromomethyl-1-methyl-2,6,7-trioxabicyclo[2.2.2]octane. Purification was achieved via chromatography on neutral

alumina. Unreacted 4-bromomethyl-1-methyl-2,6,7-trioxabicyclo[2.2.2]octane **(3.8)** was eluted by EtOAc:Hexane (1:9) (R_f = 0.42). HPTPP bicyclic ortho ester **(3.9)** was eluted via EtOAc:Hexane (9:1) (R_f = 0.49). Yield 0.322 g (75%).

^{1}H-NMR ($CDCl_3$, δ ppm):	8.87 (m, 8H, β-H), 8.24 (d, 6H, J = 7.2 Hz, H_{ortho}), 8.15 (d, 2H, J = 7.2 Hz, H_{ortho}-OH), 7.78 (m, 9H, H_{meta}, H_{para}), 7.25 (d, 2H, J = 7.2 Hz, H_{meta}-OH), 4.34 (s, 6H, 3-H), 4.06 (s, 2H, 1-H), 1.57 (s, 3H, 5-H), -2.76 (s, 2H, N-H).
^{13}C-NMR ($CDCl_3$, δ ppm):	158.0, 142.2, 135.6, 134.6, 127.8, 126.7, 120.2, 112.5, 108.9, 69.41, 66.6, 34.9, 23.5.
MS (FAB, *m/z*):	773 $[M]^+$.
UV-Vis (DCM, λ_{max} (nm)): {log ε}:	419 {5.31}, 516 {4.38}, 551 {4.07}, 591 {3.86}, 646 {3.84}.
CHN	$C_{51}H_{40}N_4O_4$ calcd: C 79.25%, H 5.22%, N 7.25%. found: C 79.00%, H 5.00%, N 7.18%.

4.14.4 HPTPP Bicyclic Ortho Ester (3.13)

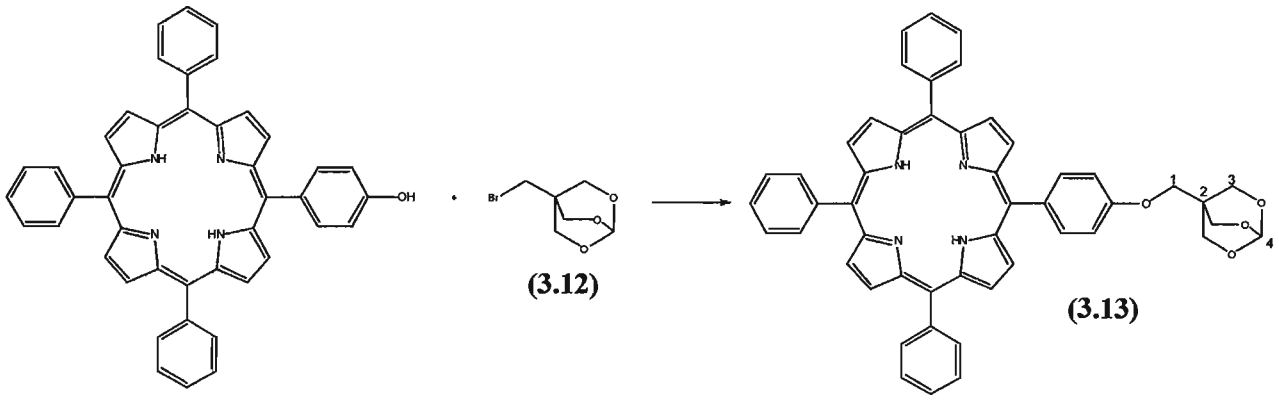

(HPTPP) **(3.12)** **(3.13)**

HPTPP (0.350 g, 0.555 mmol) was dissolved in anhydrous DMF (40 mL). To this was added solid NaH (0.0533 g, 2.22 mmol) and the mixture stirred at room temperature for 30 mins. Freshly sublimed 4-bromomethyl-2,6,7-trioxabicyclo[2.2.2]octane **(3.12)** (0.174 g, 0.832 mmol) was added and the mixture heated to 70 °C for 24 hrs. The solution was then cooled to room temperature. The solution was quenched with water and was then extracted with DCM and dried over sodium sulphate. Removal of the solvents (DCM via rotary and DMF via high vacuum) yielded the crude HPTPP bicyclic ortho ester **(3.13)** contaminated with unreacted 4-bromomethyl-2,6,7-trioxabicyclo[2.2.2]octane. Purification was achieved via chromatography on neutral alumina. Unreacted 4-bromomethyl-2,6,7-trioxabicyclo[2.2.2]octane **(3.12)** was eluted by EtOAc:Hexane (1:9) (R_f = 0.42). HPTPP bicyclic ortho ester **(3.13)** was eluted via EtOAc:Hexane (9:1) (R_f = 0.50). Yield 0.291 g (62%).

^{1}H-NMR ($CDCl_3$, δ ppm):	8.86 (m, 8H, β-H), 8.21 (d, 6H, H_{ortho}), 8.14 (d, 2H, H_{ortho}-OH), 7.79 (m, 9H, H_{meta}, H_{para}), 7.24 (d, 2H, H_{meta}-OH), 5.62 (s, 1H, 4-H), 4.34 (s, 6H, 3-H), 4.06 (s, 2H, 1-H), -2.76 (s, 2H, N-H).
^{13}C-NMR ($CDCl_3$, δ ppm):	158.1, 142.1, 135.6, 127.8, 126.7, 120.2, 119.5, 115.4, 112.5, 108.8, 69.4, 66.5, 34.9.
MS (FAB, *m/z*):	759 $[M]^+$.
IR (KBr, cm^{-1}):	3318 (N-H), 3035, 2929, 2869, 1602, 1471, 1353, 1151, 1045, 998, 962, 796, 738, 701.
UV-Vis (DCM, λ_{max} (nm)): {log ε}:	419 {5.31}, 516 {4.38}, 551 {4.07}, 591 {3.86}, 646 {3.84}.

CHN $C_{50}H_{38}N_4O_4$ calcd: C 79.14%, H 5.05%, N 7.38%.
found: C 78.96%, H 5.00%, N 7.13%.

4.14.5 HPTPP Triol (3.10)

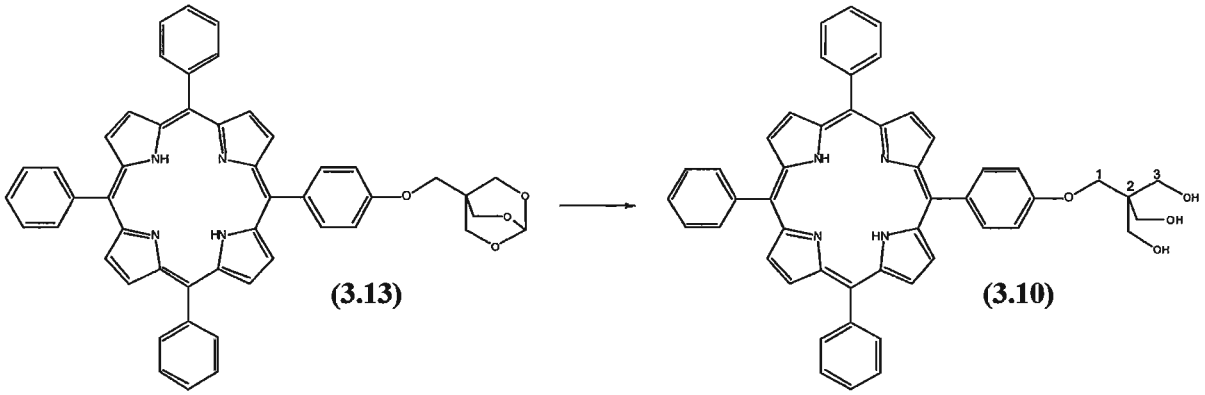

(3.13) **(3.10)**

HPTPP bicyclic ortho ester **(3.13)** (0.250 g, 0.329 mmol) was added to methanol (45 mL). To this was added water (5 mL) and 1 drop of 1 N HCl. The mixture was refluxed for 3 hrs and then allowed to cool to room temperature. To the green solution was added $NaHCO_3$ (0.00g, 0.250 mmol) and was stirred for 3 hrs longer. The purple solution was evaporated to dryness, extracted into anhydrous DCM and filtered. Evaporation of the DCM solution yielded the HPTPP triol Yield 0.241 g (98%).

^{1}H-NMR ($CDCl_3$, δ ppm): 8.86 (m, 8H, β-H), 8.21 (d, 6H, H_{ortho}), 8.14 (d, 2H, H_{ortho}-OH), 7.79 (m, 9H, H_{meta}, H_{para}), 7.31 (d, 2H, H_{meta}-OH), 4.36 (s, 2H, 1-H), 4.06 (d, 6H, 3-H), 2.38 (s, 3H, O-H), -2.76 (s, 2H, N-H).

^{13}C-NMR ($CDCl_3$, δ ppm): 158.1, 142.1, 135.6, 127.8, 126.7, 120.2, 115.4, 112.5, 108.8, 69.0, 66.5, 48.2.

MS (FAB, *m/z*): 748 $[M]^+$.

IR (KBr, cm^{-1}): 3421 (O-H), 3309 (N-H), 3050, 2954, 2873, 1473, 1247, 991, 798, 700, 653.

UV-Vis (DCM, λ_{max} (nm)): {log ε}: 419 {5.31}, 516 {4.38}, 551 {4.07}, 591 {3.86}, 646 {3.83}.

CHN $C_{49}H_{40}N_4O_4$ calcd: C 78.59%, H 5.38%, N 7.48%. found: C 78.64%, H 5.33%, N 7.83%.

4.14.6 [Zn(HPTPP-$CH_2C(CH_2OH)_3$)] (3.1)

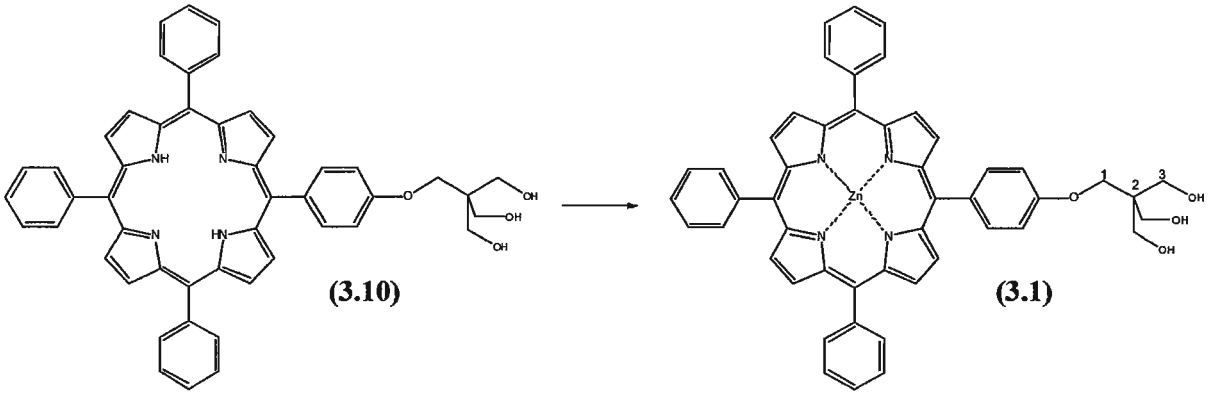

HPTPP triol **(3.10)** (0.150 g, 0.200 mmol) was dissolved in DMF. To this was added solid $Zn(OAc)_2 \cdot 2H_2O$ (0.63 g) and the mixture refluxed for 30 mins. After cooling at 4 °C for 1 hr the solution was filtered and the residue copiously washed with water to yield the ZnHPTPP triol **(3.1)**. Yield 0.158 g (97%).

^{1}H-NMR ($CDCl_3$, δ ppm): 8.86 (m, 8H, β-H), 8.21 (d, 6H, H_{ortho}), 8.14 (d, 2H, H_{ortho}-OH), 7.79 (m, 9H, H_{meta}, H_{para}), 7.31 (d, 2H, H_{meta}-OH), 4.36 (s, 2H, CH_2), 4.06 (d, 6H, CH_2O-), 2.38 (s, 3H, O-H).

MS (FAB, *m/z*): 813 $[M]^+$.

IR (KBr, cm^{-1}): 3415 (O-H), 3035, 2940, 2869, 1508, 1436, 1328, 998, 808, 701, 650.

UV-Vis (DCM, λ_{max} (nm)): {log ε}: 420 {5.34}, 548 {4.37}, 587 {3.64}.

CHN $C_{49}H_{38}N_4O_4Zn$ calcd: C 72.46%, H 4.72%, N 6.90%. found: C 72.09%, H 4.51%, N 7.00%.

4.14.7 $[P(TPP)Cl_2]^+Cl^-$ (3.14)[142]

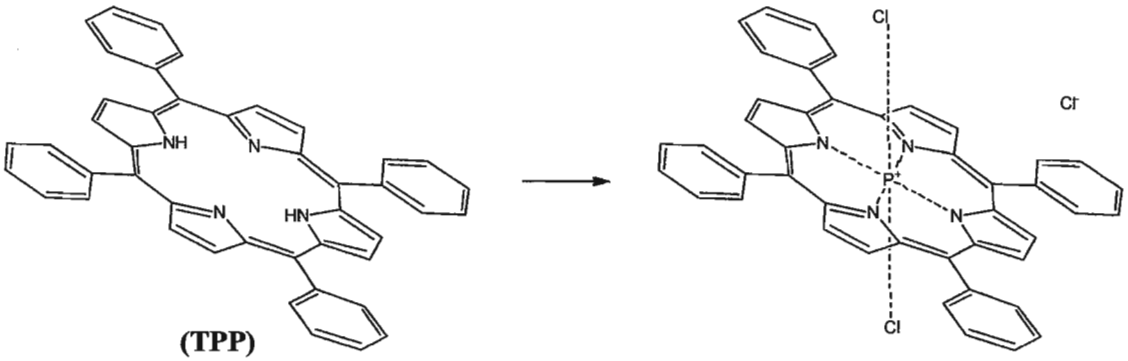

(TPP) **(3.14)**

TPP (1.00 g, 1.63 mmol) was dissolved in freshly distilled pyridine (50 mL). To this was added $POCl_3$ (9.1 mL, 97.6 mmol) and the solution refluxed at 120 °C for 24 hrs. The solution was brought to dryness and dissolved in a minimal amount of DCM. The residue was then chromatographed on neutral alumina. First cut eluted with DCM was free base TPP(R_f = 0.82). Phosphorus TPP chloride was eluted with DCM: MeOH (5% MeOH) (R_f = 0.58). Yield 0.156 g (12%).

^{1}H-NMR ($CDCl_3$, δ ppm): 9.02 (m, 8H, β-H), 8.54 (dd, 8H, H_{ortho}), 7.76 (m, 12H, H_{meta}, H_{para}).

^{31}P-NMR ($CDCl_3$, δ ppm): -229.0.

MS (FAB, *m/z*): 750 $[M]^+$.

IR (KBr, cm^{-1}): 3050, 2906, 2858, 1633, 1442, 1232, 1022, 750, 684,

425 (P-Cl).

UV-Vis (DCM, λ_{max} (nm)):
{log ε}: 439 {5.46}, 567 {4.15}, 612 {4.00}.

4.14.8 $[P(TPP)(OCH_2C(CH_2OH)_3)_2]^+Cl^-$ (3.2)

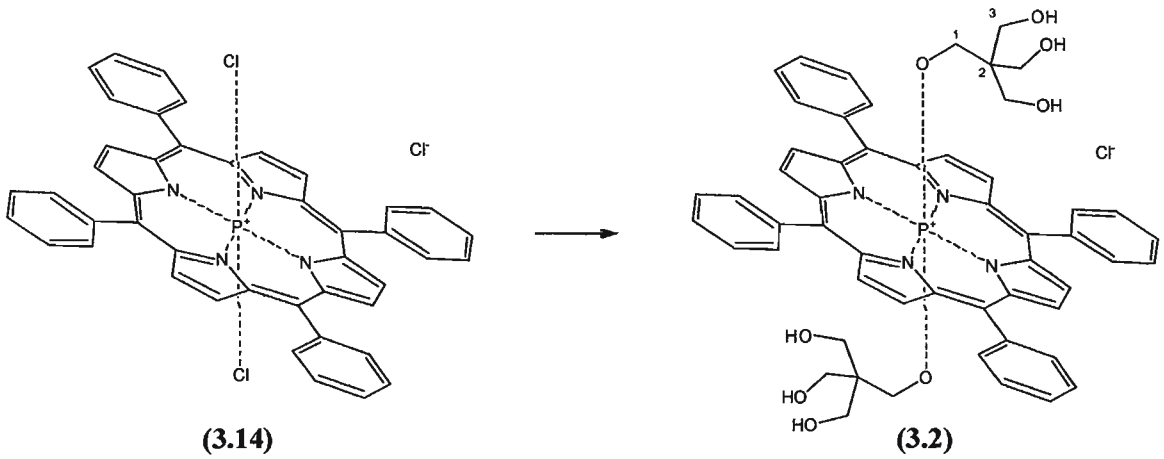

(3.14) **(3.2)**

$[P(TPP)Cl_2]^+Cl^-$ **(3.14)** (0.100 g, 0.133 mmol) was dissolved in freshly distilled pyridine (25 mL). To this was added an excess of solid pentaerythritol (2.18 g, 16.0 mmol). The resulting mixture was refluxed at 120 °C for 48 hrs. The solvent was then removed and the residue washed copiously with water and dried under vacuum. The crude product was extracted into anhydrous methanol, filtered, evaporated, and dried under vacuum to yield $[P(TPP)(OCH_2C(CH_2OH)_3)_2]^+Cl^-$ **(3.2)**. Yield 0.0783 g (62%).

^{1}H-NMR (MeOD, δ ppm): 9.22 (m, 8H, β-H), 8.30 (dd, 8H, H_{ortho}), 7.86 (m, 12H, H_{meta}, H_{para}), 1.07 (s, 12H, 3-H), -2.41 (d, 4H, 1-H).

^{31}P-NMR (MeOD, δ ppm): -177.0.

MS (FAB, *m/z*): 950 $[M]^+$, 915 ($[M]^+$ - Cl).

IR (KBr, cm^{-1}): 3343 (O-H), 3095, 2929, 2869, 1602, 1436, 1022, 819 (P-O) sh, 750, 701, 607.

UV-Vis (DCM, λ_{max} (nm)):
{log ε}: 430 {5.45}, 560 {4.37}, 602 {3.65}.

CHN: $C_{54}H_{50}N_4O_8PCl$ calcd: C 68.31%, H 5.31%, N 5.90%.
found: C 68.00%, H 5.06%, N 5.57%.

4.14.9 $[P(OEP)(C_6H_5)Cl]^+Cl^-$ (3.15)[149] and $[P(OEP)(C_6H_5)(OCH_2C(CH_2OH)_3)]^+Cl^-$ (3.3)

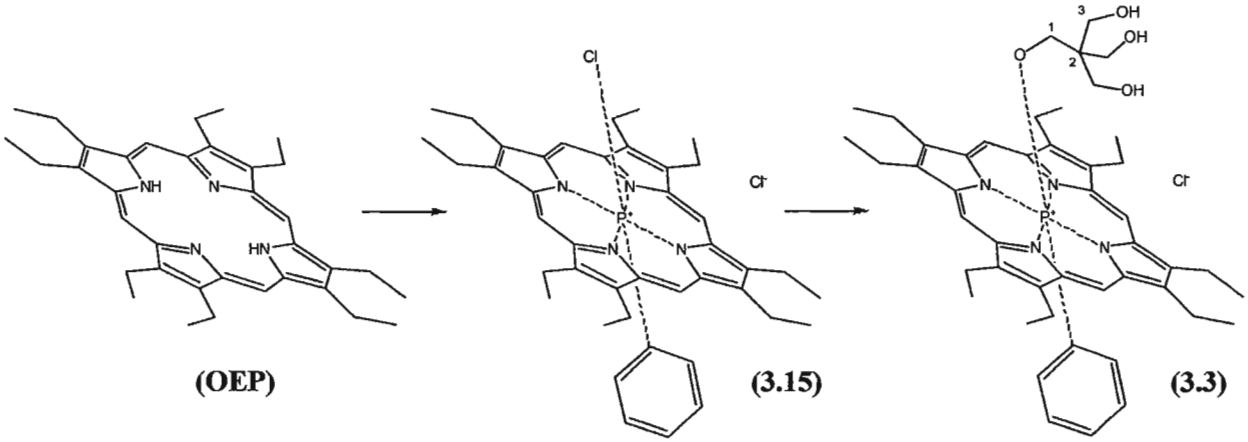

(OEP) **(3.15)** **(3.3)**

OEP (0.0500 g, 0.0935 mmol) was dissolved in anhydrous DCM (5 mL) and 2,6-dimethylpyridine (lutidine) (0.2 mL). To this was added *P,P*-dichlorophenylphosphine ($PhPCl_2$) (0.031 mL, 0.230 mmol) and the mixture refluxed for 36 hrs (occasionally more DCM was added). The solution was then brought to dryness to yield crude $[P(OEP)(C_6H_5)Cl]^+Cl^-$ **(3.15)**. To the residue was added pentaerythritol (0.763 g, 5.61 mmol) and anhydrous DCM (5 mL). The mixture was stirred at room temperature for 2 hours. Removal of the solvent yielded crude $[P(OEP)(C_6H_5)(OCH_2C(CH_2OH)_3)]^+Cl^-$ **(3.3)**. The residue was washed with water (100 mL) and thoroughly dried. Extraction into anhydrous methanol (15 mL), filtration, and evaporation yielded the porphyrin triol **(3.3)**. Yield 0.0341 g (45%).

$[P(OEP)(C_6H_5)Cl]^+Cl^-$ **(3.15)**;

^{1}H-NMR ($CDCl_3$, δ ppm): 9.43 (s, 4H, -CH OEP), 5.47 (m, 1H, Ph_{para}), 4.78 (m, 2H, Ph_{meta}), 3.90-4.10 (m, 16H, $-CH_2$ OEP), 1.81 (t, 24H, $-CH_3$ OEP), 0.53 (dd, 2H, Ph_{ortho}).

^{31}P-NMR ($CDCl_3$, δ ppm): -212.9.

$[P(OEP)(C_6H_5)(OCH_2C(CH_2OH)_3)]^+Cl^-$ **(3.3)**;

^{1}H-NMR (MeOD, δ ppm): 9.45 (s, 4H, -CH OEP), 5.42 (m, 1H, Ph_{para}), 4.75 (m, 2H, Ph_{meta}), 3.90-4.10 (m, 16H, $-CH_2$- OEP), 1.80 (t, 24H, $-CH_3$ OEP), 0.51 (dd, 2H, Ph_{ortho}), 0.09 (s, 6H, 3-H), -2.90 (d, 2H, 1-H).

^{31}P-NMR (MeOD, δ ppm): -189.6.

MS (FAB, *m/z*): 776 ($[M]^+$ - Cl).

IR (KBr, cm^{-1}): 3387 (O-H), 3053, 2964, 2932, 2874, 2424, 2362, 1637, 1405, 1015, 800 (P-O) sh, 762, 622.

UV-Vis (DCM, λ_{max} (nm)): {log ε}: 419 {5.40}, 549 {4.50}, 591 {4.59}.

CHN: $C_{47}H_{60}N_4O_4PCl$ calcd: C 69.57%, H 7.45%, N 6.90%.
found: C 69.63%, H 7.56%, N 7.01%.

Chapter 5 – References

[1] J. S. Miller, A. J. Epstein, *Mrs Bulletin* **2000**, 21-28.

[2] (a) J. S. Miller, A. J. Epstein, *Angew. Chem. Int. Ed. Engl.* **1994**, *33*, 385-415. (b) C. M. Hurd, *Contemp. Phys.* **1982**, *23*, 469-493.

[3] B. D. Cullity, C. D. Graham, *Introduction to Magnetic Materials*, Wiley, United States, **2009**.

[4] J. M. D. Coey, *Magnetism and Magnetic Materials*, Cambridge, United Kingdom, **2010**.

[5] A. Aharoni, *Introduction to the Theory of Ferromagnetism*, Oxford, United States, **2000**.

[6] G. E. Rodgers, *Descriptive Inorganic, Coordination, and Solid-state Chemistry*, Nelson Thompson Learning, Toronto, **2002**.

[7] L. Smart, E. Moore, *Solid State Chemistry: An Introduction*, Chapman and Hall, New York, **1992**.

[8] G. A. Bain, J. F. Berry, *Journal of Chemical Education* **2008**, *85*, 532-536.

[9] A. R. West, *Basic Solid State Chemistry*, Wiley, New York, **1988**.

[10] A. R. West, *Solid State Chemistry and Its Applications*, Wiley, New York, **1984**.

[11] J. Mrozinski, *Coord. Chem. Reviews* **2005**, *249*, 2534-2548.

[12] (a) J. S. Miller, *Pramana J. Phys.* **2006**, *67*, 1-16. (b) B. Tsukerblat, *Inorg. Chim. Acta* **2008**, *361*, 3746-3760.

[13] D. Gatteschi, R. Sessoli, J. Villain, *Molecular Nanomagnets*, Oxford, United States, **2006**.

[14] A. J. Tasiopoulos, A. Vinslava, W. Wernsdorfer, K. A. Abboud, G. Christou, *Angew. Chem.* **2004**, *116*, 2169 –2173.

[15] L. Bogani, A. Vindigni, R. Sessoli, D. Gatteschi, *J. Mater. Chem.* **2008**, *18*, 4750-4758.

[16] D. Gatteschi, L. Bagani, A. Cornia, M. Mannini, L. Sorace, R. Sessoli, *Solid State Sciences* **2008**, *10*, 1701-1709.

[17] J. S. Miller, A. J. Epstein, in: M. Turnbull, *Molecule-Based Magnetic Materials*, ACS Symposium Series; American Chemical Society: Washington, DC, **1996**.

[18] H. H. Wickman, A. M. Trozzolo, H. J. Williams, G. W. Hull, F. R. Merritt, *Physical Review* **1967**, *155*, 563-566.

[19] A. K. Gregson, R. L. Martin, S. Mitra, *J. Chem. Soc., Dalton Trans.* **1976**, 1458-1466.

[20] E. Coronado, P. Day, *Chem. Rev.* **2004**, *104*, 5419-5448.

[21] M. Drillon, E. Coronado, M. Belaiche, R. L. Carlin, *J. of Appl. Phys.* **1988**, *63*, 3551-3553.

[22] L. J. de Longh, A. R. Miedema, *Advances in Physics* **1974**, *23*, 1-260.

[23] D. J. Breed, K. Gilijamse, A. R. Miedema, *Physica* **1969**, *45*, 205-216.

[24] Y. Pei, M. Verdaguer, O. Kahn, J. Sletten, J.-P. Renard, *J. Am. Chem. Soc.* **1986**, *108*, 7428-7430.

[25] I. Fujita, Y. Teki, T. Takui, T. Kinoshita, K. Itoh, F. Miko, Y. Sawaki, H. Iwamura, A. Izuoka, T. Sugawara, *J. Am. Chem. Soc.* **1990**, *112*, 4074-4075.

[26] D. Gatteschi, *Magn. Reson. Chem.* **2004**, *42*, 998.

[27] R. Ziessel, G. Ulrich, R. C. Lawson, L. Echegoyen, *J. Mater. Chem.* **1999**, *9*, 1435-1448.

[28] A. Caneschi, D. Gatteschi, R. Sessoli, P. Ray, *Acc. Chem. Res.* **1989**, *22*, 392-398.

[29] J. S. Miller, J. C. Calabrese, A. J. Epstein, R. W. Bigelow, J. H. Zhang, W. M. Reiff, *Chem. Commun.* **1986**, 1026-1028.

[30] K. F. Purcell, *J. Am Chem. Soc.* **1967**, *89*, 6139-6143.

[31] (a) H. J. Buser, D. Schwarzenbach, W. Petter, A. Ludi, *Inorg. Chem.* **1977**, *16*, 2704-2710. (b) S. Ferlay, T. Mallah, R. Ouahès, P. Veillet, M. Verdaguer, *Nature* **1995**, *378*, 701-703.

[32] (a) O. Sato, T. Iyoda, A. Fujishima, K. Hashimoto, *Science* **1996**, *272*, 704. (b) N. Shimamoto, S. Ohkoshi, O. Sato, K. Hashimoto, *Inorg. Chem.* **2002**, *41*, 678-684.

[33] L. Cambi, L. Szego, *Ber. Dtsch. Chem. Ges.* **1931**, *64*, 259.

[34] P. Gamez, J. S. Costa, M. Quesada, G. Aromi, *Dalton Trans.* **2009**, 7845-7853.

[35] A. L. Barra, A. Caneschi, A. Cornia, F. F. de Biani, D. Gatteschi, C. Sangregorio, R. Sessoli, L. Sorace, *J. Am. Chem. Soc.* **1999**, *121*, 5302-5310.

[36] D. Gatteschi, *Journal of Alloys and Compounds* **2001**, *317-318*, 8-12.

[37] E. M. W. Rumberger (2004). *Magnetization Dynamics in Single-Molecule Magnets (Doctoral dissertation)*. Retrieved from ProQuest Dissertations and Theses database (UMI No. 3153694).

[38] L. M. C. Beltran, J. R. Long, *Acc. Chem. Res.* **2005**, *38*, 325-334.

[39] D. Gatteschi, R. Sessoli, *Angew. Chem. Int. Ed.* **2003**, *42*, 268-297.

[40] E. del Barco, A. D. Kent, S. Hill, J. M. North, N. S. Dalal, E. M. Rumberger, D. N. Hendrickson, N. Chakov, G. Christou, *Journal of Low Temperature Physics* **2005**, *140*, 119-174.

[41] V. Marvaud, C. Decroix, A. Scuiller, F. Tuyeras, C. Guyard-Duhayon, J. Vaissermann, M. Marrot, F. Gonnet, M. Verdaguer, *Chem. Eur. J.* **2003**, *9*, 1692.

[42] R. E. P. Winpenny, *Dalton Trans.* **2002**, 1.

[43] T. Lis, *Acta Cryst. B* **1980**, *36*, 2042.

[44] S. L. Castro, Z. M. Sun, C. M. Grant, J. C. Bollinger, D. N. Hendrickson, G. Christou, *J. Am. Chem. Soc.* **1998**, *120*, 2365.

[45] Y. C. Zhong, M. P. Sarachik, J. Yoo, D. N. Hendrickson, *Phys. Rev. B* **2000**, *62*, R9256.

[46] A. L. Barra, A. Caneschi, D. Gatteschi, D. P. Goldberg, R. Sessoli, *J. Solid State Chem.* **1999**, *145*, 484.

[47] K. Wieghardt, K. Pohl, I. Jibril, G. Huttner, *Angew. Chem. Int. Ed. Engl.* **1984**, *23*, 77.

[48] S. Accorsi, A.-L. Barra, A. Caneschi, G. Chastanet, A. Cornia, A. C. Fabretti, D. Gatteschi, C. Mortalo, E. Olivieri, F. Parenti, P. Rosa, R. Sessoli, L. Sorace, W. Wernsdorfer, L. Zobbi, *J. Am. Chem. Soc.* **2006**, *128*, 4742-4755.

[49] G. Christou, *Polyhedron* **2005**, *24*, 2065-2075.

[50] (a) H. J. Eppley, H.-L. Tsai, N. Devries, K. Folting, G. Christou, D. N. Hendrickson, *J. Am. Chem. Soc.* **1995**, *117*, 301. (b) R. Sessoli, H.-L. Tsai, A. R. Schake, S. Y. Wang, J. B. Vincent, K. Folting, D. Gatteschi, G. Christou, D. N. Hendrickson, *J. Am. Chem. Soc.* **1993**, *115*, 1804.

[51] S. M. J. Aubin, Z. M. Sun, H. J. Eppley, E. M. Rumberger, I. A. Guzei, K. Folting, P. K. Gantzel, A. L. Rheingold, G. Christou, D. N. Hendrickson, *Inorg. Chem.* **2001**, *40*, 2127-2146.

[52] A. Cornia, A. C. Fabretti, M. Pacchioni, L. Zobbi, D. Bonacchi, A. Caneschi, D. Gatteschi, R. Biagi, U. Del Pennino, V. De Renzi, L. Gurevich, H. S. J. Van der Zant, *Angew. Chem. Int. Ed.* **2003**, *42*, 1645-1648.

[53] F. Pineider, M. Mannini, C. Danieli, L. Armelao, F. M. Piras, A. Magnani, A. Cornia, R. Sessoli, *J. Mater. Chem.* **2010**, *20*, 187-194.

[54] P.-H. Lin, T. J. Burchell, L. Ungur, L. F. Chibotaru, W. Wernsdorfer, M. Murugesu, *Angew. Chem. Int. Ed.* **2009**, *48*, 9489-9492.

[55] G. Novitchi, W. Wernsdorfer, L. F. Chibotaru, J.-P. Costes, C. E. Anson, A. K. Powell, *Angew. Chem. Int. Ed.* **2009**, *48*, 1614-1619.

[56] S. R. Ritter, *Science and Technology* **2004**, *82*, 29-32.

[57] A. Cornia, A.C. Fabretti, L. Zobbi, A. Caneschi, D. Gatteschi, M. Mannini, R. Sessoli, in: R.Winpenny (Ed.), *Single-Molecule Magnets and Related Phenomena*, Structure and Bonding Book Series, Springer, Berlin, Heidelberg, **2006**.

[58] R. H. Ismayilov, W.-Z. Wang, G.-H. Lee, S.-M. Peng, *J. Chem. Soc., Dalton Trans.* **2006**, 478-491.

[59] K. V. Shuvaev, T. S. M. Abedin, C. A. McClary, L. N. Dawe, J. L. Collins, L. K. Thompson, *Dalton Trans.* **2009**, 2926-2939.

[60] I. Fernández, R. Ruiz, J. Faus, M. Julve, F. Lloret, J. Cano, X. Ottenwaelder, Y. Journaux, M. C. Muñoz, *Angew. Chem.* **2001**, *113*, 3129-3132.

[61] J. B. Goodenough, *Physical Review* **1955**, *100*, 564-573.

[62] J. B. Goodenough, *J. Phys. Chem. Solids* **1958**, *6*, 287-297.

[63] J. Kanamori, *J. Phys. Chem. Solids* **1959**, *10*, 87-98.

[64] H. Oshio, M. Nakano, *Chem. Eur. J.* **2005**, *11*, 5178-5185.

[65] O. Kahn, *Structure and Bonding*, Springer-Verlag Berlin, Heidelberg, **1987**.

[66] J. A. McCleverty, M. D. Ward, *Acc. Chem. Res.* **1998**, *31*, 842-851.

[67] C. R. Rice, S. Onions, N. Vidal, J. D. Wallis, M. C. Senna, M. Pilkington, H. Stoeckli-Evans, *Eur. J. Inorg. Chem.* **2002**, *46*, 1985-1997.

[68] F. Blau, *Ber. D. Chem. Ges.* **1888**, *21*, 1077-1078.

[69] G. R. Newkome, A. K. Patri, E. Holder, U. S. Schubert, *Eur. J. Org. Chem.* **2004**, 235-254.

[70] C. M. Amb, S. C. Rasmussen, *J. Org. Chem.* **2006**, *71*, 4696-4699.

[71] P. Thirumurugan, A. Nandakumar, D. Muralidharan, and P. T. Perumal, *J. Comb. Chem.* **2010**, *12*, 161-167.

[72] D. F. Zigler, M. C. Elvington, J. Heinecke, K. J. Brewer, *Inorg. Chem.* **2006**, *45*, 6565-6567.

[73] E. Tynan, P. Jensen, A. C. Lees, B. Moubaraki, K. S. Murray, P. E. Kruger, *Cryst. Eng. Comm.* **2005**, *13*, 90-95.

[74] D.-H. Lee, N. N. Murthy, K. D. Karlin, *Inorg. Chem.* **1997**, *36*, 5785-5792.

[75] M. Ghosh, P. Biswas, U. Flörke, K. Nag, *Inorg. Chem.* **2008**, *47*, 281-296.

[76] G. L. Starova, A. S. Denisova, E. M. Dem'yanchuk, *Journal of Molecular Structure* **2007**, *830*, 139-142.

[77] J.-M. Shi, J.-N. Chen, L.-D. Liu, *Acta Cryst.* **2006**, *E62*, m2094-2095.

[78] S. J. Min, C. J. Na, L. L. Dong, *Acta Cryst.* **2006**, *E62*, m1810-m1811.

[79] J. Wang, S. Onions, M. Pilkington, H. Stoeckli-Evans, J. C. Halfpenny, J. D. Wallis, *Chem. Commun.* **2007**, 3628-3630.

[80] S. Yamada, *Coord. Chem. Rev.* **1999**, *190-192*, 537-555.

[81] J. Wang, B. Djukic, J. Cao, A. Alberola, F. S. Razavi, M. Pilkington, *Inorg. Chem.* **2007**, *46*, 8560-8568.

[82] J. Zhang, Q. Liu, C. Duan, Y. Shao, J. Ding, Z. Miao, X. You, Z. Guo, *J. Chem. Soc., Dalton Trans.* **2002**, 591.

[83] S. A. Ross, C. J. Burrows, *Inorg. Chem.* **1998**, *37*, 5358-5363.

[84] B. K. Singh, P. Mishra, B. S. Garg, *Trans. Metal Chem.* **2007**, *32*, 1110-1116.

[85] Z. Qin, M. C. Jennings, R. J. Puddephatt, *Inorg. Chem.* **2001**, *40*, 6220-6228.

[86] R. K. Afshar, R. Bhalla, J. M. Rowland, M. M. Olmstead, P. K. Mascharak, *Inorg. Chem. Acta* **2006**, *359*, 4105-4113.

[87] O. Belda, C. Moberg, *Coord. Chem. Rev.* **2005**, *249*, 727-740.

[88] A. K. Singh, R. Mukherjee, *Inorganica Chimica Acta* **2007**, *360*, 3456-3461.

[89] J. Zhang, Q. Liu, C. Duan, Y. Shao, J. Ding, Z. Miao, X.-Z. You, Z. Guo, *J. Chem. Soc., Dalton Trans.* **2002**, 591-597.

[90] J.-Y. Qi, H.-X. Ma, X.-J. Li, Z.-Y. Zhou, M. C. K. Choi, A. S. C. Chan, Q.-Y. Yang, *Chem. Commun.* **2003**, 1294-1295.

[91] P. Laurent, H. Miyaji, S. R. Collinson, I. Prokes, C. J. Moody, J. H. R. Tucker, A. M. Z. Slawin, *Org. Lett.* **2002**, *4*, 4037-4040.

[92] H. Matsuzaki, W. Fujita, K. Awaga, H. Okamoto, *Physical Review Letters* **2003**, *91*, 1-4.

[93] J. M. Herrera, V. Marvaud, M. Verdaguer, J. Marrot, M. Kalisz, C. Mathonière, *Angew. Chem. Int. Ed.* **2004**, *43*, 5468-5471.

[94] A. Bleuzen, V. Marvaud, C. Mathonière, B. Sieklucka, M. Verdaguer, *Inorg. Chem.* **2009**, *48*, 3453-3466.

[95] O. Sato, *Journal of Photochemistry and Photobiology C: Photochemistry Reviews* **2004**, *5*, 203-223.

[96] C. C. Beedle, C. J. Stephenson, K. J. Heroux, W. Wernsdorfer, D. N. Hendrickson, *Inorg. Chem.* **2008**, *47*, 10798-10800.

[97] M. Murrie, D. J. Price, *Annu. Rep. Prog. Chem., Sect. A* **2007**, *103*, 20-38.

[98] L. Thomas, F. Lionti, R. Ballou, D. Gatteschi, R. Sessoli, B. Barbara, *Nature* **1996**, *383*, 145-147.

[99] M. Morimoto, H. Miyasaka, M. Yamashita, M. Irie, *J. Am. Chem. Soc.* **2009**, *131*, 9823-9835.

[100] E. Rivière, B. Donnio, E. Voirin, G. Rogez, J.-P. Kappler, J.-L. Gallani, *J. Mater. Chem.* **2010**, *20*, 7165-7168.

[101] F. D'Souza, G. R. Deviprasad, M. E. El-Khouly, M. Fujitsuka, O. Ito, *J. Am. Chem. Soc.* **2001**, *123*, 5277-5284.

[102] A. Harriman, K. J. Elliott, M. A. H. Alamiry, L. Le Pleux, M. Séverac, Y. Pellegrin, E. Blart, C. Fosse, C. Cannizzo, C. R. Mayer, F. Odobel, *J. Phys. Chem. C* **2009**, *113*, 5834-5842.

[103] L. R. Milgrom, *The Colours of Life: An Introduction to the Chemistry of Porphyrins and Related Compounds*, Oxford, New York, **2002**.

[104] I. Beletskaya, V. S. Tyurin, A. Y. Tsivadze, R. Guilard, C. Stern, *Chem. Rev.* **2009,** *109,* 1659–1713.

[105] K. M. Kadish, K. M. Smith, R. Guilard, *The Porphyrin Handbook: Volume 3 – Inorganic, Organmetallic, and Coordination Chemistry*, Academic Press, United States, **2000**.

[106] L. K. Stoll, M. Z. Zgierski, P. M. Kozlowski, *J. Phys. Chem. A* **2002**, *106*, 170-175.

[107] (a) M. J. Gouterman, *J. Chem. Phys.* **1959**, *30*, 1139. (b) M. Uttamlal, A. S. Holmes-Smith, *Chemical Physics Letters* **2008**, *454*, 223–228.

[108] M. D. Ward, *Chem. Soc. Rev.* **1997**, *26*, 365-375.

[109] (a) J. S. Miller, *Chem. Soc. Rev.* **2011**, *40*, 3266-3296. (b) P. M. Zielinski, M. Balanda, R. Pelka, T. Wasiutynski, W. Haase, *Czech. J. Phys.* **2004**, *54*, D543-D546.

[110] S. Sakaue, A. Fuyuhiro, T. Fukuda, N. Ishikawa, *Chem. Commun.* **2012**, *48*, 5337–5339.

[111] A. García-Rose, J. J. Fiol, B. Adrover, P. Tauler, A. Pons, I. Mata, E. Espinosa, E. Molins, *Polyhedron* **2003**, *22*, 3255-3264.

[112] S. Hu, J. Dai, X. Wu, L. Wu, C. Cui, Z. Fu, M. Hong, Y. Liang, *Journal of Cluster* Science **2002**, *13*, 33-41.

[113] M. Belohradsky, M. Budesinsky, I. Cisarova, V. Dekoj, P. Holy, J. Zavada, *Tetrahedron* **2003**, *59*, 7751-7760.

[114] C. A. Hunter, J. K. M. Sanders, *J. Am. Chem. Soc.* **1990**, *112*, 5525-5534.

[115] U. Kumar, J. Thomas, N. Thirupathi, *Inorg. Chem.* **2010**, *49*, 62-72.

[116] S. L. Jain, P. Bhattacharyya, H. L. Milton, A. M. Z. Slawin, J. A. Crayston, D. Woollins, *J. Chem. Soc., Dalton Trans.* **2004**, 862-871.

[117] (a) J.-L. Song, Z.-C. Dong, H.-Y. Zeng, W.-B. Zhou, T. Naka, Q. Wei, J.-G. Mao, G.-C. Guo, J.-S. Huang, *Inorg. Chem.* **2003**, *42*, 2136-2140. (b) A. Abragam, B. Bleaney, *Electron Paramagnetic Resonance of Transition Ions*. Oxford University Press, New York, **1970**.

[118] D. A. Tucker, P. S. White, K. L. Trojan, M. L. Kirk, W. E. Hatfield, *Inorg. Chem.* **1991**, *30*, 823-826.

[119] G. De Munno, M. Julve, F. Lloret, J. Faus, M. Verdaguer, A. Caneschi, *Inorg. Chem.* **1995**, *34*, 157-165.

[120] R.-D. Schnebeck, E. Freisinger, F. Glahé, B. Lippert, *J. Am. Chem. Soc.* **2000**, *122,* 1381-1390.

[121] G. Dong, D. Chun-ying, F. Chen-jie, M. Qing-jin, *J. Chem. Soc., Dalton Trans.* **2002**, 834-836.

[122] E. Labisbal, L. Rodriguez, O. Souto, A. Sousa-Pedrares, J. A. Garcia-Vázquez, J. Romero, A. Sousa, M. Yáñez, F. Orallo, J. A. Real, *Dalton Trans.* **2009**, 8644-8656.

[123] A. Burkhardt, E. T. Spielberg, S. Simon, H. Görls, A. Buchholz, W. Plass, *Chem. Eur. J.* **2009**, *15*, 1261-1271.

[124] A. E. Ion, E. T. Spielberg, H. Görls, W. Plass, *Inorganica Chimica Acta* **2007**, *360*, 3925–3931.

[125] L. K. Thompson, V. Niel, H. Grove, D. O. Miller, M. J. Newlands, P. H. Bird, W. A. Wickramasinghe, A.B.P. Lever, *Polyhedron* **2004**, *23*, 1175-1184.

[126] (a) P. K. Ross, M. D. Allendorf, E. I. Solomon, *J. Am. Chem. Soc.* **1989**, *111*, 4009-4021. (b) G. M. Brown, R. Chidambaram, *Acta Cryst.* **1973**, *B29*, 2393-2403.

[127] B. Bleaney, F. R. S. Bowers, *Proceedings of the Royal Society of London. Series A, Mathematical and Physical Sciences* **1952**, *214*, 451-465.

[128] B. Chiari, O. Piovesana, T. Tarantelli, P. F. Zanazzi, *Inorg. Chem.* **1993**, *32*, 4834-4838.

[129] (a) V. Tangoulis, D. A. Malamatari, K. Soulti, V. Stergiou, C. P. Raptopoulou, A. Terzis, T. A. Kabanos, D. P. Kessissoglou, *Inorg. Chem.* **1996**, *35,* 4974-4983. (b) K. Wieghardt, U. Bossek, B. Nuber, J. Weiss, J. Bonvoisin, M. Corbella, S. E. Vitols, J. J. Girerd, *J. Am. Chem. Soc.* **1988**, *110*, 7398-7411. (c) L. C. W. Baker, L. Lebioda, J. Grochowski, H. G. Mukherjee, *J. Am. Chem. Soc.* **1980**, *102*, 3276-3278.

[130] (a) Y. Kotake, T. Okauchi, A. Iijima, K. Yoshimatsu, H. Nomura, *Chem. Pharm. Bull.* **1995**, *43*, 829-841. (b) K. B. Gudasi, M. S. Patil, R. S. Vadav, R. V. Shenoy, S. A. Patil, M. Nethaji, *Spectrochimica Acta Part A* **2007**, *67*, 172–177.

[131] Y.-T. Wang, M.-L. Tong, H.-H. Fan, H.-Z. Wang, X.-M. Chen, *Dalton Trans.* **2005**, 424-426.

[132] (a) K. Gudasi, R. Vadavi, R. Shenoy, M. Patil, S. A. Patil, M. Nethaji, *Inorganica Chimica Acta* **2005**, *358*, 3799-3806. (b) A. B. P. Lever, *J. Chem. Edu.* **1968**, *45*, 711.

[133] Y. Terazono, B. O. Patrick, D. H. Dolphin, *Inorg. Chem.* **2002**, *41*, 6703-6710.

[134] K. Hirakawaa, H. Segawa, *Journal of Photochemistry and Photobiology A: Chemistry* **1999**, *123*, 67-76.

[135] (a) Y.-H. Lin, M.-T. Sheu, C.-C. Lin, J.-H. Chen, *Polyhedron* **1994**, *13*, 3091-3097. (b) P.-C. Cheng, I.-C. Liu, T.-N. Hong, J.-H. Chen, *Polyhedron* **1996**, *15*, 2733-2740.

[136] (a) D. E. Coutant, S. A. Clarke, A. H. Francis, M. E. Meyerhoff, *Journal of Chromatography A* **1998**, *824*, 147-157. (b) L.R. Milgrom, *J. Chem. Soc. Perkin Trans. I* **1984**, 1483-1487.

[137] L. Bogani, C. Danieli, E. Biavardi, N. Bendiab, A.-L. Barra, E. Dalcanale, W. Wernsdorfer, A. Cornia, *Angew. Chem. Int. Ed.* **2009**, *48*, 746-750.

[138] A. B. Padias, H. K. Hall Jr., *Macromolecules* **1982**, *15*, 217-223.

[139] T. Ishizone, T. Tominaga, K. Kitamura, A. Hirao, S. Nakahama, *Macromolecules* **1995**, *28*, 4829-4836.

[140] R. A. Findeis, L. H. Gade, *Dalton Trans.* **2003**, 249-254.

[141] A. B. Padias, H. K. Hall Jr., D. A. Tomalia, J. R. McConnell, *J. Org. Chem.* **1987**, *52*, 5305-5312.

[142] T. Barbour, W. J. Belcher, P. J. Brothers, C. E. F. Rickard, D. C. Ware, *Inorg. Chem.* **1992**, *31*, 746-754.

[143] T. A. Rao, B. G. Maiya, *Inorg. Chem.* **1996**, *35*, 4829-4836.

[144] L. Cheng, J. Ma, *Organic Preparations and Procedures International* **1995**, *27*, 224-228.

[145] J. H. K. Ky Hirschberg, R. A. Koevoets, R. P. Sijbesma, E. W. Meijer, *Chem. Eur. J.* **2003**, *9*, 4222-4231.

[146] R. J. Clay, T. A. Collom, G. L. Karrick, J. Wemple, *Synthesis* **1993**, 290-292.

[147] J. B. Paine III, W. B. Kirshner, D. W. Moskowitz, D. Dolphin, *J. Org. Chem.* **1976**, *41*, 3857-3860.

[148] H. W. Whitlock, R. Hanauer, *J. Org. Chem.* **1968**, *33*, 2169-2171.

[149] K. Akiba, R. Nadano, W. Satoh, Y. Yamamoto, S. Nagase, Z. Ou, X. Tan, K. M. Kadish, *Inorg. Chem.* **2001**, *40*, 5553-5567.

[150] R. Viguier, G. Serratrice, A. Dupraz, C. Dupuy, *Eur. J. Org. Chem.* **2001**, 1789-1795.

[151] G. M. Sheldrick, *Act. Cryst. Sec. A*, **2008**, *64*, 112-122.

[152] I. J. Bruno, C. F. Macrae, J. A. Chisholm, P. R. Edgington, P. McCabe, E. Pidcock, L. Rodriguez-Monge, R. Taylor, J. van de Streek, P. A. Wood, *J. of Appl. Cryst.* **2008**, 466-470.

[153] L. J. Farrugia, *J. of Appl. Crys.* **1997**, *30*, 565.

Appendix

6.1 – Crystallographic Data

Table 6.1: Bonds lengths [Å] for $[Zn_2(L^1)(OAc)(MeO)]_2$ **(2.6)**.

Atoms	Bond [Å]	Atoms	Bond [Å]	Atoms	Bond [Å]
Zn(1) - O(2)	2.0340(18)	Zn(1) - O(3)	1.9495(14)	Zn(1) - N(2)	2.033(2)
Zn(1) - N(3)	2.170(2)	Zn(1) - N(1')	2.173(2)	O(1) - C(6)	1.246(3)
O(2) - C(12)	1.264(2)	O(3) - C(14)	1.400(7)	N(1) - C(1)	1.364(3)
N(1) - C(5)	1.338(3)	N(2) - C(2)	1.401(3)	N(2) - C(6)	1.326(3)
N(3) - C(7)	1.344(4)	N(3) - C(11)	1.352(4)	C(1) - C(2)	1.403(3)
C(1) - C(1')	1.503(3)	C(2) - C(3)	1.397(3)	C(3) - C(4)	1.383(4)
C(4) - C(5)	1.388(3)	C(6) - C(7)	1.515(4)	C(7) - C(8)	1.380(4)
C(8) - C(9)	1.395(5)	C(9) - C(10)	1.369(5)	C(10) - C(11)	1.377(5)
C(12) - C(13)	1.506(5)				

Table 6.2: Bond angles [°] for $[Zn_2(L^1)(OAc)(MeO)]_2$ **(2.6)**.

Atoms	Angle [°]	Atoms	Angle [°]	Atoms	Angle [°]
O(2) - Zn(1) - O(3)	97.77(9)	O(2) - Zn(1) - N(2)	154.24(8)	O(2) - Zn(1) - N(3)	84.12(8)
O(2) - Zn(1) - N(1)a	94.73(8)	O(3) - Zn(1) - N(2)	106.87(9)	O(3) - Zn(1) - N(3)	122.43(10)
O(3) - Zn(1) - N(1)a	111.90(9)	N(2) - Zn(1) - N(3)	76.49(8)	N(2) - Zn(1) - N(1)a	83.15(7)
N(3) - Zn(1) - N(1)a	125.34(8)	Zn(1) - O(2) - C(12)	131.81(19)	Zn(1) - O(3) - C(14)	119.78(9)
Zn(1) - O(3) - Zn(1)c	116.97(13)	C(14) - O(3) - Zn(1)c	119.78(9)	C(1) - N(1) - C(5)	118.9(2)
C(1) - N(1) - Zn(1)a	124.59(15)	C(5) - N(1) - Zn(1)a	113.88(16)	Zn(1) - N(2) - C(2)	118.34(15)
Zn(1) - N(2) - C(6)	121.53(17)	C(2) - N(2) - C(6)	120.1(2)	Zn(1) - N(3) - C(7)	113.71(17)
Zn(1) - N(3) - C(11)	127.9(2)	C(7) - N(3) - C(11)	118.4(2)	N(1) - C(1) - C(2)	120.7(2)
N(1) - C(1) - C(1)a	117.85(19)	C(2) - C(1) - C(1)a	121.4(2)	N(2) - C(2) - C(1)	120.4(2)
N(2) - C(2) - C(3)	120.2(2)	C(1) - C(2) - C(3)	119.3(2)	C(2) - C(3) - C(4)	119.3(2)
C(3) - C(4) - C(5)	118.5(2)	N(1) - C(5) - C(4)	123.3(2)	O(1) - C(6) - N(2)	128.5(2)
O(1) - C(6) - C(7)	119.4(2)	N(2) - C(6) - C(7)	112.0(2)	N(3) - C(7) - C(6)	116.1(2)
N(3) - C(7) - C(8)	122.7(3)	C(6) - C(7) - C(8)	121.2(2)	C(7) - C(8) - C(9)	118.5(3)
C(8) - C(9) - C(10)	118.8(3)	C(9) - C(10) - C(11)	120.1(3)	N(3) - C(11) - C(10)	121.6(3)
O(2) - C(12) - C(13)	117.39(16)	O(2) - C(12) - O(2)c	125.2(3)	C(13) - C(12) - O(2)c	117.39(16)

Table 6.3: Bonds lengths [Å] for $[Cu_2(L^1)(OAc)_2]$ (**2.7**).

Atoms	Bond [Å]	Atoms	Bond [Å]	Atoms	Bond [Å]
Cu(1) - O(3)	1.9672(19)	Cu(1) - O(4)	2.4484(16)	Cu(1) - N(2)	1.927(2)
Cu(1) - N(3)	2.0006(19)	Cu(1) - N(4)	2.0077(18)	Cu(1) - O(4)c	2.5298(15)
Cu(2) - O(1)	2.531(2)	Cu(2) - O(5)	1.9385(16)	Cu(2) - O(6)	2.692(2)
Cu(2) - N(1)d	2.0455(17)	Cu(2) - N(5)d	1.9104(17)	Cu(2) - N(6)d	2.0240(17)
O(1) - C(6)	1.235(3)	O(2) - C(17)	1.231(2)	O(3) - C(23)	1.281(2)
O(4) - C(23)	1.243(3)	O(5) - C(25)	1.280(3)	O(6) - C(25)	1.243(3)
N(1) - C(1)	1.361(2)	N(1) - C(5)	1.340(3)	N(2) - C(2)	1.398(2)
N(2) - C(6)	1.340(3)	N(3) - C(7)	1.341(3)	N(3) - C(11)	1.339(3)
N(4) - C(12)	1.355(3)	N(4) - C(16)	1.341(3)	N(5) - C(13)	1.397(3)
N(5) - C(17)	1.349(3)	N(6) - C(18)	1.345(3)	N(6) - C(22)	1.336(3)
C(1) - C(2)	1.409(3)	C(1) - C(12)	1.495(3)	C(2) - C(3)	1.404(3)
C(3) - C(4)	1.376(3)	C(4) - C(5)	1.382(3)	C(6) - C(7)	1.511(3)
C(7) - C(8)	1.384(4)	C(8) - C(9)	1.391(3)	C(9) - C(10)	1.381(4)
C(10) - C(11)	1.387(4)	C(12) - C(13)	1.401(3)	C(13) - C(14)	1.400(3)
C(14) - C(15)	1.376(3)	C(15) - C(16)	1.383(3)	C(17) - C(18)	1.509(3)
C(18) - C(19)	1.385(3)	C(19) - C(20)	1.385(3)	C(20) - C(21)	1.380(4)
C(21) - C(22)	1.387(4)	C(23) - C(24)	1.509(4)	C(25) - C(26)	1.502(3)

Table 6.4: Bond angles [°] for $[Cu_2(L^1)(OAc)_2]$ **(2.7).**

Atoms	Angle [°]	Atoms	Angle [°]	Atoms	Angle [°]
O(3) - Cu(1) - O(4)	58.79(6)	O(3) - Cu(1) - N(2)	161.70(7)	O(3) - Cu(1) - N(3)	94.22(7)
O(3) - Cu(1) - N(4)	97.04(8)	O(3) - Cu(1) - C(23)	29.97(6)	O(3) - Cu(1) - O(4)c	98.81(6)
O(4) - Cu(1) - N(2)	103.06(7)	O(4) - Cu(1) - N(3)	91.32(7)	O(4) - Cu(1) - N(4)	111.84(7)
O(4) - Cu(1) - C(23)	28.89(6)	O(4) - Cu(1) - O(4)c	154.06(5)	N(2) - Cu(1) - N(3)	83.19(8)
N(2) - Cu(1) - N(4)	92.05(8)	N(2) - Cu(1) - C(23)	131.77(7)	N(2) - Cu(1) - O(4)c	98.19(7)
N(3) - Cu(1) - N(4)	156.83(7)	N(3) - Cu(1) - C(23)	91.58(8)	N(3) - Cu(1) - O(4)c	76.51(6)
N(4) - Cu(1) - C(23)	108.14(8)	N(4) - Cu(1) - O(4)c	81.79(6)	C(23) - Cu(1) - O(4)c	127.18(6)
O(1) - Cu(2) - O(5)	82.42(7)	O(1) - Cu(2) - O(6)	135.19(6)	O(1) - Cu(2) - N(1)d	87.34(7)
O(1) - Cu(2) - N(5)d	111.76(8)	O(1) - Cu(2) - N(6)d	76.10(7)	O(5) - Cu(2) - O(6)	54.30(7)
O(5) - Cu(2) - N(1)d	96.19(7)	O(5) - Cu(2) - N(5)d	165.19(10)	O(5) - Cu(2) - N(6)d	98.77(7)
O(6) - Cu(2) - N(1)d	86.51(7)	O(6) - Cu(2) - N(5)d	112.46(8)	O(6) - Cu(2) - N(6)d	117.57(7)
N(1)d - Cu(2) - N(5)d	89.00(7)	N(1)d - Cu(2) - N(6)d	155.91(8)	N(5)d - Cu(2) - N(6)d	81.26(7)
Cu(2) - O(1) - C(6)	172.78(14)	Cu(1) - O(3) - C(23)	99.92(15)	Cu(1) - O(4) - C(23)	79.00(12)
Cu(1) - O(4) - Cu(1)b	139.77(8)	C(23) - O(4) - Cu(1)b	140.84(15)	Cu(2) - O(5) - C(25)	108.00(13)
Cu(2) - O(6) - C(25)	73.86(15)	C(1) - N(1) - C(5)	119.67(19)	C(1) - N(1) - Cu(2)d	124.43(13)
C(5) - N(1) - Cu(2)d	112.59(13)	Cu(1) - N(2) - C(2)	121.43(17)	Cu(1) - N(2) - C(6)	116.22(13)
C(2) - N(2) - C(6)	121.1(2)	Cu(1) - N(3) - C(7)	111.66(13)	Cu(1) - N(3) - C(11)	127.85(18)
C(7) - N(3) - C(11)	119.6(2)	Cu(1) - N(4) - C(12)	122.32(17)	Cu(1) - N(4) - (16)	111.07(13)
C(12) - N(4) - C(16)	119.67(18)	C(13) - N(5) - C(17)	121.03(17)	C(13) - N(5) - Cu(2)d	118.85(14)
C(17) - N(5) - Cu(2)d	118.64(14)	C(18) - N(6) - C(22)	119.2(2)	C(18) - N(6) - Cu(2)d	111.47(13)
C(22) - N(6) - Cu(2)d	127.83(16)	N(1) - C(1) - C(2)	120.96(19)	N(1) - C(1) - C(12)	116.25(19)
C(2) - C(1) - C(12)	122.70(16)	N(2) - C(2) - C(1)	119.79(18)	N(2) - C(2) - C(3)	122.06(19)
C(1) - C(2) - C(3)	118.04(17)	C(2) - C(3) - C(4)	119.6(2)	C(3) - C(4) - C(5)	119.5(2)
N(1) - C(5) - C(4)	121.98(18)	O(1) - C(6) - N(2)	128.68(19)	O(1) - C(6) - C(7)	119.0(2)
N(2) - C(6) - C(7)	112.3(2)	N(3) - C(7) - C(6)	115.5(2)	N(3) - C(7) - C(8)	122.15(19)
C(6) - C(7) - C(8)	122.4(2)	C(7) - C(8) - C(9)	118.3(3)	C(8) - C(9) - C(10)	119.5(3)
C(9) - C(10) - C(11)	118.9(2)	N(3) - C(11) - C(10)	121.6(3)	N(4) - C(12) - C(1)	117.28(16)
N(4) - C(12) - C(13)	120.7(2)	C(1) - C(12) - C(13)	121.92(17)	N(5) - C(13) - C(12)	120.27(19)
N(5) - C(13) - C(14)	120.97(19)	C(12) - C(13) - C(14)	118.49(19)	C(13) - C(14) - C(15)	119.8(2)
C(14) - C(15) - C(16)	118.6(2)	N(4) - C(16) - C(15)	122.4(2)	O(2) - C(17) - N(5)	128.3(2)
O(2) - C(17) - C(18)	121.11(18)	N(5) - C(17) - C(18)	110.57(16)	N(6) - C(18) - C(17)	115.21(18)
N(6) - C(18) - C(19)	122.5(2)	C(17) - C(18) - C(19)	122.22(19)	C(18) - C(19) - C(20)	118.0(2)
C(19) - C(20) - C(21)	119.5(3)	C(20) - C(21) - C(22)	119.3(2)	N(6) - C(22) - C(21)	121.4(2)
Cu(1) - C(23) - O(3)	50.11(12)	Cu(1) - C(23) - O(4)	72.10(13)	Cu(1) - C(23) - C(24)	165.72(15)
O(3) - C(23) - O(4)	122.0(2)	O(3) - C(23) - C(24)	117.8(2)	O(4) - C(23) - C(24)	120.15(19)
O(5) - C(25) - O(6)	122.9(2)	O(5) - C(25) - C(26)	116.2(2)	O(6) - C(25) - C(26)	120.9(3)

Table 6.5: Bonds lengths [Å] for $[Ni(L^1)]_3$ **(2.8)**.

Atoms	Bond [Å]	Atoms	Bond [Å]	Atoms	Bond [Å]
Ni(1) - N(2)	2.020(4)	Ni(1) - N(3)	2.120(4)	Ni(1) - N(1)a	2.148(5)
Ni(1) - N(1)c	2.148(4)	Ni(1) - N(2)d	2.020(4)	Ni(1) - N(3)d	2.120(5)
O(1) - C(6)	1.246(6)	N(1) - C(1)	1.347(7)	N(1) - C(5)	1.343(6)
N(2) - C(2)	1.407(6)	N(2) - C(6)	1.321(5)	N(3) - C(7)	1.345(7)
N(3) - C(11)	1.330(7)	C(1) - C(2)	1.410(6)	C(1) - C(1)c	1.499(6)
C(2) - C(3)	1.391(6)	C(3) - C(4)	1.381(7)	C(4) - C(5)	1.378(7)
C(6) - C(7)	1.513(7)	C(7) - C(8)	1.383(9)	C(8) - C(9)	1.405(10)
C(9) - C(10)	1.343(10)	C(10) - C(11)	1.393(9)		

Table 6.6: Bond angles [°] for $[Ni(L^1)]_3$ **(2.8)**.

Atoms	Angle [°]	Atoms	Angle [°]	Atoms	Angle [°]
N(2) - Ni(1) - N(3)	78.94(15)	N(2) - Ni(1) - N(1)a	97.77(16)	N(2) - Ni(1) - N(1)c	81.27(15)
N(2) - Ni(1) - N(2)d	178.57(15)	N(2) - Ni(1) - N(3)d	102.19(17)	N(3) - Ni(1) - N(1)a	169.97(17)
N(3) - Ni(1) - N(1)c	89.51(16)	N(3) - Ni(1) - N(2)d	102.16(16)	N(3) - Ni(1) - N(3)d	82.02(19)
N(1)a - Ni(1) - N(1)c	99.40(17)	N(1)a - Ni(1) - N(2)d	81.30(17)	N(1)a - Ni(1) - N(3)d	89.5(2)
N(1)c - Ni(1) - N(2)d	97.79(16)	N(1)c - Ni(1) - N(3)d	169.98(16)	N(2)d - Ni(1) - N(3)d	78.91(18)
C(1) - N(1) - C(5)	118.2(4)	C(1) - N(1) - Ni(1)b	124.4(3)	C(5) - N(1) - Ni(1)b	115.6(4)
Ni(1) - N(2) - C(2)	114.9(3)	Ni(1) - N(2) - C(6)	118.2(3)	C(2) - N(2) - C(6	120.5(4)
Ni(1) - N(3) - C(7)	112.2(3)	Ni(1) - N(3) - C(11)	127.3(4)	C(7) - N(3) - C(11	119.6(5)
N(1) - C(1) - C(2)	121.8(4)	N(1) - C(1) - C(1)c	117.5(4)	C(2) - C(1) - C(1)c	120.7(5)
N(2) - C(2) - C(1)	118.8(4)	N(2) - C(2) - C(3)	123.0(4)	C(1) - C(2) - C(3	118.1(4)
C(2) - C(3) - C(4)	120.0(4)	C(3) - C(4) - C(5)	118.0(5)	N(1) - C(5) - C(4	123.8(5)
O(1) - C(6) - N(2)	127.2(4)	O(1) - C(6) - C(7)	119.5(4)	N(2) - C(6) - C(7	113.2(4)
N(3) - C(7) - C(6)	115.5(5)	N(3) - C(7) - C(8)	121.4(5)	C(6) - C(7) - C(8	123.2(5)
C(7) - C(8) - C(9)	118.3(6)	C(8) - C(9) - C(10)	119.7(7)	C(9) - C(10) - C(11	119.4(6)
N(3) - C(11) - C(10)	121.7(5)				

Table 6.7: Bonds lengths [Å] for $[Ni(L^1)]_3$ **(2.9)**.

Atoms	Bond [Å]	Atoms	Bond [Å]	Atoms	Bond [Å]
Ni(1) - N(2)	2.020(5)	Ni(1) - N(3)	2.141(6)	Ni(1) - N(1)a	2.136(7)
Ni(1) - N(1)c	2.137(6)	Ni(1) - N(2)d	2.020(5)	Ni(1) - N(3)d	2.141(7)
O(1) - C(6)	1.243(8)	N(1) - C(1)	1.356(8)	N(1) - C(5)	1.339(7)
N(2) - C(2)	1.412(7)	N(2) - C(6)	1.324(7)	N(3) - C(7)	1.347(9)
N(3) - C(11)	1.337(10)	C(1) - C(2)	1.419(8)	C(1) - C(1)c	1.496(6)
C(2) - C(3)	1.376(8)	C(3) - C(4)	1.387(13)	C(4) - C(5)	1.368(11)
C(6) - C(7)	1.513(9)	C(7) - C(8)	1.387(13)	C(8) - C(9)	1.393(14)
C(9) - C(10)	1.358(16)	C(10) - C(11)	1.386(16)		

Table 6.8: Bond angles [°] for $[Ni(L^1)]_3$ **(2.9)**.

Atoms	Angle [°]	Atoms	Angle [°]	Atoms	Angle [°]
N(2) - Ni(1) - N(3)	77.51(18)	N(2) - Ni(1) - N(1)a	95.6(2)	N(2) - Ni(1) - N(1)c	81.4(2)
N(2) - Ni(1) - N(2)d	175.3(2)	N(2) - Ni(1) - N(3)d	106.2(2)	N(3) - Ni(1) - N(1)a	166.3(2)
N(3) - Ni(1) - N(1)c	91.26(18)	N(3) - Ni(1) - N(2)d	106.2(2)	N(3) - Ni(1) - N(3)d	79.7(3)
N(1)a - Ni(1) - N(1)c	99.4(2)	N(1)a - Ni(1) - N(2)d	81.4(2)	N(1)a - Ni(1) - N(3)d	91.2(3)
N(1)c - Ni(1) - N(2)d	95.6(2)	N(1)c - Ni(1) - N(3)d	166.37(18)	N(2)d - Ni(1) - N(3)d	77.5(2)
C(1) - N(1) - C(5)	118.8(5)	C(1) - N(1) - Ni(1)b	125.2(3)	C(5) - N(1) - Ni(1)b	114.3(5)
Ni(1) - N(2) - C(2)	116.8(3)	Ni(1) - N(2) - C(6)	120.4(4)	C(2) - N(2) - C(6)	118.6(5)
Ni(1) - N(3) - C(7)	112.2(4)	Ni(1) - N(3) - C(11)	127.4(6)	C(7) - N(3) - C(11)	118.1(7)
N(1) - C(1) - C(2)	120.8(4)	N(1) - C(1) - C(1)c	118.1(5)	C(2) - C(1) - C(1)c	121.0(5)
N(2) - C(2) - C(1)	118.4(4)	N(2) - C(2) - C(3)	122.7(5)	C(1) - C(2) - C(3)	118.8(6)
C(2) - C(3) - C(4)	119.3(7)	C(3) - C(4) - C(5)	119.2(6)	N(1) - C(5) - C(4)	123.1(7)
O(1) - C(6) - N(2)	127.1(6)	O(1) - C(6) - C(7)	121.2(6)	N(2) - C(6) - C(7)	111.7(5)
N(3) - C(7) - C(6)	115.6(7)	N(3) - C(7) - C(8)	122.7(6)	C(6) - C(7) - C(8)	121.7(6)
C(7) - C(8) - C(9)	118.0(8)	C(8) - C(9) - C(10)	119.4(11)	C(9) - C(10) - C(11)	119.6(10)
N(3) - C(11) - C(10)	122.2(8)				

Table 6.9: Bonds lengths [Å] for ligand (**2.2**) molecule A and B, respectively.

Atoms	Bond [Å]	Atoms	Bond [Å]	Atoms	Bond [Å]
O(1) - C(6)	1.229(5)	N(1) - C(1)	1.348(5)	N(1) - C(5)	1.331(5)
N(2) - C(2)	1.395(5)	N(2) - C(6)	1.350(5)	N(3) - C(7)	1.343(5)
N(3) - C(10)	1.334(5)	N(4) – C(8)	1.340(6)	N(4) - C(9)	1.336(6)
C(1) - C(2)	1.425(6)	C(1) - C(1')	1.488(6)	C(2) - C(3)	1.397(6)
C(3) - C(4)	1.365(6)	C(4) - C(5)	1.375(6)	C(6) - C(7)	1.509(6)
C(7) - C(8)	1.377(6)	C(9) - C(10)	1.385(6)	N(2) - H(2)	0.94(6)

Atoms	Bond [Å]	Atoms	Bond [Å]	Atoms	Bond [Å]
O(2) - C(16)	1.226(5)	N(5) - C(11)	1.345(6)	N(5) - C(15)	1.338(5)
N(6) - C(12)	1.405(6)	N(6) - C(16)	1.346(6)	N(7) - C(17)	1.339(5)
N(7) - C(20)	1.326(5)	N(8) - C(18)	1.337(6)	N(8) - C(19)	1.330(6)
C(11) - C(12)	1.410(6)	C(11) - C(11')	1.506(6)	C(12) - C(13)	1.394(6)
C(13) - C(14)	1.375(6)	C(14) - C(15)	1.371(6)	C(16) - C(17)	1.507(6)
C(17) - C(18)	1.376(6)	C(19) - C(20)	1.388(6)	N(6) - H(6)	0.89(4)

Table 6.10: Bonds angles [°] for ligand (**2.2**) molecule A and B, respectively.

Atoms	Angle [°]	Atoms	Angle [°]	Atoms	Angle [°]
C(1) - N(1) - C(5)	121.6(4)	C(2) - N(2) - C(6)	128.9(3)	C(7) - N(3) - C(10)	115.4(3)
C(8) - N(4) - C(9)	115.5(4)	N(1) - C(1) - C(2)	119.5(4)	N(1) - C(1) - C(1')	115.4(4)
C(2) - C(1) - C(1')	125.1(4)	N(2) - C(2) - C(1)	120.0(4)	N(2) - C(2) - C(3)	122.7(4)
C(1) - C(2) - C(3)	117.3(4)	C(2) - C(3) - C(4)	121.4(4)	C(3) - C(4) - C(5)	118.4(4)
N(1) - C(5) - C(4)	121.6(4)	O(1) - C(6) - N(2)	127.1(4)	O(1) - C(6) - C(7)	119.6(4)
N(2) - C(6) - C(7)	113.3(4)	N(3) - C(7) - C(6)	117.5(4)	N(3) - C(7) - C(8)	122.3(4)
C(6) - C(7) - C(8)	120.2(4)	N(4) - C(8) - C(7)	122.3(4)	N(4) - C(9) - C(10)	122.3(4)
N(3) - C(10) - C(9)	122.3(4)				

Atoms	Angle [°]	Atoms	Angle [°]	Atoms	Angle [°]
C(11) - N(5) - C(15)	121.1(3)	C(12) - N(6) - C(16)	129.2(4)	C(17) - N(7) - C(20)	115.7(4)
C(18) - N(8) - C(19)	115.0(4)	N(5) - C(11) - C(12)	119.9(4)	N(5) - C(11) - C(11')	114.4(4)
C(12) - C(11) - C(11')	125.7(4)	N(6) - C(12) - C(11)	119.8(4)	N(6) - C(12) - C(13)	121.5(4)
C(11) - C(12) - C(13)	118.7(4)	C(12) - C(13) - C(14)	119.2(4)	C(13) - C(14) - C(15)	120.0(4)
N(5) - C(15) - C(14)	121.2(4)	O(2) - C(16) - N(6)	126.9(4)	O(2) - C(16) - C(17)	119.9(4)
N(6) - C(16) - C(17)	113.3(4)	N(7) - C(17) - C(16)	118.4(4)	N(7) - C(17) - C(18)	122.0(4)
C(16) - C(17) - C(18)	119.6(4)	N(8) - C(18) - C(17)	122.7(4)	N(8) - C(19) - C(20)	122.6(4)
N(7) - C(20) - C(19)	122.0(4)				

Table 6.11: Bonds lengths [Å] for $[Cu_3(\mathbf{L^2})(OAc)_3MeO]$ **(2.17).**

Atoms	Bond [Å]	Atoms	Bond [Å]	Atoms	Bond [Å]
Cu(1) - O(3)	2.395(6)	Cu(1) - O(4)	1.942(9)	Cu(1) - N(2)	1.930(11)
Cu(1) - N(3)	2.141(11)	Cu(1) - N(5)	2.069(8)	Cu(2) - N(1)	2.113(10)
Cu(2) - N(6)	1.931(9)	Cu(2) - N(7)	2.062(10)	Cu(2) - O(3)b	2.417(7)
Cu(2) - O(5)b	1.945(9)	Cu(3) - O(6)	1.961(9)	Cu(3) - O(7)	1.941(8)
Cu(3) - O(8)	1.946(10)	Cu(3) - O(9)	1.965(8)	Cu(3) - N(4)	2.200(11)
O(1) - C(6)	1.225(18)	O(2) - C(16)	1.228(16)	O(3) - C(28A)	1.41(8)
O(3) - C(28B)	1.45(4)	O(4) - C(22)	1.256(17)	O(5) - C(22)	1.268(17)
O(6) - C(24)	1.264(16)	O(7) - C(26)	1.249(14)	O(8) - C(24)a	1.275(15)
O(9) - C(26)a	1.232(16)	N(1) - C(1)	1.361(15)	N(1) - C(5)	1.356(17)
N(2) - C(2)	1.407(16)	N(2) - C(6)	1.364(17)	N(3) - C(7)	1.322(19)
N(3) - C(10)	1.352(19)	N(4) - C(8)	1.326(16)	N(4) - C(9)	1.36(2)
N(5) - C(11)	1.358(16)	N(5) - C(15)	1.342(18)	N(6) - C(12)	1.389(16)
N(6) - C(16)	1.335(17)	N(7) - C(17)	1.335(17)	N(7) - C(20)	1.320(19)
N(8) - C(18)	1.35(2)	N(8) - C(19)	1.31(2)	C(1) - C(2)	1.428(16)
C(1) - C(11)	1.515(17)	C(2) - C(3)	1.360(19)	C(3) - C(4)	1.380(18)
C(4) - C(5)	1.370(18)	C(6) - C(7)	1.478(18)	C(7) - C(8)	1.402(19)
C(9) - C(10)	1.40(2)	C(11) - C(12)	1.407(16)	C(12) - C(13)	1.36(2)
C(13) - C(14)	1.38(2)	C(14) - C(15)	1.396(18)	C(16) - C(17)	1.507(18)
C(17) - C(18)	1.38(2)	C(19) - C(20)	1.38(2)	C(22) - C(23)	1.49(2)
C(24) - C(25)	1.52(2)	C(26) - C(27)	1.50(2)		

Table 6.12: Bond angles [°] for $[Cu_3(L^2)(OAc)_3MeO]$ (**2.17**).

Atoms	Angle [°]	Atoms	Angle [°]	Atoms	Angle [°]
O(3) - Cu(1) - O(4)	98.9(3)	O(3) - Cu(1) - N(2)	95.4(3)	O(3) - Cu(1) - N(3)	102.1(3)
O(3) - Cu(1) - N(5)	126.3(3)	O(4) - Cu(1) - N(2)	162.8(4)	O(4) - Cu(1) - N(3)	88.0(4)
O(4) - Cu(1) - N(5)	92.3(4)	N(2) - Cu(1) - N(3)	79.5(4)	N(2) - Cu(1) - N(5)	87.0(4)
N(3) - Cu(1) - N(5)	130.8(4)	N(1) - Cu(2) - N(6)	84.9(4)	N(1) - Cu(2) - N(7)	134.9(5)
N(1) - Cu(2) - O(3)b	105.7(4)	N(1) - Cu(2) - O(5)b	97.8(4)	N(6) - Cu(2) - N(7)	80.1(4)
N(6) - Cu(2) - O(3)b	93.9(4)	N(6) - Cu(2) - O(5)b	167.7(5)	N(7) - Cu(2) - O(3)b	117.6(3)
N(7) - Cu(2) - O(5)b	89.6(4)	O(3)b - Cu(2) - O(5)b	96.9(4)	O(6) - Cu(3) - O(7)	90.8(4)
O(6) - Cu(3) - O(8)	169.6(4)	O(6) - Cu(3) - O(9)	88.0(4)	O(6) - Cu(3) - N(4)	97.1(4)
O(7) - Cu(3) - O(8)	89.1(4)	O(7) - Cu(3) - O(9)	169.1(4)	O(7) - Cu(3) - N(4)	94.9(4)
O(8) - Cu(3) - O(9)	90.1(4)	O(8) - Cu(3) - N(4)	93.3(4)	O(9) - Cu(3) - N(4)	96.0(4)
Cu(1) - O(3) - C(28A)	89(4)	Cu(1) - O(3) - C(28B)	136(4)	Cu(1) - O(3) - Cu(2)b	99.8(2)
C(28A) - O(3) - Cu(2)b	148(4)	C(28B) - O(3) - Cu(2)b	83(4)	Cu(1) - O(4) - C(22)	140.6(8)
C(22) - O(5) - Cu(2)b	131.7(9)	Cu(3) - O(6) - C(24)	121.3(8)	Cu(3) - O(7) - C(26)	121.4(9)
Cu(3) - O(8) - C(24)a	125.2(9)	Cu(3) - O(9) - C(26)a	122.1(7)	Cu(2) - N(1) - C(1)	124.9(8)
Cu(2) - N(1) - C(5)	112.9(8)	C(1) - N(1) - C(5)	119.5(10)	Cu(1) - N(2) - C(2)	120.4(9)
Cu(1) - N(2) - C(6)	119.3(8)	C(2) - N(2) - C(6)	119.3(11)	Cu(1) - N(3) - C(7)	110.9(8)
Cu(1) - N(3) - C(10)	130.8(11)	C(7) - N(3) - C(10)	118.3(12)	Cu(3) - N(4) - C(8)	120.4(9)
Cu(3) - N(4) - C(9)	121.5(8)	C(8) - N(4) - C(9)	118.1(11)	Cu(1) - N(5) - C(11)	124.8(8)
Cu(1) - N(5) - C(15)	113.8(8)	C(11) - N(5) - C(15)	119.2(10)	Cu(2) - N(6) - C(12)	120.4(8)
Cu(2) - N(6) - C(16)	119.5(8)	C(12) - N(6) - C(16)	120.1(10)	Cu(2) - N(7) - C(17)	112.6(8)
Cu(2) - N(7) - C(20)	129.8(10)	C(17) - N(7) - C(20)	117.4(12)	C(18) - N(8) - C(19)	115.0(14)
N(1) - C(1) - C(2)	120.5(11)	N(1) - C(1) - C(11)	118.3(9)	C(2) - C(1) - C(11)	121.2(10)
N(2) - C(2) - C(1)	119.3(11)	N(2) - C(2) - C(3)	122.8(11)	C(1) - C(2) - C(3)	118.0(11)
C(2) - C(3) - C(4)	120.9(12)	C(3) - C(4) - C(5)	119.4(12)	N(1) - C(5) - C(4)	121.6(12)
O(1) - C(6) - N(2)	127.9(12)	O(1) - C(6) - C(7)	120.0(12)	N(2) - C(6) - C(7)	112.1(12)
N(3) - C(7) - C(6)	117.7(11)	N(3) - C(7) - C(8)	121.8(12)	C(6) - C(7) - C(8)	120.5(13)
N(4) - C(8) - C(7)	120.7(13)	N(4) - C(9) - C(10)	121.0(13)	N(3) - C(10) - C(9)	120.1(15)
N(5) - C(11) - C(1)	118.7(9)	N(5) - C(11) - C(12)	121.3(11)	C(1) - C(11) - C(12)	120.0(11)
N(6) - C(12) - C(11)	121.2(11)	N(6) - C(12) - C(13)	119.7(11)	C(11) - C(12) - C(13)	118.9(12)
C(12) - C(13) - C(14)	119.8(13)	C(13) - C(14) - C(15)	119.6(13)	N(5) - C(15) - C(14)	121.1(13)
O(2) - C(16) - N(6)	128.0(12)	O(2) - C(16) - C(17)	120.4(12)	N(6) - C(16) - C(17)	111.5(11)
N(7) - C(17) - C(16)	115.5(11)	N(7) - C(17) - C(18)	120.0(12)	C(16) - C(17) - C(18)	124.4(12)
N(8) - C(18) - C(17)	122.8(14)	N(8) - C(19) - C(20)	123.4(15)	N(7) - C(20) - C(19)	121.4(14)
O(4) - C(22) - O(5)	125.8(13)	O(4) - C(22) - C(23)	117.5(12)	O(5) - C(22) - C(23)	116.5(13)
O(6) - C(24) - C(25)	118.9(11)	O(6) - C(24) - O(8)a	124.0(12)	C(25) - C(24) - O(8)a	117.0(12)
O(7) - C(26) - C(27)	116.8(13)	O(7) - C(26) - O(9)a	127.4(11)	C(27) - C(26) - O(9)a	115.8(11)

Table 6.13: Bonds lengths [Å] for $[C_{51}H_{42}N_4O_5]$ **(3.11)**.

Atoms	Bond [Å]	Atoms	Bond [Å]	Atoms	Bond [Å]
O(1) - C(42)	1.375(9)	O(1) - C(45)	1.441(13)	O(2) - C(48)	1.424(10)
O(3) - C(47)	1.446(11)	O(4) - C(49)	1.454(10)	O(4) - C(50)	1.340(14)
O(5) - C(50)	1.218(14)	N(1) - C(1)	1.355(10)	N(1) - C(4)	1.349(11)
N(2) - C(6)	1.361(10)	N(2) - C(9)	1.357(9)	N(3) - C(11)	1.366(9)
N(3) - C(14)	1.376(10)	N(4) - C(16)	1.357(11)	N(4) - C(19)	1.382(10)
C(1) - C(2)	1.419(10)	C(1) - C(20)	1.385(11)	C(2) - C(3)	1.348(13)
C(3) - C(4)	1.446(11)	C(4) - C(5)	1.385(12)	C(5) - C(6)	1.398(10)
C(5) - C(39)	1.511(11)	C(6) - C(7)	1.445(12)	C(7) - C(8)	1.351(12)
C(8) - C(9)	1.446(11)	C(9) - C(10)	1.419(10)	C(10) - C(11)	1.375(11)
C(10) - C(21)	1.512(11)	C(11) - C(12)	1.429(11)	C(12) - C(13)	1.335(11)
C(13) - C(14)	1.432(10)	C(14) - C(15)	1.384(11)	C(15) - C(16)	1.400(11)
C(15) - C(27)	1.521(9)	C(16) - C(17)	1.456(11)	C(17) - C(18)	1.351(12)
C(18) - C(19)	1.438(12)	C(19) - C(20)	1.400(10)	C(20) - C(33)	1.509(10)
C(21) - C(22)	1.387(13)	C(21) - C(26)	1.363(12)	C(22) - C(23)	1.407(13)
C(23) - C(24)	1.346(15)	C(24) - C(25)	1.391(14)	C(25) - C(26)	1.411(13)
C(27) - C(28)	1.390(8)	C(27) - C(32)	1.390(7)	C(28) - C(29)	1.391(8)
C(29) - C(30)	1.390(8)	C(30) - C(31)	1.390(10)	C(31) - C(32)	1.391(8)
C(33) - C(34)	1.352(13)	C(33) - C(38)	1.366(15)	C(34) - C(35)	1.407(13)
C(35) - C(36)	1.311(17)	C(36) - C(37)	1.321(16)	C(37) - C(38)	1.383(15)
C(39) - C(40)	1.381(13)	C(39) - C(44)	1.384(12)	C(40) - C(41)	1.381(12)
C(41) - C(42)	1.364(11)	C(42) - C(43)	1.375(15)	C(43) - C(44)	1.367(13)
C(45) - C(46)	1.520(12)	C(46) - C(47)	1.507(16)	C(46) - C(48)	1.479(13)
C(46) - C(49)	1.535(12)	C(50) - C(51)	1.502(15)		

Table 6.14: Bond angles [°] for $[C_{51}H_{42}N_4O_5]$ **(3.11)**.

Atoms	Angle [°]	Atoms	Angle [°]	Atoms	Angle [°]
C(42) - O(1) - C(45)	117.2(7)	C(49) - O(4) - C(50)	118.1(7)	C(1) - N(1) - C(4)	110.9(7)
C(6) - N(2) - C(9)	107.4(6)	C(11) - N(3) - C(14)	108.7(6)	C(16) - N(4) - C(19)	107.3(6)
N(1) - C(1) - C(2)	107.2(7)	N(1) - C(1) - C(20)	127.3(7)	C(2) - C(1) - C(20)	125.4(7)
C(1) - C(2) - C(3)	108.0(7)	C(2) - C(3) - C(4)	107.8(7)	N(1) - C(4) - C(3)	106.1(7)
N(1) - C(4) - C(5)	128.7(7)	C(3) - C(4) - C(5)	125.1(7)	C(4) - C(5) - C(6)	124.3(7)
C(4) - C(5) - C(39)	115.8(6)	C(6) - C(5) - C(39)	119.8(7)	N(2) - C(6) - C(5)	125.9(7)
N(2) - C(6) - C(7)	110.0(6)	C(5) - C(6) - C(7)	124.0(7)	C(6) - C(7) - C(8)	105.9(7)
C(7) - C(8) - C(9)	107.9(7)	N(2) - C(9) - C(8)	108.8(6)	N(2) - C(9) - C(10)	125.7(7)
C(8) - C(9) - C(10)	125.4(7)	C(9) - C(10) - C(11)	125.5(7)	C(9) - C(10) - C(21)	116.1(7)
C(11) - C(10) - C(21)	118.4(6)	N(3) - C(11) - C(10)	127.6(7)	N(3) - C(11) - C(12)	107.1(7)
C(10) - C(11) - C(12)	125.3(7)	C(11) - C(12) - C(13)	109.1(7)	C(12) - C(13) - C(14)	107.3(7)
N(3) - C(14) - C(13)	107.7(6)	N(3) - C(14) - C(15)	124.7(7)	C(13) - C(14) - C(15)	127.5(7)
C(14) - C(15) - C(16)	126.5(7)	C(14) - C(15) - C(27)	117.4(6)	C(16) - C(15) - C(27)	116.1(7)
N(4) - C(16) - C(15)	125.4(7)	N(4) - C(16) - C(17)	108.7(7)	C(15) - C(16) - C(17)	125.7(8)
C(16) - C(17) - C(18)	107.8(8)	C(17) - C(18) - C(19)	106.5(7)	N(4) - C(19) - C(18)	109.6(7)
N(4) - C(19) - C(20)	126.2(8)	C(18) - C(19) - C(20)	124.1(7)	C(1) - C(20) - C(19)	125.6(7)
C(1) - C(20) - C(33)	116.9(6)	C(19) - C(20) - C(33)	117.6(7)	C(10) - C(21) - C(22)	119.2(7)
C(10) - C(21) - C(26)	121.3(8)	C(22) - C(21) - C(26)	119.4(8)	C(21) - C(22) - C(23)	120.2(9)
C(22) - C(23) - C(24)	119.7(9)	C(23) - C(24) - C(25)	121.5(9)	C(24) - C(25) - C(26)	118.2(9)
C(21) - C(26) - C(25)	121.0(8)	C(15) - C(27) - C(28)	120.1(5)	C(15) - C(27) - C(32)	120.0(6)
C(28) - C(27) - C(32)	120.0(5)	C(27) - C(28) - C(29)	120.0(5)	C(28) - C(29) - C(30)	120.0(6)
C(29) - C(30) - C(31)	120.0(5)	C(30) - C(31) - C(32)	120.0(6)	C(27) - C(32) - C(31)	120.0(6)
C(20) - C(33) - C(34)	119.5(8)	C(20) - C(33) - C(38)	122.2(8)	C(34) - C(33) - C(38)	118.1(8)
C(33) - C(34) - C(35)	119.7(9)	C(34) - C(35) - C(36)	121.2(10)	C(35) - C(36) - C(37)	119.5(10)
C(36) - C(37) - C(38)	121.7(12)	C(33) - C(38) - C(37)	119.8(10)	C(5) - C(39) - C(40)	122.2(7)
C(5) - C(39) - C(44)	118.7(8)	C(40) - C(39) - C(44)	119.2(8)	C(39) - C(40) - C(41)	119.8(8)
C(40) - C(41) - C(42)	119.9(9)	O(1) - C(42) - C(41)	126.2(9)	O(1) - C(42) - C(43)	113.0(7)
C(41) - C(42) - C(43)	120.8(8)	C(42) - C(43) - C(44)	119.3(9)	C(39) - C(44) - C(43)	120.8(10)
O(1) - C(45) - C(46)	106.0(7)	C(45) - C(46) - C(47)	106.3(8)	C(45) - C(46) - C(48)	111.2(8)
C(45) - C(46) - C(49)	110.0(7)	C(47) - C(46) - C(48)	109.7(8)	C(47) - C(46) - C(49)	110.2(8)
C(48) - C(46) - C(49)	109.5(8)	O(3) - C(47) - C(46)	113.6(8)	O(2) - C(48) - C(46)	109.8(8)
O(4) - C(49) - C(46)	112.3(7)	O(4) - C(50) - O(5)	122.9(10)	O(4) - C(50) - C(51)	112.5(9)
O(5) - C(50) - C(51)	124.7(10)				

Table 6.15: Bonds lengths [Å] for $[C_{49}H_{38}N_4O_4Zn]$ **(3.25)**.

Atoms	Bond [Å]	Atoms	Bond [Å]	Atoms	Bond [Å]
Zn(1) - O(1)	2.171(5)	Zn(1) - N(1)	2.055(6)	Zn(1) - N(2)	2.052(5)
Zn(1) - N(3)	2.049(6)	Zn(1) - N(4)	2.053(5)	O(1) - C(45)	1.444(10)
O(1) - C(46)	1.434(9)	C(47) - C(45)	1.524(12)	C(47) - C(46)	1.543(11)
C(47) - C(48)	1.506(11)	C(47) - C(49)	1.517(12)	O(2) - C(48)	1.394(14)
O(3) - C(49)	1.450(12)	O(4) - C(24)	1.366(11)	N(1) - C(1)	1.355(8)
N(1) - C(4)	1.371(9)	N(2) - C(6)	1.380(9)	N(2) - C(9)	1.372(8)
N(3) - C(11)	1.374(8)	N(3) - C(14)	1.374(9)	N(4) - C(16)	1.373(9)
N(4) - C(19)	1.384(9)	C(1) - C(2)	1.437(10)	C(1) - C(20)	1.402(10)
C(2) - C(3)	1.334(11)	C(3) - C(4)	1.427(10)	C(4) - C(5)	1.411(9)
C(5) - C(6)	1.421(9)	C(5) - C(27)	1.483(10)	C(6) - C(7)	1.414(8)
C(7) - C(8)	1.357(10)	C(8) - C(9)	1.430(9)	C(9) - C(10)	1.406(10)
C(10) - C(11)	1.401(9)	C(10) - C(33)	1.478(9)	C(11) - C(12)	1.448(10)
C(12) - C(13)	1.326(11)	C(13) - C(14)	1.440(10)	C(14) - C(15)	1.403(8)
C(15) - C(16)	1.391(9)	C(15) - C(39)	1.483(10)	C(16) - C(17)	1.434(8)
C(17) - C(18)	1.348(10)	C(18) - C(19)	1.427(10)	C(19) - C(20)	1.410(10)
C(20) - C(21)	1.515(10)	C(21) - C(22)	1.402(12)	C(21) - C(26)	1.324(11)
C(22) - C(23)	1.410(14)	C(23) - C(24)	1.338(14)	C(24) - C(25)	1.360(13)
C(25) - C(26)	1.389(11)	C(27) - C(28)	1.394(10)	C(27) - C(32)	1.388(10)
C(28) - C(29)	1.377(12)	C(29) - C(30)	1.374(14)	C(30) - C(31)	1.369(14)
C(31) - C(32)	1.354(13)	C(33) - C(34)	1.363(11)	C(33) - C(38)	1.374(10)
C(34) - C(35)	1.369(12)	C(35) - C(36)	1.370(12)	C(36) - C(37)	1.332(14)
C(37) - C(38)	1.380(13)	C(39) - C(40)	1.397(10)	C(39) - C(44)	1.401(10)
C(40) - C(41)	1.372(10)	C(41) - C(42)	1.352(10)	C(42) - C(43)	1.387(10)
C(43) - C(44)	1.356(10)				

Table 6.16: Bond angles [°] for $[C_{49}H_{38}N_4O_4Zn]$ **(3.25).**

Atoms	Angle [°]	Atoms	Angle [°]	Atoms	Angle [°]
O(1) - Zn(1) - N(1)	96.09(17)	O(1) - Zn(1) - N(2)	91.43(17)	O(1) - Zn(1) - N(3)	95.14(17)
O(1) - Zn(1) - N(4)	99.40(18)	N(1) - Zn(1) - N(2)	89.8(2)	N(1) - Zn(1) - N(3)	168.76(18)
N(1) - Zn(1) - N(4)	89.0(2)	N(2) - Zn(1) - N(3)	89.6(2)	N(2) - Zn(1) - N(4)	169.16(18)
N(3) - Zn(1) - N(4)	89.5(2)	Zn(1) - O(1) - C(45)	123.6(4)	Zn(1) - O(1) - C(46)	133.0(4)
C(45) - O(1) - C(46)	91.8(5)	C(45) - C(47) - C(46)	84.7(6)	C(45) - C(47) - C(48)	113.2(7)
C(45) - C(47) - C(49)	114.0(7)	C(46) - C(47) - C(48)	116.6(7)	C(46) - C(47) - C(49)	114.3(7)
C(48) - C(47) - C(49)	111.5(7)	Zn(1) - N(1) - C(1)	126.7(5)	Zn(1) - N(1) - C(4)	126.1(4)
C(1) - N(1) - C(4)	106.2(6)	Zn(1) - N(2) - C(6)	126.9(4)	Zn(1) - N(2) - C(9)	126.9(4)
C(6) - N(2) - C(9)	105.8(5)	Zn(1) - N(3) - C(11)	125.3(4)	Zn(1) - N(3) - C(14)	126.2(4)
C(11) - N(3) - C(14)	107.7(5)	Zn(1) - N(4) - C(16)	126.4(4)	Zn(1) - N(4) - C(19)	127.4(5)
C(16) - N(4) - C(19)	106.2(5)	N(1) - C(1) - C(2)	110.0(6)	N(1) - C(1) - C(20)	125.8(7)
C(2) - C(1) - C(20)	124.3(7)	C(1) - C(2) - C(3)	106.8(7)	C(2) - C(3) - C(4)	107.6(6)
N(1) - C(4) - C(3)	109.5(6)	N(1) - C(4) - C(5)	126.0(6)	C(3) - C(4) - C(5)	124.5(7)
C(4) - C(5) - C(6)	125.2(6)	C(4) - C(5) - C(27)	117.9(6)	C(6) - C(5) - C(27)	116.8(6)
N(2) - C(6) - C(5)	124.8(5)	N(2) - C(6) - C(7)	109.7(6)	C(5) - C(6) - C(7)	125.4(6)
C(6) - C(7) - C(8)	108.0(6)	C(7) - C(8) - C(9)	106.4(6)	N(2) - C(9) - C(8)	110.1(6)
N(2) - C(9) - C(10)	125.3(6)	C(8) - C(9) - C(10)	124.6(6)	C(9) - C(10) - C(11)	124.5(6)
C(9) - C(10) - C(33)	118.8(6)	C(11) - C(10) - C(33)	116.6(6)	N(3) - C(11) - C(10)	127.1(6)
N(3) - C(11) - C(12)	108.3(6)	C(10) - C(11) - C(12)	124.5(6)	C(11) - C(12) - C(13)	107.3(6)
C(12) - C(13) - C(14)	108.7(6)	N(3) - C(14) - C(13)	107.9(5)	N(3) - C(14) - C(15)	126.0(6)
C(13) - C(14) - C(15)	126.1(6)	C(14) - C(15) - C(16)	124.8(6)	C(14) - C(15) - C(39)	116.8(6)
C(16) - C(15) - C(39)	118.4(5)	N(4) - C(16) - C(15)	126.3(5)	N(4) - C(16) - C(17)	109.2(6)
C(15) - C(16) - C(17)	124.5(6)	C(16) - C(17) - C(18)	107.9(6)	C(17) - C(18) - C(19)	107.0(6)
N(4) - C(19) - C(18)	109.8(6)	N(4) - C(19) - C(20)	124.1(6)	C(18) - C(19) - C(20)	126.2(7)
C(1) - C(20) - C(19)	125.8(7)	C(1) - C(20) - C(21)	117.3(6)	C(19) - C(20) - C(21)	116.9(6)
C(20) - C(21) - C(22)	119.2(7)	C(20) - C(21) - C(26)	122.5(7)	C(22) - C(21) - C(26)	118.3(8)
C(21) - C(22) - C(23)	119.1(9)	C(22) - C(23) - C(24)	121.2(9)	O(5) - C(24) - C(23)	118.6(9)
O(4) - C(24) - C(25)	122.7(8)	C(23) - C(24) - C(25)	118.6(8)	C(24) - C(25) - C(26)	121.0(7)
C(21) - C(26) - C(25)	121.8(8)	C(5) - C(27) - C(28)	123.0(7)	C(5) - C(27) - C(32)	120.1(7)
C(28) - C(27) - C(32)	116.9(7)	C(27) - C(28) - C(29)	120.6(8)	C(28) - C(29) - C(30)	120.5(8)
C(29) - C(30) - C(31)	119.3(9)	C(30) - C(31) - C(32)	120.4(8)	C(27) - C(32) - C(31)	122.2(8)
C(10) - C(33) - C(34)	121.4(6)	C(10) - C(33) - C(38)	122.0(7)	C(34) - C(33) - C(38)	116.6(7)
C(33) - C(34) - C(35)	122.2(7)	C(34) - C(35) - C(36)	119.9(8)	C(35) - C(36) - C(37)	119.1(8)
C(36) - C(37) - C(38)	120.9(8)	C(33) - C(38) - C(37)	121.3(8)	C(15) - C(39) - C(40)	122.5(6)
C(15) - C(39) - C(44)	120.6(6)	C(40) - C(39) - C(44)	117.0(6)	C(39) - C(40) - C(41)	121.0(6)
C(40) - C(41) - C(42)	120.5(7)	C(41) - C(42) - C(43)	120.1(7)	C(42) - C(43) - C(44)	119.9(7)
C(39) - C(44) - C(43)	121.5(7)	O(1) - C(45) - C(47)	92.0(6)	O(1) - C(46) - C(47)	91.5(5)
C(47) - C(48) - O(2)	108.6(7)	C(47) - C(49) - O(3)	114.2(8)		

Table 6.17: Crystal data and structure refinement parameters for ligands **(2.1)**, **(2.2)**, and **(2.3)**.

	Ligand (2.1)	**Ligand (2.2)**	**Ligand (2.3)**
Empirical formula	$C_{22}H_{16}N_6O_2$	$C_{20}H_{14}N_8O_2$	$C_{18}H_{22}N_4O_4$
Formula weight	396.41	398.39	358.40
Temperature	150(2) K	150(2) K	150(2) K
Wavelength (Mo Kα)	0.71073 Å	0.71073 Å	0.71073 Å
Crystal colour, Crystal description	Colourless, Plate	Beige, Needle	Yellow, Needle
Crystal size (mm x mm x mm)	0.46 x 0.15 x 0.05	0.41 x 0.04 x 0.04	0.32 x 0.05 x 0.05
Crystal system, Space group	Monoclinic, P2(1)/c	Monoclinic, P2(1)/c	Triclinic, P-1
Unit cell dimensions	a = 14.1606(13) Å, α = 90° b = 3.9083(3) Å, β = 94.593(4)° c = 16.1931(13) Å, γ = 90°	a = 7.7883(5) Å, α = 90.00° b = 15.5419(10) Å, β = 101.984(3)° c = 14.6518(9) Å, γ = 90.00°	a = 7.7833(7) Å, α = 66.448(4)° b = 10.0125(8) Å, β = 82.145(4)° c = 12.5094(10) Å, γ = 90.021(4)°
Cell volume	893.31(13) $Å^3$	1734.87(19) $Å^3$	883.64(13) $Å^3$
Z, Calculated density	2, 1.474 Mg/m^3	4, 1.525 Mg/m^3	2, 1.347 Mg/m^3
Absorption coefficient (μ)	0.100 mm^{-1}	0.106 mm^{-1}	0.097 mm^{-1}
F(000)	412	824	380
θ range for data collection	2.52 to 22.49°	1.93 to 22.50°	1.80 to 22.50°
Limiting indices	h = -15 to 14, k = -3 to 4, l = -17 to 17	h = -8 to 8, k = -16 to 16, l = -15 to 15	h = -8 to 8, k = -10 to 10, l = -13 to 13
Reflections collected / unique	10625 / 1163 [R(int) = 0.0472]	25144 / 2273 [R(int) = 0.0455]	33998 / 2309 [R(int) = 0.0495]
Completeness	99.8%	100%	99.8%
Absorption correction	Semi-empirical from equivalents	Semi-empirical from equivalents	Semi-empirical from equivalents
Max. and min. transmission	0.5382 and 0.7461	0.6575 and 0.7461	0.6574 and 0.7460
Refinement method	Full-matrix least-squares on F^2	Full-matrix least-squares on F^2	Full-matrix least-squares on F^2
Data / Restraints / Parameters	1163 / 0 / 137	2273 / 0 / 272	2309 / 0 / 238
Goodness-of-fit on F^2	1.076	1.260	1.410
Final R indices [I > 2σ(I)]	R1 = 0.0676, wR2 = 0.1768	R1 = 0.0690, wR2 = 0.1584	R1 = 0.1449, wR2 = 0.3363
R indices (all data)	R1 = 0.0753, wR2 = 0.1863	R1 = 0.0781, wR2 = 0.1735	R1 = 0.1473, wR2 = 0.3374
Largest diff. peak and hole	1.254 and -0.334 e $Å^{-3}$	0.373 and -0.382 e $Å^{-3}$	0.574 and -0.386 e $Å^{-3}$

Table 6.18: Crystal data and structure refinement parameters for compounds **(2.6)**, **(2.7)**, and **(2.8)**.

	$[Zn_2(L^1)(OAc)(MeO)]_2$ **(2.6)**	$[Cu_2(L^1)(OAc)_2]$ **(2.7)**	$[Ni(L^1)]_3$ **(2.8)**
Empirical formula	$C_{50}H_{40}N_{12}O_{10}Zn_4$	$C_{34.67}H_{26.67}N_8O_{9.33}Cu_{2.67}$	$C_{66}H_{42}N_{18}O_6Ni_3$
Formula weight	1230.42	874.08	1359.3
Temperature	150(2) K	150(2) K	150(2) K
Wavelength (Mo Kα)	0.71073 Å	0.71073 Å	0.71073 Å
Crystal colour, Crystal description	Yellow, Block	Green, Plate	Orange-brown, Block
Crystal size (mm x mm x mm)	0.36 x 0.30 x 0.25	0.33 x 0.25 x 0.05	0.50 x 0.50 x 0.12
Crystal system, Space group	Orthorhombic, Cmca	Monoclinic, C(2)/c	Rhombohedral, R-(3)c
Unit cell dimensions	a = 17.1472(8) Å, α = 90° b = 22.4405(10) Å, β = 90° c = 16.7592(7) Å, γ = 90°	a = 31.202(2) Å, α = 90° b = 9.1176(6) Å, β = 123.052(3)° c = 21.4203(14) Å, γ = 90°	a = 23.3442(16) Å, α = 90° b = 23.3442(16) Å, β = 90° c = 24.987(4) Å, γ = 120°
Cell volume	6448.8(5) $Å^3$	5107.7(6) $Å^3$	11792(2) $Å^3$
Z, Calculated density	4, 1.267 Mg/m^3	6, 1.725 Mg/m^3	6, 1.148 Mg/m^3
Absorption coefficient (μ)	1.526 mm^{-1}	1.725 mm^{-1}	0.765 mm^{-1}
F(000)	1552	2656	4176
θ range for data collection	2.85 to 27.40°	2.43 to 28.36°	2.79 to 29.46°
Limiting indices	h = -22 to 21, k = -29 to 29, l = -21 to 21	h = -41 to 41, k = -12 to 11, l = -28 to 28	h = -24 to 25, k = -25 to 25, l = -26 to 26
Reflections collected / unique	55837 / 3783 [R(int) = 0.0348]	107512 / 6375 [R(int) = 0.0643]	131481 / 1720 [R(int) = 0.0406]
Completeness	98.0%	99.5%	99.9%
Absorption correction	Semi-empirical from equivalents	Semi-empirical from equivalents	Semi-empirical from equivalents
Max. and min. transmission	0.6681 and 0.7456	0.5998 and 0.9187	0.6540 and 0.7461
Refinement method	Full-matrix least-squares on F^2	Full-matrix least-squares on F^2	Full-matrix least-squares on F^2
Data / Restraints / Parameters	3783 / 0 / 181	6375 / 0 / 373	1720 / 0 / 142
Goodness-of-fit on F^2	0.966	1.007	1.145
Final R indices [I > 2σ(I)]	R1 = 0.0393, wR2 = 0.1094	R1 = 0.0268, wR2 = 0.0679	R1 = 0.0667, wR2 = 0.1968
R indices (all data)	R1 = 0.0427, wR2 = 0.1114	R1 = 0.0368, wR2 = 0.0761	R1 = 0.0701, wR2 = 0.2012
Largest diff. peak and hole	1.851 and -0.776 e $Å^{-3}$	0.870 and -0.482 e $Å^{-3}$	1.505 and -0.462 e $Å^{-3}$

Table 6.19: Crystal data and structure refinement parameters for compounds **(2.9)**, and **(2.17)**.

	$[Ni(L^1)]_3$ **(2.9)**	$[Cu_3(L^2)(OAc)_3MeO]$ **(2.17)**
Empirical formula	$C_{66}H_{42}N_{18}O_6Ni_3$	$C_{27}H_{24}N_8O_9Cu_3$
Formula weight	1359.3	795.19
Temperature	150(2) K	150(2) K
Wavelength (Mo Kα)	0.71073 Å	0.71073 Å
Crystal colour, Crystal description	Orange-brown, Block	Green, Plate
Crystal size (mm x mm x mm)	0.30 x 0.20 x 0.02	0.16 x 0.08 x 0.06
Crystal system, Space group	Rhombohedral, R-(3)c	Triclinic, P-1
Unit cell dimensions	a = 23.843(3) Å, α = 90° b = 23.843(3) Å, β = 90° c = 20.481(6) Å, γ = 120°	a = 10.1116(7) Å, α = 94.470(3)° b = 12.3153(8) Å, β = 101.887(3)° c = 12.3153(8) Å, γ = 112.050(3)°
Cell volume	10083(3) $Å^3$	1600.56(19) $Å^3$
Z, Calculated density	6, 1.343 Mg/m^3	2, 1.650 Mg/m^3
Absorption coefficient (μ)	0.914 mm^{-1}	2.039 mm^{-1}
F(000)	4176	802
θ range for data collection	1.71 to 26.54°	1.81 to 25.00°
Limiting indices	h = -29 to 29, k = -29 to 29, l = -25 to 25	h = -12 to 12, k = -14 to 12, l = -17 to 14
Reflections collected / unique	86583 / 2331 [R(int) = 0.0775]	9299 / 5295 [R(int) = 0.0574]
Completeness	99.4%	94.1%
Absorption correction	Semi-empirical from equivalents	Semi-empirical from equivalents
Max. and min. transmission	0.6764 and 0.7454	0.6264 and 0.7454
Refinement method	Full-matrix least-squares on F^2	Full-matrix least-squares on F^2
Data / Restraints / Parameters	2331 / 0 / 152	5295 / 10 / 425
Goodness-of-fit on F^2	1.133	0.997
Final R indices [I > 2σ(I)]	R1 = 0.0620, wR2 = 0.1922	R1 = 0.0952, wR2 = 0.2440
R indices (all data)	R1 = 0.0778, wR2 = 0.2016	R1 = 0.1599, wR2 = 0.2772
Largest diff. peak and hole	1.191 and -1.166 e $Å^{-3}$	2.275 and -0.877 e $Å^{-3}$

Table 6.20: Crystal data and structure refinement parameters for compounds **(3.11)**, and **(3.25)**.

	$[C_{51}H_{42}N_4O_5]$ **(3.11)**	$[C_{49}H_{38}N_4O_4Zn]$ **(3.25)**
Empirical formula	$C_{51}H_{42}N_4O_5$	$C_{49}H_{38}N_4O_4Zn$
Formula weight	790.89	812.22
Temperature	150(2) K	150(2) K
Wavelength (Mo Kα)	0.71073 Å	0.71073 Å
Crystal colour, Crystal description	Purple, Plate	Red-purple, Plate
Crystal size (mm x mm x mm)	0.25 x 0.07 x 0.01	0.12 x 0.07 x 0.01
Crystal system, Space group	Triclinic, P-1	Triclinic, P-1
Unit cell dimensions	a = 10.9523(7) Å, α = 85.856(2)° b = 12.9843(8) Å, β = 75.726(2)° c = 17.5453(12) Å, γ = 66.293(2)°	a = 11.3437(6) Å, α = 68.272(2)° b = 13.5473(6) Å, β = 84.527(2)° c = 15.5202(8) Å, γ = 81.413(2)°
Cell volume	2213.0(2) $Å^3$	2188.71(19) $Å^3$
Z, Calculated density	2, 1.187 Mg/m^3	2, 1.232 Mg/m^3
Absorption coefficient (μ)	0.077 mm^{-1}	0.610mm^{-1}
F(000)	832	844
θ range for data collection	2.40 to 25.92°	1.63 to 22.50°
Limiting indices	h = -11 to 8, k = -13 to 11, l = -18 to 18	h = -12 to 12, k = -14 to 10, l = -16 to 16
Reflections collected / unique	18961 / 5225 [R(int) = 0.0952]	28402 / 5708 [R(int) = 0.0556]
Completeness	96.7%	99.6%
Absorption correction	Semi-empirical from equivalents	Semi-empirical from equivalents
Max. and min. transmission	0.6323 and 0.7454	0.6843 and 0.7454
Refinement method	Full-matrix least-squares on F^2	Full-matrix least-squares on F^2
Data / Restraints / Parameters	5225 / 0 / 532	5708 / 0 / 527
Goodness-of-fit on F^2	1.107	1.130
Final R indices [I > 2σ(I)]	R1 = 0.1182, wR2 = 0.2755	R1 = 0.0785, wR2 = 0.1937
R indices (all data)	R1 = 0.1787, wR2 = 0.3026	R1 = 0.0978, wR2 = 0.2034
Largest diff. peak and hole	0.383 and -0.402 e $Å^{-3}$	1.128 and -0.421 e $Å^{-3}$